

**Three-terminal tandem solar cells
enabled by back-contacted bottom cells
featuring passivating, carrier-selective
polysilicon based junctions**

Von der Fakultät für Elektrotechnik und Informatik
der Gottfried Wilhelm Leibniz Universität Hannover
zur Erlangung des akademischen Grades

Doktor-Ingenieur
(Dr.-Ing.)

genehmigte Dissertation

von

Dipl.-Ing.
Michael Rienäcker
geb. Häberle

2022

1. Referent: Prof. Dr. rer. nat. Robby Peibst
2. Referent: Prof. Dr. Uwe Rau
Tag der Promotion: 16. November 2021

Kurzzusammenfassung

Die vorliegende Arbeit untersucht Rückkontakt-Bottomsolarzellen mit passivierenden und ladungsträger-selektiven POLO-Kontakten mit drei Anschlüssen (3T-POLO-IBC-Bottomzelle). Sie bilden das Fundament monolithischer Tandemsolarzellen mit drei Anschlüssen. Diese neuartigen Tandemsolarzelle erlaubt die Verwendung von Subzellen, dessen Fotoströme fehlangepasst sind. Damit bietet diese Tandemsolarzellen-Technologie Flexibilität bei der Materialauswahl der Subzellen, einfache Herstellbarkeit und Robustheit gegenüber spektraler Änderung des einfallenden Lichts im Tages- und Jahresverlauf. Es werden drei aufeinander aufbauende Bausteine der 3T-POLO-IBC-Bottomsolarzelle untersucht: Erstens, der passivierende und ladungsträger-selektive POLO-Kontakt. Zweitens, die Integration von POLO-Kontakten auf der Rückseite der Solarzelle. Drittens, die Funktionsweise einer Bottomzelle mit drei Anschlüssen.

Im ersten Teil wird der Prozess der Ladungsträgerextraktion an selektiven Kontakten zum Fotoabsorber theoretisch ergründet. Die Selektivität eines Kontaktes wird auf der Grundlage von (reaktions-) kinetischen Betrachtungen am Kontakt als das Ratenverhältnis gewollter Prozesse zu ungewollten Prozessen definiert. Die Extraktionseffizienz von Ladungsträgern am Kontakt wird als das Verhältnis der externen Spannung gegenüber der internen Spannung aus thermodynamischen Gesichtspunkten abgeleitet. Um den vereinheitlichender Charakter der Definitionen in dieser Arbeit hervorzuheben, werden die bestehenden Literatur-Definitionen aus den Definitionen in dieser Arbeit berechnet. Die Selektivität und Extraktionseffizienz werden miteinander korreliert und daraus der Wirkungsgrad einer Solarzelle mit vorgegebener Kontaktselektivität errechnet. Nach der detaillierten theoretischen Untersuchung der Selektivität werden die Eigenschaften von n^+ und p^+ POLO-Kontakten untersucht. Es werden niedrige Sättigungsstromdichten zwischen 2 fA/cm^2 und 18 fA/cm^2 und gleichzeitig Kontaktwiderstände zwischen $0,4 \text{ m}\Omega\text{cm}^2$ und $10 \text{ m}\Omega\text{cm}^2$ ermittelt. Es wird gezeigt, dass der effiziente Ladungsträgertransport der Majoritäten durch Pinholes im Grenzflächenoxid sichergestellt wird. Der resultierende logarithmische Selektivitäts-Koeffizient von POLO-Kontakten wird auf über 15 bestimmt. Damit gehören POLO-Kontakte zu den Kontakten mit der höchsten Selektivität und sind für Solarzellen mit höchsten Effizienzen prädestiniert.

Die POLO-Kontakte werden auf der Rückseite einer Rückkontaktzelle mit POLO-Kontakten für beide Polaritäten integriert. Dabei formt das p^+ und n^+ dotierte Poly-Si auf der Rückseite der Solarzelle einen parasitären, gradierten p^+n^+ -Übergang im defektreichen Poly-Si mit einer Ladungsträgerlebensdauer von wenigen Pikosekunden. Die resultierende Rekombination limitiert die erreichbare Effizienz der POLO-IBC-Zelle auf etwa 18%. Aus diesem Grund wird der parasitäre Übergang während des Zellherstellungsprozesses entfernt, indem ein Graben zwischen die n^+ - und p^+ -dotierten Poly-Si-Regionen nasschemisch eingebracht wird. Die POLO-IBC-Zelle mit isolierten n^+ - und p^+ Poly-Si-Gebieten erzielt einen zertifizierten Wirkungsgrad von 24,25%.

Für den letzten Baustein wird die POLO-IBC-Zelle um einen dritten POLO-Kontakt ergänzt und die 3T-IBC-Bottomzelle mittels Strom-Spannungsmessungen im Detail untersucht. Zuerst werden die unterschiedlichen Realisierungsmöglichkeiten für eine 3T-Tandemsolar einsortiert

und die dazugehörige Nomenklatur vorgestellt. Dabei werden zwei verschiedene 3T-IBC-Bottomzellen-Architekturen unterschieden. Eine Unijunction-Bottomsolarzelle enthält einen einzigen Minoritätsladungsträgerkontakt und zwei Majoritätsträgerkontakte. Eine Bipolar-Junction-Bottomsolarzelle hingegen hat zwei Minoritätsladungsträgerkontakte und einen einzigen Majoritätsladungsträgerkontakt.

Beide 3T-Bottomzell-Architekturen werden auf Basis eines modifizierten Herstellungsprozesses für POLO-IBC-Solarzellen realisiert. Das Funktionsprinzip und die Verlustmechanismen werden mit Hilfe von J - V -Messungen an beleuchteten Bauelementen und mit Hilfe analytischer Modellierung untersucht. Die Experimente zeigen, dass der dritte Kontakt einer 3T-Unijunction- und Bipolar-Junction-Bottomzelle das Sammeln oder Injizieren von zusätzlichen Minoritäts- oder Majoritätsladungsträgern aus der oder in die Bottomzelle ermöglicht. Im Idealfall ist die Leistungsabgabe einer solchen 3T-Bottomzelle nahezu unabhängig von der Stromdichte, die von der Topzelle angelegt wird. Daher ist keine Stromanpassung beider Subzellen erforderlich. Allerdings verursacht der Transport von Majoritätsladungsträgern bzw. Minoritätsladungsträgern durch die Unijunction- bzw. Bipolar-Junction-Bottomzelle hindurch einen Verlust, welcher jedoch durch eine gezielte Auslegung der Bottomzelle vernachlässigbar klein ausfallen kann. Die Auslegung wird im Detail erläutert. Schließlich wird eine 3T-Unijunction-Bottomzelle mit einem texturierten n^+ -POLO-Frontkontakt mit einem Wirkungsgrad von 20,3% und eine vereinfachte siebgedruckte PERC-ähnliche 3T-Bipolar-Junction-Bottomzelle mit 14,4% entwickelt. Letztere ist ein attraktiver Ansatz, um die dominierende PERC-Technologie in einer kostengünstigen Tandemsolarzelle mit maximaler Energieausbeute zu nutzen.

Abschließend wird der erste 3T-GaInP//POLO-IBC-Tandemzellen-Demonstrator mit einem Wirkungsgrad von 27,3% hergestellt und ein Netto-Wirkungsgradgewinn von 0,9% im Vergleich zum 2T-Betrieb der 3T-Tandemzelle demonstriert.

Abstract

This thesis investigates back-contacted (IBC) bottom solar cells with passivating and carrier-selective POLO contacts with three terminals (3T-POLO-IBC cell). Such cells form the foundation of monolithic three-terminal tandem solar cells. This novel tandem solar cell enables the use of sub-cells with mismatched photocurrents. Thus, this tandem solar cell technology platform offers the flexibility with respect to subcell material selection, the ease of fabrication, and a robustness to spectral variations of incident light over the course of the day and year. Three building blocks of the 3T POLO IBC bottom solar cell, which are based on each other, are examined: First, the passivating and carrier-selective POLO contact. Second, the integration of POLO contacts on the rear side of a solar cell. Third, the principle of operation of a bottom cell with three terminals.

In the first part, the process of charge carrier extraction at selective contacts to the photoabsorber is theoretically explored. The selectivity of a contact is defined on the basis of

(reaction) kinetic considerations at the contact in terms of the rate ratio of desired processes to undesired processes. The extraction efficiency of charge carriers at the contact is derived as the ratio of the external voltage versus the internal voltage from a thermodynamic point of view. To emphasize the unifying nature of the definitions in this thesis, the existing literature definitions are calculated from the definitions in this thesis. The extraction efficiency is related to the selectivity coefficient of the contact and the limiting efficiency of a silicon solar cell with given contact selectivity is calculated accordingly. After the detailed theoretical investigation on selectivity, the properties of n^+ and p^+ POLO contacts are examined. Low saturation current densities between 2 fAcm^2 and 18 fAcm^2 and contact resistivities between $0.4 \text{ m}\Omega\text{cm}^2$ and $10 \text{ m}\Omega\text{cm}^2$ are found at the same time. It is shown that the efficient carrier transport of majority carriers is ensured by pinholes in the interfacial oxide. The resulting logarithmic selectivity coefficient of POLO contacts is determined to be above 15, which is one of the highest values measured. This makes POLO contacts predestined for solar cells with the highest efficiencies.

POLO contacts are integrated on the rear side of a back-contact cell with POLO contacts for both polarities. Thereby, the p^+ and n^+ doped poly-Si on the backside of the solar cell form a parasitic graded p^+n^+ junction within the defect-rich poly-Si with a carrier lifetime of a few picoseconds. The arising recombination limits the achievable efficiency of the POLO-IBC cell to about 18%. For this reason, the parasitic junction is removed during the cell fabrication process by wet-chemically introducing a trench between the n^+ - and p^+ -doped poly-Si regions. The POLO-IBC cell with isolated n^+ - and p^+ poly-Si regions achieves a certified efficiency of 24.25%.

For the last part, a third POLO contact is added to the POLO-IBC cell and the 3T-IBC bottom cell is studied in detail using current-voltage measurements. First, the different realization options for a 3T tandem solar are sorted and the corresponding nomenclature is presented. Two different 3T IBC bottom cell architectures are identified. The first one – the unijunction bottom solar cell – contains a single minority carrier contact and two majority carrier contacts. The second one – the bipolar junction bottom solar cell – on the other hand, has two minority carrier contacts and a single majority carrier contact.

Both 3T bottom cell architectures are fabricated based on a modified POLO-IBC fabrication process. The principles of operation and loss mechanisms are elucidated using J - V measurements on illuminated devices and by means of analytical modeling. The experiments show that the third contact of a 3T unijunction and bipolar junction bottom cell allows the collection or injection of additional minority or majority carriers from or into the bottom cell. Ideally, the power output of such a 3T bottom cell is nearly independent of the current density applied by the top cell. Therefore, no current matching of both subcells is required. However, the transport of majority carriers or minority carriers through the unijunction or bipolar junction bottom cell causes a loss, which, however, can be made negligible by a specific design of the bottom cell. The design rules are explained in detail. After the detailed investigations, a 3T unijunction bottom cell with a textured n^+ -POLO front contact with an efficiency of 20.3% and a simplified screen-printed PERC-like 3T bipolar junction bottom cell with 14.4% are developed. The latter is an attractive approach to utilize the dominant PERC technology in a low-cost tandem solar cell with maximum energy yield.

Finally, the first 3T GaInP//POLO-IBC tandem cell demonstrator is fabricated with an efficiency of 27.3% and a net efficiency gain of 0.9% is demonstrated compared to the 2T operation of the 3T tandem cell.

Contents

1. Introduction	1
2. Theory	5
2.1. Theory of energy conversion	5
2.1.1. Equilibrium thermodynamics: Carnot's reversible heat engine	5
2.1.2. Non-equilibrium thermodynamics: Endo-reversible heat engine	6
2.2. Fundamental semiconductor theory	8
2.2.1. Semiconductor in thermodynamic equilibrium	8
2.2.2. Non-equilibrium thermodynamics of semiconductor devices	10
2.3. Solar cell	12
2.3.1. Working principle of solar cells	12
2.3.2. Current-voltage characteristic of a solar cell	13
2.3.3. Performance parameter of a solar cell	15
2.4. Tandem solar cell	17
2.5. Transistor	18
3. Characterization methods	23
3.1. Photo-conductance decay method	23
3.2. Contact resistivity measurement	25
3.2.1. Contact resistivity	25
3.2.2. Transfer length method	26
3.3. Current-voltage characterisation of solar cells	27
3.3.1. Illuminated J - V characteristic	27
3.3.2. Dark J - V characteristic	28
3.3.3. J_{SC} - V_{OC} characteristic	28
3.3.4. Local ideality factor	28
4. State-of-the-art	31
4.1. Selectivity of passivating contacts	31
4.1.1. Quantitative definition of selectivity	31
4.1.2. Quantification of selectivity	33
4.1.3. Impact of selectivity on the efficiency of solar cells	34
4.2. Passivating poly-Si-on-Oxide (POLO) carrier-selective junction	35
4.2.1. Historical evolution	35
4.2.2. Notation	37
4.2.3. Fabrication	37
4.2.4. Junction properties	40

4.2.5. Transport mechanism	40
4.3. Three-terminal tandem cell	41
5. Selectivity and carrier extraction efficiency of contacts	43
5.1. The role and definition of contacts and the absorber of a solar cell	44
5.1.1. Photo-absorber	44
5.1.2. Contacts	45
5.2. Definition of selectivity and extraction efficiency	47
5.2.1. Selectivity	47
5.2.2. Extraction efficiency	48
5.3. Derivation and classification of the specific definitions in the literature	52
5.3.1. Selectivity of carrier-selective contacts	52
5.3.2. Electrode selectivity	58
5.4. Relationship of selectivity and carrier extraction efficiency	60
5.5. Performance of contact selectivity-limited solar cells	63
5.6. Chapter summary	66
6. Passivated carrier-selective POLO junctions to mono-crystalline silicon	69
6.1. Fabrication of POLO junction samples	69
6.2. Minority carrier transport	71
6.3. Majority carrier transport	72
6.3.1. Aluminum/polysilicon contact resistance	73
6.3.2. Combined aluminum/polysilicon/c-Si contact resistance	74
6.4. Transport mechanism	75
6.5. Selectivity of POLO junctions	76
6.6. Chapter summary	77
7. Interdigitated back-contact cell with POLO junctions	79
7.1. Fabrication process for POLO-IBC cell	79
7.2. Parasitic recombination in lateral polysilicon <i>pn</i> -junction	81
7.2.1. Current-voltage characteristic of lateral poly-Si <i>pn</i> -junctions	81
7.2.2. Recombination behavior of POLO-IBC cells with and without parasitic poly-Si <i>pn</i> -junctions	85
7.3. Performance of POLO-IBC cell	88
7.3.1. Optics	89
7.3.2. Recombination	90
7.4. Device simulation of a POLO-IBC cell	92
7.4.1. Recombination behavior	92
7.4.2. Series resistance	95
7.4.3. Practical efficiency limit of POLO-IBC cells – a free energy loss analysis	96
7.5. Chapter summary	97

8. Three-terminal interdigitated back-contact bottom cell	99
8.1. Taxonomy and nomenclature	101
8.1.1. Bottom solar cell	101
8.1.2. Top solar cell	103
8.1.3. Three-terminal tandem solar cell	103
8.1.4. Loading topology	103
8.2. Fabrication and characterization of 3T bottom cells	104
8.2.1. Cell fabrication process of the 3T unijunction bottom cell	104
8.2.2. Cell fabrication process of the 3T bipolar junction bottom cell	105
8.2.3. Characterization	106
8.3. Operating principle of 3T bottom cells	107
8.3.1. Unijunction bottom cell	108
8.3.2. Bipolar junction bottom cell	114
8.3.3. Summary of the common principles of operation	118
8.4. Equivalent circuit model	119
8.4.1. Model of a unijunction bottom cell	119
8.4.2. Model of a bipolar junction bottom cell	124
8.5. High performance unijunction bottom cell	136
8.5.1. Cell fabrication process	136
8.5.2. Cell performance	140
8.6. Simplified PERC-like three-terminal bipolar junction bottom cells	141
8.6.1. Cell fabrication process	141
8.6.2. Base contact definition	145
8.6.3. Cell performance	150
8.7. Chapter summary	151
9. Three-terminal GaInP//Si tandem cell demonstrator	153
9.1. Fabrication of the demonstrator	153
9.2. Performance of the demonstrator	154
10. Summary	157
A. Appendix	195
A.1. Supplementary material for the section on lateral poly-Si <i>pn</i> junctions	195
A.1.1. Diffusion profile	195
A.1.2. Calculation of <i>J-V</i> characteristic by mean of PC1D	195
A.1.3. Reverse-bias characteristic of the poly-Si <i>pn</i> -junction	196
A.2. Supplementary material for the section on the performance of POLO-IBC cell	198
A.2.1. Sunrays simulations	198
A.3. Supplementary material for chapter on selectivity and extraction efficiency .	200
A.3.1. Electron transfer reaction	200
A.3.2. Selectivity calculated from the generalized charge control relation . .	202
A.3.3. Equivalent circuit model for a contact selectivity-limited solar cell . .	202
A.3.4. Relationship between power conversion efficiency and selectivity . . .	206

A.3.5. Maximum power conversion efficiency for a contact-limited solar cell	210
A.4. Supplementary for the section on unijunction bottom cells	212
A.4.1. Model parameters for 2T-operated 3T cell	212
A.4.2. Distributed series resistance in a unijunction 3T bottom cell	216
A.5. Supplementary for the section on bipolar junction bottom cells	219
A.5.1. Derivation of Ebers-Moll model with photo-generation	219
A.5.2. Calculation of Γ	225
A.5.3. Calculation of the maximum power point for equipotential operation of a bipolar junction bottom cell	227
A.5.4. PC1D simulation of bipolar junction bottom cell	229
A.5.5. Derivation equation 8.17 for the design guideline of bipolar junction bottom cells	229
A.5.6. Calculation of the current-mismatch loss factor χ	230
A.5.7. Calculation of the tandem efficiencies for a 3T tandem with a bipolar junction bottom cell	231
A.5.8. 3T operation of the simplified PERC-like 3T bipolar junction cell	233
B. List of symbols	237
C. List of publication	249
C.1. Peer-reviewed journal articles	249
C.2. Conference proceedings	251
C.3. Given conference talks	253
D. Acknowledgment (Danksagung)	255

1. Introduction

Climate change is seriously threatening the livelihood of humanity and represents the greatest challenge for the twenty-first century. The world is on a path towards a global temperature increase of well above 2 °C with the consequence of an irreversible climate change that will make large parts of the world uninhabitable and leave a conflict-ridden world of starvation, chronic fresh water shortages and refugee movement [1–5]. To mitigate climate change and its consequences, the world has to take action and decarbonize its economies. Especially, burning of fossil fuels for electricity generation has to be phased out completely and replaced with renewable energy resources by 2050 [3, 6]. Moreover, the energy demand of the end-user sector (transportation, builds and industry) has to be covered by low-carbon sources and electrification in the future [7–11]. The generation of electricity from solar energy – photovoltaic (PV) energy conversion – plays a decisive role in avoiding green house gas emissions and in mitigating global warming [12–17].

Since Chapin, Fuller and Pearson demonstrated the first practical silicon solar cell at Bell Laboratories in 1954 [18], the silicon solar cell has become the dominant PV technology, while taking about 60 years to achieve a cumulative installed PV power generation capacity of more than 100 GW in 2013 [19]. Today, less than a decade later, the annually added capacity exceeds 100 GW and yields a cumulative installed capacity of more than 600 GW, which corresponds to about 3% of the global electricity generation [19, 20]. It is expected that PV can cover 30% and 50% of the global electricity generation by 2035 and 2050, respectively [14].

The incredible success of PV is based on the massive module prize reduction from about 70 $\$/W_{\text{peak}}$ in 1978 to about 0.2 $\$/W_{\text{peak}}$ in 2020 [21]. The prize reduction follows the learning curve – also known as Swanson’s law – with a learning rate of approximately 20% [22], which is partly a result of research efforts to increase the performance and lower the manufacturing cost of solar cells [23–26]. An improvement in module performance can further reduce the PV system costs [27]. But how far can efficiency be increased and what are possible levers for improvement?

In principle, the efficiency of silicon solar cell can be improved until the calculated theoretical maximum efficiency of 29.5% [28, 29] is reached. However, the average efficiency in mass production of passivated emitter and rear cells (PERC) amounts to approximately 23% in 2020 [30]. A synergistic energy gain analysis (SEGA) [31] of a projected future PERC technology reveals that the largest efficiency gain can be achieved by improving the electron- and hole-collecting contacts by implementing passivating and carrier-selective contact [32]. Among others [33, 34], a polysilicon-based passivating and carrier-selective contact is a promising approach to be implemented as evolutionary upgrade of the current PERC technology [32, 35, 36].

In order to significantly increase the cell efficiency, even beyond the theoretical limit of 29.5% for silicon single-junction solar cells [28, 29], inherent carrier thermalization loss has to be addressed by splitting the spectrum through multiple junctions stacked optically in series [37]. Applying this approach, monolithic and electrically series-connected multijunction solar cell with efficiencies of up to 35.5% [38] for dual-junction, 37.9% [39] for triple-junction and 47.1% [40] for six-junction solar cells have been achieved under concentrated illumination. Unfortunately, prohibitively expensive syntheses methods and materials were essential for such highly efficient III-V compound semiconductor tandem solar cells in the past, which restricted their usage to space applications and niche markets.

Recently increasing research interest is dedicated to potentially low cost, but highly efficient tandem concepts based on Si wafer bottom cells for terrestrial, non-concentrated applications [41, 42]. Bottom cells based on Si wafer technology are an excellent choice for dual-junction solar cell applications thanks to an ideal bandgap of Si of 1.1eV, the abundance and non-toxicity, highly developed and cost-competitive manufacturing technology, high efficiency and market-dominance. The perfect tandem partner with a wide band gap around 1.7 eV [43, 44] for a current-matched two-terminal tandem and nearly as good properties, as Si has for bottom cells, is hard to find.

The current-matching constraint can be avoided by using a three-terminal tandem, which provides a large flexibility regarding the usage of a broader range of band gaps for top and bottom cell and a higher robustness against spectral variations. Both aspects allow to achieve higher cell efficiency and energy yields. For practical solar cells, it is necessary to integrate the third terminal at the rear side of the tandem cell by using industrial-type interdigitated back contact (IBC) bottom cells.

In this thesis, the definition of selectivity as the central property of carrier-selective contacts is discussed and the respective electrical properties of polysilicon-based junctions are investigated. Then, the polysilicon-base passivating contacts are integrated on the rear side of an interdigitated back-contact solar cell with a certified efficiency of 24.25% to demonstrate the high quality of the polysilicon passivating contacts on device level. Subsequently, the interdigitated back-contact cell is modified such that a third polysilicon passivating contact is integrated on the front side in order to study the physics of different three-terminal bottom cell architectures for tandem application. Finally, the first three-terminal (3T) tandem solar cell, which comprises a 3T IBC bottom cell with polysilicon-based junctions and a GaInP top, with an efficiency of 27.3% is demonstrated.

Thesis structure

The presented thesis contains ten chapters, which are organized as follows.

Chapter 1 introduces the reader to the topic and provides the structure of the thesis.

Chapter 2 summarizes the basic theoretical concepts – thermodynamics of energy conversion, semiconductor theory and the basics of solar cells and transistors.

Chapter 3 contains a brief description of the methods used.

Chapter 4 outlines the state of the field in the literature for the selectivity definition, polysilicon-based passivating contacts and three-terminal tandem solar cells.

Chapter 5 discusses the process of charge carrier extraction at a selective contact and defines the selectivity and carrier extraction efficiency. It compares the definitions made with the literature and calculates the power conversion efficiency of a contact selectivity-limited solar cells.

Chapter 6 presents the electrical properties – recombination and transport – of the used polysilicon-based junctions and calculates the selectivity coefficient for the junctions. Furthermore, it studies the correlation between pinhole density in the interfacial SiO₂ and the transport properties.

Chapter 7 covers the integration of the polysilicon-based junctions on the rear side of interdigitated back-contact solar cells. The properties of the parasitic p^+n^+ -junction forming within the defective polysilicon layer at the rear side, its resulting detrimental effect on the cell performance, and how the isolation of p^+ and n^+ doped polysilicon regions improves the performance are presented.

Chapter 8 extends the interdigitated back-contact solar cells with a third polysilicon-based contact to enable the investigation of three-terminal back-contacted bottom solar cells for the application in three-terminal tandems. It presents the different possibilities to form a three-terminal tandem solar cell and the corresponding nomenclature. For the bottom cell, two different three-terminal bottom cell architectures – the unijunction and bipolar junction bottom cell – are possible. Both cell types are experimentally investigated, equivalent circuit models are developed and evaluated with the experimental data. Design rules for both bottom cell types are provided. Finally, a high performance unijunction cell and a simplified PERC-like bipolar junction cell are presented.

Chapter 9 demonstrates the first three-terminal tandem demonstrator comprising a back-contacted bottom cell.

Chapter 10 resumes the thesis.

2. Theory

2.1. Theory of energy conversion

The processes of energy conversion are omnipresent and essential for the modern society. The theory of energy conversion – the thermodynamics – was born in the nineteenth century as a consequence of the attempt to understand and to improve the invented steam engine [45]. At first thermodynamics dealt with systems in thermodynamic equilibrium, but in the twentieth century the theory was extended to described processes out of equilibrium. In the following, both theories are briefly summarized as far as necessary in this thesis, especially in chapter 5. A complete presentation of the theory can be found in the textbook of Kondepudi and Prigogine [45] or De Groot and Mazur [46] for example.

The conversion of energy in the following is outlined for heat engines as a natural example for thermodynamics, but the presented concepts are generally valid for other types of conversion processes – especially for the conversion of chemical energy into electrical energy as discussed for solar cells in chapter 5.

2.1.1. Equilibrium thermodynamics: Carnot’s reversible heat engine

Equilibrium thermodynamics is the study of systems in equilibrium and the transition of systems from one equilibrium state to another. In equilibrium, a system reaches the state of maximum entropy and the entropy production rate vanishes. The vanishing entropy production rate implies that all (thermodynamic) forces acting on the system and any net energy or net particle fluxes vanish [45]. The system attains the state of minimum energy and remains in this equilibrium state, such that any process of the system is required to be reversible.

In order to describe the energy conversion from heat to work within this framework, Sadi Carnot considered a reversible thermodynamic cycle – the Carnot cycle, which converts heat energy into work [47]. Figure 2.1a shows the graphical representation of a Carnot heat engine operating between a hot and cold heat reservoir with temperatures T_H and T_C , respectively. In one cycle, an amount of heat $Q_H = T_H\Delta S$ is provided by the hot reservoir to the engine and one part of the heat $Q_C = T_C\Delta S$ leaves the engine to be reabsorbed by the cold reservoir. ΔS is the amount of entropy transferred between the reservoirs and the engine due to the extracted and absorbed heat. Since the engine is assumed to be reversible, entropy is conserved, such that incoming entropy equals the outgoing entropy. Furthermore, the energy is conserved within the engine and the engine converts the remaining part of the heat energy to work $\mathcal{W} = Q_H - Q_C = (T_H - T_C)\Delta S$. The Carnot efficiency

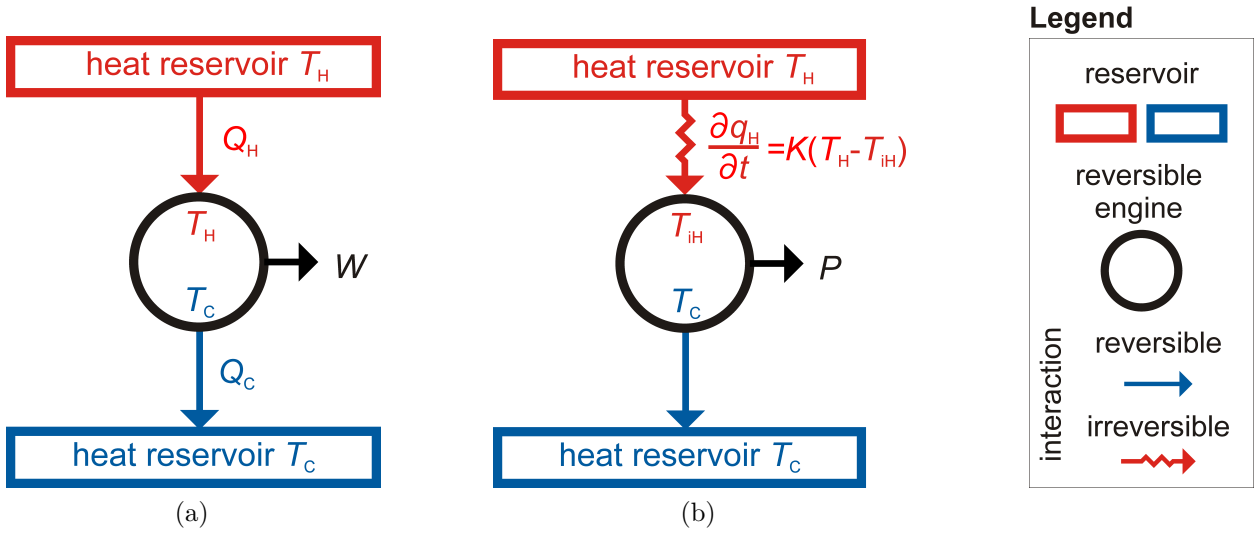


Figure 2.1.: Schematic representation of (a) the reversible Carnot heat engine and (b) the irreversible Novikov engine. The irreversible interaction is indicated by the wavy arrow and reversible interaction by the straight arrow. The Carnot cycle is quasi-static and the Novikov cycle has a finite duration.

$$\eta_C = \frac{W}{Q_H} = 1 - \frac{T_C}{T_H} \quad (2.1)$$

represents an upper limiting efficiency for all heat engines operating between two heat reservoirs and solely depends on the temperature of the reservoirs. However, Carnot's cycle and heat engine rely on equilibrium thermodynamics and reversible processes, which require the energy conversion process to occur infinitely slow to ensure that the rate of heat transfer is almost zero [48, 49]. Therefore, a reversible engine takes an infinitely long time t_C to complete one Carnot cycle and the power output $P = \frac{W}{t_C}$ of such a heat engine vanishes.

2.1.2. Non-equilibrium thermodynamics: Endo-reversible heat engine

Real energy converters exhibit finite rates for transfer processes and become irreversible. A thermodynamic force F (e.g. temperature gradient) responsible for a flux density J (e.g. heat flux density) drives the macroscopic system out of its equilibrium state and the system has to be described by non-equilibrium thermodynamics [45]. Linear irreversible thermodynamics provide a solid non-equilibrium theory to describe systems with irreversible processes near their equilibrium state [45, 46, 50]. For this purpose, the system is divided in smaller subsystems, which are assumed to be in a local equilibrium and the flux density J of the irreversible transport between the subsystems is assumed to depend linearly on the

thermodynamic force¹ F via the transport coefficient L [45, 46].

$$J = L \cdot F \quad (2.2)$$

The local thermodynamic equilibrium assumption allows to use a similar formalism as for the description of a system in thermodynamic equilibrium. Any linear transport process results in a finite entropy production rate $\frac{\partial s}{\partial t}$

$$\frac{\partial s}{\partial t} = J \cdot F = \frac{J^2}{L} \quad (2.3)$$

and dissipates a heat flux density $\frac{\partial q_{\text{irr}}}{\partial t} = T \cdot \frac{\partial s}{\partial t}$, which shows a quadratic dependence on the flux density. A well-know example of the latter relationship is the Joule heating due to an electric current flow through a conductor.

Based on the picture of linear irreversible thermodynamics, a class of irreversible engines has been constructed [51–55] – the endoreversible² engines. Figure 2.1b shows the schematic diagram of an endoreversible heat engine³, which consists of a reversible engine supplemented by a dissipative (irreversible) interaction with the hot reservoir. The calculation of the power output P and the efficiency η_{mpp} at maximum power output is – aside from power maximization – similar to the calculation for the Carnot engine from above and details can be found elsewhere [53, 55]. The resulting power output with a linear transport law of heat conduction $\frac{\partial q_{\text{H}}}{\partial t} = K \cdot (T_{\text{H}} - T_{\text{iH}})$ (Newton’s law) from the hot reservoir to the engine with heat conductance K reads

$$P = K(T_{\text{H}} - T_{\text{iH}}) \cdot \left(1 - \frac{T_{\text{C}}}{T_{\text{iH}}}\right). \quad (2.4)$$

The Novikov heat engine generates maximum power if $T_{\text{iH}} = \sqrt{T_{\text{H}}T_{\text{C}}}$ and the efficiency at this point of operation is

$$\eta_{\text{mpp}} = 1 - \sqrt{\frac{T_{\text{C}}}{T_{\text{H}}}}. \quad (2.5)$$

This Novikov efficiency⁴ corresponds to the efficiency of a heat engine at maximum power output and is considerably lower than the maximum possible efficiency of the engine. The latter is achieved by operating the engine reversibly so that $T_{\text{iH}} = T_{\text{H}}$ and $P = 0$. Then the efficiency of the Novikov engine equals the Carnot efficiency η_{C} . By comparing the irreversible and reversible engines, an interesting correlation between the efficiency at maximum power output η_{mpp} and the efficiency without any fluxes⁵ with $P = 0$ is found. For an engine with linear irreversible interactions with the reservoirs, the relation reads

$$\eta_{\text{mpp}} = 1 - \sqrt{1 - \eta_{\text{C}}}. \quad (2.6)$$

¹Note that the flux densities and forces are vectors and the the L is a transport matrix, in general. Herein, scalar quantities are assumed for simplicity, which reflects single dimensional transport.

²Endoreversible means reversible inside.

³This engine is referred to as Novikov engine [53], but also Chambadal engine [56] or Curzon-Ahlborn engine [54] were discussed.

⁴More often referred to as Curzon-Ahlborn efficiency.

⁵In the language of an electrical engineer, this point of operation corresponds to open-circuit conditions.

This relationship was found to be universal for symmetrically dissipating engines in the low-dissipation limit, where the transport from the “hot” reservoir is of the same order as the transport to the “cold” reservoir [57]. However, for highly asymmetric transport – as it is present at carrier-selective contacts in solar cells – the following upper bound was found.

$$\eta_{\text{mpp}} = \frac{\eta_C}{2 - \eta_C} \quad (2.7)$$

2.2. Fundamental semiconductor theory

The central property of a semiconductor material – the electrical conductivity – motivated Alessandro Volta and later Michael Faraday to name this class of materials “semiconductor” [58]. In a semiconductor, “free” electron and hole charge carriers with an elementary charge $\pm q$ provide an electron conductivity σ_n and hole conductivity σ_p to the total conductivity σ .

$$\sigma = \sigma_n + \sigma_p = q(\mu_n n + \mu_p p) \quad (2.8)$$

The electron (hole) conductivity is determined by the electron (hole) mobility μ_n (μ_p) and the electron (hole) concentration n (p). The calculation of the latter is a fundamental exercise in semiconductor theory and occupies many textbooks on semiconductor device physics [59–66]. In the following, the main concepts are briefly summarized for semiconductors in thermodynamic equilibrium and non-equilibrium.

2.2.1. Semiconductor in thermodynamic equilibrium

The general definition of thermodynamic equilibrium in section 2.1 has several specific implications in semiconductor theory and is implicitly or explicitly used to derive equilibrium electron and hole carrier concentrations [59–66].

Figure 2.2a depicts the band diagram representation – electron energy versus position – of the junction between a p -type and n -type semiconductor. The grey regions of the band diagram represent the neutral p -type and n -type semiconductor regions, where the space charge $\rho(x)$ (purple solid line) vanishes. The conduction band edge E_C and valence band edge E_V mark the lowest state for electrons in the conduction band and holes in the valence band, respectively. For a three-dimensional semiconductor, the density of states for electrons in the conduction band and for holes in the valence band increases like $\sqrt{E - E_C}$ and $\sqrt{E_V - E}$, respectively. In the “forbidden” gap $E_G = E_C - E_V$, also band gap, between E_C and E_V , energy states do not exist in a perfect crystal.

In order to obtain the equilibrium carrier concentration of electrons and holes, it is necessary to know how many of the available states are occupied. The Fermi-Dirac distribution function

$$f(E) = \frac{1}{\exp\left(\frac{E - E_F}{k_B T}\right) + 1} \quad (2.9)$$

provides the probability of occupancy for electrons and holes in equilibrium, where k_B is the Boltzmann constant, T is the temperature and E_F is the Fermi-level. At a temperature of

0 K, the distribution function is a step function, where the Fermi-level E_F labels the highest and lowest occupied energy level for electrons and holes, respectively. At higher temperatures, the step function is smeared, such that also electron states slightly above the Fermi level and hole states below the Fermi level are occupied. For non-degenerated semiconductors, the Maxwell-Boltzmann distribution function often approximates the Fermi-Dirac function. In summary, the equilibrium carrier concentration is controlled by the position of the Fermi level with respect to E_C and E_V . The equilibrium carrier concentration for electrons n_0 and holes p_0 within the Maxwell-Boltzmann approximation calculates as follows.

$$n_0 = N_C \exp\left(\frac{E_F - E_C}{k_B T}\right) \quad (2.10)$$

$$p_0 = N_V \exp\left(\frac{E_V - E_F}{k_B T}\right) \quad (2.11)$$

N_C and N_V are the effective density of states of the conduction and valence band, respectively. In the context of equation 2.11, it becomes obvious that the semiconductor on the left hand side in Figure 2.2a has a large equilibrium hole concentration, because the Fermi level is close to E_V , and it is referred to as p -type semiconductor. Analogous considerations for the right hand side in figure 2.2a reveal a n -type semiconductor.

According to the law of mass action (equation 2.12), the product of the equilibrium carrier concentrations n_0 and p_0 has to be constant and equal to the intrinsic carrier concentration n_i of approximately 10^{10} cm^{-3} for silicon at room temperature [67, 68].

$$n_0 p_0 = N_C N_V \exp\left(-\frac{E_G}{k_B T}\right) = n_i^2 \quad (2.12)$$

If the initially separated p -type and n -type semiconductors are brought in contact, holes from the hole-rich p -type region diffuse into the electron-rich n -type region and vice versa and recombine. The transition region between neutral p -type and n -type regions is depleted and negative and positive space charges (purple curve in figure 2.2a) remain on the p -type and n -type side of the transition region, respectively, due to the uncompensated charges of the immobile dopant ions. The light yellow part in figure 2.2a highlights this transition region – the space charge region or depletion region – between n -type and p -type doped regions. The space charges induce an electric field $E(x)$, which results in a drift current of charge carriers opposing the diffusion of charge carrier due to the gradient of the chemical potential. A balance is established between the two driving forces, so that the thermodynamic driving force – the gradient of the electrochemical potential i.e. the Fermi level E_F – and the carrier flux vanishes. It follows that, in equilibrium, a single Fermi level exists, which is constant with position.

The equilibrium electron charge carrier density on the n -type side of the depletion region n_{n0} can be related with the electron charge carrier density on the p -type side n_{p0} by using equation 2.10 and the work functions $q\Phi_n$ and $q\Phi_p$ of the n -type and p -type semiconductor.

$$n_{n0} = n_{p0} \exp\left(\frac{q(\Phi_n - \Phi_p)}{k_B T}\right) = n_{p0} \exp\left(\frac{q\Phi_{Bi}}{k_B T}\right) \quad (2.13)$$

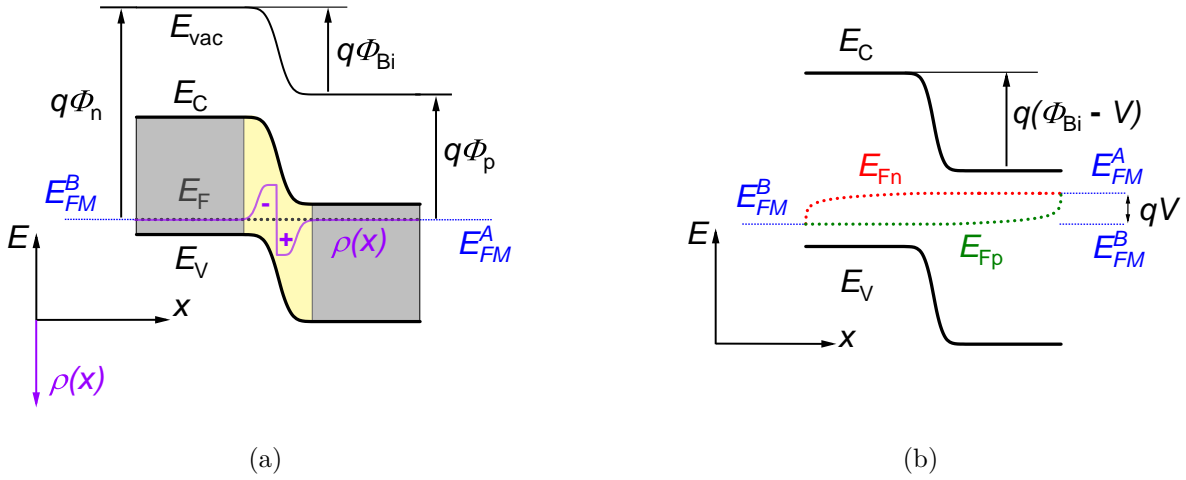


Figure 2.2.: Band diagram of a pn junction (a) in equilibrium and (b) with forward-bias voltage. In figure 2.2a, grey and light yellow regions correspond to the quasi-neutral and space charge regions, respectively. E_{vac} is the vacuum level and all other quantities are define in the text.

The work function difference, which is the driving force⁶ for the diffusive exchange of charge carriers in the depletion region, is balanced by the built-in potential Φ_{Bi} . Note that equation 2.13 with the law of mass action in equation 2.12 allows to calculate the built-in voltage as a function of the majority carrier concentrations n_{n0} and p_{p0} on either side of the pn junction. The bending of the bands in the depletion region follows the electrostatic potential energy $-q\phi(x)$. Poisson's equation 2.14 describes the electrostatics and relates the charge distribution $\rho(x)$ in the semiconductor with a permittivity ϵ to the resulting electrical field $\mathcal{E}(x)$ and the electrostatic potential $\phi(x)$.

$$-\frac{d\mathcal{E}(x)}{dx} = \frac{d^2\phi(x)}{dx^2} = -\frac{\rho(x)}{\epsilon} \quad (2.14)$$

2.2.2. Non-equilibrium thermodynamics of semiconductor devices

In order to perform any action in a semiconductor, an external force (e.g. an electric field due to a voltage bias) has to be applied to the semiconductor in equilibrium and the equilibrium is disturbed. In such a non-equilibrium situation, linear irreversible thermodynamics [69–71] describe the semiconductor near its equilibrium state by using linear flux-force transport relationships and quasi-Fermi-Dirac distribution functions.

Figure 2.2b depicts the band diagram of the pn junction from figure 2.2a in forward bias. An electrostatic potential difference $V = \frac{1}{q}(E_{\text{FM}}^{\text{A}} - E_{\text{FM}}^{\text{B}})$ is applied between the electron-selective

⁶In fact, the work function difference represent the chemical potential difference between the n -type and p -type semiconductor regions, which is the true driving force.

contact A with the Fermi level $E_{\text{FM}}^{\text{A}} \approx E_{\text{Fn}}$ and hole-selective contact⁷ B with $E_{\text{FM}}^{\text{B}} \approx E_{\text{Fp}}$. The equilibrium Fermi level E_{F} splits due to the distortion from equilibrium into two quasi-equilibrium Fermi levels – a hole quasi-Fermi level E_{Fp} and an electron quasi-Fermi level E_{Fn} – and the occupation of states is described by quasi Fermi-Dirac or quasi Maxwell-Boltzmann distribution functions. The charge carrier concentration from the equilibrium equations 2.10 and 2.11 are replaced in quasi-equilibrium by the following expression.

$$n = n_0 + \Delta n = N_{\text{C}} \exp\left(\frac{E_{\text{Fn}} - E_{\text{C}}}{k_{\text{B}}T}\right) \quad (2.15)$$

$$p = p_0 + \Delta p = N_{\text{V}} \exp\left(\frac{E_{\text{V}} - E_{\text{Fp}}}{k_{\text{B}}T}\right) \quad (2.16)$$

The excess electron carrier concentration Δn equals the excess hole carrier concentration Δp due to carrier conservation. The pn product reads

$$np = (n_0 + \Delta n)(p_0 + \Delta p) = n_{\text{i}}^2 \exp\left(\frac{E_{\text{Fn}} - E_{\text{Fp}}}{k_{\text{B}}T}\right) \quad (2.17)$$

Since E_{Fn} and $-E_{\text{Fp}}$ are the electrochemical potentials of electrons and holes, the quasi-Fermi level splitting $\Delta\mu = E_{\text{Fn}} - E_{\text{Fp}}$ in the pn product represents the electrochemical affinity of the generation-recombination processes [45, 70] of the system, which is a measure of how far from equilibrium the system is operating.

The applied bias voltage V reduces the band bending of the pn junction, which leads to an increase of minority charge carriers at the edges $-x_{\text{p}}$ and x_{n} of the depletion region. This yields the important law of the junction similar to equation 2.13 in equilibrium.

$$n_{\text{n}}(x_{\text{n}}) = n_{\text{p}}(-x_{\text{p}}) \exp\left(\frac{q(\Phi_{\text{Bi}} - V)}{k_{\text{B}}T}\right) \quad (2.18)$$

The desired action for a forward biased pn junction is the onset of a current flow upon forward biasing, which is described by a linear correlation between the thermodynamic force and the charge carrier flux. In a semiconductor, the gradient of the quasi-Fermi level drives a charge carrier flow, which is often subdivided in a drift current density due to a gradient of the electrostatic potential (electric field \mathcal{E}) and a diffusion current density driven by a gradient in carrier concentration.

$$J_{\text{n}} = \mu_{\text{n}}n \frac{dE_{\text{Fn}}}{dx} = q\mu_{\text{n}}n\mathcal{E} + qD_{\text{n}} \frac{dn}{dx} \quad (2.19)$$

$$J_{\text{p}} = \mu_{\text{p}}p \frac{dE_{\text{Fp}}}{dx} = q\mu_{\text{p}}p\mathcal{E} - qD_{\text{p}} \frac{dp}{dx} \quad (2.20)$$

⁷In the case of a pn junction, the highly doped n -type region and highly doped p -type region ensure that the recombination kinetics of “any” contact with a symmetric and high recombination rate are majority carrier selective and the contact’s Fermi level is pinned to the majority carrier (quasi) Fermi levels of the semiconductor.

D_n and D_p are the diffusion coefficients and J_n and J_p are the current densities for electrons and holes, respectively.

To completely model a semiconductor device like a solar cells or a bipolar junction transistors, the transport laws, the Poisson equation and the following continuity equations for electrons and holes form a set of fundamental semiconductor device equations.

$$\frac{\partial n}{\partial t} = \frac{1}{q} \frac{\partial J_n}{\partial x} - (R - G) \quad (2.21)$$

$$\frac{\partial p}{\partial t} = -\frac{1}{q} \frac{\partial J_p}{\partial x} - (R - G) \quad (2.22)$$

The continuity equation reflects the particle conservation, where the particle density can only change in time at a particular position, if particles either flow to another position or if they are generated with a generation rate G or annihilated with a recombination rate R . The generation and recombination in solar cells occurs mainly through the Auger process, radiative band-to-band and non-radiative, traps-assisted Shockley-Read-Hall (SRH) processes in the volume or at the surface of a semiconductor.

2.3. Solar cell

For decades, Shockley's understanding on the physics of electrons and holes in semiconductors [72] and the operation of pn -junctions [60] shaped the language of solid-state solar cells and Shockley's diode theory still successfully describes most classical solar cells. However, a solar cell is an energy converter in first place and therefore several authors made the attempt to provide a picture of solar cells in the language of energy converters, namely thermodynamics [64, 73–80]. In the following, the thermodynamic picture is used to qualitatively present the working principle of a solar cell and Shockley's diode theory is used to motivate the current-voltage characteristic and the double-diode equivalent circuit model of a solar cell.

2.3.1. Working principle of solar cells

The energy conversion of incident heat radiation from the sun into electricity in a photovoltaic energy converter proceeds in two steps [64]: first the heat radiation is converted into chemical energy and, in a second step, the chemical energy converts into electrical energy. For each of the conversion processes, the solar cell requires an appropriate conversion apparatus. Figure 2.3 shows a schematic representation of a solar cell.

If light from the sun is absorbed by the photo-absorber of the solar cell, each photon generates an excited electron-hole pair (exciton), which dissociates in free electrons and holes. The absorber can be thought of as a balloon [81] containing an excited electron-hole gas with a chemical energy⁸, i.e. the quasi-Fermi level splitting. Figuratively speaking, the chemical energy of the gas represents the pressure in the “absorber balloon”. A protective skin

⁸The absorber is assumed to be a quasi-neutral region, which is field free.

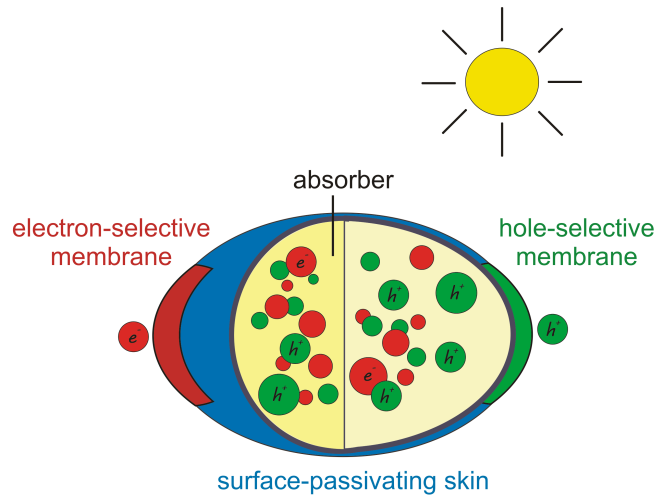


Figure 2.3.: Schematic representation of a solar cell inspired by Cuevas *et al.* [81]. The sliced sphere consists of an absorber (yellow) with a surface-passivating skin (blue) and an electron-selective (red) and hole-selective membrane (green).

envelopes the absorber balloon to prevent a leak of the gas – recombination of electrons and holes – at the surface and thus the skin maintains the pressure inside the balloon. In order to convert the chemical energy of the electron-hole gas within the balloon into electrical energy, the positive and negative charge carriers – electrons and holes – have to be separated by collection of each charge carrier at a charge carrier-selective membrane. The perfect electron-selective membrane is completely transparent for electrons, such that electrons can cross the membrane without dissipating energy. However, holes can not permeate through the perfect electron-selective membrane and have to be collected at the hole-selective membrane. The separated electrons and holes can now flow in an external circuit and perform work. Since one part of the present thesis investigates the properties of polysilicon-based passivating and carrier-selective contacts⁹, chapter 5 is dedicated to describe a carrier-selective contact in detail and to define a “selectivity” metric for carrier-selective contacts.

2.3.2. Current-voltage characteristic of a solar cell

The current-voltage (J - V) characteristic of a solar cell is often derived from Shockley’s diode theory [60] of a pn junction as shown in figure 2.2b and discussed in section 2.2¹⁰. However, the J - V characteristic can also be obtained within a single-dimensional “ballon representation” of the solar cell from integrating the continuity equation 2.21 for electrons between the electron-selective contact at position $x = 0$ and the hole-selective contact at

⁹Carrier-selective contact is used as a synonym for carrier-selective membrane.

¹⁰A detailed Shockley-type derivation of the J - V characteristic can be found in the appendix A.5.1, where the characteristic of a bipolar junction transistor is derived, by assuming that one of the two pn junctions is shorted and recombination takes place in the base region.

2.3. SOLAR CELL

$x = W_B$ to obtain the following balance equation:

$$J = J_n(0) + J_p(0) = q \int_0^{W_B} G(x) dx - q \int_0^{W_B} R(x) dx + J_p(0) + J_n(W_B) \approx J_{Ph} - qW_B R \quad (2.23)$$

The total current density $J = J_n(0) + J_p(0)$ leaving a solar cell at the electron-selective contact is the difference between the generated (blue term) and recombined (red and orange terms) current density. The generated current density is almost exclusively due to photo-generation and blue term defines the photo-generation current density J_{Ph} . The electrons (holes) collected by the hole-selective (electron-selective) contact cause the orange part of the recombination current density, but can be neglected for perfectly selective and passivating contacts. If the surface-passivating skin perfectly passivates the surface, the remaining recombination current density (red term) reflects the recombination in the absorber. For homogeneous recombination in the absorber, the red term in equation 2.23 simplifies to $qW_B R$. The total rate of recombination R has different contributions due to different recombination mechanisms within the absorber and depends on the quasi-Fermi level splitting $\Delta\mu$, which is controlled by the external voltage $V = \frac{\Delta\mu}{q}$ between the perfect electron-selective and hole-selective contacts for a given photo-generation.

At low-level injection (LLI) condition – where $\Delta n \ll n_0$ or $\Delta p \ll p_0$ – the rate of recombination for radiative, Auger and SRH recombination is proportional to the pn product, such that recombination rate¹¹ $R_{i,LLI}$ of each recombination process i reads [82]

$$R_{i,LLI} = R_{i,LLI,0} \cdot \left(\frac{pn}{n_i^2} - 1 \right) = R_{i,LLI,0} \cdot \left(\exp \left(\frac{qV}{k_B T} \right) - 1 \right), \quad (2.24)$$

where $R_{i,LLI,0}$ is a constant prefactor.

Using equation 2.23 with $R_{i,LLI}$ yields the simplest version of the J - V characteristic of a solar cell – the single-diode model:

$$J(V) = J_{Ph} - J_{01} \left[\exp \left(\frac{qV}{m_1 k_B T} \right) - 1 \right] \quad (2.25)$$

$J_{01} = qW_B \cdot \sum_i R_{i,LLI,0}$ denotes the reverse saturation current density or recombination prefactor [82] of a diode with an ideality factor $m_1 = 1$ and quantifies the recombination in a solar cell.

The simplified assumption made for the derivation of the single-diode model restricts the model to ideal solar cells at low-level injection. One particular deviation of practical solar cell's J - V characteristics from the single-diode model can result from the fact that SRH generation and recombination within the depletion region or high level injection effects can not be neglected. At high-level injection (HLI) conditions – $\Delta p \gg p_0$ or $\Delta n \gg n_0$ – the recombination rate can often be describes by [82]

$$R_{i,HLI} = R_{i,HLI,0} \cdot \left(\frac{pn}{n_i^2} \right)^{1/m} = R_{i,HLI,0} \cdot \exp \left(\frac{qV}{m k_B T} \right), \quad (2.26)$$

¹¹This relation is due to the fact that each of the processes can be described as first-order recombination reactions similar to the electron transfer reaction detailed in the appendix A.3.1.

where $R_{i,\text{HLI},0}$ is a constant prefactor and m is the ideality factor. For Auger recombination at HLI the ideality factor $m = \frac{2}{3}$ and for SRH recombination at HLI $m = 2$. For depletion region recombination, an ideality factor of $m = 2$ is typically assumed in textbooks [61, 83, 84]. However, it was pointed out by several authors that a voltage-independent ideality factor of two is not accurate for the case of generation and recombination in the depletion region [85–90].

To account for the different recombination mechanisms in the J - V curve, at least one additional recombination current density with an ideality m_2 and a recombination prefactor J_{02} are superposed to the single-diode model to yield a double-diode model. Another deviation from the single-diode model arises from the fact that the series resistance R_S is non-zero and the shunt resistance R_{SH} is finite. The J - V characteristic of the double-diode model with series and shunt resistance is calculated as follows.

$$J(V) = J_{\text{Ph}} - J_{01} \left[\exp \left(\frac{q(V + JR_S)}{m_1 k_B T} \right) - 1 \right] - J_{02} \left[\exp \left(\frac{q(V + JR_S)}{m_2 k_B T} \right) - 1 \right] - \frac{V + JR_S}{R_{\text{SH}}} \quad (2.27)$$

Figure 2.4a shows the shifted current-voltage characteristic $[J_{\text{Ph}} - J(V)]$ for a solar cell with Lambertian light trapping, which is limited by intrinsic recombination – radiative and Auger recombination – of a n -type silicon absorber with a thickness of 110 μm and a resistivity of 2 Ωcm . In the framework of the equivalent circuit model in equation 2.27, the two parallel diodes with an ideality factor of unity for the radiative recombination and Auger recombination at low-level injection conditions and an ideality factor of $\frac{2}{3}$ for Auger-recombination at high-level injection represent the intrinsic recombination within the bulk. The recombination prefactors (saturation current densities) of the diodes are determined to $1.33 \cdot 10^{-15} \text{ A/cm}^2$ for the diode with $m = 1$ and $3.27 \cdot 10^{-21} \text{ A/cm}^2$ for the diode with $m = \frac{2}{3}$. $R_S = 0$ and $R_{\text{SH}} = \infty$ of the solar cell, because such effects are excluded in this model calculation [28]. The double-diode model with the chosen parameters gives a good agreement with the J - V characteristic of the detailed balance calculation.

The fact that even the J - V characteristic of a “perfect” solar cell requires two diodes, underlines the usefulness of the double-diode model. Practical solar cell usually require an even more complex equivalent circuit model to achieve good agreement with the measured J - V characteristic.

2.3.3. Performance parameter of a solar cell

The purpose of a photovoltaic power converter is the conversion of the incident power density P_{in} of the heat radiation into the electrical power density P . Figure 2.4b shows the light J - V and the corresponding P - V characteristic of the Auger-limited solar cell from figure 2.4a. The power density P has a maximum value at the maximum power point (mpp) with a maximum power point voltage V_{mpp} and a maximum power point current density J_{mpp} . The efficiency η is defined at this maximum power point as the ratio between the maximum output power density $P_{\text{mpp}} = J_{\text{mpp}} V_{\text{mpp}}$ and the incident power density P_{in} .

$$\eta = \frac{P_{\text{mpp}}}{P_{\text{in}}} = \frac{J_{\text{mpp}} V_{\text{mpp}}}{P_{\text{in}}} \quad (2.28)$$

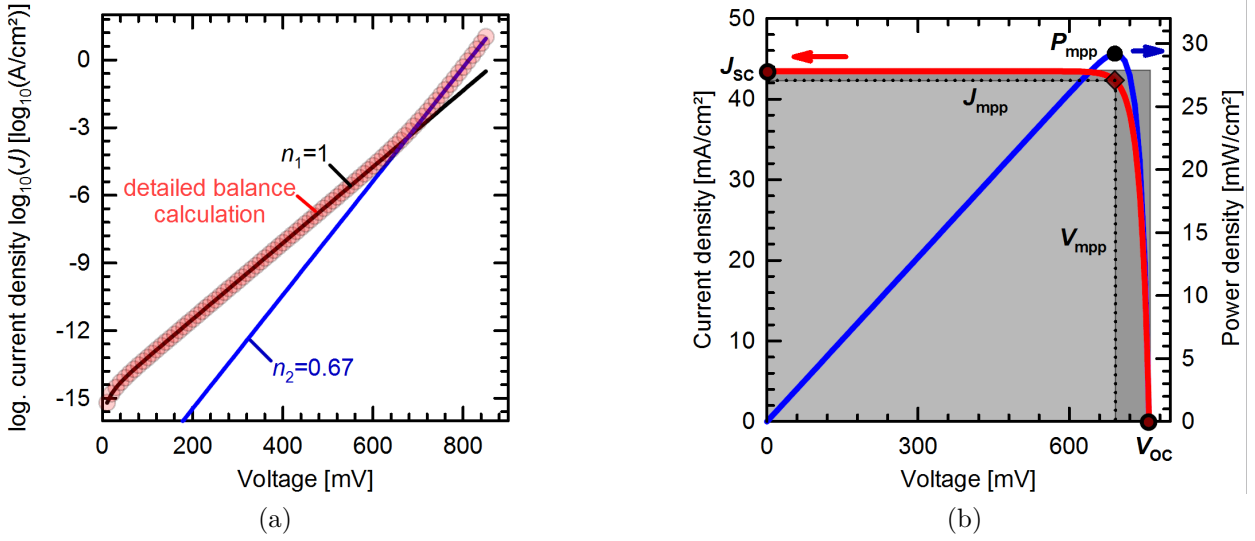


Figure 2.4.: (a) Shifted light J - V characteristic in a semi-logarithmic representation of the Auger-limited solar cell on a $2\ \Omega\text{cm}$ n -type doped $110\ \mu\text{m}$ -thick wafer with Lambertian light trapping according to the detailed balance calculation of reference [28]. (b) Light J - V (red solid line) and P - V (blue solid line) characteristic of the Auger-limited cell in (a). The data was kindly provided by S. Schäfer.

The efficiency of the Auger-limited solar cell in figure 2.4a amounts to a value of $29.2\%^{12}$. Although the efficiency of a solar cell is the most important performance parameter, it is useful to consider three additional parameters for a proper interpretation of the solar cell's performance.

The first parameter, the short-circuit current density J_{SC} approximately equals the photo-generated current density, which reflects the incident spectrum, the optical properties of the solar cell and the collection probability for photo-generated carriers in the solar cell. Typical values for the J_{SC} of a silicon solar cell under AM1.5G illumination spectrum are in the order of $40\ \text{mA}/\text{cm}^2$. The J_{SC} of the Auger-limited solar cell in figure 2.4b exhibits $43.47\ \text{mA}/\text{cm}^2$. The second parameter, the open-circuit (OC) voltage of the solar cell can be directly derived from the single-diode model with $J(V) = 0$ and depends on the recombination prefactor $J_{0\text{m}}$, the ideality factor m_{OC} of the cell at OC and the photo-generated current density J_{Ph} .

$$V_{\text{OC}} = \frac{m_{\text{OC}} k_{\text{B}} T}{q} \ln \left(\frac{J_{\text{Ph}}}{J_{0\text{m}}} + 1 \right) \quad (2.29)$$

Therefore, V_{OC} reflects the recombination behavior of the solar cell. The Auger-limited solar cell shows an ideality factor of $2/3$ and a $J_{0\text{m}}$ of $3.27 \cdot 10^{-21}\ \text{A}/\text{cm}^2$ around OC and exhibits a V_{OC} of $755\ \text{mV}$. The third parameter, the fill factor FF describes the “squareness” of the

¹²Note that the maximum efficiency for Si solar cells amounts to 29.5% [28, 29] and the lower value of 29.2% corresponds to a Si solar cell with a $110\ \mu\text{m}$ -thick n -type wafer with a resistivity of $2\ \Omega\text{cm}$.

light J - V characteristic. The fill factor is called the fill factor because it indicates how much area the light gray rectangle ($J_{\text{mpp}} \cdot V_{\text{mpp}}$) fills in the dark gray rectangle ($J_{\text{SC}} \cdot V_{\text{OC}}$).

$$\text{FF} = \frac{J_{\text{mpp}} V_{\text{mpp}}}{J_{\text{SC}} V_{\text{OC}}} \quad (2.30)$$

For the Auger-limited cell a FF of 89% is obtained. The maximum FF of a solar cell depends on its V_{OC} and can be calculated analytically¹³ according to Green [91]. The actual FF can be lower due to several effect like series and shunt resistance.

Finally, the efficiency is calculated as the product of J_{SC} , V_{OC} and the FF normalized by the incident power density.

$$\eta = \frac{J_{\text{SC}} V_{\text{OC}} \text{FF}}{P_{\text{in}}} \quad (2.31)$$

A view point on the efficiency beyond the J - V characteristic and its calculation is provided by P. Würfel [64]. The process of converting the incident heat radiation from the sun (photons) into maximum electrical power output is subdivided in single conversion process steps with their own conversion efficiencies. The efficiency of the final process is obtained by multiplication of the efficiencies of all sub-processes.

$$\eta = \eta_{\text{abs}} \cdot \eta_{\text{thermalization}} \cdot \eta_{\text{thermodynamic}} \cdot \eta_{\text{extract,OC}} \cdot \text{FF} \quad (2.32)$$

The incoming light is absorbed with an absorption efficiency η_{abs} . The absorbed photons generated electron-hole pairs with an energy larger than the band gap of the absorber and thermalize into the band edges. The thermalization process has an efficiency $\eta_{\text{thermalization}}$. The efficiency $\eta_{\text{thermodynamic}}$ reveals how much energy of the thermalized electron-hole pairs is converted into chemical energy. Now the absorber contains electron-hole pairs with a chemical energy, which has to be converted in electrical energy with a conversion efficiency $\eta_{\text{extract,OC}}$. This efficiency is added here, but P. Würfel assumes this process to occur loss-free [64]. Since the efficiency $\eta_{\text{extract,OC}}$ is unity for a loss-free conversion, Würfel does not list it in his process sequence. However, this conversion process and efficiency is related to the contact's ability to extract charge carrier and will be discussed in chapter 5 in detail. The last factor is the already known fill factor FF.

The efficiency according to P. Würfel are controlled by the four conversion efficiencies. The absorption efficiency η_{abs} and thermalization efficiency $\eta_{\text{thermalization}}$ can be optimized simultaneously by providing only photons with an energy slightly above the band gap of the absorber. A practical realization of the latter is a multi-junction or tandem solar cell.

2.4. Tandem solar cell

A multi-junction or tandem solar cell consists of at least two sub-cells comprising absorbers with a wide band gap and a narrow band gap. The wide-band gap top cell absorbs the

¹³Green's approximation takes into account that the ideality factor of the solar cell is not necessarily unity in the framework of a single-diode model. This implies that the ideality factor around OC and mpp should be equal in order that Green's approximation yields accurate values for the FF.

incident high energy photons above the band gap and transmits the photons with an energy below the band gap to the bottom cell with a narrower band gap. The bottom cell absorbs all transmitted photons with an energy above its band gap. The tandem architecture minimizes the losses due to incomplete absorption and thermalization.

The practical realization of a tandem solar cell requires semiconductor materials with a suitable band gap and electronic quality. Probably the most sophisticated solar cell ever built is a six-junction III-V solar cell with an efficiency of 47.1% [40]. However, reducing the enormous manufacturing cost of such III-V multi-junction cells, while maintaining cell performance, is the main issue and an ongoing task [92].

Besides the question of the choice for top and bottom cells materials, the internal interconnection of tandem solar cells, the associated number of terminals and the corresponding cell architecture; the module and system integration scheme is of great importance, especially for terrestrial photovoltaics systems [93–95]. For dual-junction solar cell, top and bottom cells are commonly either interconnected in series or not interconnected at all. The latter interconnection scheme requires that each sub-cell has its own independent sub-circuit working at its own maximum power point and therefore needs four terminals (4T) for a mechanically stacked dual-junction solar cell. Since top and bottom cell operate electrically independent from each other, the top and bottom cell polarity can be of arbitrary type. Moreover the large flexibility of 4T tandems compared to series-connected two-terminal (2T) tandems enables the usage of a broader range of band gaps for top and bottom cell as well as a higher robustness against spectral variations, which leads usually to higher cell efficiency and energy yields. However, the fabrication of additional transparent conductive layers, metal grids and insulating layers in-between top and bottom cell and the integration of 4T tandems in cost-effective modules and systems is challenging [96].

In a two-terminal tandem solar cell, the top cell and bottom cell diodes are directly joining to form a series-connected tandem cell and both cell diodes need to be short-circuited via a coupling layer (tunneling or recombination junction). Since series-connected cells have to share the same current, the sub-cells in this type of architecture have to be current-matched, which implies a more stringent band gap selection and a higher sensitivity to changes of the illumination spectrum. Nevertheless, the fabrication of cells is simplified and state-of-the-art single-junction module and system integration can be applied.

A less familiar internal interconnection scheme yielding a tandem solar cell with three terminals is discussed in chapters 4 and 8 in detail. The bipolar junction bottom cell as one possibility for the bottom cell of such a tandem solar cell exhibits a similar architecture as a bipolar junction transistor. Therefore, bipolar junction bottom cells will be described by adapting established models from the transistor theory later in this thesis. Transistors and their theory are summarized in the following.

2.5. Transistor

In 1947/1948, Bardeen and Brattain [97, 98] discovered the transistor amplification effect and Shockley developed the theory of pn junctions and invented the bipolar junction transistor [60] at Bell Labs. The invention of this solid-state switch triggered the era of microelectronics.

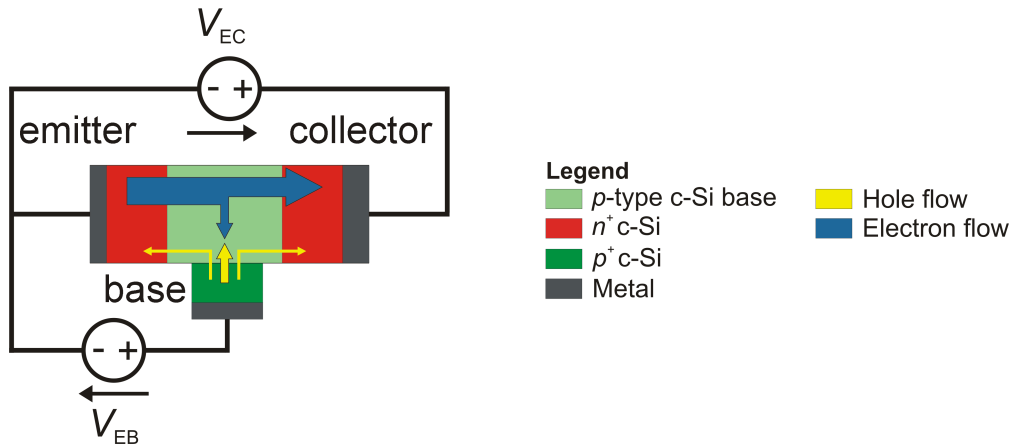


Figure 2.5.: Schematic layer structure of a bipolar junction transistor in common-emitter configuration. The voltage sources and the carrier flows indicate the situation for a bipolar junction transistor in forward-active mode.

Figure 2.5 shows the layer structure of a npn bipolar junction transistor. Each of the n -type layers – the emitter and the collector – form a pn junction with the p -type base. Thus, a transistor is a three-terminal device with an emitter, a base and a collector terminal. The corresponding band diagram of the bipolar junction transistor in equilibrium resembles that of two pn junction diodes with built-in voltages $\Phi_{Bi,EB}$ and $\Phi_{Bi,BC}$, which are connected back-to-back via the p -type base (figure 2.6a).

The main task of a transistor is to control the resistance for the current transfer from the emitter contact to the collector contact through the base by means of the base contact. In order to drive a current flow from the emitter towards the collector, a voltage V_{EC} has to be applied between the emitter and collector contact. However, the “resistance” for the current transfer between emitter and collector contacts is controlled by the emitter-base junction¹⁴. If the emitter-base junction is forward biased, then electrons are injected (or emitted) from the emitter into the base region and the electron carrier concentration in the base increases. The equilibrium Fermi-level from figure 2.6a splits in two separate quasi Fermi-levels in figure 2.6b. If the collector-base junction is shorted or reverse-biased, the electron concentration at this junction is depleted. The concentration gradient in the nearly field-free base region, i.e. the gradient of the electron quasi Fermi level, drives a diffusive electron current from the emitter to the collector contact. The bipolar junction transistor operates in forward-active mode, where a small control current of holes injected at the base contact – the base current – amplifies a large current from the emitter to the collector contact. The amplification factor or common-emitter current gain β_F for the forward-active mode is the ratio of the collector current density J_C versus base current J_B and has a value of more than 50 for typical bipolar junction transistors. The common-emitter current gain quantifies the performance of a bipolar junction transistor and can be re-expressed by the common-base

¹⁴The emitter-base junction is relevant for the forward active mode, since the collector-base junction is typically shorted or even reverse-biased.

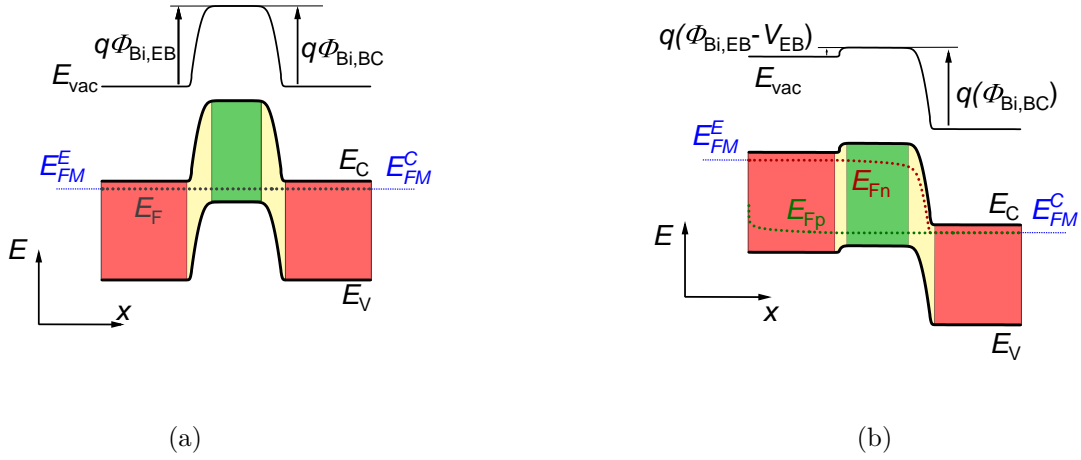


Figure 2.6.: Band diagram of a bipolar junction transistor in (a) equilibrium and in (b) forward-active mode. The red and green regions indicate the n -type and p -type quasi-neutral regions and the light yellow region is the space-charge region.

current gain or transport factor α_F , which is the ratio of the collected current at the collector contact J_C versus the injected current at the emitter contact J_E .

$$\alpha_F = \frac{\beta_F}{\beta_F + 1} = \alpha_T \gamma_E \quad (2.33)$$

Thus, the performance of a bipolar junction transistor depends on the product of the base transport factor α_T and the emitter injection efficiency γ_E . The base transport factor reflects the minority carrier transport through the base and the emitter injection efficiency describes the quality of the emitter contact.

The bipolar junction transistor can also operate in reverse-active mode, when the emitter-base junction is shorted or reverse-biased and the collector-base junction is forward-biased. In this case, the collector injects electrons into the base, which flow towards the emitter and are collected at the reverse-biased emitter-base junction. The performance parameters β_R and α_R for the reverse-active mode operation are defined similar to those of the forward-active mode, but the emitter and collector current density are interchanged. Since the forward-active mode is the typical operation mode of a bipolar junction transistor, the transistor is designed such that the forward current gain is maximized. Typically, $\beta_F \gg \beta_R$, because the emitter injection efficiency γ_E is made higher than the collector injection efficiency γ_C due to the fact that the emitter is much heavier doped than the collector.

For the use in electrical circuit models, Ebers and Moll developed an equivalent circuit model for the large signal behavior of bipolar junction transistors [99]. The Ebers-Moll injection model¹⁵ as shown in figure 2.7 can be interpreted qualitatively as a superposition of the forward-active and reverse-active mode operations. In forward-active mode, the collector-base diode is reverse-biased and the reverse current density $J_R = 0$, while the emitter-base junction

¹⁵A derivation of the Ebers-Moll model from drift-diffusion model can be found in the appendix A.5.1.

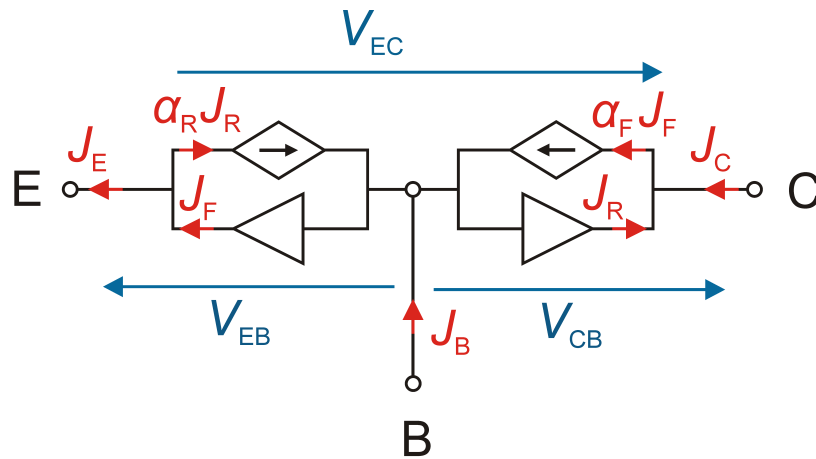


Figure 2.7.: Ebers-Moll equivalent circuit of the injection model of a bipolar junction transistor.

is forward-biased and the forward current density $J_F > 0$. The current-controlled current source with the current density $\alpha_F J_F$ represents the current density transferred through the base. In reverse-active mode, $J_F = 0$ and $J_R > 0$, such that the current-controlled current source with the current density $\alpha_R J_R$ again represents the current density transferred through the base. The superposition of both operation mode justifies the equivalent circuit model in figure 2.7.

3. Characterization methods

3.1. Photo-conductance decay method

In a semiconductor device like a solar cell, the generation and recombination processes of minority charge carriers play a decisive role. The conductivity of the semiconductor depends on the charge carrier density (equation 2.8) and the charge carrier density increases upon illuminating the semiconductor due to photo-generation of an excess carrier density Δn . The excess carrier density Δn can be determined from the excess conductance $W \cdot \Delta\sigma$ with the sample thickness W and excess conductivity $\Delta\sigma$ by

$$W \cdot \Delta\sigma = qW(\mu_n + \mu_p)\Delta n \quad (3.1)$$

The photo-conductance decay measurements in this thesis are performed with the WCT-120 lifetime tester from Sinton Instruments, which measures the conductivity of the sample inductively via a coil. The experimental setup is illustrated schematically in figure 3.1. The illumination is applied by a simple flash lamp and the illumination intensity is calibrated via a reference solar cell.

After applying the short flash illumination to generate an initial excess carrier density Δn_0 in the test wafer, the excess carrier density Δn along with the excess photo-conductivity $\Delta\sigma$ decays due to the recombination of excess minority charge carriers. The rate of change $\frac{\partial\Delta n}{\partial t}$ of Δn with time is describe by the continuity equation 2.21. Under the assumption of a spatially homogeneous carrier distribution ($\frac{\partial J_n}{\partial x} = 0$) the continuity equation reads

$$\frac{\partial\Delta n}{\partial t} = G - R_{\text{eff}} = G - \frac{\Delta n}{\tau_{\text{eff}}} \quad (3.2)$$

The Δn -dependent effective recombination lifetime $\tau_{\text{eff}}(\Delta n)$ describes the rate of recombination R and provides a directed measure to study recombination processes in semiconductor materials [100–102]. For high lifetimes, which are typically required for high performance solar cells, the lifetime can be determined from the transient decay of Δn after the illumination is turned off, such that $G = 0$ in equation 3.2.

The obtained τ_{eff} represents an effective lifetime of the sample, which is a consequence of the total recombination rate R_{eff} . The total recombination rate is the sum of the Auger and radiative recombination, Shockley-Read-Hall (SRH) recombination in the bulk and at the surface. Therefore, the effective lifetime calculates as

$$\frac{1}{\tau_{\text{eff}}} = \frac{1}{\tau_{\text{Auger+rad}}} + \frac{1}{\tau_{\text{bulk}}} + \frac{1}{\tau_{\text{surf}}} \quad (3.3)$$

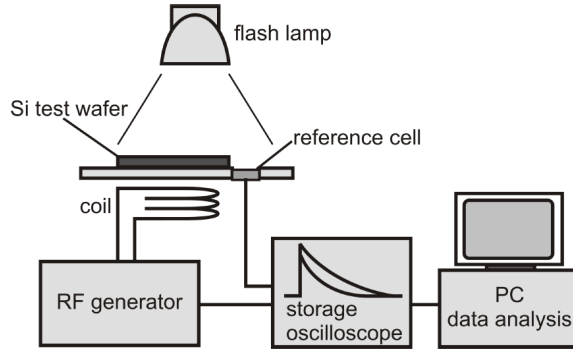


Figure 3.1.: Setup of the Sinton lifetime tester [103]

with the lifetime $\tau_{\text{Auger+rad}}$ due to Auger and radiative recombination, the lifetime τ_{bulk} due to SRH recombination in the bulk and the lifetime τ_{surf} due to surface recombination. From the point of view of solar cell development, it is often useful to compare the implied J - V parameters of solar cell precursors. For that purpose, the lifetime $\tau_{\text{eff}}(\Delta n)$ is often translated into an implied J - V characteristic by using the fact that the recombination rate R is directly proportional to a recombination current density J_{rec} .

$$J_{\text{rec}} = qWR = qW \frac{\Delta n}{\tau_{\text{eff}}} \quad (3.4)$$

The implied open-circuit voltage $iV_{\text{OC}} = \frac{E_{\text{Fn}} - E_{\text{Fp}}}{q}$ is calculated from the pn product in equation 2.17. Of course, the conversion of $\tau_{\text{eff}}(\Delta n)$ into the implied J - V characteristic can also be used under certain conditions¹ to convert the J_{SC} - V_{OC} characteristic into a lifetime characteristic as performed in chapter 7.

Furthermore, the surface recombination rate in equation 3.3 is often quantified by a surface saturation current density J_{0s} according to the following definition [101, 104–107].

$$J_{\text{rec,surf}} = J_{0s} \left(\frac{n_s p_s}{n_{i,s}^2} - 1 \right) = qW \frac{\Delta n}{\tau_{\text{surf}}} \quad (3.5)$$

n_s and p_s are charge carrier densities for electrons and holes, respectively and $n_{i,s}$ is the intrinsic carrier density at the surface of the semiconductor. Using equation 3.5 in equation 3.3 and assuming high level injection conditions ($n_s p_s \approx \Delta n^2$), the surface saturation current density can be determined from the following equation, if the slope of the Δn -dependent inverse of the Auger-corrected lifetime $\frac{1}{\tau_{\text{eff}}} - \frac{1}{\tau_{\text{Auger+rad}}}$ is evaluated.

$$\frac{1}{\tau_{\text{eff}}} - \frac{1}{\tau_{\text{Auger+rad}}} = \frac{1}{\tau_{\text{bulk}}} + \frac{2J_{0s}}{qWn_{i,s}^2} \Delta n \quad (3.6)$$

For a symmetric lifetime sample with two equivalent surfaces, each surface contributes a recombination current density to the total recombination, which is taken into account with the

¹The J_{SC} should reflect the photo-generation current density and the $V_{\text{OC}} \approx iV_{\text{OC}}$. The former is valid if the series resistance is not too large and the latter is true for highly carrier-selective contacts.

factor 2 in front of the J_{0s} term in equation 3.6. The described method for the determination of J_{0s} was first reported by Kane and Swanson [101] and is denoted as the slope method according to Kane and Swanson.

3.2. Contact resistivity measurement

The contact is an essential component of a solar cell, as it is the contact that enables the extraction of charge carriers from the absorber. Since this thesis partly deals with the properties of contacts, in particular with the properties of passivating and carrier-selective POLO contacts, an essential property - the contact resistivity - is introduced below and the transfer length method (TLM) for the determination of the contact resistivity is briefly summarized.

3.2.1. Contact resistivity

A contact between the semiconductor and the metal can be implemented in many different ways. For example, direct metal-semiconductor (M-S) contacts [108], conductor-insulator-semiconductor (C-I-S) contacts [109] and many other types of contacts have been studied in the literature [110]. The carrier transport from the semiconducting absorber into the metal depends on the specific physics of the contact, but for many contacts the current-voltage characteristic for the partial carrier transport – electron or holes – can be approximated by a rectifying behavior similar to Schottky’s M-S contact [109, 111].

$$J = J_0 \left[\exp \left(\frac{qV}{mk_B T} \right) - 1 \right] \quad (3.7)$$

The diode prefactor J_0 and the ideality factor m depend on the physics of the contact. The desired electron-selective and hole-selective contact to a solar cell is required to efficiently transport electrons and holes from the absorber to the metal contact, respectively, and the voltage drop due to transport of the desired species should be as low as possible. According to Fonash [112, p. 123] and Fahrenbruch and Bube [113, p. 187], such contacts are denoted as ohmic or quasi-Ohmic selective contacts and the transport properties can be quantified by a specific contact resistance ρ_c . The term ohmic implies that the J - V characteristic of the contact is linear, the constant resistance is small and no photovoltaic effect occurs at an ohmic contact. The specific contact resistance – also contact resistivity – ρ_c is then simply the inverse of the slope of the J - V characteristic at $V = 0$.

$$\rho_c = \left(\frac{dJ}{dV} \Big|_{V=0} \right)^{-1} \quad (3.8)$$

In practice, however, perfectly ohmic contacts are rarely achieved, because the J - V characteristic follows equation 3.7 rather than being linear. As long as the exponent $\frac{qV}{mk_B T}$ in equation 3.7 is close to zero for the desired current density, equation 3.7 can be made linear by means

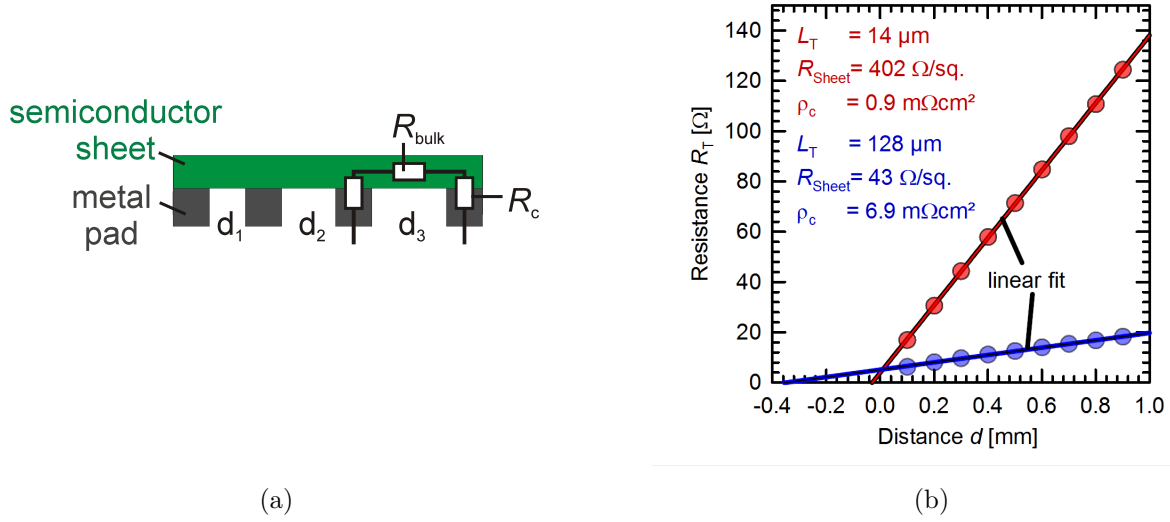


Figure 3.2.: (a) Schematic cross-section of a transfer length test structure. (b) Example of the measured data for the TLM samples from chapter 6.3.

of a first-order Taylor approximation and the contact resistivity according to equation 3.8 reads

$$\rho_c = \frac{mk_B T}{qJ_0} \quad (3.9)$$

This type of contact is denoted as quasi-ohmic contact.

3.2.2. Transfer length method

For ohmic and quasi-ohmic contacts, the transfer length method (TLM) can be used to determine the value of the contact resistivity [111]. Figure 3.2a shows the schematic cross-section of a TLM test sample comprising a thin semiconductor sheet, which is contacted by metal pads with a distance $d = d_1, d_2, \dots$ apart from each other. The current-voltage I - V characteristic is measured between adjacent metal pads and the total resistance R_T , which is the sum of twice the contact resistance R_c and the lateral bulk transport resistance R_{bulk} through the sheet, is calculated. R_T is evaluated for several distances d and R_T as a function of the distance d is obtained as shown in figure 3.2b. For the simplest case, R_T is a linear function of d , since R_{bulk} increases linearly with distance and $2R_c$ stays constant. Therefore, the slope of the obtained linear fit to the data corresponds to the sheet resistance R_{Sheet} of the semiconductor sheet and the intercept with the R_T -axis yields twice the contact resistance R_c . In figure 3.2b, the sample from the red data set has a higher sheet resistance than the sample from the blue data and therefore the slope of the red data is steeper than for the blue data.

To extract the contact resistivity ρ_c from the contact resistance R_c , the correct area through which the current flows must be determined. Since the sheet resistance of the semiconductor

sheet is finite, the charge carriers underneath a metal pad experience a resistance, while flowing through the semiconductor sheet. In order to minimize the lateral resistance contribution of current flowing beneath the contact, the current would try to enter or leave the metal pad as close to the edge of the metal pad as possible. On the other hand, the contact resistivity of the metal-semiconductor contact is finite too and the current would like to occupy as much of the contact's area as possible to minimize the contribution from the contact resistance. However, the latter implies that the current flows a long distance through the semiconductor sheet and causes a large lateral resistance contribution. Finally, the current flows along the path of least resistance and most of the current has entered or left the metal pad at a distance $L_T = \sqrt{\frac{\rho_c}{R_{\text{Sheet}}}}$ away from the contact's edge, which is called the transfer length. The contact resistivity can be calculated from

$$\rho_c = \frac{R_c \cdot Z \cdot L_T}{\coth\left(\frac{L}{L_T}\right)}, \quad (3.10)$$

where Z is the contact's length perpendicular to direction of the current flow and L is the contact's width in direction of the current flow.

The model for equation 3.10 is only accurate for one-dimensional current flow within the semiconducting sheet and restricts equation 3.10 to thin and conductive sheets. For the case, where two-dimensional current flow is important, Eidelloth and Brendel have reported an advanced analysis method [114], where equation 3.10 is replaced by a more complex expression.

3.3. Current-voltage characterisation of solar cells

For the development of solar cells, the characterization of the finished solar cell using current-voltage characteristics is an essential method. Three common types of current-voltage J - V characteristics exist: the illuminated J - V , the dark J - V and the J_{SC} - V_{OC} characteristic.

3.3.1. Illuminated J - V characteristic

As discussed in section 2.3, the illuminated J - V (also light J - V) characteristic is the most important characteristic of a solar cell and contains information on the performance parameters of the solar cell under investigation. In order to obtain an accurate light J - V characteristic, which allows to compare devices independent of the measurement setup, the solar cell has to be measured under standard test conditions (STC). A measurement under STC implies that the solar cell's temperature is held at 25 °C, while illuminated with a AM1.5G spectrum with an intensity of 100 mW/cm² during the J - V measurement. Since it is demanding to generate such a spectrum with high accuracy in the lab, accurate measurements are usually performed by an accredited certification lab and the measured result are denoted as certified measurement. Unfortunately, a certified measurement is time consuming and costly, and is only performed for carefully selected solar cells.

For all the other solar cells with two terminals in this thesis, the light J - V is determined at a

cell's temperature of approximately 25 °C in a LOANA solar cell characterization system from pv tools. The illumination is applied by a narrow-band infrared LED illumination source, whose intensity is adjusted such that the current density of a reference cell corresponds to a calibrated solar cell under STC illumination. This procedure is only accurate if the calibrated cell is almost identical to the probed cell. The measurement procedure and setup for three-terminal solar cells is outline in chapter 8.

3.3.2. Dark J - V characteristic

In addition to the light J - V , the dark J - V and the J_{SC} - V_{OC} characteristics and the comparison of the different characteristics provides important information on the physical properties of the solar cell. The dark J - V characteristic is described similar as in equation 2.27, but $J_{\text{Ph}} = 0$ and J becomes negative.

$$J(V) = J_{01} \left[\exp \left(\frac{q(V - JR_S)}{m_1 k_B T} \right) - 1 \right] + J_{02} \left[\exp \left(\frac{q(V - JR_S)}{m_2 k_B T} \right) - 1 \right] - \frac{V - JR_S}{R_{\text{SH}}} \quad (3.11)$$

If the dark characteristic curve is plotted semi-logarithmically, the recombination parameters J_{01} , J_{02} , m_1 and m_2 can be theoretically determined from it. From this analysis, the dominant recombination paths in a solar cell at dark conditions can be identified. At low and high voltages, the shunt and series resistance can be derived, respectively. Since the recombination behavior and the resistance parameters of the solar cell often change upon applying illumination, the solar cell parameters should rather be extracted close to the operation conditions, i.e. under illumination. Therefore, the analysis from above is usually applied to the J_{SC} - V_{OC} characteristic.

3.3.3. J_{SC} - V_{OC} characteristic

For the J_{SC} - V_{OC} characteristic, the short-circuit current density and open-circuit voltage are measured for different illumination intensities. The obtained characteristic is theoretically almost the same as for a series resistance-free dark J - V characteristic.

$$J_{\text{SC}} = J_{01} \left[\exp \left(\frac{qV_{\text{OC}}}{m_1 k_B T} \right) - 1 \right] + J_{02} \left[\exp \left(\frac{qV_{\text{OC}}}{m_2 k_B T} \right) - 1 \right] - \frac{V_{\text{OC}}}{R_{\text{SH}}} \quad (3.12)$$

The comparison of the J_{SC} - V_{OC} with the dark J - V characteristic can be used to determine the series resistance.

Moreover, the recombination parameter for the solar cell under illumination can be extracted from the J_{SC} - V_{OC} characteristic. Measuring the J_{SC} - V_{OC} characteristic is very similar to the Suns- V_{OC} method and can be translated into a lifetime curve $\tau_{\text{eff}}(\Delta n)$ to study the different recombination paths of the solar cell.

3.3.4. Local ideality factor

From the three different J - V characteristics, a lot of information about a solar cell can be gained, especially if the local ideality factor of the three different characteristics is taken into

account. The local diode ideality factor m of the shifted light J - V , dark J - V and J_{SC} - V_{OC} corresponds to the inverse slope of the respective $\ln(J)$ - V characteristic and calculates as follows:

$$m(V) = \frac{q}{k_B T} \cdot \left[\frac{d \ln(J)}{dV} \right]^{-1} \quad (3.13)$$

The m - V characteristic contains bumps, humps and lumps, which can be ascribed to different effect in a solar cell and to gain an understanding on the physical mechanisms affecting the solar cell's performance [115].

4. State-of-the-art

4.1. Selectivity of passivating contacts

4.1.1. Quantitative definition of selectivity

In recent years, several authors defined metrics for the selectivity of contacts to solar cells quantitatively [116–124]. The different approaches are not identical in terms of defining the region of the contact, which provides selectivity, nor with regard to the assumed processes involved in the carrier extraction at the contact. The definitions can be classified in two categories: the first category of definitions compares the transport coefficients for electron and hole transport through the contact [118–120, 123] and the second one compares the internal versus external voltage [117, 121, 122, 124] of the solar cell. The different definition are briefly listed here. A detailed discussion is found in chapter 5.

Pysch *et al.*, Bivour *et al.* and Glunz *et al.* [121, 122, 125, 126] quantify the selectivity by comparing the implied open-circuit voltage iV_{OC} with the external open-circuit voltage V_{OC} . They propose to either use the difference [121, 122] or the ratio [122, 125, 126] of V_{OC} and iV_{OC} as a figure of merit of selectivity.

Brendel and Peibst [120, 127] calculate the resistances from the inverse slopes of the current-voltage characteristics at a voltage across the contact of $V = 0$. They assume a diode-like minority carrier recombination current density $J_m = J_c \cdot [\exp(\frac{V}{V_T}) - 1]$ with recombination parameter J_c and thermal voltage V_T , and a linear majority carrier current density-voltage characteristic $J_M = \frac{V}{\rho_c}$ with a contact resistivity ρ_c . In this case, the selectivity is determined from J_c and ρ_c as

$$S_{Brendel} = \frac{\rho_m}{\rho_M} = \frac{\left(\frac{dJ_m}{dV}\Big|_{V=0}\right)^{-1}}{\left(\frac{dJ_M}{dV}\Big|_{V=0}\right)^{-1}} = \frac{V_{th}}{J_c \cdot \rho_c} \quad (4.1)$$

Smit [118] provides a detailed discussion on the selectivity of contacts. He provide two different possibilities. The first compares the resistivities of minority and majority carrier transport within the selective contact and result in a similar formula as that of Brendel and Peibst. Second, Smit defines another possibility for a selectivity metric as $V_{OC}/\Delta V_{OC}$

Koswatta and Onno *et al.* define¹ their partial specific contact resistances ρ_n and ρ_p at open circuit conditions as the potential drop $E_{FM} - E_{Fn}$ and $E_{FM} - E_{Fp}$ across the contact due to the quasi-Fermi level gradient ∇E_{Fn} and ∇E_{Fp} divided by the corresponding partial current density j_n and j_p ²:

$$\rho_n = \frac{1}{q} \cdot \frac{E_{Fn} - E_{FM}}{j_n} \quad (4.2a)$$

$$\rho_p = \frac{1}{q} \cdot \frac{E_{FM} - E_{Fp}}{j_p} \quad (4.2b)$$

Onno *et al.* define the selectivity metric η_{ASU} ^{3,4} as follows

$$\eta_{ASU} = \frac{\rho_m}{\rho_M + \rho_m} = \frac{E_{Fn} - E_{FM}}{E_{Fn} - E_{Fp}} = \frac{V_{OC}}{iV_{OC}} \quad (4.3)$$

and found that under open-circuit conditions ($j_{total} = j_p - j_n = 0$) their definition of the selectivity corresponds to the ratio of the external voltage V_{OC} to the implied voltage iV_{OC} . According to the equivalent circuit model proposed by Onno *et al.* [124], Onno *et al.* conclude that the resistors act as a voltage divider between the implied and external voltage.

Tan *et al.*, Weber *et al.* and Roe *et al.* [119, 123, 128, 129] choose a picture of the contact commonly used in photo-electrochemistry, which is often applied to molecular, organic or dye-sensitized solar cells [62, 130–132]. In this framework, electrons and holes from the conduction and valence band states are transferred to electrons and holes within the „contact region“ and vice versa via an electron-transfer reaction. The transfer reaction can be described as a chemical reaction according to Gurney-Gerischer-Marcus (GGM) rate theory [133–138] with the corresponding rate constant k^C and k^V for the conduction and valence band reaction, respectively. The net exchange current density for electrons between the conduction band and the contact reads⁵

$$j_n = j_{0n} \cdot \left(\frac{n_S}{n_{S0}} - 1 \right) \quad (4.4)$$

and the exchange current density for holes between valence band and contact is

$$j_p = j_{0p} \cdot \left(\frac{p_S}{p_{S0}} - 1 \right) \quad (4.5)$$

¹This definition is similar to the physical interpretation of recombination processes with recombination resistances [72]. Shockley and Read define this resistances as $R_n = \frac{E_{Fn} - E_{Ft}}{U_{cn}} = q^2 \rho_n$ and $R_p = \frac{E_{Ft} - E_{Fp}}{U_{cp}} = q^2 \rho_p$, where E_{Ft} is the energy level of the trap and $U_{cn} = -\frac{j_n}{q}$ and $U_{cp} = \frac{j_p}{q}$ are the recombination rates.

²Note that, in accordance to Onno *et al.*, the current densities are defined such that electron (hole) current points from the contact (absorber) towards the absorber (contact). This implies that the electron current density is positive, if electrons flow into the contact.

³In contrast to Onno *et al.*, the chosen symbol for „selectivity“ indicates that the definition of Onno *et al.* is an efficiency rather than a selectivity. This fact will be discussed in chapter 5.

⁴Electrons are assumed as minority charge carriers.

⁵A derivation of the exchange current densities is found in A.3.1.

Where j_{0n} (j_{0p}) are the equilibrium exchange current densities, n_S (p_S) the carrier concentration and n_{S0} (p_{S0}) the equilibrium carrier concentrations of electrons (holes) at the surface. Weber *et al.* and Roe *et al.* define (electron) selectivity as the ratio of equilibrium exchange current densities j_{0n} and j_{0p} for the charge transfer reactions at the contact.

$$S_{n,Weber} = \frac{j_{0n}}{j_{0p}} \quad (4.6)$$

Shockley *et al.* and Kroemer faced a similar challenge to quantify the performance of emitter junctions in bipolar junction transistors. Shockley came up with the emitter injection efficiency γ as „the fraction of emitter current carried by holes“ for a *pn*p transistor [139]. In this case, the hole and electron current density are the majority and minority carrier current density j_M and j_m in the *p*-type emitter contact, respectively and the emitter injection efficiency is

$$\gamma = \frac{j_M}{j_M + j_m} \quad (4.7)$$

The emitter injection efficiency for typical transistors has to be a number close to 1 (0.98-1) and already a tiny difference in γ has a large impact on the performance of a bipolar junction transistor. If base recombination is neglected, the common-emitter current gain β , which is the measure for the performance of a transistor, is directly proportional to the inverse of the „emitter deficit“. Therefore, Kroemer pointed out that the „emitter deficit“ ($1 - \gamma$) is a more appropriate figure of merit for the performance [140] and that the emitter deficit for typical transistors with γ close to one is approximately the ratio of the minority and majority carrier current density.

$$1 - \gamma \approx \frac{1 - \gamma}{\gamma} = \frac{j_m}{j_M} = \frac{1}{\beta} \quad (4.8)$$

Emitter injection efficiency is frequently used to characterize bipolar junction transistor devices with homo-junctions [141] and hetero-junctions [142], but the emitter deficit was also used to study metal-semiconductor [143] and metal-insulator-semiconductor [144] junctions. Note that Kroemer’s definition is not equivalent, but somewhat similar to that of Weber *et al.*.

In contrast to the selectivity figure for solar cells, the emitter injection efficiency is an established figure for bipolar junction transistors and a large data base and models for different emitter contacts exist.

4.1.2. Quantification of selectivity

1. Pysch *et al.* [125, 126] introduce a method, which allows to measure the internal and the external voltage of an asymmetric silicon wafer sample with either an electron or a hole selective contact and a thin transparent conducting oxide (TCO) contact on each side of the wafer⁶. A photo-conductance decay and a *Suns-V_{OC}* measurement

⁶This sample architecture restricts the method to a special sort of contacts and excluded important examples based on metal-insulator-semiconductor systems.

reveal the iV_{OC} and V_{OC} value, respectively. Using the ratio of the two values the selectivity metric η_{ASU} can be calculated. The accuracy of this simple method strongly depends on how accurate iV_{OC} and V_{OC} can be determined and on the calibration of both measurement techniques to each other. Feldmann reported a measurement error of $iV_{OC} - V_{OC}$ in the range of 5 mV for solar cell test samples with an iV_{OC} of about 700 mV. This translates to an accuracy of better than 1% [145, p. 123]. Stolterfoht *et al.* [146] replaced the photo-conductance decay and $Suns - V_{OC}$ method by absolute photo-luminescence technique and current-voltage measurements of full devices for the iV_{OC} and V_{OC} determination, respectively and studied carrier-selective contacts to organic-inorganic metal halide perovskite absorbers. However, the measurement uncertainty in this study is probably even higher than 1% and the discussion is of qualitative nature.

2. The value of the selectivity figure according to Brendel and Peibst can be found by measuring the recombination prefactor J_c of a symmetric silicon wafer sample following the method of Kane and Swanson [101] and the contact resistivity ρ_c by using transfer length method [111, 147–149] or a method proposed by Cox and Strack [150].
3. Tan *et al.* [128] used an interdigitated back-contact solar cell with a third semiconductor/electrolyte contact to probe the ratio of equilibrium exchange current densities at the front contact. At open-circuit conditions, the sum of electron and hole exchange current density has to vanish and the ratio of equilibrium exchange current densities is obtained as follows.

$$S_{n,Weber} = \frac{j_{0n}}{j_{0p}} = \frac{(1 - \frac{ps}{ps0})}{(1 - \frac{ns}{ns0})} = \frac{\exp(\frac{qV_{p^+,OC}}{kT}) - 1}{\exp(-\frac{qV_{n^+,OC}}{kT}) - 1} \quad (4.9)$$

$V_{p^+,OC}$ is the open-circuit voltages between the electrolyte front contact and the rear p^+ contact and $V_{n^+,OC}$ the open-circuit voltage between the electrolyte front contact and the rear n^+ contact. If perfectly selective n^+ and p^+ rear contacts and constant quasi-Fermi levels in the quasi-neutral wafer region are assumed, then $q \cdot V_{p^+,OC} = E_{FM} - E_{Fp}$ and $q \cdot V_{n^+,OC} = E_{FM} - E_{Fn}$ indicate the position of the Fermi level E_{FM} within the contact with respect to the quasi-Fermi level of holes E_{Fp} and electrons E_{Fn} . The selectivity metric according to Weber *et al.* can then be quantified by measuring $V_{p^+,OC}$ and $V_{n^+,OC}$.

4.1.3. Impact of selectivity on the efficiency of solar cells

Young *et al.* [151] and Bullock *et al.* [152] calculated the maximum achievable efficiency for a silicon solar cell, when the area fraction of a contact with a particular recombination prefactor J_c and contact resistivity ρ_c is optimized. They found that, for an optimized area fraction, the efficiency is approximately only dependent on the product of J_c and ρ_c . Since the selectivity metric according to Brendel and Peibst [120] is proportional to the inverse of this product, Brendel *et al.* [120, 127] pointed out that the ultimate efficiency limit of a

contact-limited silicon solar cell with optimum contact area fraction is only a function of their selectivity metric. Therefore, the higher the selectivity of a selective contact (partially covering the surface area) is, the higher is the achievable ultimate efficiency limit. Rau and Kirchartz [153] demonstrated that this correlation between ultimate efficiency limit and selectivity also holds for the selectivity definition of Weber *et al.* and Roe *et al.*.

However, Glunz *et al.* [122] argue that, in order to achieve high efficiency, it is not sufficient for a contact to have a high selectivity⁷, but furthermore needs interfacial passivation between the contact and the absorber and a reasonable contact resistivity. Glunz's statement is also supported by Onno *et al.* [124] and Weber *et al.* [119]. Weber *et al.* pointed out that an interfacial layer, which reduces the transfer of electrons and holes from the absorber into the metal electrode equally, does not affect the asymmetry of the carrier transport, but improves the passivation of the contact. For a fixed selectivity value, the contact can have different abilities to passivate and to conduct.

However, instead of inserting an interfacial layer, one can also adjust the contact area fraction and leave the non-contacted region perfectly passivated. The global passivation and conduction properties of the solar cell can be scaled by the area fraction, such that, for each selectivity value, one single optimum between passivation and conduction properties is found. A prominent example is the partial aluminium back-surface field contact and the selective emitter of a PERC cell or point contacts of a point contact IBC cells. The mesoporous TiO₂ electron contact to organic-inorganic metal halide perovskite absorbers with a large area fraction is another prominent example.

4.2. Passivating poly-Si-on-Oxide (POLO) carrier-selective junction

Classification of the author's contribution to the field

The author had his first contact with the topic of POLO junctions during his internship at ISFH in 2013/2014, where he worked directly with U. Römer and R. Peibst on the first implementation steps of POLO-IBC cells with point contacts and their interconnection by laser welding [154]. However, only in 2015, the author started his PhD studies at ISFH and in 2016 he was one of the first to demonstrate an interdigitated back-contact cell with POLO junctions for both polarities with an efficiency close to 24% [155], which was the early precursor for the *p*-type POLO-IBC record cell with 26.1% [156]. Furthermore, the author determined the selectivity of the POLO junctions [157] and contributed to the clarification of the transport mechanisms in POLO junctions [158, 159].

4.2.1. Historical evolution

In the early 1970s Takagi *et al.* discovered a greatly enhanced performance of bipolar junction transistors [160], when in-situ doped poly-crystalline silicon layers were used as an alternative

⁷Note that selectivity for Glunz *et al.* means something different compared to Brendel and Peibst.

4.2. PASSIVATING POLY-SI-ON-OXIDE (POLO) CARRIER-SELECTIVE JUNCTION

diffusion source for the emitter formation of BJTs. Thereafter, several authors [141, 142, 161–171] studied poly-silicon emitter contacts and SIPOS (semi-insulating poly-crystalline silicon) contacts for BJTs. A thin interfacial silicon oxide - intentionally or unintentionally grown - was identified between the poly-silicon layer and mono-crystalline silicon surface. This semiconductor-insulator-semiconductor (SIS) emitter junction caused the strong improvement of emitter injection efficiency compared to conventional metal-semiconductor junctions [141, 142, 167–172] and the polysilicon emitter technology is now state-of-the-art technology for bipolar junction transistors for decades [173].

For a solar cell, an improved emitter injection efficiency is equivalent to a higher carrier selectivity of the (emitter) junction⁸ and directly has an impact on conversion efficiency [120, 127]. Based on a similar interpretation⁹ in 1980, Fossum and Shibib proposed to replace metal-semiconductor junctions of a solar cell by a polysilicon emitter [174], whereupon the polysilicon- or SIPOS-contact solar cell was subject to a small number of papers between 1980 and 2000 [175–186]. Impressively high open circuit voltages of 720 mV [177, 179] and promising combinations of saturation current densities and contact resistivity [181] have been achieved, but cell efficiencies were limited to 15.3% [184]¹⁰.

Only in 2010, SunPower Corp. presented a large area interdigitated back-contact solar cell with „passivated contacts“ and a champion efficiency of 24.2% [188], which was further increased to 25.2% [189] in 2016. Even if SunPower did not disclose the contact scheme of their „passivated contacts“ at that time, their publication and patent activity suggested polysilicon-based contacts [190–199].

Frank Feldmann *et al.* [200–202] from Fraunhofer Institute for Solar Energy Systems (Fh-ISE) and Udo Römer *et al.* [154, 203–205] from Institute for Solar Energy Research Hamelin (ISFH) pioneered the rediscovery of polysilicon based passivating and carrier-selective contacts for silicon solar cells in 2013 and by now many research groups followed:

- National Renewable Laboratory (NREL) and Silevo Inc. in 2014 [206, 207]
- Georgia Institute of Technology, Australian National University and ECN [208–210] in 2015
- Delft University of Technology and Ecole polytechnique fédérale de Lausanne (EPFL) [211–213] in 2016
- Korean University, LG and the Chinese Academy of Science [214–216] in 2017
- the French National Institute for Solar Energy (INES), Trina Solar Energy Co., Mitsubishi Electric Corporation, Nagoya University, Solar Energy Research Institute of Singapore (SERIS) and ISC Konstanz [217–223] in 2018.

⁸This equivalence will be discussed in 6.5

⁹In fact, the authors presented a detailed minority-carrier transport model for a polysilicon contact in terms of an effective surface recombination velocity at the polysilicon emitter contact and concluded that the reduced surface recombination velocity of a polysilicon emitter compared to metal-semiconductor contacts, is beneficial for solar cells and could strongly improve the conversion efficiency.

¹⁰Note that the record efficiency of silicon solar cells evolved from below 20% to 25% in the same period using diffused metal-semiconductor junctions [187], which made other junction concepts less attractive.

The ever-increasing interest in recent years and the rapid progress in the field promote polysilicon based junctions as a promising candidate for future industrial solar cells. Indeed, polysilicon based junctions are considered to be the next evolutionary step of industrial solar cells [224]. For example, Trina Solar and Jinko Solar evaluate such cell concepts on industrial large area solar cells and have both reported cell efficiencies close to 25% [225, 226].

In the following, the fabrication, the properties and physics of such junctions are recapitulated by means of representative result from the literature.

4.2.2. Notation

Throughout the years, such poly-silicon-based contact schemes received various notations. While *poly-Si emitter* and *SIPOS contact* were common in the early days, Feldmann *et al.* popularized the term *Tunnel Oxide Passivated Contact (TOPCon)* [201], which suggests that homogeneous carrier tunneling is the dominating carrier transport mechanism through the junction. But theoretical [205, 227] and experimental [158, 159, 228, 229] studies indicate that homogeneous tunneling is not always dominating. Thus, *POLy-Si-on-Oxide (POLO)* was proposed as a more general notation for carrier selective junctions to crystalline silicon, which are based on poly-crystalline silicon-rich layers deposited on a passivating interfacial silicon oxide [227]. This thesis follows this general notation and all carrier selective junctions comprising a (partially) poly-crystalline silicon-rich layer deposited on a silicon oxide are condensed in the term POLO junction.

4.2.3. Fabrication

In order to form a POLO junction to a c-Si wafer, the wafer surface is oxidized and a silicon-rich layer is deposited on top of the interfacial silicon oxide. The silicon-rich layer is doped by a p-type or n-type dopant and a junction formation annealing is performed. Finally, the POLO junction can be hydrogenated to passivate the remaining defects at the interface between silicon oxide and c-Si wafer surface.

Interfacial oxide growth

The interfacial oxide can either be grown at low temperatures by using wet chemistry, UV-induced photo-oxidation [230], field-induced anodization [231] and plasma-enhanced chemical vapour deposition (PECVD) [232–234], or at elevated temperature during a thermal oxidation. For POLO junctions, acidic solutions provide a low-cost wet-chemical oxidation approach by means of aqueous solutions with hydrochloric acid (HCl) [204], caro's acid (H_2SO_5) [206], nitric acid (HNO_3) [200, 204, 208, 209, 211, 213, 214, 223, 235], concentrated nitric acid (HNO_3 with H_2SO_4) [236], hydrogen peroxide (H_2O_2) [215] or ozone-containing de-ionized water [217, 219, 220, 230, 237]). All these wet-chemical oxidations, the UV-induced oxidation and the field-induced anodization usually yield a 1 nm – 2 nm thin silicon oxide with a large portion of substoichiometric silicon oxide species (Si_2O , SiO) near the silicon surface [238, 239]. The substoichiometric species cause a high defect density D_{it} between $5 \cdot 10^{11}$ and $1 \cdot 10^{13} \text{ cm}^{-2} \text{ eV}^{-1}$ at the as-grown Si/SiO_x and a poor passivation quality [239]. A detailed

4.2. PASSIVATING POLY-SI-ON-OXIDE (POLO) CARRIER-SELECTIVE JUNCTION

overview is found in reference [239]. The nitric acid oxidation of Si (NAOS) [235] and the oxidation in ozone-containing water [230] are the most popular low-temperature methods for POLO junctions.

Thermally grown oxides for POLO junctions are formed in a tube furnace between 600–800 °C with a dry O₂ flow and usually yield 1 nm – 3.6 nm [204, 207, 212, 221, 240, 241] thick oxides with a lower portion of substoichiometric SiO_x compared to low-temperature SiO_x and with a less defective Si/SiO_x interface¹¹.

For industrialization purposes, it would be beneficial to perform the thermal oxidation step in-situ, thus during the silicon deposition process, and in-situ low-pressure oxidation [218, 222, 243] and plasma-enhanced chemical vapour deposition (PECVD) [232–234] are promising approaches in this direction. Alternatively, the wet-chemical oxidation, which can be integrated in the cleaning procedure, is a candidate for industrial implementation.

Silicon deposition

The silicon-rich layer is deposited either by chemical vapour deposition (CVD) using low-pressure (LPCVD) [36, 204, 211, 212, 218, 222, 243], atmospheric-pressure (APCVD) [244] and plasma-enhanced (PECVD) [36, 206, 208, 209, 213–215, 217, 219, 221, 245, 246] chemical vapour deposition, or by physical vapour deposition (PVD) using electron beam evaporation (EBE) [223] and sputtering techniques [247]. Furthermore, inkjet printing of a liquid silicon-precursor was reported [248]. All deposition techniques have their specific advantages. For example, LPCVD produces high quality hydrogen-free amorphous or polycrystalline films in a high-throughput quartz furnace at elevated temperatures. PECVD amorphous films deposited at lower temperatures are of poorer quality and contain a large fraction of hydrogen, which provokes blistering phenomena during high temperature annealing [249]. Nonetheless, high-throughput inline PECVD processes for high quality POLO contacts were demonstrated recently [221, 250]. APCVD represents a deposition method at atmospheric pressures and avoids complex plasma generation modules [244].

A drawback of all mentioned CVD methods is the need for hazardous precursor gases (e.g. silan, diboran, phosphine). This disadvantage is removed by using non-toxic target materials in PVD systems. Furthermore, for PVD, PECVD and APCVD, the deposition occurs on one side of the wafer only, which simplifies solar cell fabrication.

Aside from the deposition method, the composition of the silicon-rich layer affects the properties of the POLO junction: Many groups use pure silicon, while others add carbon [145, 251], oxygen [177, 213, 245] or nitrogen [252, 253]. Silicon-rich silicon carbide¹² layers are exclusively deposited by PECVD and contain carbon of only a few percent in order to reduce blistering of the hydrogen-rich PECVD layer. Moreover, carbon hinders the complete crystallization of the layer upon annealing at high temperatures, thus the layers stay mostly amorphous and show increased parasitic absorption for short wavelengths similar to a-Si [254,

¹¹For an approximately 50 nm thick Alnealed SiO_x grown at 1000 °C, a defect density as low as $1 \cdot 10^9 \text{ cm}^{-2} \text{ eV}^{-1}$ and among the best passivation for a silicon surface was demonstrated [242]

¹²The notation silicon carbide is misleading, since the layer contain a very small amount of carbon and a better notation would be carbon-containing silicon layer. However, the original notation from the literature is used here.

255], which causes a twice as high parasitic loss as for poly-Si layers under AM1.5G spectrum [256, 257]. Oxygen is added to increase the transparency of the POLO contact, especially in the infrared [179, 213, 245, 258], and nitrogen-containing silicon was studied for boron diffusion barriers, in order to improve the passivation of the interfacial oxide [252, 253].

Doping

The silicon-rich layer can either be undoped, *p*-type doped with group III elements (boron, aluminium, gallium, indium) or *n*-type doped with group V elements (phosphorous, arsenic, antimony). The dopant-containing species (e.g. diboran or phosshine) are supplied in-situ during silicon deposition [36, 200, 206, 208, 213, 221, 259] or ex-situ by using a boron- or phosphorus-containing glass [204, 209, 212, 222, 260], ion implantation [211, 261–264], spin-on dopant [265] etc. as the dopant source. Ex-situ doping requires post-deposition diffusion and activation in a high-temperature furnace anneal.

Junction formation annealing

The silicon-rich layer on the interfacial silicon oxide forms the POLO junction upon annealing between 750 °C and 1050 °C. The silicon layer crystallizes partially or completely¹³, dopant atoms diffuse into the silicon layer and pass over into an electrically active state. Dopant atoms diffuse through the interfacial silicon oxide layer into the wafer and form a shallow buried junction in the wafer [209, 262, 264, 266, 267].

Above about 750 °C, silicon oxide and silicon react, produce mobile species, the silicon/silicon oxide interface rearranges and reduces the interface defect density [169, 181, 229, 268–271]. On the other hand, the same decomposition reaction and rearrangement creates local disruptions in the silicon oxide layer and induces a degradation of the surface passivation [169, 229]. The thermal budget necessary to degrade the interfacial oxide depends on the stoichiometry and thickness of the oxide [239, 269, 272]. As a general rule it was found, that the thermal stability of the oxide layer increases with increasing thickness of the layer and the less substoichiometric oxide species it contains [204, 239, 240, 269, 272].

Junction formation is traditionally performed in a tube furnace for several minutes. Another approach, a fast firing process, which potentially can be integrated with the co-firing of screen-printed contacts, was recently demonstrated to yield POLO junctions with reasonable properties¹⁴ [244, 273]. Since the junction formation process of the latter is fast (<10 s at >750 °C), practically no indiffusion and probably no rearrangement of the silicon oxide occurs. The induced junction formed at the wafer interface is sensitive to interface defects and a subsequent passivation via hydrogenation is vital [273].

It is well-known (e.g. from metal-oxide-semiconductor transistor technology) that hydrogen improves the passivation quality of a Si-SiO_x interface by saturating dangling bonds and defects [274]. This hydrogenation approach is applied to POLO junctions by annealing them either in a molecular hydrogen containing forming gas [36, 209, 213], with a deposited solid

¹³Carbon containing layers usually stay amorphous.

¹⁴A J_0 of 11 fA/cm² and ρ_c of 73 mΩcm for an *n*-type contact [273]

4.2. PASSIVATING POLY-SI-ON-OXIDE (POLO) CARRIER-SELECTIVE JUNCTION

source of atomic hydrogen-rich Al_2O_3 [212, 275–277] or SiN_x layers [36, 212, 275, 277] or in a hydrogen plasma [278]. During the annealing, hydrogen diffuses from the source through the intrinsic or doped poly-Si layer towards the Si-SiO_x interface and passivates defects within the poly-Si and the Si-SiO_x interface [218, 279, 280]. Stodolny *et al.* found that a combination of Al_2O_3 and SiN_x layers in combination with fast firing yields the largest improvements [277].

4.2.4. Junction properties

The application of carrier selective POLO junctions to solar cells requires a high selectivity of the POLO junctions, thus a combination of low saturation current density J_0 with low contact resistivity ρ_c [120, 127].

Except *p*-type POLO junctions on textured silicon surfaces, excellent passivations in terms of $J_0 \lesssim 30 \text{ fA/cm}^2$ after a forming gas anneal (FGA)¹⁵ and $J_0 \lesssim 10 \text{ fA/cm}^2$ after hydrogenation¹⁶ were demonstrated for various oxide growth, silicon deposition or doping techniques [36, 223, 244, 247, 281]. Prior to hydrogenation, POLO junctions with thicker and more stoichiometric, thus thermally more stable, oxides exhibit lower J_0 values due to a higher allowable thermal budget during the formation annealing and the related enhanced reconstruction at the SiO_x/Si interface and the reduction of the defect density. Boron doped POLO junctions, especially with thin oxides, usually perform slightly poorer than phosphorous doped junctions, which is attributed to several effects, such as boron enhanced silicon oxide breakup and defects related to the boron pileup at the SiO_x/Si interface [206, 265]. To avoid the latter, boron can be replaced by gallium, which improved the passivation quality of *p*-type POLO junctions for planar silicon (100) surfaces [265]. For *p*-type POLO junctions on textured Si, the SiO_x/Si(111) interface is well known to have a higher defect density compared to SiO_x/Si(100) interface and therefore features a higher surface recombination velocity and J_0 values higher by approximately an order of magnitude [237, 282]. However, recent optimization of the hydrogenation treatment led to excellent J_0 values of down to 8 fA/cm^2 for boron doped *p*-type POLO junctions on textured Si and closed the gap to POLO junctions on planar Si and *n*-type POLO junctions on textured Si [277].

Beside the excellent passivation with $J_0 < 10 \text{ fA/cm}^2$, *p*-type and *n*-type POLO junctions simultaneously provide an excellent electrical contact resistance $\rho_c < 10 \text{ m}\Omega\text{cm}^2$ to the c-Si wafer [157, 240, 243, 252, 283]. Such POLO junctions with the corresponding carrier selectivity values S_{10} above 15–16 are electrically „invisible“ to the solar cell and the conversion efficiency is not limited by contacts anymore.

4.2.5. Transport mechanism

The carrier transport across the POLO junction, which determines contact resistivity, depends on the interplay of the stoichiometry and thickness of the oxide and the thermal budget of the junction formation annealing. While for oxides much thinner than 2 nm, carriers tunnel

¹⁵This is about the same state as directly after junction formation anneal, since FGA was shown to be a less effective method compared to hydrogen plasma treatment or annealing with hydrogen donating layers.

¹⁶This means in the following hydrogen plasma treatment or annealing with hydrogen donating layers.

efficiently through the interfacial oxide [284–286], it is hard to explain the observed low resistivities for thicker oxides [157, 240] with tunneling alone. Peibst *et al.* presented an alternative transport model based on current flow through pinholes [205], which form during junction formation, and confirmed pinhole transport to be dominant for thick oxides [158, 159]. Recently, Forchert *et al.* presented a detailed model, which is capable to calculate recombination and transport properties of POLO junctions [287].

4.3. Three-terminal tandem cell

Classification of the author’s contribution to the field

In the year 2015, the team at NREL initiated a fruitful and still ongoing collaboration with the author of this thesis on the topic of 3T tandem solar cells. The 3T IBC bottom cell for tandem applications was by that time unexplored in the literature (except for Nagashima’s work). Through the pioneering contributions of the NREL team in collaboration with the author of this thesis in the last few years, the 3T tandem solar cell has nowadays become popular and is currently studied by many research groups.

In detail, the author fabricated 3T-IBC unijunction bottom cell and investigated the modes of operation of such bottom cells. He was among the first presenting the results as an opening plenary talk at 33rd EUPVSEC in 2017 [288, 289]. He also investigated the working principles of bipolar junction bottom cells and presented the results along with the first PERC-like 3T bottom cell at the IEEE PVSC 2019 [290, 291]. In collaboration with M. Schnabel *et al.* [292, 293], the first working 3T tandem solar cell comprising an IBC cell was demonstrated. In collaboration with E. L. Warren, a taxonomy and nomenclature for 3T tandems was proposed [294].

In addition to the 2T and 4T tandem cell architectures as introduced in chapter 2, a third architecture – the three-terminal (3T) tandem – exists. If a third contact is added to a series-connected 2T cell between the sub-cells, an extra current can be collected in such a mid-contacted three-terminal (3T) tandem cell. The mid-contacted 3T tandem cell has been proposed in the past [295–310] almost exclusively for III-V materials. While several publications utilizes the three-terminal device to probe and current-match 2T tandems, almost all of them recognized that adding a third mid-contact to a 2T tandem omits the need for current-matching and enables a monolithic tandem solar cell, which combines the monolithic design of 2T tandems and the flexibility of 4T tandems cell. More recently, Marti *et al.* proposed and demonstrated a three-terminal heterojunction bipolar transistor solar cell [311–315].

Beside the advantages of the third terminal, the interdigitated grid on the front side, which is needed for the third terminal, implies an active cell area loss of the top cell, doubles the shadowing losses and complicates the fabrication process [297].

For this reason, it is beneficial to move the third terminal from the front side to the rear side of the tandem cell by using industrial-type interdigitated back contact (IBC) bottom

4.3. THREE-TERMINAL TANDEM CELL

cells. Around the millennium, Nagashima *et al.* [316] proposed this approach for the reverse-connected tandem cell with a bottom cell comprising two majority carrier contacts. But only in 2017, Nagashima's work was rediscovered by several authors. Warren *et al.* [317, 318], Schnabel *et al.* [319] and Rienäcker *et al.* [288, 289] promoted to use this concept for current-mismatched tandem cells. Adhyaksa *et al.* [320] proposed to use Nagashima's architecture for a perovskite/silicon tandem cell comprising a bottom cell with two minority carrier contacts. Nagashima *et al.* and Warren *et al.* elaborated the device physics by using sophisticated semiconductor device simulators and demonstrate that both concepts might work. However, a complete and comprehensive picture of 3T-IBC bottom cells, an experimental verification of the simulations in reference [316, 321] and [318] and an equivalent circuit model as use in reference [93–95] for mid-contacted 3T tandem cells was first provided by the author of this thesis [288–291]. Djebbour *et al.* performed a detailed simulation study of 3T III-V/Si tandem cells [322] and Sandbergen *et al.* [323] performed optical simulations for 3T perovskite/Si tandem solar cells. Warren *et al.* provided a taxonomy and nomenclature for 3T tandem cells [294].

To demonstrate the proposed 3T concept, Schnabel *et al.* was able to fabricate the first series-connected 3T GaInP//Si tandem solar cell with an efficiency of 27.3% [292, 293] and VanSant *et al.* a series-connected 3T GaAs//Si tandem cell with 21.3% [324, 325]. Furthermore, Tayagaki *et al.* demonstrated a similar 3T GaAs//Si tandem cell [326, 327]. Tockhorn *et al.* [328] and Wagner *et al.* [329, 330] presented the first perovskite/Si tandem cell with an efficiency of 17.1%.

Module integration of 3T tandem solar cells is challenging and several author studied different aspect [93–95, 331–334] of stringing 3T tandem cells and energy yield calculation were performed [95, 335]. Finally, measurement procedures for 3T tandem cell have been reported [293, 327, 328, 336].

5. Selectivity and carrier extraction efficiency of contacts

Background to the origins of the following chapter and why it was written

Shortly before starting my PhD studies in 2015 on the topic around charge carrier-selective POLO contacts, U. Würfel, A. Cuevas and P. Würfel published their popular paper on “Charge carrier separation in solar cells” [116] and pointed out that selective membranes with asymmetric conductivity for holes and electrons are necessary for charge separation. While the author of this thesis noticed the paper, he didn’t pay much attention to it at that time. Only through the work of Rolf Brendel on the topic of selectivity in 2015/2016 and through the encouragement of Robby Peibst to work on this subject, the author started following the literature of “selectivity definition”. For the author it was clear at that time that the definition according to Brendel and Peibst [127] should be applied to quantify the carrier-selectivity of contacts [155]. The author was the more surprised about the hint of M. Bivour [121] at the EUPVSEC in 2017 and S. Glunz [122] that the definition of Brendel and Peibst is not compatible with a typical phenomenon observed for non-traditional selective contacts that the V_{OC} deviates from iV_{OC} .

Selectivity was still not in the author’s focus in 2018, because he was busy with his investigations on three-terminal bottom and tandem cells. However, the inspiration to work on selectivity came threefold in 2018. First, the author found Weber’s 3T device during his literature research, which was used to study the selectivity of organic contacts to silicon solar cells [119]. Second, during the work on bipolar junction bottom cells from chapter 8, the author learnt that “emitter injection efficiency” is used to measure the quality of transistor contacts¹. The third source of inspiration was the talk “*A Novel Calix[4]arene-based MOF for highly selective NO₂ Detection*” from Marcel Schulze at the NanoDay 2018 of the Laboratory of Nano and Quantum Engineering in Hanover. The talk had little to do with the work of the author on solar cells, but it pointed him to the generality of the selectivity concept and by this later also to the definition in the field of reaction chemistry. While the idea of the selectivity definition as found below was born and written down in 2019, it took the author much effort to get all the ideas and definitions sorted and written down clearly – at least for the author. The definition of the extraction efficiency on the other hand was born during the sorting and was inspired by the work of Koswatta [117] and Onno *et al.* [124] on their selectivity metric, by the picture of conversion processes and their efficiencies provided by P. Würfel [64] and the early work of De Vos on endoreversible engines [337]. M. Mancini from Technische Universität

Clausthal, Germany, helped sorting the ideas with thermodynamics.

A. Onno provided guidance in understanding his definition and was always open to discussion and questions on the selectivity topic. His comments on the content of the chapter in its earlier form in 2020 and the critical questions and discussions of R. Brendel helped to shape the content around the precise spatial definition of the contact. In particular, the definition of the selective electrode was the result of R. Brendel's persistent and constructive discussion around the spatial boundary of the contact at the electrode. However, the motivation to work on the selectivity definition was driven not only by inspiration, but also by the confusion that several different definitions exist. It was not clear to the author from the current literature how the definitions were related and why so many definitions were necessary. Therefore, in the following chapter, the author makes an attempt to provide guidance to some extent and to present a unified version of a definition.

The chapter is structured as follows. First, the role and functions of the components of a solar cell are outlined and the spatial and process-wise definition of a carrier-selective contact and carrier-selective electrode is provided. Then the selectivity and extraction efficiency are defined and discussed in detail before deriving the specific selectivity definitions found in the literature from the definition in this thesis. In the second part of this chapter, the correlation between the selectivity and extraction efficiency is provided, which is the basis to calculate the performance of a contact selectivity-limited solar cell.

5.1. The role and definition of contacts and the absorber of a solar cell

The energy conversion of incident heat radiation from the sun into electricity proceeds in two steps: first the heat radiation is converted into chemical energy and, in a second step, the chemical energy converts into electrical energy [64]. For each of the conversion processes, the solar cell requires an appropriate conversion apparatus: the photo-absorber for the conversion of heat radiation into chemical energy and the contacts for the conversion of chemical energy into electrical energy. Figure 5.1a shows the band diagram representation of a solar cell, which consists of an absorber layer, an electron-selective contact A and a hole-selective contact B.

5.1.1. Photo-absorber

In a quasi-neutral photo-absorber, absorbed photons generate an excited electron-hole gas with a chemical potential equal to the splitting of the quasi-Fermi levels $\Delta\mu = E_{Fn} - E_{Fp}$ for electrons E_{Fn} and holes E_{Fp} [76, 338]. At open-circuit voltage conditions, the quasi-Fermi

¹Robby Peibst encouraged the author to use the 3T device to measure contacts selectivity and pointed out to the author that he had used the ratio of minority and majority carrier current densities as a measure of the contacts quality in reference [205].

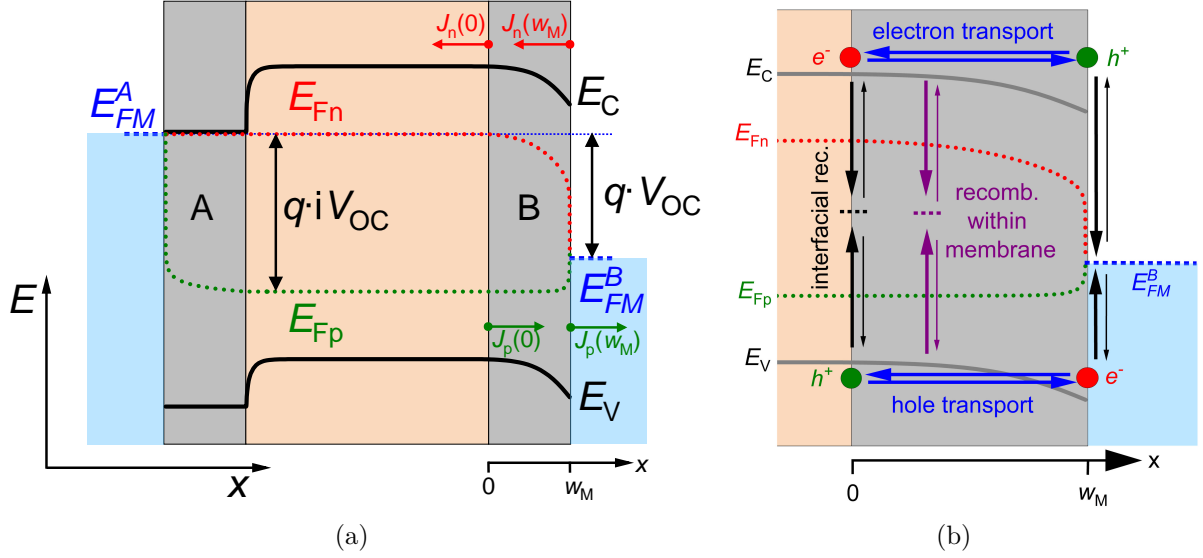


Figure 5.1.: (a) Band diagram of an illuminated and open-circuited solar cell consisting of an absorber layer (light orange), a highly doped electron-selective contact (homojunction, grey region A) and a mobility junction for the hole-selective contact (grey region B). (b) Magnification of the hole-selective contact B of Fig. 5.1a supplemented with possible carrier transfer processes (indicated by arrows).

level splitting is given by the internal voltage iV_{OC} , thus $\Delta\mu = q \cdot iV_{OC}$. The region with almost constant quasi-Fermi level splitting represented by an internal voltage iV_{OC} defines the absorber. In the ideal case of negligible transport losses (infinite mobilities for electrons and holes) in the absorber, the quasi-Fermi levels are spatially constant, as shown in Figure 5.1a.

5.1.2. Contacts

To convert the chemical energy of the excited electron-hole gas into electrical energy, electrons and holes have to be extracted separately by applying electron- and hole-selective contacts between the absorber and the electrode with a Fermi-level E_{FM} . The electrode represents a highly recombination active site, not necessarily a metal electrode, where the two separated quasi-Fermi levels E_{Fn} and E_{Fp} of the absorber have collapsed into a single Fermi-level E_{FM} ². According to references [117, 124, 189], the transition region between the absorber with nearly constant quasi-Fermi level splitting and the electrode defines the carrier-selective membrane, which is responsible for the asymmetry of the transport of electrons and holes [116]. The

²Note that the spatial position, where the quasi-Fermi level collapse into a single Fermi level, is not sharply defined and may depend on the point of operation, if this position does not correspond to the semiconductor/metal interface.

5.1. THE ROLE AND DEFINITION OF CONTACTS AND THE ABSORBER OF A SOLAR CELL

“bulk electrode region” (blueish part in Fig. 5.1a)³ is explicitly excluded in this definition of the carrier-selective contact because selectivity requires at least two competing processes in order to select one process over the other. However, within the bulk electrode solely one transport process is found. Nevertheless, the bulk electrode is an essential part of the contact of a solar cell, which may induce additional (Ohmic) transport losses. A carrier-selective contact, which includes the bulk region of the electrode, is denoted as the carrier-selective contact plus electrode or in brief the “carrier-selective electrode”.

The ability of the carrier-selective contact to extract the desired sort of carriers into the electrode, while blocking the other ones – namely the carrier-selectivity – determines the position of E_{FM} with respect to E_{Fn} and E_{Fp} . Figure 5.1a shows a highly-doped and highly selective electron-selective contact on the left hand side and an undoped mobility junction for the moderately hole-selective contact on the right hand side. The difference of the Fermi levels E_{FM}^A and E_{FM}^B of the two electrodes A and B is the external voltage of the solar cell i.e. the open-circuit voltage V_{OC} at open-circuit conditions, thus $q \cdot V_{OC} = E_{FM}^A - E_{FM}^B$. Note that the spatial definition of selective contacts applies to homogeneous and heterogeneous selective membrane regions, so it may contain several different material or heterointerfaces.

Beside the spatial definition of a carrier-selective contact, it is important to take into consideration the carrier transfer processes within the selective contact and at its boundaries. Figure 5.1b depicts such potentially occurring carrier transfer processes (reaction) of the carrier selective contact B. The electrons and holes in Fig. 5.1b are solely describe by the energy value E and the position x . If for simplicity only one of the properties – E or x – can change during a transfer process, it becomes clear that two kinds of processes can be distinguished: vertical recombination-generation processes along the energy coordinate E and horizontal transport processes⁴ along the position coordinate x .

At a fixed position, an electron in the conduction band and a hole in the valence band can recombine or can be generated e.g. via a trap state (dotted black, purple and blue lines in Fig. 5.1b). The recombination-generation processes can take place at the boundaries/interfaces of the contact (black arrows in Fig. 5.1b) or within the selective contact (purple arrow in Fig. 5.1b).

For a horizontal process along the x coordinate, transport of electrons and holes from the absorber through the selective contact into the electrode and vice versa takes place (blue arrows in Fig. 5.1b). Since the recombination-generation and transport processes are interdependent, they form a complex network of processes, which can be treated by a coupled system of differential equations.

In the end, it is debatable, which process should be considered to describe the properties of a selective contact and this will be discussed in section 5.2.1. However, at least three processes are essential: the recombination at the interface to the electrode and the transport processes of electrons and holes through the membrane. The electrons and holes at the electrode

³The electrode region also includes any majority carrier transport region at the membrane-electrode interface e.g. metal-semiconductor interface.

⁴Strictly speaking, spacial transport is an irreversible process and implies dissipation of free energy. Thus, transport is not strictly along the x coordinate, but always results in a gradient of the corresponding quasi-Fermi level. In contrast, the recombination-generation process can be restricted to a single position in space and can take place along the E coordinate.

interface recombine approximately instantaneously, which ensures that the quasi-Fermi levels of electrons and holes collapse into a single Fermi level. Since the single Fermi level is an intrinsic property of the electrode, any contact to the electrode requires the recombination process at the electrode and justifies the term “contact” of a selective contact. The competing electron and hole transport processes across the membrane must be strongly asymmetric to provide charge carrier separation [116]. The asymmetry corresponds to the carrier selectivity of such a contact.

In addition to the three fundamental processes, any recombination process within the membrane and at the boundaries leads to a reduction of the quasi-Fermi level splitting in the absorber and corresponds to the passivation properties of a carrier selective contact [122]. If these recombination channels are minimized, then the absorber is well passivated and the contact is called a passivating, carrier selective contact.

5.2. Definition of selectivity and extraction efficiency

The two properties defined below – the selectivity and extraction efficiency – both describe the properties of contacts to extract desired carrier vs. undesired carriers. The difference of both quantities is that the selectivity is a kinetic property and the extraction efficiency is a thermodynamic one. In order to achieve a certain extraction efficiency, the selectivity has to reach a certain value for a given internal voltage.

5.2.1. Selectivity

The definition of the selectivity in this thesis is inspired by the fact that the electron and hole transfer processes from the absorber into the electrode and vice versa can be understood and described in terms of competing “chemical” reactions⁵.

In analogy to the (rate) selectivity definition of competing chemical reactions [339] in the field of reaction kinetics, selectivity S of a selective contact/electrode in this thesis is defined as the ratio of the net transfer rate r_D of the desired process versus the effective net transfer rate r_U of all undesired processes.

$$S_{kin} = \frac{r_D}{r_U} = \frac{q \times r_D}{q \times r_U} = \frac{J_M(w_M)}{J_m(x)} \quad (5.1)$$

If the transfer rates r_D and r_U are multiplied by the elementary charge q , the rates can be translated into current densities. The selectivity is then defined by the ratio of the desired current density $J_M(w_M)$ of majority charge carriers and the undesired current density $J_m(x)$ of minority charge carriers⁶. The majority carrier leave the contact at $x = w_M$ towards the electrode. The minority charge carriers either leave the absorber at $x = 0$ towards the contact or they leave the contact at $x = w_M$ towards the electrode, which results in

⁵For a detailed discussion of the contact from a chemists point of view, see appendix A.3.1.

⁶Note that the terms majority and minority carrier refer to the desired and undesired carrier, which differs from the usually used definition of this terms for the absorber region.

two different versions of selectivity. Both undesired current densities – $J_m(x = 0)$ and $J_m(x = w_M)$ – differ by a generation-recombination current density J_{rg} within the selective membrane. Consequently, the selectivity definition with $J_m(x = w_M)$ excludes the generation-recombination current density J_{rg} , but the selectivity with $J_m(x = 0)$ takes J_{rg} into account. To better distinguish between the two possibilities, the former is denoted by S and the latter by S^* .

The inverse of the defined ratio of current densities in equation 5.1 corresponds to Kroemers definition of *injection deficit* [140] and underlines the usefulness of the definition. Kroemer proposed the injection deficit as a figure of merit for contacts in bipolar junction transistors [140] and the injection deficit was quantified theoretically and experimentally for metal-semiconductor and metal-insulator-semiconductor contacts [143, 144].

At this point, it should be emphasized that Weber *et al.* [119] and Roe *et al.* [123] have defined their selectivity metric based on a similar idea of charge transfer reactions, which was first worked out for a semiconductor-electrolyte contact by Tan *et al.* [128]. However, their definition is considerably different to that in this thesis. First, the selective contact in their definition is restricted to an interface and thus it has no spacial extent. Second, Weber *et al.* and Roe *et al.* define their selectivity metric by the ratio of constant equilibrium exchange current densities or “diode prefactors” rather than current densities, which are dependant on the point of operation of the solar cell. As will become evident in section 5.3, the definition of Weber *et al.* and Roe *et al.* corresponds to the selectivity coefficient S_0 for the special case of transport via thermionic emission at the contact.

For the general – but non-specific – definition of selectivity in equation 5.1, one has to specify the rates of the processes or the respective current densities from appropriate models of the contact region. This exercises will be performed in section 5.3 for specific examples to reproduce the specific definitions from the literature.

5.2.2. Extraction efficiency

Since Chapin, Fuller and Pearson created the first practical silicon solar cell at Bell Labs [18], several author have made attempts to find a thermodynamic model to take account for the fact that a solar cell is an energy converter [64, 73–80]. The energy conversion of radiation into electricity in a solar cell takes place in two conversion steps: First the heat radiation is converted into chemical energy in the form of an excited electron-hole gas and second the chemical energy of the electron-hole gas converts to electrical energy at the contact. Almost all thermodynamic approaches [64, 73–80] assume implicitly or explicitly that the conversion of chemical into electrical energy is loss-free. That is why they focus on the conversion of heat radiation to chemical energy and model the thermodynamics of a solar cell similar to a heat engine⁷ ($\frac{qV_{OC}}{E_G}$) is equal to the Carnot efficiency at open-circuit conditions [64, 74, 78]. In that reports, the open-circuit voltage in fact corresponds to the quasi-Fermi level splitting ($q \cdot iV_{OC}$) and is only equal to the (external)

⁷This term is frequently found in the papers of Baruch *et al.* [78, 340] and refers to the thermodynamic efficiency of the conversion of incident radiation with semiconductor with a band gap E_G into an (internal) open-circuit voltage.

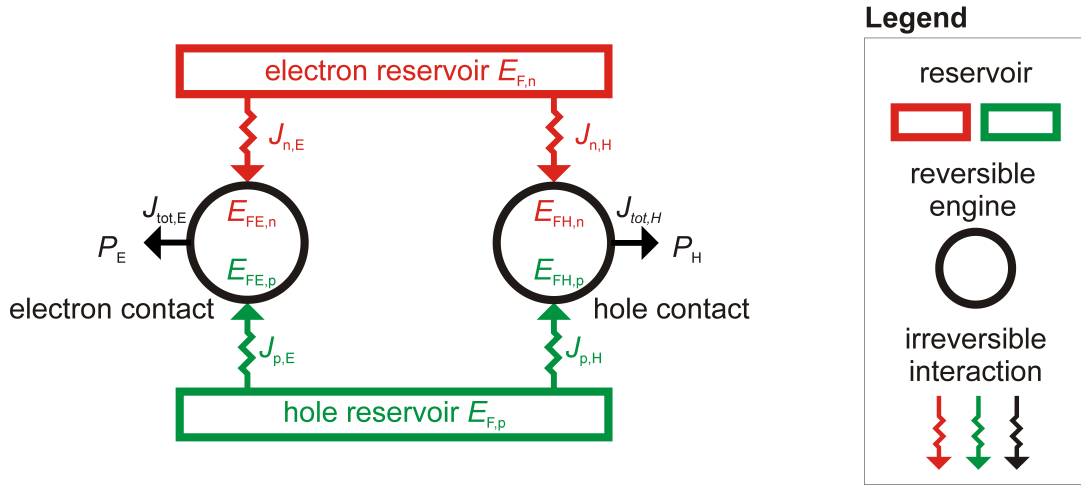


Figure 5.2.: Thermodynamic representation of the conversion process of chemical energy to electrical energy. An isothermal, endo-reversible (electro-)chemical engine for hole (electron) extraction between the two particle reservoirs models the hole (electron) selective contact.

open-circuit voltage V_{OC} , if perfect conversion of chemical to electrical energy is assumed. In the following, the conversion process of chemical into electrical energy is discussed in terms of thermodynamics.

The thermodynamic model of this process is based on endoreversible chemical engines [337, 341–345] and is depicted in Fig. 5.2. In order to simplify the discussion, the detailed description of the conversion process of heat radiation into chemical energy is excluded and represented it by its end-product, namely by a quasi-constant⁸ particle reservoirs for thermalized conduction band electrons (red box in Fig. 5.2) and for valence band holes (green box in Fig. 5.2) with their respective electrochemical potentials $E_{F,n}$ and $-E_{F,p}$. The sum of electrochemical potentials for both reservoirs corresponds to the quasi Fermi level splitting $\Delta\mu = E_{F,n} - E_{F,p}$ in the absorber. Both reservoirs interact via irreversible transport with a reversible chemical engine (black circle in Fig. 5.2) for hole extraction and with another for electron extraction (red and green arrows in Fig. 5.2), which mediates the endoreversible conversion of chemical into electrical energy. At the chemical engine of the electron contact, electrons with a chemical potential $E_{F,n}$ flow irreversibly from the electron reservoir into the engine and – due to the transport resistance⁹ – dissipate a part of the initial chemical energy into heat, such that the electrons in the engine have a chemical potential $E_{FE,n}$. One part of the electron flux leaves the engine towards the hole reservoir and dissipates its chemical energy into heat, which is equivalent to holes irreversibly flowing from the hole reservoir with

⁸The quasi-constant reservoir is justified by assuming steady-state conditions. When a particle is removed from the reservoir, it is instantaneously replaced from the conversion process of heat radiation to chemical energy.

⁹Transport resistance does not necessarily mean electrical resistance, but something, which induces friction such that entropy is produced proportional to the flux density. Of course, the flux of electrons through a conductor is one particular example.

a chemical potential $-E_{F,p}$ into the engine and resulting in a chemical potential $-E_{FE,p}$ in the engine. Another part of the electrons converts its chemical energy into electrical energy and leaves the engine. For this conversion, the electrons and holes, which flow into the engine, use their chemical potential to enable the separation of the electrons from holes. Since the engine is reversible, particles, energy and entropy are conserved in the engine. The balance equation for the particle flux, represented by an electrical current density, reads as:

$$J_{tot,E} = J_{E,n} + J_{E,p} \quad (5.2)$$

$J_{tot,E}$ is the total electrical current density and $J_{E,n}$ and $J_{E,p}$ are the partial electron and hole current density at the electron contact.

The energy flux balance equation reads as:

$$P_E = \frac{1}{q}(J_{E,n} \cdot E_{FE,n} - J_{E,p} \cdot E_{FE,p}) \quad (5.3)$$

P_E is the electrical energy flux of electrons flowing out of the engine and $E_{FE,n}$ and $-E_{FE,p}$ are the electron and hole electrochemical potentials of in-flowing electron and hole currents densities. At the electrode, it can be assumed that the electrochemical potential of electrons and holes $E_{FE,n} = -E_{FE,p} = E_{FE}$, such that the quasi Fermi level splitting in the electrode vanishes.

Similar considerations for the hole contact lead to the following particle balance equation.

$$J_{tot,H} = J_{H,p} + J_{H,n} \quad (5.4)$$

$J_{tot,H}$ is the total electrical current density and $J_{H,n}$ and $J_{H,p}$ are the partial electron and hole current density at the hole contact.

The energy flux balance for the hole contact is as follows.

$$P_H = \frac{1}{q}(J_{H,p} \cdot E_{FH,p} - J_{H,n} \cdot E_{FH,n}) \quad (5.5)$$

P_H is the electrical energy flux of holes flowing out of the engine and $E_{FH,n}$ and $-E_{FH,p}$ are the electron and hole electrochemical potentials of in-flowing electron and hole currents densities.

As for the electron contact, the electrochemical potential $E_{FH,n} = -E_{FH,p} = -E_{FH}$.

In order to obtain the total energy flux, which can be used to perform work in the external circuit (total power output), one has to balance the particle and energy flux in the external circuit¹⁰, where the total current density of holes and electrons compensate $J_{tot,H} = J_{tot,E} = J$ and the total power output P_{out} is simply the current density J flowing through the external circuit multiplied by the potential difference between the electrodes.

$$P_{out} = P_E + P_H = \frac{J}{q}(E_{FE} - E_{FH}) \quad (5.6)$$

The total chemical energy influx, which is consumed in the conversion process of chemical into electrical energy, is defined as the sum of the chemical potentials of both reservoirs

¹⁰This would correspond to another electrical engine, which converts electrical energy into useful work.

$\Delta\mu = E_{F,n} - E_{F,p}$ multiplied by the total particle flux density $\frac{1}{q}J$ flowing between both reservoirs. The efficiency of the conversion process, namely the carrier extraction efficiency, is the ratio of the total electrical power output P_{out} versus total chemical energy influx P_{in} .

$$\eta_{extract} = \frac{P_{out}}{P_{in}} = \frac{J \cdot (E_{FE} - E_{FH})}{J \cdot (E_{F,n} - E_{F,p})} = \frac{qV_{ext}}{\Delta\mu} \quad (5.7)$$

The carrier extraction efficiency turns out to be the ratio of the external electrical potential qV_{ext} versus the internal chemical potential $\Delta\mu$ of a solar cell, which is indeed the efficiency of the conversion of chemical energy into electrical energy.

The extraction efficiency for a single contact can be found, if one assumes the other contact to be perfectly reversible, which implies for a hole contact for example that $E_{FH} = E_{F,p}$. In the case, when both contacts are perfectly reversible, the extraction efficiency is unity, such that the inner chemical potential is converted loss-free into external electrical work. The overall carrier extraction process in this case is denoted to be reversible.

Under open-circuit conditions, the efficiency is as follows.

$$\eta_{extract,OC} = \frac{V_{OC}}{iV_{OC}} \quad (5.8)$$

The derivation of the extraction efficiency at OC in equation 5.8 reveals that the ratio of internal versus external voltages at OC is indeed a measure of the contact's ability to extract charge carriers selectively and was frequently used as a measure of contact's selectivity by several authors [121, 122, 124, 125, 146] in the past. This is also consistent with the finding of Koswatta [117] and Onno *et al.* [124], who observed that the ratio of voltages correlates with the partial resistances of the selective contact in their drift-diffusion simulations. Later, Onno *et al.* explained the correlation by using an analytic derivation from drift-diffusion model based on pseudo-linear transport laws for electrons and holes. Smit [118] on the other hand proposed the inverse of the ratio in equation 5.8. Both, Onno *et al.* and Smit denoted the ratio to the "selectivity metric", but the author of this thesis suggests to use extraction efficiency instead.

For the reader, it may sound strange to define and accept an extraction efficiency at open-circuit condition, since neither charge carriers nor power are extracted at this operating condition. The extraction efficiency at open-circuit conditions can be interpreted as a Carnot-like efficiency, where also neither a (heat) flux is present nor power is extracted (see section 2.1). To the author's best knowledge, this is the first time that equation 5.7 and 5.8 were derived from endoreversible thermodynamics and the latter was interpreted as a Carnot-like efficiency to convert the chemical energy of photogenerated carriers in the absorber into electrical energy at a carrier-selective contact.

Even if it is tough to accept $\eta_{extract,OC}$ at first, $\eta_{extract,OC}$ and especially its analogy to the Carnot efficiency are a powerful observation, which allows to correlate the measurable voltages under open-circuit conditions with the extraction efficiency at maximum power output and to calculate the maximum achievable solar cell efficiency of a contact selectivity-limited solar cell on the basis of thermodynamic principles (see section 5.5).

One possibility to determine the extraction efficiency $\eta_{extract,mpp}$ at maximum power output

5.3. DERIVATION AND CLASSIFICATION OF THE SPECIFIC DEFINITIONS IN THE LITERATURE

is to calculate the point of maximum power output from equations 5.3, 5.5 and 5.6. It would require to specify the transport laws for each of the irreversible interactions and to solve the algebra. An alternative approach¹¹ with less effort is to use the universal relationship [57] between the Carnot efficiency and the respective efficiency at maximum power output from equation 2.7, which yields

$$\eta_{\text{extract,mpp}} = \frac{\eta_{\text{extract,OC}}}{2 - \eta_{\text{extract,OC}}} \quad (5.9)$$

This simple equation will be used in section 5.5 to calculate the power conversion efficiency of a contact selectivity-limited solar cell.

5.3. Derivation and classification of the specific definitions in the literature

The selectivity as defined in equation 5.1 and the extraction efficiency as defined in equation 5.7 require additional specific information to be correlated with “measurable” properties of the contact:

1. One has to decide, whether the electrode bulk region should be include for the selectivity considerations or not.
2. The carrier transfer processes of the desired and undesired charge carriers have to be selected – probably even for multiple regions in the case of non-homogeneous selective membranes.
3. The functional relationships between the process rates/current densities for the desired and undesired processes have to be described based on the properties of the contact and as a function of the internal and external voltage.

5.3.1. Selectivity of carrier-selective contacts

Weber *et al.*, Roe *et al.*, Koswatta, Smit and Onno *et al.* chose the simplest possible model system of a carrier-selective contact without electrode bulk region. They included the instant recombination at the electrode interface and the transport of electrons and holes from the absorber through the membrane into the electrode¹². For the latter process with the species $i=n,p$, linear irreversible transport (LIT) theory¹³ [69] provides a linear relationship $J_i = L_i \cdot F_i$ between the current density J_i , the transport coefficient L_i of the membrane and

¹¹In fact, Esposito *et al.* [57] do calculate the maximum power point and assume generalized transport “laws” to obtain a general relationship for asymmetric transport properties.

¹²Moreover, Smit [118] discussed how generation and recombination processes within the membrane can be included.

¹³Linear irreversible transport theory is used here for two reasons: 1. LIT is a general description of transport, which is also used in thermodynamics as pointed out in section 2.1. 2. In contrast to the drift-diffusion model, which is a local theory, LIT requires that the transport coefficient is constant and independent of position. Thus, the use of LIT can be interpreted here as an empiric and “global” approach.

5.3. DERIVATION AND CLASSIFICATION OF THE SPECIFIC DEFINITIONS IN THE LITERATURE

the thermodynamic driving force F_i , which depends on the internal and external voltages. In terms of semiconductor physics, the transport laws in equation 2.19 and 2.20 locally represent such linear laws, where the driving force is given by the gradient of the quasi-Fermi level potential $\frac{1}{q} \frac{dE_{Fi}}{dx}$ and the transport coefficient is the conductivity $\sigma_i(x)$ of the membrane. This local transport law can be used to find the selectivity, since the current densities are constant in the membrane due to the lack of recombination or generation, but the local quantities are hard to access. For this reason, the local laws from drift-diffusion model are reformulated by Onno *et al.* [124]. Furthermore, the generalized charge control model, which is based on the drift-diffusion model, is used to find the ratio of the current densities at the boundaries of the selective membrane in the upcoming discussion.

Assuming that both transport processes can be described by the linear relationships with constant transport coefficients¹⁴ as required by LIT, then the selectivity from equation 5.1 is calculated as the product of a constant selectivity coefficient $S_0 = \frac{L_M}{L_m}$ with the transport coefficients L_M and L_m for the desired and undesired process, respectively, and the function $\Sigma(F_M, F_m)$, which depends on the driving forces F_M for the desired process and F_m for the undesired process.

$$S = \frac{J_M}{J_m} = S_0 \cdot \Sigma(F_M, F_m) \quad (5.10)$$

The selectivity coefficient S_0 is in agreement with the discussion of Würfel *et al.* [116], who proposed that the partial carrier conductivities at a contact have to be asymmetric. The value of the function $\Sigma(F_M, F_m)$ depends on the state of operation of the solar cell and its importance shouldn't be underestimated. Schmidt, Peibst and Brendel [281] for example introduce such a voltage-dependent factor in an "updated" version of their selectivity definition compared to their prior definition [120] only to remove the voltage-dependence in their definition of the selectivity metric, but they don't pay attention to the voltage-dependent factor. Anyhow, their definition differs from the definition in this thesis and the voltage-dependent function in equation 5.10 is worth discussing.

At open circuit condition (OC), the desired process is in a detailed balance equilibrium with the undesired process, such that J_M equals J_m . The contact is equally selective for both types of carriers and the selectivity is unity. The driving forces $F_{M,OC}$ and $F_{m,OC}$ at OC adjust themselves in such a way as to permit a detailed balance equilibrium between the desired and undesired process and the value of the function $\Sigma(F_{M,OC}, F_{m,OC})$ takes the value of $\frac{1}{S_0}$. Conclusively, if the driving forces at OC and the functional relationship Σ are known, the selectivity coefficient of the carrier-selective contact can be determined as follows.

$$S_0 = \frac{1}{\Sigma(F_{M,OC}, F_{m,OC})} \quad (5.11)$$

As will be discussed in subsection 5.4, equation 5.11 relates the extraction efficiency η_{OC} at OC as defined in equation 5.8 to the selectivity coefficient S_0 , since the driving forces are related to the internal and external voltages.

In order to be a unifying definition, the general definition of selectivity and extraction

¹⁴The validity of the assumption of constant transport coefficients resulting in a constant selectivity coefficient will be discussed below.

5.3. DERIVATION AND CLASSIFICATION OF THE SPECIFIC DEFINITIONS IN THE LITERATURE

efficiency in this thesis should be specifiable to recover the specific definitions of the references [117, 119, 123, 124]. To derive the definitions from the literature, assumptions about the current densities J_M and J_m from the literature will be used at open-circuit conditions.

Exponential carrier transport laws

Weber *et al.* and Roe *et al.* assume that the selective contact is define by an interface between $x = 0$ and $x = w$ with $w \rightarrow 0$, where charge transfer takes place between the absorber at $x = 0$ and the electrode at $x = w$ by thermionic emission. The current density under such assumptions is driven by a carrier concentration difference at the interface. The electron (hole) carrier concentration at the boundary of the membrane with the absorber $n(0)$ ($p(0)$) are denoted as the surface electron (hole) concentration n_S (p_S). The electron (hole) carrier concentration at the boundary of the membrane with the electrode $n(w)$ ($p(w)$) correspond to the equilibrium concentrations $n(w) = n_{S0}$ and $p(w) = p_{S0}$ due to the infinitely fast equilibration at this interface¹⁵. The transport law reads [119, 123] for electrons

$$J_n = J_{0n} \cdot \left| \frac{n_S}{n_{S0}} - 1 \right| \quad (5.12)$$

and for holes

$$J_p = J_{0p} \cdot \left| \frac{p_S}{p_{S0}} - 1 \right| \quad (5.13)$$

The equilibrium exchange current densities J_{0n} for electrons and J_{0p} for holes are identified as the “transport coefficients” L_i and the functions $\left| \frac{n_S}{n_{S0}} - 1 \right|$ and $\left| \frac{p_S}{p_{S0}} - 1 \right|$ correspond to the “driving forces”¹⁶ F_i . Inserting the exponential law¹⁷ into the selectivity definition (equation 5.1) at OC ($S = 1$) yields

$$S_{p,OC} = 1 = \frac{J_{0p}}{J_{0n}} \cdot \frac{\left| \frac{p_{S,OC}}{p_{S0}} - 1 \right|}{\left| \frac{n_{S,OC}}{n_{S0}} - 1 \right|} \quad (5.14)$$

The orange part represents the selectivity coefficient S_{0p} as defined by Weber *et al.* and Roe *et al.*. The blue part is the driving force containing function Σ . Solving the equation for S_{0p} gives

$$S_{0p} = \frac{J_{0p}}{J_{0n}} = \frac{\left| \frac{n_{S,OC}}{n_{S0}} - 1 \right|}{\left| \frac{p_{S,OC}}{p_{S0}} - 1 \right|} \quad (5.15)$$

The left hand side (black/orange part) equals the definition of Weber *et al.* and Roe *et al.*, while the blue part correspond to equation 5.11. Tan *et al.* [128] derived the relationship

¹⁵Details are found in the appendix A.3.1.

¹⁶Note that the transport coefficients and driving forces are chosen such that all constant factors are absorbed in the transport coefficient and the operation point dependent quantities represent a normalized driving forces. However, the units of transport coefficients and driving forces do not correspond to usual units.

¹⁷Exponential refers here to the exponential dependence of the concentrations with the internal and external voltages.

5.3. DERIVATION AND CLASSIFICATION OF THE SPECIFIC DEFINITIONS IN THE LITERATURE

between the carrier concentrations and the quasi-Fermi levels for a semiconductor-electrolyte contact and found the following relationship.

$$S_{0p} = \frac{\left| \frac{n_{S,OC}}{n_{S0}} - 1 \right|}{\left| \frac{p_{S,OC}}{p_{S0}} - 1 \right|} = \frac{\exp\left(\frac{E_{Fn,OC}(0) - E_{FM,OC}^B}{k_B T}\right) - 1}{\exp\left(\frac{E_{FM,OC}^B - E_{Fp,OC}(0)}{k_B T}\right) - 1} = \frac{\exp\left(\frac{qV_{OC}}{k_B T}\right) - 1}{\exp\left(\frac{q(iV_{OC} - V_{OC})}{k_B T}\right) - 1} \quad (5.16)$$

The semiconductor is assumed to be in high level injection to ensure flat quasi-Fermi levels in the absorber and flat conduction and valence bands. Substituting the quasi-Fermi level differences by the measurable voltages yields an interesting and useful relationship, which relates the selectivity coefficient S_0 with the internal and external voltage of the device at OC and therefore with the extraction efficiency $\eta_{\text{extract,OC}}$ at OC.

The reader may wonder how the description of Tan *et al.*, Weber *et al.*, and Roe *et al.* applies to the selective membrane with finite width w in Figure 5.1a and 5.1b, and whether the relationships from equations 5.12, 5.13 and 5.15 also apply to it. This question is briefly addressed under simplified assumptions for a solar cell operating at open-circuit conditions in the following.

If one assumes that in the membrane region of the hole-selective contact in figure 5.1a neither recombination nor generation of free carriers takes place and the membrane is nearly field-free, then the electron and hole transport can be considered independent from each other. The latter assumption is strictly only fulfilled for a nearly flat electrostatic potential within the membrane i.e. flat conduction and valence bands.

The absorber is illuminated and excess charge carriers are generated in the absorber. The electron and hole carrier concentration $n(w)$ and $p(w)$ at the electrode is lower¹⁸ than $n(0)$ and $p(0)$ at the absorber/membrane interface and a concentration gradient across the membrane region drives a current density J_n and J_p of the electron and hole charge carriers through the selective membrane towards the electrode, respectively. Electrons and holes recombine at the electrode and maintain their lower concentrations $n(w)$ and $p(w)$. The independent diffusive transport of electrons and holes through the membrane justifies the use of equations 5.12 and 5.13. Using equation 2.15 and 2.15 to evaluate the carrier concentrations yields¹⁹ for electrons

$$J_n = J_{0n} \cdot \left| \frac{n(0)}{n(w)} - 1 \right| = J_{0n} \cdot \left[\exp\left(\frac{E_{Fn} - E_{FM}^B}{k_B T}\right) - 1 \right] \quad (5.17)$$

and for holes

$$J_p = J_{0p} \cdot \left| \frac{p(0)}{p(w)} - 1 \right| = J_{0p} \cdot \left[\exp\left(\frac{E_{FM}^B - E_{Fp}}{k_B T}\right) - 1 \right] \quad (5.18)$$

Assuming a solar cell at OC with a perfectly electron-selective contact ($E_{FM}^A = E_{Fn}$) as in figure 5.1a, then $E_{Fn} - E_{FM}^B = q \cdot V_{OC}$ and $E_{FM}^B - E_{Fp} = q \cdot (iV_{OC} - V_{OC})$ and the relationship of Tan *et al.* from equation 5.15 is obtained by inserting the “forces” into equation 5.11.

¹⁸This obviously applies only to lowly doped contacts.

¹⁹To obtain both equations, one has to assume $|E_C(0) - E_C(W)| \ll E_{Fn} - E_{FM}^B$ and $|E_V(0) - E_V(W)| \ll E_{FM}^B - E_{Fp}$, thus almost flat conduction and valence bands throughout the contact. This assumption only holds for special cases. Thus, the validity is limited.

5.3. DERIVATION AND CLASSIFICATION OF THE SPECIFIC DEFINITIONS IN THE LITERATURE

One special case, which fulfills the requirement, that most of the membrane is field-free, is a doped contact with a high hole selectivity. The hole quasi-Fermi level of such a contact is almost flat and implies that $(iV_{OC} - V_{OC}) \ll \frac{k_B T}{q}$. The transport law in equation 5.18 approximates to a linear transport law by a 1st order Taylor expansion. The transport of holes in this case is not necessarily due to diffusion only, but for such a flat quasi-Fermi level the diffusive law and drift law are almost indistinguishable. At the end it is a transport governed by the drop of electrochemical potential. The selectivity coefficient with the linear approximation reads

$$S_{0p} = \frac{k_B T}{q \rho_{0p} J_{0n}} = \frac{\exp\left(\frac{qV_{OC}}{k_B T}\right) - 1}{\frac{q(iV_{OC} - V_{OC})}{k_B T}} \quad (5.19)$$

where $\rho_{0p} = \frac{k_B T}{q J_{0p}}$ represents a constant resistivity for hole (majority) carriers through the membrane. The formula on the left-hand side of equation 5.19 has the same form as proposed by Brendel and Peibst [120] and by Smit [118]. Brendel and Peibst define the selectivity coefficient S_0 as the ratio between the resistivities for majority and minority carrier transport motivated by the picture of U. Würfel, A. Cuevas and P. Würfel [116]. They postulate that the majority carrier resistance corresponds to the contact resistance and the the minority carrier transport resistance is governed by recombination at the contact [120, 281]. However, their definition lacks to define the selective contact spatially in detail. Therefore, it was not clear from the definition – at least for the author of this thesis – what the resistances for minority and majority carriers imply exactly²⁰. Rau and Kirchartz [153] recently compared the definition of Roe *et al.* [123] and Brendel and Peibst [120] and have made a clear distinction between both of them. The former was denoted as the selectivity definition with “kinetic character” and the latter was interpreted as the resistive definition. As we will see below, the latter definition corresponds to an electrode selectivity, whereas the former contact selectivity coefficient S_0 is approximately infinitely high due to efficient majority carrier transport through the membrane. This ensures that $V_{OC} \approx iV_{OC}$ and the extraction efficiency at OC approaches unity.

In summary, the assumption of independent exponential laws, as used by Weber *et al.* and Roe *et al.*, describes selective contacts with a finite membrane width if quasi-neutrality within the membrane is ensured e.g. for highly selective contacts. The transport law for the majority carriers simplifies to a linear one for an almost flat majority carrier quasi-Fermi level. The condition for the latter ($(iV_{OC} - V_{OC}) \ll \frac{k_B T}{q}$) implies that the extraction efficiency is better than 0.96 for silicon solar cells with an iV_{OC} between 600 mV and 750 mV.

Lastly, it should be emphasized that the independent treatment of minority and majority carrier transport is a simplification and its validity is restricted to special cases. Therefore, the definition of Weber *et al.* and Roe *et al.* is a special case, which however covers many practical contacts. Anyhow, the definition in this thesis is more general than that and also allows to describe a more general case, where the membrane is not necessarily field-free and generation or recombination is allowed. One example of such a treatment is found in the appendix A.3.2, where a generalized charge control model is used to describe the transport

²⁰A private communication with R. Brendel revealed that the spatial definition of the selective contact he had in mind does at least include the electrode.

5.3. DERIVATION AND CLASSIFICATION OF THE SPECIFIC DEFINITIONS IN THE LITERATURE

through the membrane and to find the ratio of the desired and undesired current densities. The selectivity coefficient S_0 becomes dependent on the point of operation, but it is still described by the average conductivities for majority and minority carriers at a particular point of operation.

Pseudo-linear carrier transport laws

Another approach to describe the transport within the selective membrane was proposed by Onno *et al.* [124], who derive a pseudo-linear transport law for electrons and holes from drift-diffusion equations. A partial resistance for electrons and holes is defined, which itself depends on the position of the quasi-Fermi levels E_{Fn} and E_{Fp} for electrons and holes at the absorber/membrane boundary, respectively, and the electrode/membrane boundary E_{FM} . It reads for electrons

$$J_n = \frac{1}{\bar{\rho}_n} \cdot \frac{|E_{Fn} - E_{FM}^B|}{q} \quad (5.20)$$

and for holes

$$J_p = \frac{1}{\bar{\rho}_p} \cdot \frac{|E_{Fp} - E_{FM}^B|}{q} \quad (5.21)$$

Assuming a perfectly electron-selective contact ($E_{FM}^A = E_{Fn}$) and open-circuit conditions, then $E_{Fn} - E_{FM}^B = q \cdot V_{OC}$ and $E_{FM}^B - E_{Fp} = q \cdot (iV_{OC} - V_{OC})$. The pseudo-linear laws inserted into the selectivity definition 5.1 for the hole selectivity at open-circuit conditions ($S_{p,OC} = 1$) yields

$$S_{p,OC} = \frac{\bar{\rho}_n}{\bar{\rho}_p} \cdot \frac{iV_{OC} - V_{OC}}{V_{OC}} = \frac{\bar{\rho}_n}{\bar{\rho}_p} \cdot \left(\frac{iV_{OC}}{V_{OC}} - 1 \right) = 1 \quad (5.22)$$

The ratio of average carrier resistances is identified as one version of a selectivity coefficient, which is not the same as that of Weber *et al.* and Roe *et al.*. In particular, it is voltage-dependent and somehow similar to the ratio of average conductivities as derived from the charge control model in appendix A.3.2, but is not necessarily the same value due to a different averaging method²¹ used by Onno *et al.* and in appendix A.3.2. By putting the resistance values on one side of the equation and the voltages on the other side and rearranging equation 5.22, Koswatta's and Onno's relationship between the partial resistances $\bar{\rho}_n$ and $\bar{\rho}_p$ for electrons and holes, respectively, and the ratio of the internal and external voltage is found as follows.

$$\eta_{extr,OC} = \frac{V_{OC}}{iV_{OC}} = \frac{\bar{\rho}_n}{\bar{\rho}_n + \bar{\rho}_p} \quad (5.23)$$

This quantity was referred to as the selectivity metric by Koswatta [117] and Onno *et al.* [124]. As derived in section 5.2.2, the ratio of external versus internal voltage at OC can be identified to be an efficiency of the contact to convert chemical energy of electrons and

²¹Onno *et al.* use an integral over the energy coordinate and the charge control model uses an integral over the space coordinate.

5.3. DERIVATION AND CLASSIFICATION OF THE SPECIFIC DEFINITIONS IN THE LITERATURE

holes in the absorber into electrical energy provided to the external circuit²². For this reason, the author of this thesis advocates calling the quantity extraction efficiency rather than selectivity. Anyhow, this quantity measures the ability of the contact to extract the desired over the undesired carriers and was derived from the selectivity definition in this thesis, which underlines the unifying character of the definition.

5.3.2. Electrode selectivity

As a final example, the definition of electrode selectivity is derived. This is particularly relevant to recover the definition of Brendel and Peibst. The electrode selectivity includes the electrode region in addition to the carrier-selective contact. This electrode region is not necessarily the bulk of the metal wire, but reflects any additional external²³ resistance, which is assigned to the contact. The transport of carriers through the electrode region causes an additional Ohmic voltage drop $\Delta V_{\text{electrode}} = \rho_{\text{electrode}} \cdot J_{\text{total}}$ due to a current density J_{total} flowing through the electrode region with a resistivity $\rho_{\text{electrode}}$. The resistivity contains the contact resistivity ρ_C , but can also contain other contributions as needed. The voltage drop $\Delta V_{\text{electrode}}$ reduces the terminal voltage V_{term} compared to the voltage V as measured between the membrane/electrode interface of the hole-selective contact and the perfectly electron-selective contact without bulk electrode resistance. If one uses the ‘‘exponential transport law’’ from equation 5.18 representing the hole transport within the membrane and includes an additional external Ohmic voltage drop $\Delta V_{\text{electrode}}$, the transport law for the majority carriers (holes) reads

$$J_p = J_{0p} \left(\exp \frac{q(iV - V_{\text{term}} - \Delta V_{\text{electrode}})}{k_B T} - 1 \right), \quad (5.24)$$

where iV corresponds to the internal voltage in the absorber. For the minority carrier (electron) current density from equation 5.17, the transport law reads

$$J_n = J_{0n} \left(\exp \frac{q(V_{\text{term}} + \Delta V_{\text{electrode}})}{k_B T} - 1 \right). \quad (5.25)$$

Assuming a highly selective hole electrode – resulting $q(iV - V_{\text{term}} - \Delta V_{\text{electrode}}) \ll k_B T$ – and a point of operation far away from open-circuit or short-circuit conditions ($V_{\text{OC}} \gg V_{\text{term}} \gg \Delta V_{\text{electrode}}$), then the total current density is dominated by the hole current density $J_{\text{total}} \approx J_p$. The 1st order Taylor approximation of the hole transport law J_p yields a transport law for the majority carrier as follows.

$$J_p = \frac{1}{\frac{k_B T}{q J_{0p}} + \rho_{\text{electrode}}} \cdot (iV - V_{\text{term}}) \quad (5.26)$$

²²Remember that at OC the extraction efficiency corresponds to a Carnot-like quantity, where no power is provide.

²³External means that the resistance is outside of the selective membrane, where quasi-Fermi level splitting is present.

5.3. DERIVATION AND CLASSIFICATION OF THE SPECIFIC DEFINITIONS IN THE LITERATURE

The electrode selectivity \hat{S}_p of a hole-selective contact calculates to

$$\hat{S}_p = \frac{\frac{k_B T}{q}}{(\rho_{0p} + \rho_{\text{electrode}}) \cdot J_{0n}} \cdot \frac{iV - V_{\text{term}}}{\frac{k_B T}{q} \cdot \left(\exp \frac{qV_{\text{term}}}{k_B T} - 1 \right)}, \quad (5.27)$$

where $\rho_{0p} = \frac{k_B T}{qJ_{0p}}$ is the resistance for hole transport through the membrane.

The blue part of equation 5.27 corresponds to the electrode selectivity coefficient, which is similar to the selectivity coefficient of a highly selective contact in equation 5.19, but contains the additional electrode resistance. If $\rho_{\text{electrode}} = 0$, then the electrode selectivity coefficient equals that in equation 5.19 exactly. If on the other hand, the sum of both resistances is interpreted as the contact resistance $\rho_C = \rho_{0p} + \rho_{\text{electrode}}$, then the electrode selectivity becomes

$$\hat{S}_p = \frac{\frac{k_B T}{q}}{\rho_C \cdot J_{0n}} \cdot \frac{iV - V_{\text{term}}}{\frac{k_B T}{q} \cdot \left(\exp \frac{qV_{\text{term}}}{k_B T} - 1 \right)}. \quad (5.28)$$

The blue quantity in equation 5.28 corresponds to the (electrode) selectivity coefficient as defined by Brendel and Peibst [120] and the black factor is similar to the voltage factor in the updated version of the definition of Schmidt, Peibst and Brendel [281] but not exactly the same. The difference in the voltage factor is obviously due to the definition of the selectivity by using resistances [281] compared to current densities in this thesis. Schmidt, Brendel and Peibst define the minority carrier resistance $\rho_m = \frac{J_m}{iV}$ and if the majority carrier resistance $\rho_M = \rho_C = \frac{J_M}{iV - V_{\text{term}}}$, then the derived electrode selectivity has to be multiplied by $\frac{iV}{iV - V_{\text{term}}}$ to exactly²⁴ recover the definition of Schmidt, Brendel and Peibst [281]. The conversion factor between both definitions is typically a large number, such that both quantities do not exhibit the same order of magnitude.

From the point of view of selecting the undesired processes, J_{0n} as defined by Brendel and Peibst contains all recombination processes of the selective contact [120] rather than only the minority carrier transport through the membrane.

If the definition in this thesis is similar to Brendel's definition, the reader may wonder what is the added value of the definition in this thesis. At this point, it should be emphasized again that Brendel's definition is as special case of the definition in this thesis, which is only valid for contacts, where the external voltage equals the internal voltage at open-circuit conditions ($V_{\text{OC}} \approx iV_{\text{OC}}$). The latter is almost always fulfilled for "traditional" contacts in Si solar cells, but is often violated for "non-traditional" contacts. Consequently, the definition of Brendel and Peibst cannot be applied to such contacts. On the other hand, one may argue that the condition $V_{\text{OC}} \approx iV_{\text{OC}}$ should always be ensured for high efficiency solar cells, but for the same reason also $\Delta V_{\text{electrode}}$ should vanish. Both conditions are on an equal footing and a more general requirement – which is obvious and trivial – is that the terminal voltage V_{term} should be as close to the internal voltage iV as possible. In the sense of low-dissipative selective electrodes, equation 5.27 has been derived from the more general definition in this

²⁴Note that V_{term} in the exponential function in the denominator is in fact $V = V_{\text{term}} + \Delta V$ and was approximated for simplicity. Furthermore, if the majority carrier transport through the membrane is efficient, then $V = iV$ as in the definition in reference [281].

5.4. RELATIONSHIP OF SELECTIVITY AND CARRIER EXTRACTION EFFICIENCY

thesis and is valid for all contacts, which obey the condition that $V_{\text{term}} \approx iV$ and imply a low loss due to carrier extraction – independently where the dissipation happens.

5.4. Relationship of selectivity and carrier extraction efficiency

In the previous sections 5.2.1, 5.2.2 and 5.3, the ability of a contact to selectively extract the desired carriers over the undesired carriers was discussed. The framework of carrier kinetics defined the (rate) selectivity of the contact/electrode and the framework of endoreversible thermodynamics defined the extraction efficiency of the contact. Both figures, the selectivity S and the extraction efficiency η_{extract} have one thing in common - they relate the internal chemical potential $\Delta\mu = q \cdot iV$ and external electrical potential qV_{ext} in equation 5.10 and 5.7. For any given internal potential, the extraction efficiency can be calculated from the selectivity ratio $\frac{S}{S_0}$, if the functional relationship of internal and external voltage in $\Sigma(F_M, F_m)$ is known. This relationship at open-circuit condition was derived in 5.15, where $S_{\text{OC}} = 1$, and leads to the following correlation²⁵ between the selectivity coefficient S_0 and the extraction efficiency $\eta_{\text{extract,OC}}$ for a given internal voltage iV_{OC} .

$$S_0 = \frac{\exp\left(\frac{qiV_{\text{OC}}}{k_B T} \cdot \eta_{\text{extract,OC}}\right) - 1}{\exp\left(\frac{qiV_{\text{OC}}}{k_B T} \cdot (1 - \eta_{\text{extract,OC}})\right) - 1} \quad (5.29)$$

Figure 5.3a shows the correlation between the extraction efficiency and the selectivity coefficient at open-circuit conditions for different internal voltages iV_{OC} . It is evident that the higher the internal voltage is, the higher the selectivity coefficient has to be in order to achieve an extraction efficiency close to unity. This is not surprising, because the equilibrium exchange current density J_{0m} for the minority carriers has to decrease to allow an increase of the internal voltage at a give illumination, but the equilibrium exchange current density J_{0M} for majority carriers has to stay the same to support the extraction of photo-generated carriers. Moreover, if S_0 is constant, as assumed in equation 5.29, it is expected that the extraction efficiency will be close to unity for low iV_{OC} values due to low illumination intensity and decrease at high iV_{OC} . Indeed, a deviation of Suns- iV_{OC} and Suns- V_{OC} characteristics is frequently observed for high iV_{OC} values at high illumination levels [121, 125, 126, 346–348]. At very high illumination levels, the V_{OC} of the Suns- V_{OC} characteristic was frequently observed to even drop with increasing illumination level [125, 126, 346, 347] and it can be speculated that, at such illumination levels, S_0 decreases with increasing illumination level and the extraction efficiency reduces stronger than predicted for a constant selectivity.

In the following, approximations for two limiting cases - low and high extraction efficiency with high iV_{OC} - provide simple explicit relations between extraction efficiency and selectivity.

²⁵The following discussion does solely applies to contact selectivity because at OC not external current flows and the electrode selectivity is the same as the contact selectivity. However, the same discussion for electrode selectivity and extraction efficiency can be conducted at a different point of operation e.g. maximum power point.

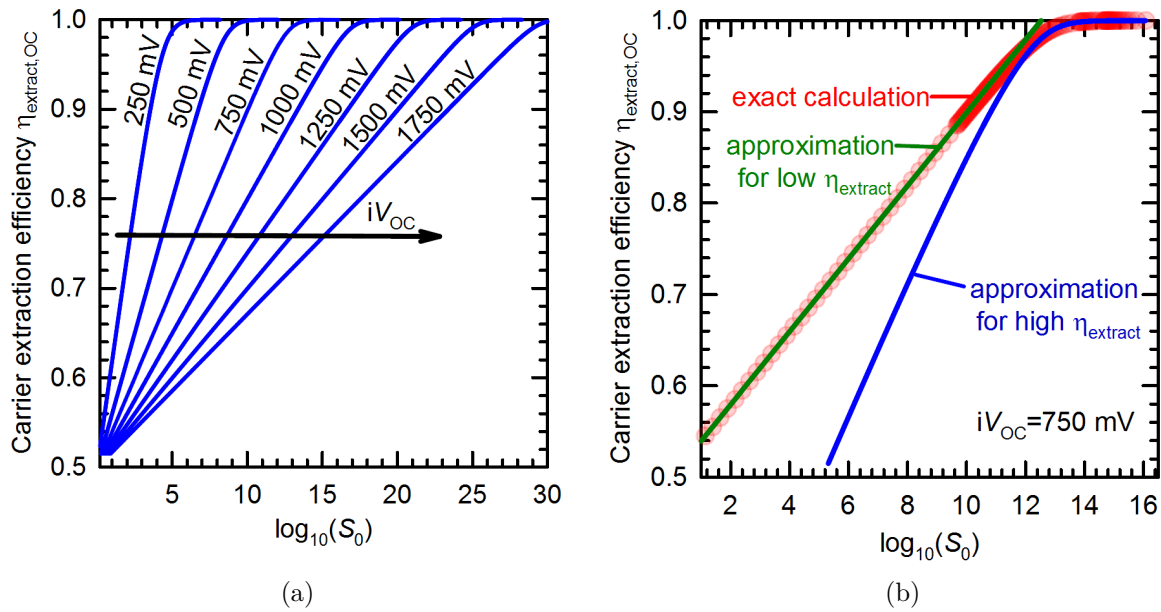


Figure 5.3.: (a) Exact calculation of the relationship between carrier extraction efficiency and selectivity coefficient at open-circuit conditions for different internal voltages iV_{OC} and (b) approximations of the relationship for low and high extraction efficiency for an internal voltage of 750 mV.

5.4. RELATIONSHIP OF SELECTIVITY AND CARRIER EXTRACTION EFFICIENCY

1. If the extraction efficiency is close to unity, thus $q(iV_{\text{OC}} - V_{\text{OC}})$ is small compared to $k_B T$, and $q i V_{\text{OC}}$ is large compared to $k_B T$, then equation 5.29 simplifies to

$$S_0 = \frac{\eta_{\text{extract,OC}}}{1 - \eta_{\text{extract,OC}}} \cdot \frac{\exp \frac{q V_{\text{OC}}}{k_B T}}{q V_{\text{OC}} / k_B T} \quad (5.30)$$

In Figure 5.3b the approximation (blue solid line) and exact calculation (red circles) coincide for high S_0 values, but differ for S_0 smaller than about 10^{13} . The accuracy for the predicted S_0 of this approximation for an iV_{OC} of 750 mV is better than 20% for an extraction efficiency better than 0.99, which corresponds to $\log_{10}(S_0) \approx 13$. For $\log_{10}(S_0) \gg 13$, the extraction efficiency is close to unity, and internal voltage and external voltage are almost indistinguishable. The contact's extraction efficiency does not limit the solar cell efficiency, which is consistent with the *low-injection regime* reported by Roe *et al.* [123]. Since the term *low-injection regime* has usually a different meaning in semiconductor device physics, it is suggested to use *internal voltage limited* regime instead, because the solar cell's efficiency will be limited by the internal voltage (e.g. surface or bulk recombination) rather than by the extraction efficiency of the contact.

2. For a lower extraction efficiency, where $q(iV_{\text{OC}} - V_{\text{OC}}) \gg k_B T$ and $q i V_{\text{OC}} \gg k_B T$, equation 5.29 is approximately

$$\ln S_0 = \frac{2\eta_{\text{extract,OC}} - 1}{\eta_{\text{extract,OC}}} \cdot \frac{q V_{\text{OC}}}{k_B T} = (2\eta_{\text{extract,OC}} - 1) \cdot \frac{q \cdot i V_{\text{OC}}}{k_B T} \quad (5.31)$$

In Figure 5.3b, this approximation (green solid line) matches the exact calculation for low S_0 values, but deviates at higher S_0 values. The accuracy for the predicted S_0 of this approximation for an iV_{OC} of 750 mV is better than 20% for an extraction efficiency below 0.94. Equation 5.31 refines the finding of Roe *et al.* [123] that $V_{\text{OC}} \approx \frac{k_B T}{q} \ln S_0$ in this *selectivity-limiting* regime.

Furthermore, equation 5.31 can be rewritten in terms of the open-circuit voltage loss $\Delta V_{\text{OC}} = iV_{\text{OC}} - V_{\text{OC}}$, which is frequently used by several authors as a selectivity metric [121, 122, 146], to yield

$$\Delta V_{\text{OC}} = \frac{1}{2} i V_{\text{OC}} - \frac{k_B T}{2q} \ln S_0 = \Delta V_{\text{OC,max}} - \ln(10^{(k_B T/2q)}) \cdot \log_{10}(S_0) \quad (5.32)$$

with $\Delta V_{\text{OC,max}}$ as the maximum possible voltage loss of $\frac{1}{2} i V_{\text{OC}}$ at a single non-selective contact, where electron and hole transfer processes are equally efficient, with $S_0 = 1$. Indeed, the open-circuit voltage loss is an indirect measure of the selectivity, but it is not suitable for a quantitative comparison of selectivity between distinctly different samples (e.g. different absorber), because it cannot be assumed in general that iV_{OC} is constant for different samples. For such cases, the selectivity coefficient S_0 in equation 5.31 or the extraction efficiency can serve as a figure of merit. However, ΔV_{OC} represents a relevant quantity from cell's performance point of view.

To summarize, carrier extraction efficiency and selectivity are closely related and explicit, easy to apply formulas are derived above, which refine the findings from the literature. From a practical point of view, it is interesting to calculate the maximum achievable power conversion efficiency for a contact-limited solar cell with a given selectivity. Brendel *et al.* [120, 127, 349] and Rau and Kirchartz [153] performed such calculations by using an equivalent circuit model of the solar cell, where the contact area fraction was optimized. They obtained a maximum power conversion efficiency as function of $\log_{10}(S_0)$ with a similar shape as the carrier extraction efficiency in figure 5.3b, which raises two questions: Does the calculated maximum power conversion efficiency reflect the carrier extraction efficiency? Is it possible to directly calculate the maximum power conversion efficiency for a given selectivity coefficient and internal voltage from the relationship between extraction efficiency and selectivity?

5.5. Performance of contact selectivity-limited solar cells

In order to calculate the performance of a selectivity-limited solar cell, one can use an appropriate equivalent circuit model and simply calculate the maximum power output²⁶. In the following, the “thermodynamic approach” based on the found correlation between the extraction efficiency and selectivity from the previous sections is promoted.

First, let us consider a solar cell with perfectly selective contacts, which is limited by intrinsic recombination and Lambertian light trapping only. The silicon solar cell on a $2\ \Omega\text{cm}$ n -type doped $110\ \mu\text{m}$ -thick wafer with Lambertian light trapping [28] is similar to that used by Brendel *et al.* [127]. In the case of perfect contacts, the J - V characteristic is governed by radiative recombination and Auger-recombination within the wafer bulk. The J - V characteristic of such a solar cell is determined following Schäfer and Brendel [28] and was kindly provided by S. Schäfer. The J - V characteristics of the cell is depicted in figures 2.4b and 2.4a and was discussed in section 2.3. The efficiency $i\eta = \eta(S_0 \rightarrow \infty)$ of the cell calculates as

$$i\eta = \frac{iJ_{\text{MPP}} \cdot iV_{\text{MPP}}}{P_{\text{in}}} \quad (5.33)$$

with the incident power density P_{in} , the implied current density $iJ_{\text{MPP}} = J_{\text{MPP}}(S_0 \rightarrow \infty)$ and the implied voltage $iV_{\text{MPP}} = V_{\text{MPP}}(S_0 \rightarrow \infty)$ at maximum power point operation. The considered solar cell exhibits an implied efficiency $i\eta$ of 29.2% with an implied open-circuit voltage iV_{OC} of 755 mV.

Now, one of the two selective contacts to the solar cell is allowed to have a finite selectivity coefficient, such that the extraction efficiency falls below unity. Furthermore, it is assumed that attaching the contact to the solar cell does not alter the recombination behavior of the solar cell²⁷. The contact-limited solar cell exhibits the following efficiency $\eta(S_0)$ with a

²⁶This is outlined in the appendix A.3.3 and A.3.4.

²⁷This requirement is not obvious, but is implicitly assumed for the endoreversible chemical engine in section 5.2.2. Another detailed explanation is found in the appendix A.3.4 using the passivation efficiency of the contact. This assumption leads to the maximum possible efficiency for a give S_0 .

5.5. PERFORMANCE OF CONTACT SELECTIVITY-LIMITED SOLAR CELLS

current density $J_{\text{MPP}}(S_0)$ and voltage $V_{\text{MPP}}(S_0)$ at maximum power point operation.

$$\eta(S_0) = \frac{J_{\text{MPP}}(S_0) \cdot V_{\text{MPP}}(S_0)}{P_{\text{in}}} \quad (5.34)$$

If the implied efficiency and the contact-limited efficiency are compared by dividing one with the other, then the efficiency ratio can be correlated with the extraction efficiency $\eta_{\text{extract,MPP}}(S_0) = \frac{V_{\text{MPP}}(S_0)}{iV_{\text{MPP}}}$ at maximum power point operation.

$$\frac{\eta(S_0)}{i\eta} = \frac{J_{\text{MPP}}(S_0)}{iJ_{\text{MPP}}} \cdot \frac{V_{\text{MPP}}(S_0)}{iV_{\text{MPP}}} \approx \eta_{\text{extract,MPP}}(S_0) \quad (5.35)$$

As discussed in the appendix A.3.4, the current density ratio $\frac{J_{\text{MPP}}(S_0)}{iJ_{\text{MPP}}}$ can be assumed to remain approximately unity for $\log_{10}(S_0)$ values down to 4, where the concepts derived in section 5.2.1 and 5.3 are anyhow questionable. For this reason, it can be safely concluded for the range of interesting selectivity coefficients that the ratio of the contact-limited efficiency versus implied efficiency is determined by the extraction efficiency $\eta_{\text{extract,MPP}}(S_0)$ at maximum power point.

The challenge is now to correlate the extraction efficiency $\eta_{\text{extract,MPP}}(S_0)$ with the selectivity coefficient S_0 . Fortunately, the relationship between the extraction efficiency $\eta_{\text{extract,OC}}$ at OC and the selectivity coefficient was derived in the previous sections and a correlation between the Carnot efficiency and the efficiency at maximum power point from reference [57] was used to relate the carrier extraction efficiency at OC and MPP. The latter relation adapted from reference [57] (blue in equation 5.36) is approximately the same as the relation found from the equivalent circuit calculations (red in equation 5.36) in the appendix A.3.4 and reads

$$\eta_{\text{extract,mpp}} = \frac{\eta_{\text{extract,OC}}}{2 - \eta_{\text{extract,OC}}} \approx 2 \cdot \eta_{\text{extract,OC}} - 1 \quad (5.36)$$

The approximation is accurate for the “low dissipation” regime, which is consistent with the regime, where the blue part of equation 5.36 is valid. For $\eta_{\text{extract,OC}} > 0.73$, the deviation between the blue and red part of equation 5.36 is better than 20%_{rel.}. Using the relationship between $\eta_{\text{extract,OC}}$ and S_0 for the selectivity-limited regime in equation 5.31, one finds for the extraction efficiency at MPP

$$\eta_{\text{extract,mpp}} = \frac{k_{\text{B}}T}{q \cdot iV_{\text{OC}}} \cdot \ln S_0 = \frac{k_{\text{B}}T}{q \cdot iV_{\text{OC}}} \cdot \ln(10) \cdot \log_{10}(S_0) \quad (5.37)$$

The power conversion efficiency of a contact selectivity limited solar cell with this relation and equation 5.35 reads

$$\eta(S_0) = \frac{i\eta}{iV_{\text{OC}}} \cdot \frac{k_{\text{B}}T}{q} \cdot \ln(10) \cdot \log_{10}(S_0) \quad (5.38)$$

The derived equation establishes a simple relationship between the power conversion efficiency and the selectivity coefficient, which is solely based on thermodynamic considerations and

the selectivity definition in this thesis. It uses three well known input parameters: 1. $i\eta$ and iV_{OC} for the limitation by the absorber and 2. the selectivity coefficient S_0 for the limitation by the selective contact. The conversion efficiency $\eta(S_0)$ is linearly dependent on the logarithmic selectivity coefficient $\log_{10}(S_0)$ in this selectivity-limited regimes, which is only an approximation of equation 5.29 for extraction efficiencies at OC below about 0.94. The slope of equation 5.38 is determined by the parameters of the absorber limited solar cell and amounts to 2.29% for Auger-limited silicon solar cell from above. Brendel *et al.* [127] also identified this linear regime and gave an equation based on a fit to the numerically determined data in the linear regime, which is reproduced here for ease of comparison [127, equation 16]:

$$\frac{\eta_{f_c, max=1}}{\%} = 2.452 \cdot \log_{10}(S_0) - 4.424 \quad (5.39)$$

The straight line in reference [127] has a slope of 2.45%, which is consistent with the slope calculated here. Unlike the equation 5.38, the equation 5.39 has its intercept with the ordinate not at the origin, but at $\eta(S_0 = 1) = -4.424$ and causes a shift of both lines. Several potential reasons for the shift between both lines are discussed in appendix A.3.4. One reason could be that equation 5.36 is not perfectly accurate. Another reason is the difference of “selectivity” definitions as was also recently pointed out by Rau and Kirchartz [153]. While equation 5.38 was derived from the definition of contact selectivity, equation 5.39 corresponds to electrode selectivity. For the latter, the optimization procedure yields an optimum between passivation and resistance, such that passivation of the contact is reduced and results in a lower internal voltage compare to the case, where contact selectivity is not limiting. In contrast to that, the internal voltage iV_{OC} in equation 5.38 is assumed to stay constant and limited by the intrinsic recombination in the absorber²⁸. Form this fact, it is expected that the PCE as derived in this thesis should predict a higher efficiency compared to reference [127].

To calculate $\eta(S_0)$ for the full range of S_0 , equation 5.29 is used instead of the approximated equation 5.31 and the calculated $\eta(S_0)$ is depicted in figure. The PCE for a contact-selectivity limited solar cell as calculated by the analytic equations based on thermodynamic considerations in this thesis exhibits a similar functional shape as that calculated by Brendel *et al.* [127], but – as discussed – the linear part of the red line is shifted with respect to the black line. In summary, the question²⁹ raised in section 5.4 can be answered as follows: The maximum achievable PCE of a contact selectivity-limited solar cells almost completely reflects the extraction efficiency at maximum power point operation and can be directly calculated from the selectivity coefficient by using a thermodynamic relationship between extraction efficiency at maximum power and open-circuit operation conditions.

²⁸For further discussion, the reader is referred to the appendix A.3.4, where also the passivation of a contact is taken into account.

²⁹The questions were the following: Does the calculated maximum power conversion efficiency reflects the carrier extraction efficiency? Is it possible to directly calculate the maximum power conversion efficiency for a given selectivity coefficient and internal voltage from the relationship between extraction efficiency and selectivity?

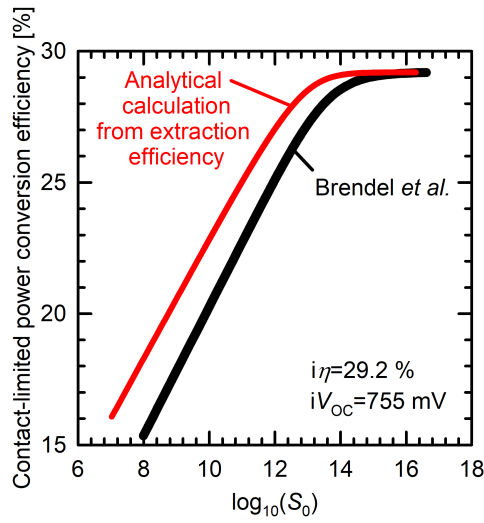


Figure 5.4.: The maximum PCE of a contact-limited solar cell with a Si absorber. Comparison of the maximum PCE of the analytical calculation from equations 5.35, 5.36 and 5.29 (red solid line) with the calculation of Brendel *et al.* [127, equation 16] (black solid line)

5.6. Chapter summary

In this chapter, the process of carrier extraction at a contact to an absorber is discussed from different point of views. The spatial and process-wise definition of a carrier-selective contact is discussed in detail and the carrier-selective contact including and excluding the electrode is distinguished, which leads to the definition of the carrier-selective electrode and carrier-selective contact, respectively. A general definition of selectivity is provided base on a definition borrowed from chemical reaction kinetics. The carrier extraction process can be considered in the framework of partial electron and hole transfer reactions at the conduction and valence bands, respectively, and the rate asymmetry of the partial reactions defines the voltage-dependent (rate) selectivity $S(V)$ of a carrier-selective contact and electrode. At open-circuit condition, the rate of electron and hole transfer reactions is required to be equal by detailed-balance considerations and $S(V_{OC}) = 1$. From this relationship, a selectivity coefficient S_0 is found, which corresponds to the ratio of the equilibrium exchange current densities for the electron and hole transfer reactions. The selectivity coefficient S_0 is equivalent to the definition of Weber *et al.* [119] and Roe *et al.* [123].

Furthermore, the carrier extraction process is elucidated from thermodynamics point of view, where an endo-reversible chemical engine represents the process of carrier extraction from an absorber, where carriers have a chemical potential, into the metal contact, where carriers have an electrical potential. Thus, the efficiency of the conversion process of chemical into electrical power defines the extraction efficiency of a contact. At open-circuit condition, the extraction efficiency $\eta_{\text{extract,OC}}$ is defined by the ratio of the external open-circuit voltage V_{OC} and the internal open-circuit voltage iV_{OC} , which is consistent with the definition of Onno *et al.* [124] and Pysch *et al.* [125], Bivour *et al.* [121] and Glunz *et al.* [122] as a measure of

selectivity.

To be a unifying definition, the definition must recover each individual definition from the literature for a specific set of assumptions. This exercise is performed by using the general definition in this thesis and the specific assumptions from the literature. Indeed, the definition in this thesis is able to reproduce the definitions from the literature and highlights the specific boundaries of validity for each definition.

Even if the extraction efficiency and selectivity describe the same carrier extraction process, it should be noted that both quantities represent different point of views and have distinctly different orders of magnitude. Moreover, the detailed investigation on the selectivity definition and the definition of the extraction efficiency provides an extremely important relationship between the selectivity coefficient and the extraction efficiency at open-circuit operation conditions, which forms the basis for the derivation of the power conversion efficiency for a contact selectivity-limited solar cell based on thermodynamics considerations. An analytic expression for the power conversion efficiency as a function of the selectivity coefficient is derived, which matches that from numerical optimization of passivation and resistance as calculated by Brendel *et al.* [127]. The derived correlation reveals that the PCE of a contact selectivity-limited solar cells is determined by a thermodynamic quantity – the extraction efficiency at maximum power point operation – and provides a thermodynamic picture of the carrier extraction process in solar cells.

6. Passivated carrier-selective POLO junctions to mono-crystalline silicon

The following chapter is partly based on peer-review papers published in [157] and [158]. The properties of the POLO junctions were determined by M. Boßmeyer during his Diploma thesis. The author supervised M. Boßmeyer.

D. Tetzlaff, T. Wietler and J. Krügener developed the TMAH etch process at Leibniz Universität Hannover to determine the pinhole density and applied the process to the TLM samples used in the Diploma thesis of M. Boßmeyer.

The following chapter studies the electrical properties of POLO junctions by means of photo-conductance decay method and contact resistance measurements to determine the selectivity coefficient.

6.1. Fabrication of POLO junction samples

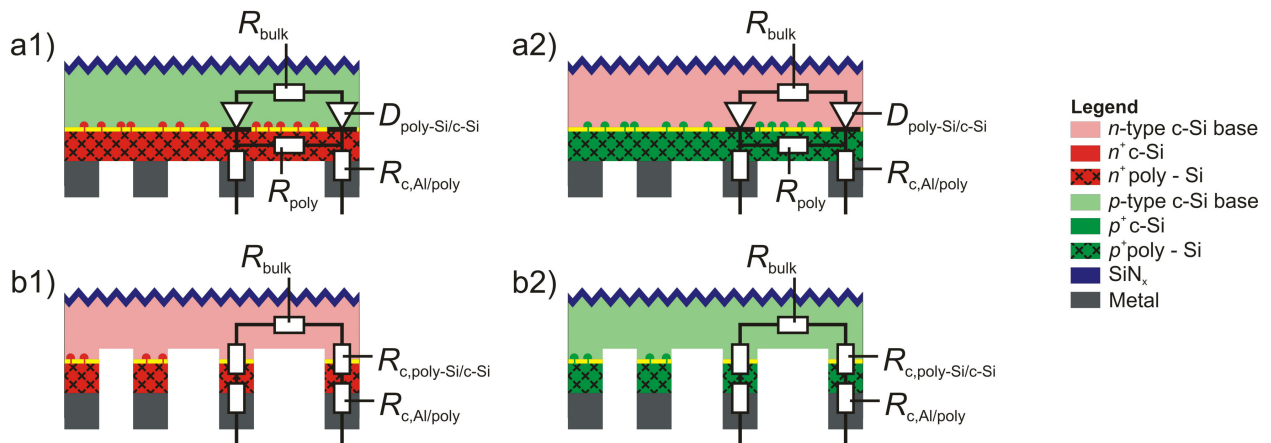


Figure 6.1.: Schematic drawing of TLM test structures for the determination of the contact resistivity between aluminum and n^+ poly-Si (a1) and between aluminum and p^+ poly-Si (a2), TLM test structures for the determination of the combined junction resistivity of Al / n^+ poly-Si / c-Si (b1) and Al / p^+ poly-Si / c-Si junctions (b2)

For the following experiments n-type and p-type float zone (FZ) silicon wafers with a base resistivity of $2.5 \Omega\text{cm}$ and $1.5 \Omega\text{cm}$, respectively, and a thickness of $300 \mu\text{m}$ are used. A 2.1 nm

thin thermal silicon dioxide layer grows on both sides of the substrate wafers in a tube furnace oxidation at 700 °C. Then, 220 nm thick intrinsic, amorphous Si (a-Si) layer is deposited in a low pressure chemical vapor deposition (LPCVD) furnace at 550 °C on top of the silicon oxide. The *i*-a-Si is doped by ion implantation with 2×10^{15} boron ions/cm² and an energy of 10 keV resulting in *p*-a-Si. For the *n*-type doped a-Si, ion implantation is performed with 5×10^{15} phosphorus ions/cm² and an energy of 20 keV. The sample denoted as *n*-type *counterdoped* (*cd*) receive a boron implantation with a dose of 1.25×10^{15} boron ions/cm² at an energy of 10 keV and a phosphorus implantation with a dose of 5×10^{15} phosphorus ions/cm² at an energy of 20 keV. The phosphorus species overcompensates the boron doping and yields effectively *n*-type doped a-Si. After doping, a silicon oxide grows at 900 °C in a pyrogenic oxidation¹ for 30 min and the POLO junction forms in a high temperature annealing step in nitrogen atmosphere at 1050 °C in a tube furnace. The annealing duration of the junction formation annealing is varied between 30 min and 80 min. Four kind of symmetric test structures are obtained after junction formation:

- n^+ POLO / *p*-type c-Si / n^+ POLO (a1)
- p^+ POLO / *n*-type c-Si / p^+ POLO (a2)
- n^+ POLO / *n*-type c-Si / n^+ POLO (b1)
- p^+ POLO / *p*-type c-Si / p^+ POLO (b2)

The structures (a1) and (b1) are either solely phosphorus or counterdoped. The samples with a high-low junction (b1, b2) at first serve as lifetime samples to extract the corresponding recombination prefactor $J_{C,poly}$ from photoconductance decay measurements directly after junction formation and forming gas anneal. After that, the same samples are used to determine the combined contact resistance of the aluminum/polysilicon/c-Si contact.

For this purpose, the four symmetric test structures are processed further to transfer length measurement (TLM) samples as follows. A single-sided HF etch and a subsequent KOH etch remove the poly-Si layer on the front side to avoid parasitic current flow through the poly-Si layer on the front side during TLM measurements. The thick thermal oxide on the rear side is stripped and a thick silicon nitride layer is deposited on the front side as an electrical isolation. A short HF dip prior to the thermal vacuum evaporation of aluminum on the rear side in a high-throughput tool (ATON) dissolves the native silicon dioxide layer from poly-Si. In order to ensure, that the POLO junction is intact after metallization and the majority carrier transport occurs across the the aluminium/poly-Si and poly-Si/c-Si interface, some TLM samples of each set of test structures are inspected exemplary via scanning electron microscopy after measurement and Al removal in phosphoric acid. It is confirmed that

¹Accidentally, the p^+ POLO samples (b2) were not oxidized. It was observed in subsequent experiments that the oxidation dissolves boron dopants in the grown silicon dioxide and thus reduces the available concentration of dopants in the poly-Si layer. Since the boron implantation dose is optimized for a junction formation process with prior oxidation, the missing oxidation process leads to a larger boron concentration within the poly-Si during the junction formation annealing. The resulting stronger in-diffusion of boron into c-Si wafer leads to an enhanced recombination.

aluminum does not spike through the poly-Si layer.

After metallization, photolithography and wet chemical etching pattern the Al layer and yield a TLM pattern with pad lengths of 3 mm, a pad width of 100 μm and a spacing of a multiple of $d = 100 \mu\text{m}$. For the structures b1 and b2 (Fig. 6.1), where the poly-Si layer has the same doping polarity as the wafer, reactive ion etching removes the poly-Si in between the aluminum pads by using the Al pads as masks. Thus, the current has to flow from the Al into the poly-Si and subsequently from the poly-Si into the c-Si and vice versa (see equivalent circuits in Fig. 6.1 b1 and b2). The obtained contact resistivity represents a combined resistivity for the contacts between Al and poly-Si and the poly-Si and c-Si. In order to distinguish between both contributions, the contact resistivity between poly-Si and Al is determined separately on test structures a1 and a2, which feature continuous poly-Si layers between the metal fingers and a *pn* junction between the base and the poly-Si layer. Thus, the current flows from one Al finger exclusively through the poly-Si layer into the next Al finger (Fig. 6.1 a1 and a2).

Special care was taken to exclude measurement artifacts of the TLM method such as edge currents. For this purpose, the samples were laser scribed and cleaved to fit the Al finger width of 3 mm with a distance of about 50 μm between the cleaved edge and the metal finger edge.

All presented contact and junction resistivity values are measured on samples without post-metallization annealing.

6.2. Minority carrier transport

The recombination prefactor, also saturation current density, $J_{C,poly}$ summarizes the properties of the minority carrier transport from c-Si wafer towards the metal contact and the recombination of minority carriers on their way to the metal contact. Photoconductance decay measurements directly after junction formation annealing process of the TLM test samples (b1,b2) and using the Auger recombination model from Richter *et al.* [350] for *p*-type samples or from Veith-Wolf *et al.* [29] for *n*-type samples and the band gap narrowing model from Schenk [351] reveals the corrected inverse lifetime $1/\tau_{corr}$. Figure 6.2 illustrates the injection-dependent, corrected inverse lifetime of one exemplary sample of each of the three different POLO junctions investigated here. For the n^+ POLO and the cd n^+ POLO sample, the method of Kane and Swanson [101] was applied at an injection level close to $10 \cdot N_D$ to determine the saturation current density. Since the doping concentration of the wafer for the p^+ POLO samples amounts to about $1.1 \times 10^{16} \text{ cm}^{-3}$, high level injection conditions for the wafer would already be close to the doping concentration within the doped junction ($2 - 3 \times 10^{18} \text{ cm}^{-3}$) and would by far exceed the data range obtained for the p^+ POLO sample in Figure 6.2. An upper bound for the saturation current density of this samples with a high minority carrier lifetime material is obtained from a low injection level analysis according to Reichel *et al.* [352] at an injection level of $1 \times 10^{15} \text{ cm}^{-3}$.

After the short high temperature annealing (30 min.), the POLO junctions exhibit saturation current densities of 2 fA/cm² for n^+ POLO junctions and between 2 fA/cm² and 3 fA/cm² for n^+ POLO junctions formed by counterdoping (cd). After the long high temperature

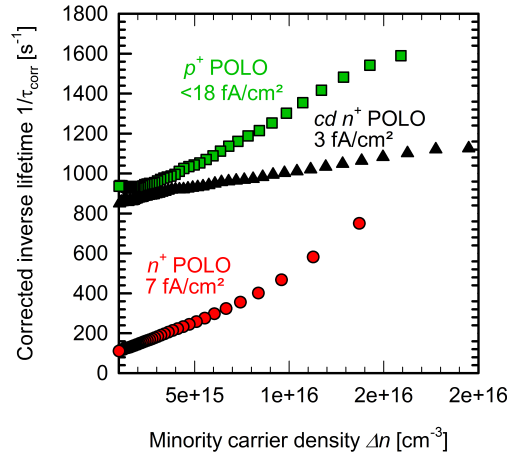


Figure 6.2.: Injection-dependent, corrected inverse lifetime of the n^+ (red), $cd\ n^+$ (black) and p^+ (green) POLO junctions with the highest selectivity as summarized in table 6.1.

annealing (80 min.), the POLO junctions feature saturation current densities of 7 fA/cm^2 for n^+ POLO junctions and between 4 fA/cm^2 and 9 fA/cm^2 for n^+ POLO junctions formed by counterdoping. For the high temperature annealing with a duration of 60 min, the p^+ POLO junctions achieve saturation current densities below 18 fA/cm^2 .

The $J_{C,poly}$ values for the n^+ (cd) POLO junction are consistent with the reported record values in the literature (see 4.2.4) and increase with increasing annealing duration. Römer *et al.* speculated that this results from an increasing areal density of pinholes in the interfacial silicon oxide [204]. This hypothesis was confirmed by Tetzlaff *et al.* [353] and by Wietler *et al.* [158].

The value for the p^+ POLO junction is slightly higher than the record values found in the literature. This is probably due to the lack of the intended oxidation process prior to the junction formation annealing process and the used low level injection analysis. However, a similar process with prior oxidation for the p^+ POLO junction applied to a lightly doped n -type wafer as reported in chapter 7 yields $J_{C,poly}$ down to 4 fA/cm^2 .

6.3. Majority carrier transport

A POLO contact, which has the same polarity as the wafer base, is called (base-)majority carrier contact and the majorities almost exclusively carry the current of the current-voltage characteristic in the dark. The dark current-voltage measurement of the TLM test samples provides direct access to the majority carrier transport.

For all test structures, an Ohmic behavior is verified when measuring the current-voltage characteristic between two pads. The resistance $R(d)$ is determined as a function of the pad spacing d with four-point measurements, using a Karl Süss PA 200 probe station and a

Keithley 4200 analyzer. The $R(d)$ curves show linear behavior² and the junction resistivity is analyzed by using the model of Eidelloth and Brendel [114] in order to take into account the 2-dimensional current flow in the wafer. The sheet resistance values R_{Sheet} determined from the slope of the $R(d)$ curve are crosschecked with the R_{Sheet} values from four-point probe (4PP) measurements. The sheet resistances are in excellent agreement.

An extensive uncertainty analysis of TLM measurements concerning the input parameter and TLM analysis itself, e.g. geometry of TLM structures or finite lateral conductivity of metal pads, was performed. For the evaluation of the uncertainty, the procedure recommended by the GUM (Guide to the Expression of Uncertainty in Measurements) [354–356], namely the propagation of distributions by Monte Carlo simulations, was used. With the determined systematic uncertainties and the resulting distributions of R and d of $R(d)$ lines, the distributions of the slope and the intercept of $R(d)$ are extracted by using a least-square fitting procedure. Then the implicit, non-linear equation derived by Eidelloth and Brendel [114] is solved for the distributions of the slope and the intercept, as well as the metal pad width and length and the wafer thickness as input parameter. This analysis yields an average value for the contact resistivity and a standard uncertainty. Since this analysis is time consuming, it was performed only for some particular samples, which represent the different orders of magnitude of contact resistivities. A relative standard uncertainty of approximately 10% for contact resistivities of $10 \text{ m}\Omega\text{cm}^2$, 30% for $1 \text{ m}\Omega\text{cm}^2$, 50% for $10^{-1} \text{ m}\Omega\text{cm}^2$, 70% for $10^{-2} \text{ m}\Omega\text{cm}^2$ and 100% for $10^{-3} \text{ m}\Omega\text{cm}^2$ was evaluated, which is in good agreement with the errors extracted by an error analysis for a simplified TLM evaluation equation [357].

6.3.1. Aluminum/polysilicon contact resistance

Figure 6.3a summarizes the Al / poly-Si contact resistivity values obtained on the TLM samples (a1) and (a2) for two different POLO junction formation annealing durations. For both annealing processes, the median of the contact resistivity between Al and n^+ poly-Si is below $0.1 \text{ m}\Omega\text{cm}^2$. Since the n^+ doped poly-Si exhibits surface doping concentrations above $1 \times 10^{20} \text{ cm}^{-3}$, low contact resistivities have been expected from the literature on Al / c-Si and Al / poly-Si contacts [111, 358]. For p^+ poly-Si, the surface doping concentration is about $2 \times 10^{19} \text{ cm}^{-3}$. According to the literature [111, 358], low contact resistivity values in the order of $10^{-3} \text{ m}\Omega\text{cm}^2$ should be implied. The lowest contact resistivity for p^+ poly-Si in Figure 6.3a is consistent to the literature and amounts to $2 \times 10^{-3} \text{ m}\Omega\text{cm}^2$. However, the median results are unexpectedly high and amount to $2 \text{ m}\Omega\text{cm}^2$ for the 30 min anneal, and to $0.1 \text{ m}\Omega\text{cm}^2$ for the 80 min anneal. For the 60 min. anneal the contact resistivity is measured on a single sample to $0.9 \text{ m}\Omega\text{cm}^2$ (not shown in Figure 6.3a). The reason for the observed higher resistivities is unclear and could not be clarified, which implies that the contribution of the Al / poly-Si contact cannot be distinguished from the poly-Si / c-Si junction of the combined Al/ poly-Si / c-Si junction resistivities in the following. Nevertheless, the values obtained are sufficiently low for solar cell applications.

²An example of the measured $R(d)$ of the POLO samples is found in section 3.2 in figure 3.2b.

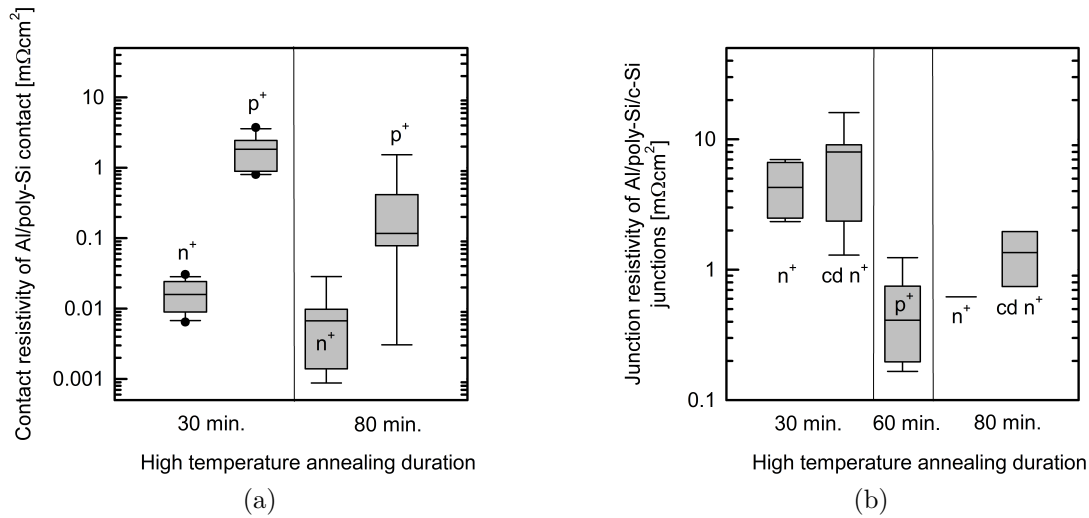


Figure 6.3.: (a) Specific contact resistances between Al and n^+ doped (p^+ doped) poly-Si. The contact resistances are extracted with 1-dimensional TLM analysis. (b) Combined specific junction resistivity between Al and n^+ doped (p^+ doped) poly-Si and between n^+ doped (p^+ doped) poly-Si and c-Si. The junction resistivities are extracted with the method of Eidelloth and Brendel [114].

6.3.2. Combined aluminum/polysilicon/c-Si contact resistance

The combined Al / poly-Si / c-Si junction resistivities for two different annealing durations are depicted in Figure 6.3b. For the Al / n^+ poly-Si / n -type c-Si junction resistivities the expected dependency on the POLO junction annealing process shows up. The higher the thermal budget, the lower the junction resistivities. This finding is consistent with the picture of a certain break-up of the interfacial oxide upon annealing [205, 227, 240]. In general, the junction resistance values are very low, with median values below $10 \text{ m}\Omega\text{cm}^2$. For the 80 min anneal, they are even lower than $1 \text{ m}\Omega\text{cm}^2$. It should be mentioned, that many data points of Al / n^+ poly-Si / n -type c-Si junction (and counterdoped structures) are not shown, because the junction resistivity has such a small value ($\ll 1 \text{ m}\Omega\text{cm}^2$) that it is not possible to apply the analysis of Eidelloth and Brendel [114]. Therefore, it can be assumed that the mean resistivity value of n^+ POLO junctions for the long anneal is lower than $1 \text{ m}\Omega\text{cm}^2$, which is in accordance with recently published results by Kokbudak *et al.* and Fong *et al.* [243, 283]. For the Al / p^+ poly-Si / p -type c-Si junction resistivity on samples with a junction formation annealing of 60 min, the median junction resistivity is $0.4 \text{ m}\Omega\text{cm}^2$.

Since the Al / n^+ poly-Si contact resistivity is about two orders of magnitude smaller than the combined resistivity, the latter attributes to the the n^+ poly-Si / c-Si junction. In case of p^+ POLO junctions, it cannot be distinguished between the Al / p^+ poly-Si and the p^+ poly-Si / c-Si junction because the Al / p^+ poly-Si contact resistivity and the combined resistivity are of the same order of magnitude. The upper limit for the p^+ poly-Si / c-Si junction resistivity is less than $1 \text{ m}\Omega\text{cm}^2$.

6.4. Transport mechanism

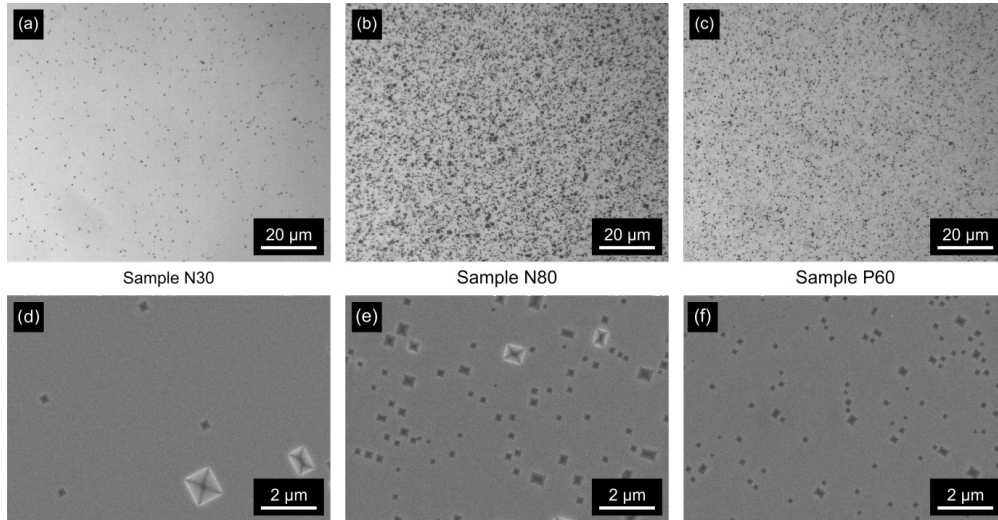


Figure 6.4.: Optical microscopy ((a)-(c)) and scanning electron microscopy ((d)-(f)) images of POLO samples annealed at 1050 °C after etching TMAH. Sample N30, N80 and P60 correspond to the $cd\ n^+$, n^+ and p^+ POLO samples in table 6.1. Reproduced from [158], with the permission of AIP Publishing.

Pinhole-mediated carrier transport [205, 227] is the likeliest model for the carrier transport in a POLO junction with an interfacial silicon oxide thicker than 2 nm. Proving the existence of pinholes, the pinhole model predicts a pinhole density between about 10^5 cm^{-2} and 10^9 cm^{-2} for POLO junctions with good electrical properties [205, 227]. Finding pinholes with such a density using transmission electron microscopy is a demanding task [229, 359]. For this reason, Tetzlaff *et al.* developed a large area magnification method of nanometer-sized pinholes by using highly etch rate selective tetramethylammonium hydroxide (TMAH) etching [353, 360]. On the account of a several orders of magnitude larger silicon etch rate over silicon oxide of the TMAH solution, TMAH etches the poly-Si layer of a POLO junction and stops at the interfacial silicon oxide. In the presence of a pinhole in the interfacial silicon oxide layer, TMAH underetches the silicon oxide and leaves an etch pit in the silicon substrate underneath the pinhole. The etch pit density (EPD) as determined by optical or scanning electron microscopy provides a direct measure of the pinhole density in the interfacial silicon oxide [353, 360].

In order to correlate the pinhole density and the electrical properties of a POLO junction and to examine the validity of the pinhole-mediated transport model, the selective etching method was applied to the TLM test samples from the previous sections³. Figure 6.4 depicts the optical and scanning electron microscopy images of three different samples. Table 6.1 summarizes the resulting EPDs and the electrical properties of two n^+ POLO samples with annealing durations of 30 min and 80 min and a p^+ POLO sample with an annealing duration

³A detailed discussion can be found in reference [158].

6.5. SELECTIVITY OF POLO JUNCTIONS

Table 6.1.: Saturation current density, junction resistivity, etch pit density and selectivity of POLO junctions formed at 1050 °C with a 2.1-nm thin interfacial oxide

Sample	Anneal duration [min]	$J_{C,poly}$ [fA/cm ²]	$\rho_{C,poly}$ [mΩcm ²]	EPD [cm ⁻²]	S_{10}
cd n^+	30	3	9.1	$6.6 \cdot 10^6$	15
n^+	80	7	0.6	$1.1 \cdot 10^8$	15.8
p^+	60	<18	0.4	$1.6 \cdot 10^8$	>15.5

of 60 min. In general, all examined samples show a considerable density of pinholes, while the sample with the lowest thermal budget exhibits the lowest density together with the lowest $J_{C,poly}$ and highest $\rho_{C,poly}$. During a longer junction formation annealing of the n^+ POLO junction, the pinhole density increases and causes a decrease of $\rho_{C,poly}$. The higher $J_{C,poly}$ of 7 fA/cm² for the n^+ POLO sample with 80 min. annealing originates from a higher Auger recombination⁴ of about 3.5 fA/cm² of the stronger and deeper in-diffusion of phosphorous underneath the interfacial oxide, which on the other hand stronger shields minority carriers from recombining at the silicon oxide interface or within a pinhole and weakens the effect of an enlarged pinhole density.

The found pinhole densities were used as input parameters in Wietler *et al.* [158] for the pinhole model proposed by Peibst *et al.* [205, 363] to predict $\rho_{C,poly}$. The modeled and measured $\rho_{C,poly}$ are in excellent agreement [158] and corroborate the conclusion that the major carrier transport mechanism in POLO junctions with a >2 nm thick interfacial silicon oxide is indeed mediated by pinholes. Moreover, Folchert *et al.* studied the temperature dependency of the junction resistivity for one of the cd n^+ POLO sample with 30 min annealing duration and found excellent agreement with pinhole-mediated carrier transport [159].

6.5. Selectivity of POLO junctions

Lastly, the selectivity of the POLO junction should be discussed. As detailed in 4.1.1, the selectivity has been defined in several fashions and implied different techniques for the determination of selectivity.

The definition of selectivity proposed by Brendel and Peibst has the advantage that it uses the established methods for the determination of J_c and ρ_c and thus allows an exact determination of both parameters. Selectivity according to Brendel and Peibst [120] can be then calculated from J_c and ρ_c as determined for POLO contacts in the previous sections. The highest selectivity values S_{10} according to Brendel and Peibst for different samples are given in table 6.1. All POLO junctions achieve values beyond 15, which is sufficiently high for Si solar cells to ensure that the carrier extraction efficiency is almost unity.

⁴The recombination is calculated by using the program EDNA 2 [361, 362] for measured ECV doping profile. The Auger contribution for the cd n^+ POLO sample with 30 min anneal in table 6.1 is about 0.5 fA/cm²

6.6. Chapter summary

In this chapter, n^+ and p^+ POLO junction with an interfacial silicon oxide thickness larger than 2 nm are prepared and their electrical properties are investigated. For n^+ POLO junction after a short (30 min) junction formation anneal, a saturation current density of 2 fA/cm² and simultaneously a junction resistivity of below 10 mΩcm² is determined. For n^+ POLO junction with a long anneal (80 min), a saturation current densities of 7 fA/cm² and simultaneously a junction resistivity of 0.6 mΩcm² is found. For the p^+ POLO junction with a 60 min-anneal, a saturation below 18 fA/cm² and simultaneously a junction resistivity of 0.4 mΩcm² is observed.

The excellent junction properties of POLO junctions were shown to result from a pinhole density in the order of between $5 \cdot 10^6$ cm⁻² and $1 \cdot 10^8$ cm⁻² and the transport is mediated by pinholes as predicted by Peibst *et al.* [205, 363]. The resulting logarithmic selectivity according to Brendel and Peibst [120] of POLO junctions exhibits values larger than 15.

7. Interdigitated back-contact cell with POLO junctions

Parts of the following chapter are based on peer-reviewed papers in reference [155, 157]. The presented POLO-IBC cell builds on existing processes and ideas that have been developed for years at ISFH for different technologies. In particular, A. Merkle has contributed to these processes and cell development. The presented POLO-IBC cell has been developed in the EU-project HERCULES, where A. Merkle, R. Peibst and the author have been working together. U. Römer developed the POLO technology in his PhD thesis at ISFH. The author has developed the inkjet process for the structuring of the POLO-IBC cell and A. Merkle has developed or adapted all essential processes for the fabrication of the POLO-IBC cell. The author established the cell process for the POLO-IBC cell for the first time at ISFH and supervised the fabrication of the first POLO-IBC cells in close collaboration with A. Merkle and R. Peibst. A. Merkle supervised the fabrication of the 24.25% efficient cell and performed most of the measurements. The author analyzed the cell and performed all simulations.

The samples with isolated poly-Si p^+n^+ -junctions were designed, partially fabricated, measured, simulated and analyzed by the author. The fabrication of the POLO-IBC cell with parasitic poly-Si p^+n^+ -junction was supervised and partly performed by the author. The author measured the cells and performed the modelling.

In the following chapter, POLO junctions are integrated on the rear side of an interdigitated back-contact cell. The formed parasitic poly-Si p^+n^+ -junction on the rear side of the cell and its influence on the cell performance is investigated in detail. The parasitic junction is removed and a POLO-IBC cell with isolated p^+ and n^+ poly-Si regions is presented and analysed.

7.1. Fabrication process for POLO-IBC cell

Small ion-implanted and inkjet-patterned interdigitated back contact solar cells with POLO junctions for both polarities (POLO-IBC cells) with an active cell area of $20\text{ mm} \times 20\text{ mm}$ are processed on saw-damage etched $156\text{ mm} \times 156\text{ mm}$ n -type Czochralski silicon wafers with a base resistivity of $3.75\ \Omega\text{cm}$ and a thickness of $160\ \mu\text{m}$. In addition, full-area implanted boron and counterdoped (boron overcompensated by phosphorus) POLO reference regions are integrated on the wafer to facilitate process monitoring.

7.1. FABRICATION PROCESS FOR POLO-IBC CELL

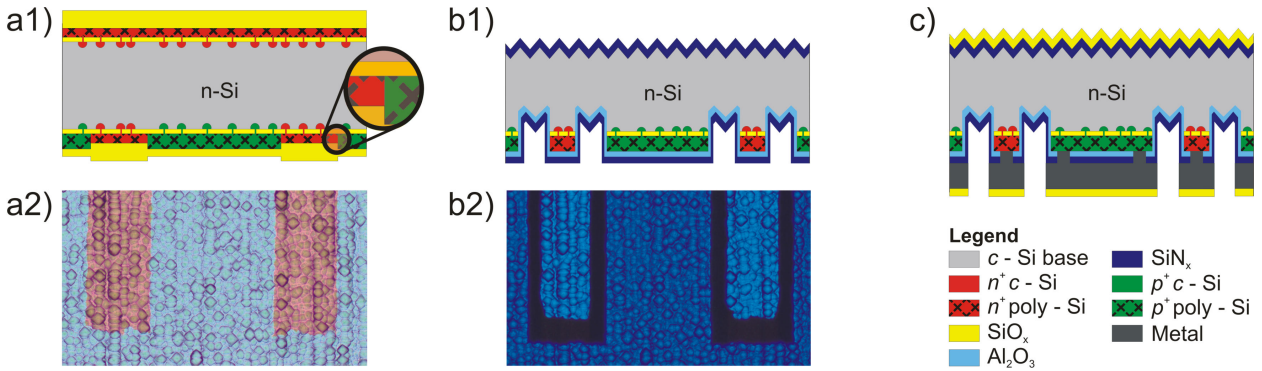


Figure 7.1.: (a1) Cell precursor before and (b1) after texturization yielding a trench between the p^+ and n^+ poly-Si regions. (a2) and (b2) show the corresponding top view micrographs (field of view: $1200\ \mu\text{m} \times 600\ \mu\text{m}$) of the rear side of the cell precursors (a1, b1). (c) Schematic drawing of a final POLO-IBC cell with POLO junctions for both polarities separated by a textured trench.

After growing a 2.1 nm thin thermal silicon dioxide layer on a RCA-cleaned wafer in a tube furnace, undoped amorphous silicon (a-Si) is deposited on both sides by using LPCVD. Hereafter, the front side of the wafer receives a full-area phosphorus implantation, followed by masked phosphorus and full-area boron implantations on the rear side. For the latter the phosphorus locally overcompensates the boron and an interdigitated pattern with different pitches between $603\ \mu\text{m}$ and $1175\ \mu\text{m}$ (Fig. 7.1(a1) and (a2)) is formed. For the masking of the implantations, a sputtered dielectric layer (SiO_x) is patterned by inkjet-printed hotmelt wax (Pixdro LP50 from Meyer Burger) and a subsequent wet-chemical etching in hydrofluoric acid (HF).

After the removal of the dielectric implant mask, a high temperature treatment at $1050\ ^\circ\text{C}$ with a duration of 60 min is performed, in order to form the POLO junctions. During this step, a thick silicon dioxide layer grows on top of the poly-Si during a wet thermal oxidation. The detailed fabrication parameters for the POLO junctions are the same as in subsection 6.1. Figure 7.1 (a1) shows a cross-section of the sample at this precursor stage. At this stage, as presented in Figure 7.1 (a2), the p^+ and n^+ poly-Si at the rear side touch each other and form a parasitic lateral pn junction within the poly-Si.

In the next process step, the thermally grown SiO_2 layer is patterned via inkjet printing a hotmelt wax mask on the rear side and subsequently etching in HF. At the same time, HF removes the SiO_2 from the front side of the wafer. The remaining SiO_2 on the rear acts as an etching barrier for a subsequent texturization process, which yields a textured front side and a separation of n^+ POLO BSF and p^+ POLO emitter regions by a textured trench of a width of $100\ \mu\text{m}$.

After removing the SiO_2 mask, the cell precursors are passivated with a silicon nitride double layer on the front side and an aluminum oxide/silicon nitride layer stack on the rear side. Figures 7.1(b1) and (b2) depict the precursor stage of the cell, where the parasitic pn junction within the poly-Si is removed and the cell is passivated.

In order to create contact openings, the rear side dielectric layers are locally ablated using a

picosecond UV laser (SUPER-RAPID from Lumera). The circular local contact openings with a diameter of 40 μm are arranged in two interrupted lines for the p^+ poly-Si region and a single interrupted line for the n^+ poly-Si region. The obtained contact opening fraction (area of contact openings referred to the respective areas of emitter and BSF) amounts to 2.5% for the emitter and 2% for the BSF region. The contact openings fraction with respect to the total cell area is about 2.4%. After laser contact opening, an additional silicon dioxide layer is sputtered on the front side passivation layer to improve the optics and the cell is anneal at 360 °C on a hot plate to cure the sputter damage.

A 10 μm -thick layer of aluminium is vacuum evaporated on the rear side in an industrial high-throughput tool from Applied Materials. The evaporated aluminium layer grows as a compact and almost smooth layer on the planar regions (n^+ POLO BSF and p^+ POLO emitter). In the textured trench region, the aluminium layer exhibits high roughness due to self-shadowing effect of the oblique evaporation angle with respect to the pyramidal facets [364, 365]. Then the aluminum layer is capped in the same tool with a sputtered 80 nm-thin SiO_x layer. The SiO_x layer covers the smooth surfaces conformally, but cannot do the same for the rough aluminium layer in the trench region. This fact is used in the subsequent etching step in phosphoric acid to selectively remove the Al in the trench region, while preserving the Al in the planar regions. The latter process is referred to as the self-aligned RISE contact separation [366–368].

7.2. Parasitic recombination in lateral polysilicon *pn*-junction

One key challenge for the integration of POLO junctions into IBC cells is the formation of parasitic *pn*-junctions with poor recombination behavior within the highly defective poly-Si [155, 193, 196, 240, 369, 370]. In the following, the current-voltage characteristic of isolated lateral poly-Si *pn*-junctions and its influence on the recombination behavior of POLO-IBC cells with and without parasitic poly-Si *pn*-junctions is studied.

7.2.1. Current-voltage characteristic of lateral poly-Si *pn*-junctions

Samples with isolated lateral poly-Si *pn*-junctions as shown in Figure 7.2a serve as test structures for the four-point measurements of the current density-voltage (J - V) characteristic, using a Karl Süss PA 200 probe station and a Keithley 4200 analyzer.

The sample preparation is briefly as follows. Intrinsic a-Si is deposited on top of a 100 nm thick silicon dioxide, which acts as dielectric isolation layer against the Si substrate. Full-area boron (dose: $2 \times 10^{15} \text{ cm}^{-2}$) implantation and counterdoping with masked phosphorous (dose: $5 \times 10^{15} \text{ cm}^{-2}$) implantation, wet oxidation and junction formation at 1050 °C for 60 min is performed. The thermally grown SiO_2 is removed in HF. A full area deposited aluminum layer forms the electrical contact with the poly-Si. It is patterned by means of inkjet printing an etch barrier and wet chemically etching the aluminum.

¹Details on the estimation of the diffusion profiles and the field strength are found in appendix A.1.1.

7.2. PARASITIC RECOMBINATION IN LATERAL POLYSILICON PN-JUNCTION

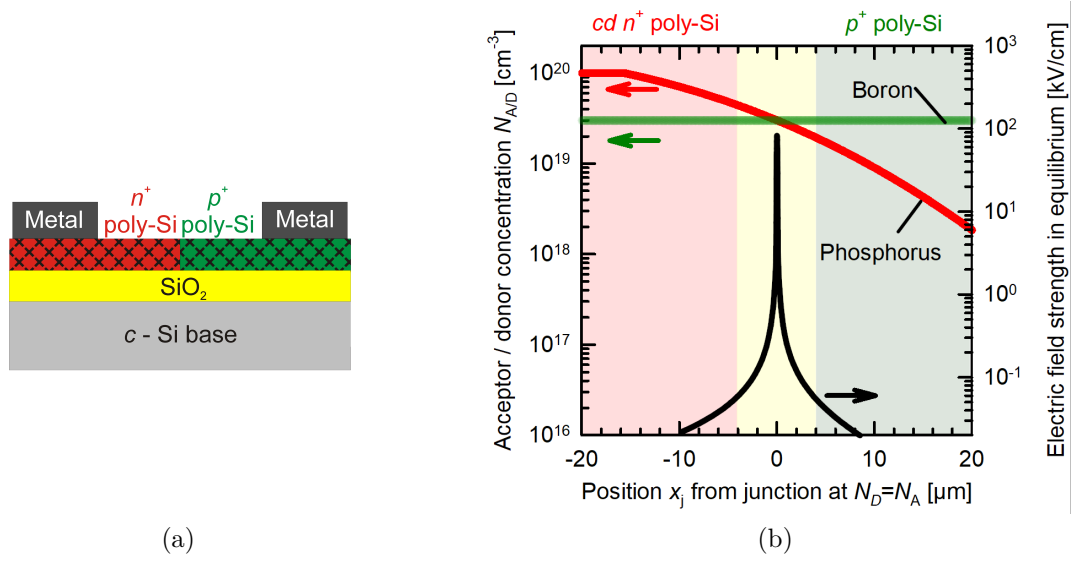


Figure 7.2.: (a) Schematic cross-section of the sample to measure the J - V characteristic of the isolated poly-Si pn -junctions. (b) Estimated lateral boron (green line) and phosphorus (red line) dopant distribution at the poly-Si pn -junction and the resulting electric field strength (black line) in equilibrium¹.

In order to obtain the current density from the measurement of the current-voltage characteristic, it is essential to know the relevant area for the scaling. In the case of the samples with the isolated pn -junctions, the cross-sectional area of the pn -junction is of interest. In the following a pn -junction cross-sectional area of $8.7 \cdot 10^{-6} \text{ cm}^2$ is used as calculated from the product of the length of the pn -junction of 5.8 mm and its height of approximately 150 nm. The height corresponds to the p^+ poly-Si thickness after oxidation. This makes sense because the poly-Si thickness is determined by the oxidation prior to the high temperature annealing at 1050 °C. At this stage, the thickness of the p^+ and n^+ poly-Si amounts to 150 nm and 110 nm, respectively. During the junction formation at 1050 °C, phosphorus diffuses several micrometer from the n^+ region into the boron-doped p^+ region and forms an interdiffused pn -junction within the 150 nm-thick poly-Si layer.

Figure 7.2b illustrates the estimated lateral diffusion profiles of phosphorus and boron at the poly-Si pn -junction, which shape the properties of the junction. The center of the depletion region at $x_j = 0$ lies approximately 16 μm away from the n^+ doped poly-Si region with constant phosphorus concentration and supports the assumption that $x_j = 0$ is within the 150 nm-thick poly-Si layer. The net charge density close to $x_j = 0$ in equilibrium can be approximated by a linear relationship $\rho(x_j) = N_D - N_A = a \cdot x_j$ and the interdiffused lateral pn -junction is denoted as a linearly graded junction with impurity gradient a . The impurity gradient for the diffusion profile in figure 7.2b amounts to $3.1 \cdot 10^{22} \text{ cm}^{-4}$. When analyzing the electrostatics of the linearly graded junction by solving Poisson's equation 2.14 within the depletion approximation [61], one obtains the width of the depletion or space-charge region (SCR) W_0 of about 130 nm and the electric field strength distribution

as shown in figure 7.2b. At this conditions, the maximum field strength in the depletion region at zero-bias of about 0.1 MV/cm is rather small to enable field-enhanced tunneling, but field-enhanced Shockley-Read-Hall (SRH) recombination is already significant [371, 372]. Thus, Shockley-Read-Hall recombination dominates the J - V characteristic of the lateral pn -junction in this thesis and the J - V characteristic obeys equation 7.1.

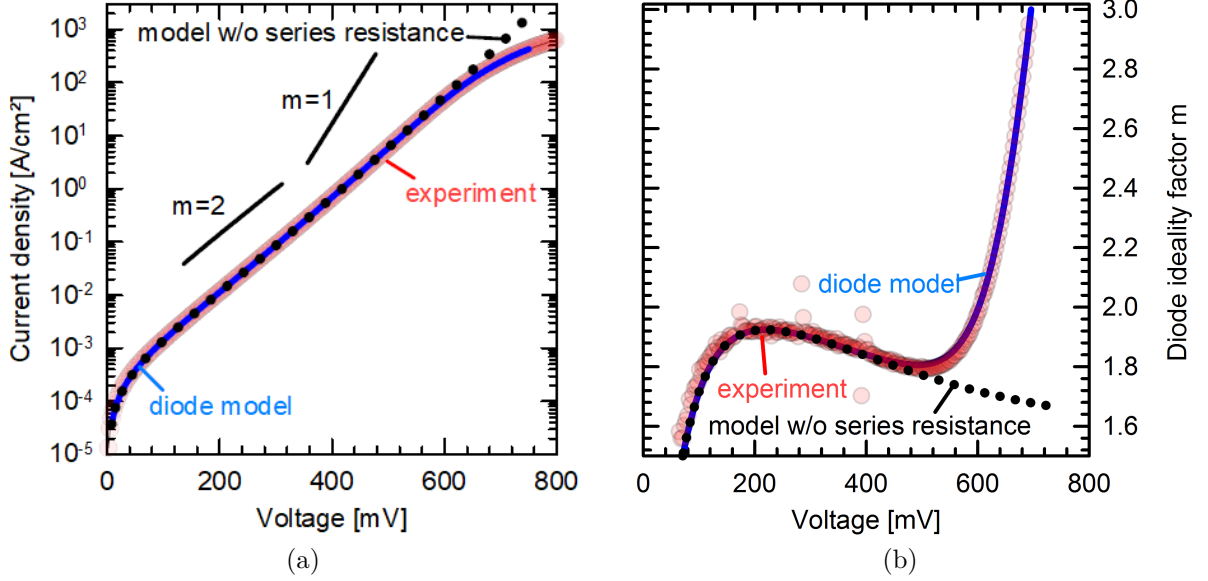


Figure 7.3.: (a) Current-voltage characteristic and (b) diode ideality factor of the isolated lateral poly-Si pn -junction test structure as shown in Figure 7.2a. A two-diode model (blue solid line) with variable ideality factors and a series resistance fits the experimental data (red circles). The diode characteristic without series resistance (black dotted line) is derived from the diode model with series resistance by setting it to zero.

Figure 7.3a illustrates the measured J - V characteristic of the lateral poly-Si pn -junction, which exhibits an exponential voltage-dependency with a local ideality factor m close to 2 and saturates at high voltages due to series resistance. A high ideality factor is consistent with defect-mediated space charge region recombination [85, 86, 88–90, 371–373], which in its simplest form can be approximated at forward bias condition with $V \gg \frac{k_B T}{q}$ as follows².

$$J_{\text{SCR}} = \frac{qn_i W_0}{2\tau_r} \cdot \exp\left(\frac{qV}{2k_B T}\right) \quad (7.1)$$

n_i , W_0 and τ_r are the intrinsic carrier concentration, the width of the SCR at $V = 0$ and the charge carrier lifetime within the SCR. Equation 7.1 corresponds to a single diode model

²Note that this approximation is not accurate, because it assumes a voltage-independent SCR width, which assures a constant pre-exponential factor and ideality factor. However, this model is frequently used in textbooks due to its simple form.

7.2. PARASITIC RECOMBINATION IN LATERAL POLYSILICON PN-JUNCTION

without series resistance, where the pre-exponential factor is the saturation current density. The simple single diode model allows only a rough analysis of the experimental data in a narrow range of moderate voltages. As shown in figure 7.3b, the reason for that is obviously the ideality factor-voltage (m - V) characteristic of the diode, which is injection-dependent rather than constant and smaller than two. The ideality factor rises from $m < 1$ at low voltages ($V < \frac{k_B T}{q}$) to a maximum of 1.93 at a voltage between 200 mV and 300 mV. Then it decreases again until above 500 mV series resistance starts to play a significant role and causes the ideality factors to rise steeply. The m - V characteristic is consistent with more sophisticated models [86–89, 374] and numerical solution [85, 90].

For the sake of simplicity³, a single diode model following equation 7.1 is used to fit the J - V data in Figure 7.3a in the voltage range between 200 mV and 500 mV and to roughly estimate the order of magnitude of the charge carrier recombination lifetime τ_r within the poly-Si pn -junction. The diode fit yields a pre-exponential factor of 2.56×10^{-4} A/cm² and predicts a charge carrier lifetime τ_r of about 40 ps for $W_0 = 130$ nm and $n_i = 1 \cdot 10^{10}$ cm⁻³. The lifetime is in good agreement with reported values by Dutoit and Sollberger [375], by Peibst *et al.* [376] and by Hollemann *et al.* [377], and induces a strong recombination within the parasitic lateral pn -junction.

To investigate the influence of the recombination within the parasitic poly-Si junction on the overall performance of the POLO-IBC cell by means of equivalent circuit modelling in the following subsection, a two-diode equivalent circuit model with an additional series resistance (red part of the circuit in figure 7.4) is used to obtain an equivalent circuit model representation of the parasitic junction. The diode model incorporates the correct voltage-dependence of the ideality factor by using the series resistance $R_{S,para}$, the individual ideality factors $m_{P,1}$ and $m_{P,2}$ of the two diodes and the corresponding saturation current densities $J_{P,01}$ and $J_{P,02}$ as free parameters to fit the J - V and m - V characteristics. The blue solid lines in figure 7.3 depict the J - V and m - V characteristic of the two-diode model calculation with $J_{P,01} = 2 \cdot 10^{-5}$ A/cm², $J_{P,02} = 2.23 \cdot 10^{-4}$ A/cm², $m_{P,1} = 1.607$, $m_{P,2} = 2.089$ and $R_{S,para} = 1.42 \cdot 10^{-4}$ Ω cm². The modelled data in blue coincides with the experimental data in red and the deviation of the current densities (ideality factors) at each voltage point above 100 mV is below 1.5% (1%).

While the combination of the two diodes represent the recombination of the parasitic junction, the series resistance originates most likely from lateral transport in the poly-Si layer between the metal pad and the pn -junction⁴ and therefore is specific for the test structure rather than the parasitic pn -junction. The resistance-corrected two-diode model is illustrated as black dotted line in figure 7.3.

³In appendix A.1.2 a more sophisticated device simulator is used to confirm the simplified procedure.

⁴The absolute value of the series resistance of $1.42 \cdot 10^{-4}$ Ω cm² results from scaling the current to the area of the pn -junction. Before scaling, the resistance amounts to 16 Ω , which is about the same as the estimated resistance for the lateral transport.

7.2.2. Recombination behavior of POLO-IBC cells with and without parasitic poly-Si pn -junctions

In the following, the J - V and m - V characteristics of a POLO-IBC cell with a parasitic poly-Si pn -junction (pn cell) is compared with a POLO-IBC cell, where p^+ and n^+ poly-Si regions were separated by means of a wet-chemical removal of the parasitic pn -junction (trench cell). Both cell fabrication processes follow subsection 7.1, but for the former the patterning of the thermally grown SiO_2 for the trench separation is omitted in order to keep the parasitic junction. Furthermore, inkjet printing and wet-chemical etching is used for the contact opening and the metal contact separation of the cell with parasitic junction instead of laser contact opening and RISE contact separation as for the trench cell. Nevertheless, both cell types are similar except for the parasitic junction and the appearing differences in J - V and m - V characteristics mainly reflect the influence of the latter. The $J_{\text{SC}}-V_{\text{OC}}$ characteristic and the J - V characteristic in dark conditions and under AM1.5G illumination are measured with the solar cell analysis system LOANA from pv-tools GmbH.

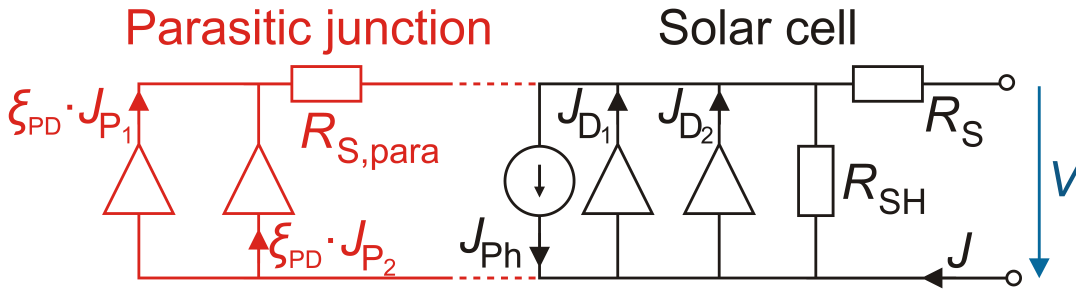


Figure 7.4.: Equivalent circuit model of a solar cell with a parasitic junction. A two-diode model with diodes D_1 and D_2 , a series resistance R_S , a shunt resistance R_{SH} and a photo-generating current source (J_{Ph}) represents the solar cell without the parasitic junction (black circuit model). The isolated parasitic junction consists of two parallel diodes P_1 and P_2 with a resistance $R_{S,para}$ in series (red circuit). The model for a solar cell with parasitic junction is found by parallel interconnection of the model without parasitic junction with the isolated parasitic junction. This is indicated by red dotted lines between both sub-circuits.

Figure 7.4 shows an equivalent circuit model of such a solar cell with a parasitic poly-Si pn -junction. The parasitic pn -junction, represented by a two-diode model with a series resistance (red circuit in figure 7.4), adds to a two-diode model of the solar cell without parasitic junction (black circuit in figure 7.4) in a parallel connection [240]. As evident from the model, the parasitic junction increases the dark current of the solar cell, modifies the ideality factor and diminishes the cell performance.

Figure 7.5 compares the dark J - V characteristic and the m - V characteristic of the $J_{\text{SC}}-V_{\text{OC}}$

7.2. PARASITIC RECOMBINATION IN LATERAL POLYSILICON PN-JUNCTION

measurement⁵ of the cell with and without parasitic junction. As expected, the dark current density of the cell with parasitic junction is by more than one order of magnitude higher than for the trench cell. The local ideality factor of the cell with a parasitic junction at low voltages is larger than 2 due to a rather low shunt resistance of $40 \text{ k}\Omega\text{cm}^2$ and drops to about 1.75 at 450 mV, where it matches the local ideality factor of the trench cell. Above that voltage, the ideality of the trench cell decreases steadily until it reaches 1 at 720 mV. The ideality of the cell with parasitic junction remains around 1.7 and then increases again for voltages above 550 mV. This trend of the m - V characteristic of the cell with parasitic junction above 400 mV resembles the m - V characteristic as already observed for the isolated parasitic junction with a finite $R_{S,\text{para}}$ (Fig. 7.3b).

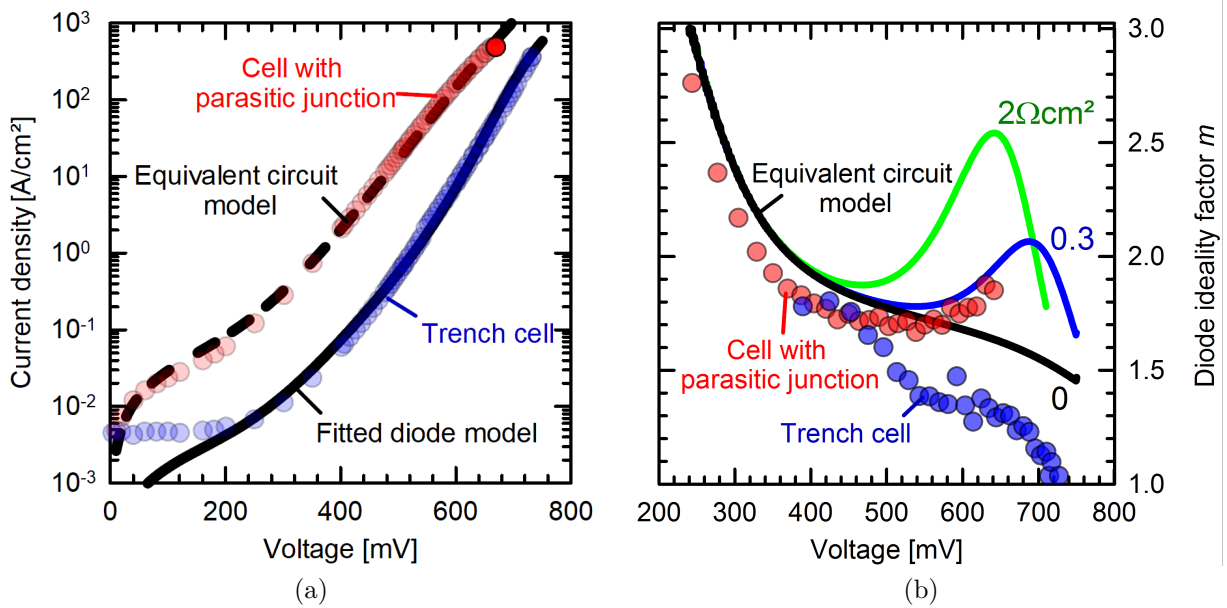


Figure 7.5.: (a) Dark current-voltage characteristic of the cell with and without parasitic junction. (b) Local ideality factor of the cells in (a) calculated from the $J_{\text{SC}}-V_{\text{OC}}$ characteristic, which is free of series resistance effects in contrast to the dark J - V in (a). A two-diode model (blue solid line) with variable ideality factors and a series resistance fits the experimental data (red circles). The calculated m - V characteristic of the cell with parasitic junction (solid lines in (b)) is derived from the same diode model as in (a), but with $R_S = 0$ and $R_{S,\text{para}} = 0 \Omega\text{cm}^2$, $0.3 \Omega\text{cm}^2$ and $2 \Omega\text{cm}^2$.

Beside the qualitative discussion of the cell's characteristic, the equivalent circuit model in figure 7.4 is suited to predict the J - V and m - V characteristic of the cell with a parasitic junction, when the characteristic of the trench cell and that of the isolated parasitic junction

⁵ $J_{\text{SC}}-V_{\text{OC}}$ characteristic blinds out the series resistance effects of the cell as compared to the dark J - V . Therefore, m - V characteristic reflects the recombination behaviour of the cell – even at large voltages, where otherwise the series resistance dominates.

are known. The model parameters of the isolated parasitic junction were determined in the previous subsection and the model parameter of the trench cell are calculated by fitting a two-diode model to the dark J - V of the trench cell as shown in figure 7.5a. The the fit yields the following model parameters: $J_{D,01}=28 \text{ fA/cm}^2$ with $m_{D1} = 1$, $J_{D,02}=2.8 \text{ nA/cm}^2$ with $m_{D2} = 2$, $R_S=0.4 \text{ }\Omega\text{cm}^2$ and $R_{SH}=700 \text{ k}\Omega\text{cm}^2$. As the series resistance and shunt resistance differ for the trench cell and the cell with parasitic junction, the values as found for the cell with parasitic junction of $R_S =0.6 \text{ }\Omega\text{cm}^2$ and $R_{SH}=40 \text{ k}\Omega\text{cm}^2$ are used for the equivalent circuit model calculation.

The contributions of the black and red sub-circuits to the superposed model in figure 7.4 is obtained by weighting the parameters of each sub-circuit with their area fractions. The area fraction of the trench cell remains 1, because it is assumed that both cells exhibit the same characteristic if the parasitic junction is removed. The areal fraction ξ_{PD} of the parasitic junction with respect to the cell area A_{cell} is obtained as

$$\xi_{PD} = \frac{A_{PD}}{A_{\text{cell}}} = \frac{L_{PD} \cdot d_{PD}}{A_{\text{cell}}}, \quad (7.2)$$

where the area of the parasitic junction A_{PD} is deduced from the length L_{PD} and the height d_{PD} of the junction. The pn meander length density $\frac{L_{PD}}{A_{\text{cell}}}$ of the parasitic pn -junction of the cell from figure 7.5a is calculated to $20.4 \text{ cm}_{pn}/\text{cm}^2_{\text{cell}}$ from the geometry of the applied mask for ion implantation. As discussed above for the isolated pn -junction, the height of the junction d_{PD} corresponds to the thickness of the p^+ poly-Si layer of 150 nm. Therefore, the areal fraction for the parasitic junction amounts to $3.06 \cdot 10^{-4}$ and the diode parameter for the parasitic junction become $\xi_{PD} \cdot J_{P,01}=6.12 \text{ nA/cm}^2$ with $m_{P,1} = 1.607$ and $\xi_{PD} \cdot J_{P,02}=68.3 \text{ nA/cm}^2$ with $m_{P,2} = 2.089$. The series resistance $R_{S,para}$ is adjusted to the experimental data. The calculated and experimental m - V characteristic in figure 7.5b gives only a good agreement, if $R_{S,para} \approx 0.2\text{-}0.3 \text{ }\Omega\text{cm}^2$ (blue solid line). For other values of $R_{S,para}$ (black and green solid line), calculated and experimental m - V characteristic deviate significantly at high voltages. A resistance value of about $0.2 \text{ }\Omega\text{cm}^2$ coincides with a conservative estimate of the sum of resistances for lateral electron and hole transport⁶ to the parasitic pn -junction of $0.089 \text{ }\Omega\text{cm}^2$ and $0.095 \text{ }\Omega\text{cm}^2$, respectively. Therefore, it can be concluded that $R_{S,para}$ originates from lateral transport.

Finally, the dark J - V characteristic of a cell with parasitic junction is calculated by using the equivalent circuit model with the given model parameter from above. Figure 7.5a reveals a remarkably good agreement of the calculated J - V characteristic and the experimentally determined dark J - V characteristic for a cell with a parasitic junction. The relative deviation of the current densities at each voltage point is below 20%. The fact that the addition of a parasitic junction to a trench cell replicates the cell with a parasitic junction, indicates that any difference in performance between both cells originates from the parasitic junction. Table 7.1 summarizes the modeled and measured performance metrics for both cell types. The modeled performance metrics for the trench cell only moderately reproduce the experimental ones, which is associated with the moderately well fitted diode model due to a non-ideal recombination behavior of the trench cell (see figure 7.5a). The source of this non-ideality

⁶The resistances were calculated according to Wyeth [378].

7.3. PERFORMANCE OF POLO-IBC CELL

is discussed in section 7.3. The model 2 for the cell with parasitic junction, on the other hand, achieves a better agreement with the experimental data, especially with FF and pFF. A less optimal anti-reflection coating of the cell with parasitic junction leads to a lower J_{SC} as compared with the trench cell.

A comparison of model 1 and model 3 with the same J_{SC} indicates that adding a parasitic junction with an area fraction of $3 \cdot 10^{-4} \text{ cm}^2_{pn}/\text{cm}^2_{cell}$ to a trench cell leads to a performance loss of about 70 mV in V_{OC} , 10%_{abs} in FF and 5%_{abs} in efficiency. However, the performance improves significantly upon a reduction of the area fraction by a factor of ten in model 4 and a cell with an efficiency of about 23% is predicted. Such a reduction of the area fraction can either be implemented by reducing the poly-Si layer thickness or by using an interrupted trench as has been patented by SunPower Corp. [192, 193]. If the area fraction of the parasitic junction is optimized such that the parasitic effect of the junction on the forward characteristic is minimized, then the implementation of the parasitic junction can even be beneficial. The reverse breakdown characteristic of the junction equips the cell with an integrated bypass diode [379]. The poly-Si *pn*-junction discussed in subsection 7.2.1 exhibits a breakdown voltage of about 5.5 V (see appendix A.1.3).

Table 7.1.: Performance metrics of modeled and measured cells with and without parasitic junction. Model 1 is the black two-diode model from figure 7.4. Model 2, 3 and 4 represent the superposed model (red and black circuit) from figure 7.4 with different input parameters.

		J_{SC} [mA/cm ²]	V_{OC} [mV]	FF [%]	pFF [%]	η [%]
trench	exper. ^a	41.57 ± 0.79	727.1 ± 2.5	80.23 ± 0.52	-	24.25 ± 0.49
	model 1	41.57	718	82.9	84.3	24.5
parasitic junction	exper. ^b	39.44	634	72.8	75.6	18.2
	model 2 ^c	39.44	648	72.0	75.1	18.4
	model 3 ^d	41.57	650	73.0	75.2	19.7
	model 4 ^e	41.57	706	78.6	80.1	23.1

^a Certified measurement at Fraunhofer ISE CalLab.

^b In-house measurement with LOANA cell tester.

^c J_{SC} , R_S and R_{SH} of cell with parasitic junction assumed.

^d J_{SC} , R_S and R_{SH} of trench cell assumed.

^e Parameters as for model 3, but with a ten times smaller area fraction $\xi_{PD} = 3 \cdot 10^{-5}$ of parasitic junction.

7.3. Performance of POLO-IBC cell

In order to access the full potential of a POLO-IBC cell, a complete removal of the parasitic poly-Si *pn*-junction is performed. Figure 7.6 shows the certified current (power) density-voltage characteristic J - V (P - V), the quantum efficiency and reflectance data of an ion-implanted, photolithography-free POLO-IBC cell with trench separation⁷. For the AM 1.5G reference spectrum, the POLO-IBC cell generates a maximum power density of 24.25 mW/cm² with a

⁷Cell results for this cell architecture were for the first time presented at the 6th International Conference on Silicon Photovoltaics, Chambéry, France in 2016 [155].

short-circuit current density J_{SC} of 41.57 mA/cm², an open-circuit voltage V_{OC} of 727.1 mV and a fill factor FF of 80.23%.

In the following, the optical and recombination properties of the POLO-IBC cell are discussed and input parameters for a device simulation are determined. The device simulation of the cell forms the basis to examine the influence of recombination and junction resistance of the POLO junction on the cell performance.

7.3.1. Optics

The measured J_{SC} is consistent with the predicted photo-generated current density of 41.57 mA/cm² from an area-weighted average of the Sunrays simulation for the boron-doped, phosphorus-doped and trench cell regions. Figure 7.6a depicts the averaged reflectance from the simulation, which provides a good framework to discuss optical losses. The deviation between simulation and experiment at short and long wavelengths arises most likely from the uncertainty in the input parameters for the used materials.

The double layer anti-reflection coating on the front side of the cell provides a low reflectance of the cell between 300 nm and 1000 nm (figure 7.6a) and the current loss due to front side reflection amounts to 0.42 mA/cm² from the simulation. In addition to that, the 12 nm-thick SiN_y passivation layer absorbs 0.24 mA/cm² of the incoming light. At wavelengths above 1000 nm, the properties of the optics of the rear side of the cell show up. Parasitic absorption within the poly-Si and aluminum cause a loss of about 0.96 mA/cm² and 0.43 mA/cm², respectively. The loss due to transmission in the trench region amounts to 0.63 mA/cm².

The largest loss of 2.06 mA/cm² originates from the escape reflectance due to a finite absorption path length of a non-perfect light trapping scheme. A comparison of a raytracing simulations of the cell with a perfect planar versus textured rear side – as the reference for an improved trapping scheme – reveals that about 0.8 mA/cm² are lost due to the planar rear side of the cell.

It can be speculated that the optical properties of the POLO-IBC cell from figure 7.6a are similar to the 25% efficient cell of SunPower Corp. with a thickness of 145 μm [380], which exhibits a J_{SC} of 41.53 mA/cm². In contrast to that, Kaneka Corp. has reported a short-circuit current density of 42.3 mA/cm² for a 165 μm-thick cell with an efficiency of 26.3%. The J_{SC} of the latter is the same as for the simulated POLO-IBC cell with a perfect planar rear side (table A.2) and it can be speculated that Kaneka’s cell implements a textured rear side to enhance the absorption path length. Thus, enhancing the absorption path length with a textured rear side for the POLO-IBC cell, halving the thickness of the poly-Si layers and of the passivating front SiN_y layer, and optimizing the dielectric layer thickness on the rear side would boost the J_{SC} by more than 1 mA/cm². Alternatively, a thicker c-Si wafer can be used, which allows approximately the same J_{SC} improvement [156, 381].

After correcting the external quantum efficiency with the measured reflectance and the simulated parasitic absorption in the anti-reflection coating [382], the internal quantum efficiency reflects the carrier collection efficiency of the cell. The POLO-IBC cell collects the photo-generated carriers with a collection efficiency of almost unity over the entire wavelength

⁸Details can be found in appendix A.2.1.

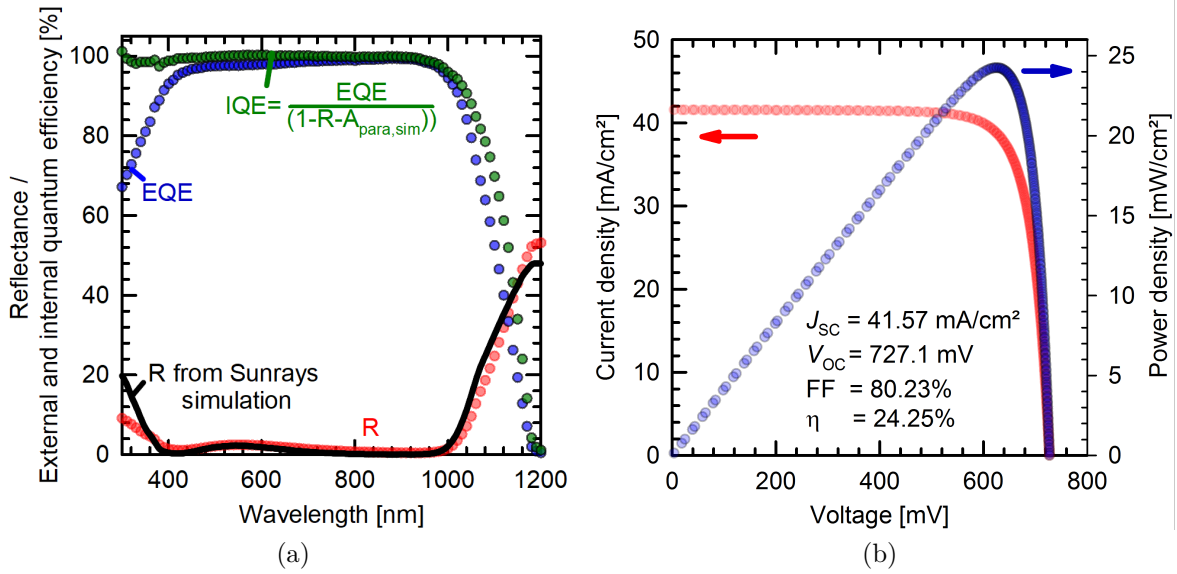


Figure 7.6.: (a) Reflectance R , external quantum efficiency EQE and internal quantum efficiency IQE and (b) certified current-voltage and power-voltage measurements of a 24.25% efficient POLO-IBC cell. The internal quantum efficiency is obtained by dividing the EQE by $1 - R - A_{para,sim}$, where $A_{para,sim}$ is the parasitic absorption in the anti-reflection coating⁸.

range and highlights the high quality of the cell.

7.3.2. Recombination

A low recombination rate in the bulk and at the surfaces of the cell provides the high V_{OC} of the POLO-IBC cell. On symmetric reference samples with a resistivity of $3.75 \Omega\text{cm}$, a saturation current density J_{0,n^+} of 3 fA/cm^2 and J_{0,p^+} of 4 fA/cm^2 for the n^+ and p^+ POLO contacts, $J_{0,front}$ of 15 fA/cm^2 for the front side passivation and $J_{0,rear}$ of 6 fA/cm^2 for the trench passivation on the rear side is found. The SRH bulk lifetime⁹ of the boron-doped p^+ (counterdoped n^+) POLO reference sample amounts to 2 ms (10 ms) and of the phosphorous-doped n^+ POLO sample to more than 100 ms. This strong improvement of the SRH bulk lifetime for samples with phosphorous-containing POLO junctions is consistent with an impurity gettering effect during the junction formation annealing as reported by Krügener *et al.* [266]. Since the precursor of the cell contains each of the differently doped poly-Si layers during the gettering process, it is impossible to predict the correct SRH bulk lifetime from the reference samples for the final cell.

At cell level, the J_{SC} - V_{OC} characteristic of the cell contains information about the recombination behavior of the cell and can be used to calculate the effective minority carrier lifetime

⁹The intrinsic lifetime, which takes only radiative and Auger-recombination into account, amounts to 120 ms.

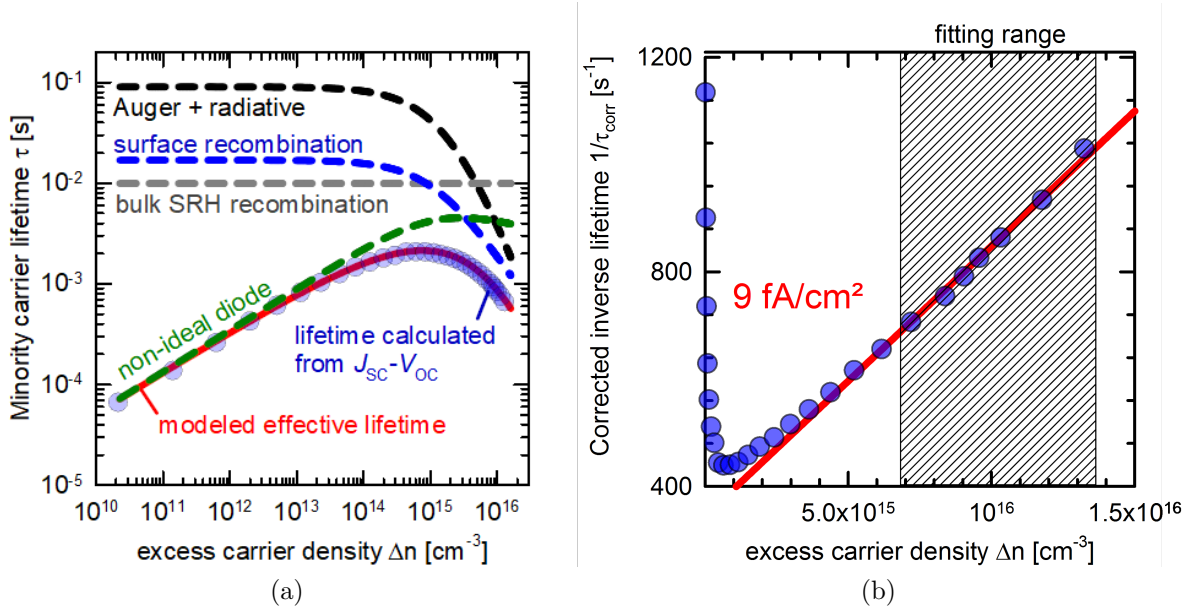


Figure 7.7.: (a) Measured and modeled effective minority carrier lifetime and (b) corrected inverse lifetime calculated from $J_{SC}-V_{OC}$ characteristic of a 24.25% efficient POLO-IBC cell.

vs. excess carrier density curve [102, 383] under the assumption of homogeneous carrier distribution and steady-state conditions [384, eq. 7 and 9 under steady-state conditions]. The $J_{SC}-V_{OC}$ characteristic was measured using the solar cell analysis tool LOANA from pytools with an infrared light emitting diode (LED) array with an emission wavelength of 850 nm. The expected photogeneration is as homogeneous as for a photo-conductance decay measurement with an infrared filter (cutoff at 750 nm).

Figure 7.7a (blue circles) shows the effective minority carrier lifetime of the POLO-IBC cell, which first increases with decreasing excess carrier density and then decreases again. By fitting a modeled effective lifetime curve (red solid line) to the experimental data, the effective lifetime can be decomposed in Auger- and radiative recombination (black dashed line), surface recombination (blue dashed line) and constant SRH bulk recombination (grey dashed line). The SRH bulk lifetime τ_{bulk} and the total surface saturation current density $J_{0S,total}$ are then obtained from the model. It is evident from figure 7.7a, that the model can only match the experimental lifetime curve if a parallel non-ideal diode recombination path with ideality larger than unity is added (green dashed line). Thus, the model for the effective carrier lifetime contains four free parameters: the SRH bulk lifetime τ_{bulk} , the total surface recombination current density $J_{0S,total}$ and the ideality factor m_{rec} and saturation current density $J_{0,rec}$ of the non-ideal diode recombination.

In order to minimize the number of adjustable parameters for the modeled effective lifetime, the total surface recombination current density $J_{0S,total}$ is determined to 9 fA/cm² in figure 7.7b according to Kane and Swanson [101] from the experimental lifetime data in figure 7.7a, which is obtained from $J_{SC}-V_{OC}$ measurements. However, the total area-weighted surface

recombination current density calculated from the PCD measurement of the reference samples amounts to 19 fA/cm². This difference is most likely due to the fact that the front surface reference with 15 fA/cm² does not reflect the situation in the final cell. If the total surface recombination current density of 9 fA/cm² as determined from figure 7.7b is correct and the area-weighted saturation current densities from the reference samples of the rear side of the cell are subtracted from the former, then it can be speculated that the front surface recombination current density $J_{0,front}$ is restricted to values below 5 fA/cm², which is a typical value for SiN_y double layer passivations measured on similar wafer material in other batches. If the model parameters of the lifetime model are adjusted to $\tau_{bulk}=10$ ms, $J_{OS,total}=9$ fA/cm², $m_{rec}=1.7$ and $J_{0,rec}=0.4$ nA/cm², the modeled effective lifetime in figure 7.7b matches the experimental lifetime within $\pm 5\%$ at each data point. At an implied maximum power point voltage of 636 mV, which corresponds to an excess carrier density of about 1.5×10^{15} cm⁻³, the recombination consists of 7% Auger and radiative recombination, 20% SRH bulk recombination, 27% surface recombination and 46% non-ideal diode recombination. The strong non-ideal recombination along with the series resistance limit the fill factor to 80.23% for the POLO-IBC cell.

7.4. Device simulation of a POLO-IBC cell

In order to break down the loss channels of the POLO-IBC cell and to use an appropriate baseline device model for the subsequent series resistance analysis, the Quokka2-implementation [385, 386] of the Conductive Boundary model [387] and the following input parameters from the previous subsection or reference samples are used: $J_{0,p^+}=4$ fA/cm², $J_{0,n^+}=3$ fA/cm², $J_{0,front}=5$ fA/cm², $J_{0,trench}=6$ fA/cm², $\tau_{bulk}=10$ ms, specific wafer resistance $\rho_{bulk}=3.75$ Ωcm, sheet resistance $R_{sheet,n^+}=118$ Ω/□ and $R_{sheet,p^+}=239$ Ω/□ of the 188 μm-wide n^+ and 552 μm-wide p^+ poly-Si layer, a unit cell width (pitch) of 952 μm perpendicular to the finger and a trench width of 106 μm. The geometry of the respective contact openings was described in subsection 6.1. The non-contacted and contacted poly-Si regions exhibit the same passivation properties. The generation profile is derived from an analytic model [388] fitted to the measured reflection in figure 7.6a. Since the parasitic absorption at the front side of the cell is neglected during the fitting procedure, it is expected that the photogeneration is slightly overestimated. The external circuit of the simulation adds a shunt resistance R_{SH} of 10 MΩcm² and an external recombination diode with an ideality factor m_{rec} of 1.7 and a saturation current density $J_{0,rec}=0.4$ nA/cm².

7.4.1. Recombination behavior

Figure 7.8a depicts the measured $J_{SC}-V_{OC}$ characteristics and the characteristic of the simulated cell with (red solid line) and without (green solid line) the external recombination diode. The simulated cell with external diode matches the measured characteristic within a maximum deviation of 12% at each data point and underlines the necessity of the recombination path with higher ideality to fit the measurement.

Since the LOANA system measures the J_{SC} with a flash lamp rather under a AM1.5G

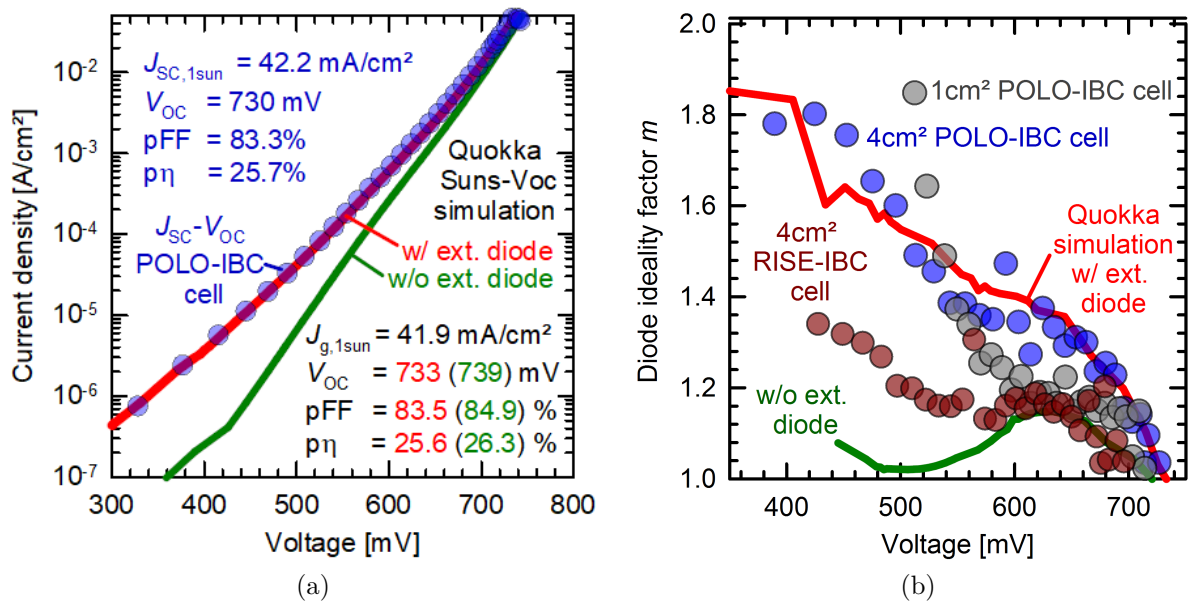


Figure 7.8.: (a) Current-voltage characteristic and (b) local ideality factor of a Quokka simulated cell with (red solid line) and without an external diode (green solid line) and of the analysed 24.25% efficient POLO-IBC cell (blue circles). For comparison, (b) shows the m - V characteristic of a 4 cm² RISE-IBC cell with an efficiency 23.7% (red circles) and of a 1 cm² POLO-IBC bottom cell with a floating n^+ POLO front contact (grey circles) as discussed in section 8.

spectrum, the J_{SC} is determined from a reference cell, which has to be calibrated to a similar cell as the measured one. In the case of the measurement in figure 7.8a, no calibrated measurement of a POLO-IBC cell was available and the reference cell was calibrated to the RISE-IBC cell published in reference [389], which has distinctly different properties compared to the POLO-IBC cell. Therefore, the J_{SC} of the POLO-IBC cell is strongly overestimated. The correct J_{SC} of the cell of 41.57 mA/cm^2 is by about 0.3 mA/cm^2 lower than the simulated one, which results from the overestimation of the photogeneration profile in the simulation by neglecting the parasitic front side absorption of approximately 0.3 mA/cm^2 . The simulated V_{OC} of 733 mV , the pseudo fill factor pFF of 83.5% and the pseudo efficiency $p\eta$ of 25.6% are in accordance with the measured V_{OC} of 730 mV , pFF of 83.3% and $p\eta$ of 25.7% . The ideality factor of the simulated (red solid line) cell follows that of the measured cell (blue circles) in figure 7.8b. This reflects the good agreement of J_{SC} - V_{OC} characteristics and validates the model.

If the external recombination diode is turned off, then the simulated J_{SC} - V_{OC} characteristic deviates significantly from the experimental one, the ideality factor (green solid line in figure 7.8a) decreases from 1.3 to 1.1 at maximum power point voltage V_{mpp} and the simulation predicts a gain in V_{OC} and pFF of 6 mV and $1.4\%_{\text{abs}}$, respectively. The corresponding $p\eta$ of 26.3% can be considered as a projection for a POLO-IBC cell, where the recombination with higher ideality can be suppressed.

The origin of the non-ideal recombination of the external diode is hard to pinpoint because several sources can be responsible for it. The small cell size of 4 cm^2 and the cleaved edge can act as a resistance-limited recombination mechanism and induce the poor recombination behavior [90, 390, 391]. A 4 cm^2 RISE-IBC cell without poly-Si junctions [389] (red circles) and a 1 cm^2 POLO-IBC cell with a n^+ POLO front surface field (grey circles) should show similar non-ideal recombination behavior as the 4 cm^2 POLO-IBC cell, if edge recombination is important. However, the idealities of the 4 cm^2 RISE-IBC and 1 cm^2 POLO-IBC cell follow that of the simulated cell without the external diode. This suggests that edge recombination is not the dominating recombination mechanism at voltages around 600 mV and above. In the case of the 4 cm^2 POLO-IBC cell, an incompletely removed parasitic poly-Si pn -junction could also be the origin of the different behavior. With a significant areal fraction, e.g. several percent of the initial areal density, the parasitic junction would increase the ideality factor and reduce the performance. Indeed, the reverse dark J - V characteristic of a cell processed on the same wafer indicates a breakdown around 5.5 V , but the current density is limited by a high resistance. From the reverse characteristic, an areal density of up to 5×10^{-6} or 2% of the initial areal density of the parasitic junction can be estimated, which is sufficient to significantly reduce the pFF. Lastly, the surface passivation at the front side, which is in high level injection around 600 mV , can provide a pathway for the non-ideal recombination behavior. Since the SiO_2 for the anti-reflection coating was sputtered onto the front surface passivation and the observed detrimental damage of the passivation was cured during an annealing at 360°C , the front surface passivation is a good candidate for the non-ideal recombination behavior. Indeed, a degradation of the pFF and subsequent regeneration upon moderate annealing of the final cell was observed and can be an indication for the degradation and re-passivation of such a surface.

Finally, it is concluded that the external diode recombination originates from a non-optimized cell process, which is hard to pinpoint. An improved ideality for the 1 cm² POLO-IBC cell, which is close to the ideality of the simulated cell without external diode recombination, is demonstrated in figure 7.8b. This cell has an n^+ POLO passivating contact on the front side instead of a dielectric passivation layer stack and the trench width is slightly increase to ensure a complete removal of the parasitic junction.

7.4.2. Series resistance

The total series resistance of the cell R_S is composed of contributions from the transport within the metal grid $R_{S,met.}$, from the lateral current flow within the poly-Si layers $R_{S,poly}$, the current flow within the base $R_{S,base}$, from the POLO junction $R_{S,poly/c-Si}$ at the poly-Si/c-Si interface and the Al/poly-Si contact $R_{S, Al/poly-Si}$. The series resistance is analytically described as the sum of these contributions.

Since the POLO junction resistivity cannot be taken into account directly in Quokka 2¹⁰, the POLO junctions are represented by their recombination current densities at an imaginary poly-Si/c-Si interface and by a combined contact resistivity ρ_c within the contacted area. The combined junction resistivity is defined as the area weighted superposition of the contact resistivity at the Al/poly-Si interface and the junction resistivity at the poly-Si/c-Si interface, which is attributed to the Al/poly-Si interface.

$$\rho_c = \rho_{c,Al/poly-Si} + \frac{A_{Al/poly-Si}}{A_{poly-Si/c-Si}} \cdot \rho_{c,poly-Si/c-Si} \quad (7.3)$$

ρ_c represents the combined junction resistivity, $\rho_{c, Al/poly-Si}$ the contact resistivity of the Al/poly-Si contact, $\rho_{c, poly-Si/c-Si}$ the junction resistivity of the poly-Si/c-Si junction and $A_{Al/poly-Si}$ and $A_{poly-Si/c-Si}$ the respective contact areas of both junctions.

For the definition of the combined junction resistivity, an infinite conductivity of the poly-Si layer is assumed, so that the area $A_{poly-Si/c-Si}$ is independent of any transfer length and no current crowding effects occur beneath the Al/poly-Si contact. This assumption can be relaxed by introducing a transfer area $A_{T,poly-Si/c-Si}$ into 7.3, similar to the transfer length of TLM measurements. Equation 7.3 is therefore a lower limit for the combined junction resistivity. In contrast to that, if the lateral conductivity of the poly-Si layer tends to zero, then no lateral current flows through the poly-Si layer and $A_{poly-Si/c-Si} = A_{Al/poly-Si}$ in equation 7.3. The sum of $\rho_{c, Al/poly-Si}$ and $\rho_{c, poly-Si/c-Si}$ is the upper limit for the junction resistivity. Both limits are used for the Quokka simulations.

This simplification enables one to include the contact resistivity of the Al/poly-Si interface and the junction resistivity of the poly-Si/c-Si interface into the Quokka model, which already considers the other series resistance terms $R_{S,poly}$ and $R_{S,base}$. The series resistance from the metal grid $R_{S,met}$ is calculated analytically [392] to about 20 m Ω cm² for the 20 mm \times 20 mm cell with an aluminum thickness of 10 μ m and is taken into account as an external series

¹⁰In Quokka 2, a single contact interface is defined via a conductive boundary with a saturation current density, a contact resistivity and sheet resistance. For the POLO-IBC cell, one needs two interfaces, the poly-Si/c-Si and the Al/poly-Si interface, for an exact representation.

resistance in the simulation.

The series resistance is simulated as double level light series resistance [393] as implemented in a Quokka series resistance curve simulation and the J - V data is extracted from illuminated J - V simulations.

To calculate the combined junction resistivity for the p^+ POLO contact, the median values of the measured resistivities in section 6.3 of $\rho_{c, Al/poly-Si}=0.9 \text{ m}\Omega\text{cm}^2$ and $\rho_{c,poly-Si/c-Si}=0.4 \text{ m}\Omega\text{cm}^2$ for the 60 min annealing process and the area fraction of the laser contact opening $\frac{A_{Al/poly-Si}}{A_{poly-Si/c-Si}}$ of 2.5% are used. The resulting lower and upper limit according to equation 7.3 for the p^+ POLO contact amounts to $0.91 \text{ m}\Omega\text{cm}^2$ and $1.3 \text{ m}\Omega\text{cm}^2$ and is set to $1 \text{ m}\Omega\text{cm}^2$ in the simulation. For the n^+ POLO contact, only measurements for the junction formation anneal with 30 min and 80 min were performed and it can be assumed that the value for junction resistivity of the poly-Si/c-Si contact for an anneal with a duration of 60 min is between the mean values of $1.3 \text{ m}\Omega\text{cm}^2$ and $8 \text{ m}\Omega\text{cm}^2$ for the process with a duration of 80 min and 30 min, respectively. The lower and upper limits for the combined junction resistivity of the n^+ POLO contact amount to $0.04 \text{ m}\Omega\text{cm}^2$ and $8 \text{ m}\Omega\text{cm}^2$.

When the combined junction resistivity for the n^+ POLO contact is varied between the lower and upper boundary in the R_S -curve simulation, then the simulated POLO-IBC cell exhibits a series resistance between $0.26 \Omega\text{cm}^2$ and $1.26 \Omega\text{cm}^2$. For a combined junction resistivity of $1.2 \text{ m}\Omega\text{cm}^2$ for the n^+ POLO contact, the simulated series resistance coincides with the experimental series resistance of $0.4 \Omega\text{cm}^2$ and confirms the low junction resistivity of POLO junctions on cell level. The corresponding simulated light J - V characteristic matches the LOANA-measured characteristic (figure 7.9a), except that the J_{SC} from LOANA measurement is overestimated. Since the V_{OC} and the fill factor FF of the cell are functions of the logarithm of the illumination level [91], the slightly higher J_{SC} leaves V_{OC} and FF mostly unaffected. As already observed for the J_{SC} - V_{OC} characteristic in figure 7.8a, V_{OC} and FF of the simulated cell are by about 5 mV and 0.3% higher than in the measurement. This indicates that the recombination behavior in the model does not perfectly reflect the experimental situation. However, the simulated cell is still a good approximation of the experimental cell within the typical measurement error and provides an insight into the loss mechanisms in the cell.

7.4.3. Practical efficiency limit of POLO-IBC cells – a free energy loss analysis

The developed Quokka model provides access to the breakdown of loss channels within the 24.25%-efficient POLO-IBC cell by means of the free energy loss analysis [394]. The loss analysis of the simulated POLO-IBC cell in figure 7.9b reveals that the cell is limited by the resistance loss in the wafer and poly-Si layers, followed by bulk recombination, recombination

¹¹The in-house measured illuminated J - V , which is used here for comparison with simulations, is accompanied by the full set of J - V characteristics: dark J - V , J_{SC} - V_{OC} , series resistance from double level light method [393]. This set of J - V characteristics was used throughout this chapter to obtain the input parameters for the simulations. Therefore, it makes sense to compare the simulation with the in-house measurement. However, for an absolute performance comparison, the certified J - V measurement with an efficiency of 24.25% should be referred to.

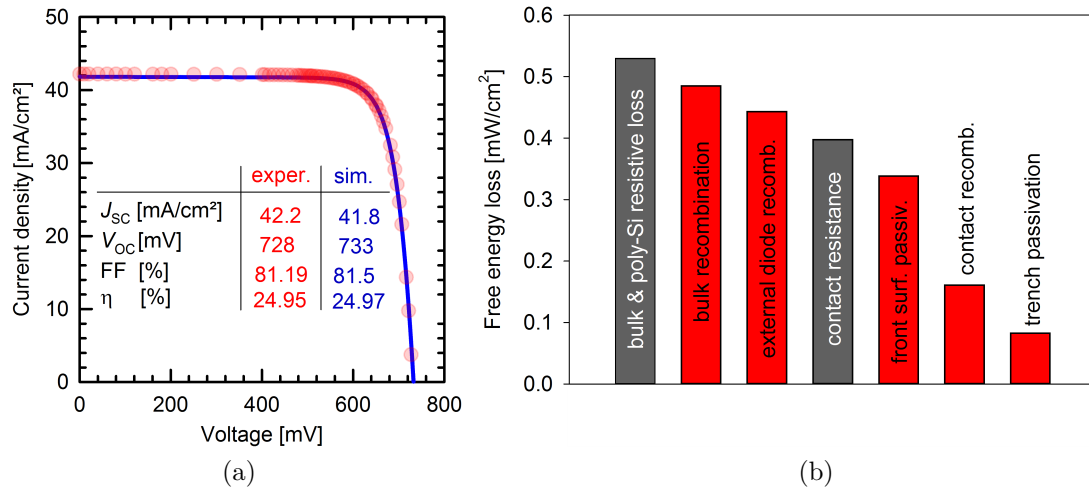


Figure 7.9.: (a) Simulated (blue solid line) and LOANA-measured¹¹(red circles) illuminated current-voltage characteristic of the certified 24.25% efficient POLO-IBC cell. (b) Free energy loss analysis of the simulated POLO-IBC cell. Grey bars represent resistive losses and red bars recombination losses.

in the external diode, resistance loss at the contact interface and front surface recombination. The transport resistance in the bulk and poly-Si layer can be eliminated by using smaller features (e.g. smaller pitches or point contacts) and/or less resistive wafer material. Bulk recombination can be suppressed by increasing the minority carrier diffusion length with high lifetime float-zone (*p*-type) material. The external diode recombination is avoided by careful process optimization, e.g. by using a front surface field or low resistive wafers to ensure low-level injection conditions at the front side of the cell. The large contribution of the contact resistance is probably due to the small contacting fraction of the Al/poly-Si interface and a non-optimized laser opening process of the dielectric layers, which might lead to contact resistivities of the Al/poly-Si contact of around $1 \text{ m}\Omega\text{cm}^2$.

If the four electrical loss channels are addressed and reduced to almost zero, the potential of the POLO-IBC cell is far above 26% [381]. By further improving the optics, it can be speculated that the practical efficiency limit of this cell is above 27% [395]. In fact, the subsequent development of the presented POLO-IBC cell to a photolithography-patterned POLO-IBC cell on a thick $1 \Omega\text{cm}$ FZ *p*-type wafer has led to efficiencies as high as 26.1% [156] and to pseudo efficiencies of cell precursors around 27% [156, 395].

7.5. Chapter summary

In this chapter, a photolithography-free fabrication process flow for an interdigitated back-contact cell with POLO junction for both polarities was presented, the challenges of integrating

polysilicon-based contact on the rear side and the properties of the resulting POLO-IBC cell were discussed.

First, when implementing p^+ and n^+ doped poly-Si on the rear side of the cell, the touching n^+ and p^+ regions form a parasitic p^+n^+ graded junction within the poly-Si reduces the performance of the POLO-IBC cell significantly. To understand the influence of the parasitic junction on the performance of the cell, the parasitic junction was studied isolated from the cell on test samples. It was found that the J - V characteristic of the isolated parasitic junction reproduces the expected behavior, when strong depletion region recombination takes place. The estimated carrier lifetime responsible for the strong recombination is in the order of several picoseconds.

In a second step, the parasitic junction was removed during the cell fabrication process and the dark and light J - V characteristic of the final cell were determined. The characteristic of the cell with removed parasitic junction was superposed with the characteristic of the isolated parasitic junction and excellent agreement was observed between this superposed characteristic and the characteristic of a cell comprising a physical parasitic junction. Thus, it was concluded that it is essential to remove the parasitic p^+n^+ poly-Si junction almost completely.

The photolithography-free cell process with the implemented trench separation of the n^+ and p^+ doped poly-Si regions of a POLO-IBC cell yielded a POLO-IBC cell with a certified power conversion efficiency of 24.25%. A detailed analysis of the optics and the recombination behavior of the cell is presented. A pronounced non-ideal recombination path is observed, which leads to a high local ideality factor at maximum power point and significantly reduces the pFF. Next, the certified POLO-IBC cell was simulated by using Quokka and the determined input parameters. In order to correctly reproduce the non-ideal recombination behavior of the measured cell, an external diode with an ideality factor of 1.7 and a saturation current density of 0.4 fA/cm² has to be included. In that case, the J_{SC} - V_{OC} and the m - V characteristic of simulated and measured cell show a good agreement. The determined contact resistances are included to calculate the illuminated J - V characteristic and a good agreement is achieved, which highlights that the excellent properties of POLO junctions from chapter 6 are maintained in the final device. Finally, a free energy loss analysis is performed to identify main loss channels and a practical efficiency limit for the POLO-IBC cell above 27% is anticipated.

8. Three-terminal interdigitated back-contact bottom cell

Parts of this chapter are based on references [288–291, 294], which are the result of a fruitful collaboration between the National Renewable Energy Laboratory, Denver, Colorado and the author of this thesis. The collaboration on the topic of three-terminal tandem solar cells was initiated back in 2015 by A. Tamboli, S. Essig, P. Stradins and R. Peibst.

E. L. Warren, W. E. McMahon, M. Rienäcker, K. VanSant, R. C. Whitehead, R. Peibst and A. C. Tamboli developed the taxonomy, nomenclature and loading topology for 3T tandems.

All three-terminal devices were designed by the author and fabricated mostly by H. Kohlenberg and the author. The author measured all devices, analysed the data and modeled the devices by means of equivalent circuit modeling. E. L. Warren, M. Schnabel and R. Peibst contributed to the discussion of the working principles of unijunction devices. E. L. Warren performed Sentaurus simulations, which supported the understanding.

P. Stradins and the author derived the Ebers-Moll model under illumination and discussed the working principles of the bipolar junction bottom cells. They came up with the simplified picture of a diffusion resistance for the minority carrier transport through the cell [291].

The author developed the laser contact opening process for the high efficiency unijunction bottom cell. He invented and developed the simplified PERC-like bipolar junction bottom cell based on the idea from R. Peibst for the PERC-like single-junction POLO-IBC cell.

In previous sections, an interdigitated back-contact cell with passivating and carrier-selective POLO contacts was developed, which on one hand maximizes the photo-generating current through the back-contact configuration and on the other hand maximizes the open-circuit voltage by using passivating and carrier-selective contacts. Solar cells of this type have already achieved an efficiency of 26.7% with a-Si/c-Si heterojunction contacts on *n*-type wafers [396] and an efficiency of 26.1% with POLO contacts on *p*-type wafers [156]. As a result, the potential of single-junction silicon solar cells with a theoretical limiting efficiency of 29.5% [28, 29] is nearly exploited¹. To further improve the efficiency significantly, the inherent hot

¹This statement is the personal opinion of the author. Of course, about 3% is still a significant difference. Considering the complexity of the record Si cells, it seems to the author that it is easier to achieve higher efficiencies with a tandem solar cell.

carrier thermalization loss has to be addressed e.g. by splitting the solar spectrum through multiple junctions stacked optically in series [37].

In the simplest version of a tandem solar cell comprising a POLO-IBC cell, a separately fabricated wide band gap top solar cell is mechanically stacked on a POLO-IBC cell from the previous section. Top and bottom solar cells share the solar spectrum, but operate electrically independent from each other in a four-terminal (4T) tandem configuration. Theoretically, a 4T dual-junction solar cell with a Si bottom cell is capable of achieving an efficiency well above 40% for a wide range of top cell band gaps [44, 397]. Practically, such a 4T-GaInP//POLO-IBC and a 4T-GaAs//POLO-IBC dual-junction solar cell with a conversion efficiency of 31.5% [398] and 32.6% [399, 400], respectively, were demonstrated with bottom cells similar to that presented in section 7. Furthermore, a 4T-GaInP/GaAs//POLO-IBC triple-junction solar cells with a conversion efficiency of 35.4% [398] was fabricated. This highlights the efficiency potential of a tandem cell over the single-junction POLO-IBC cell and establishes a benchmark for Si-based tandem solar cells.

An alternative to mechanically stacking the sub-cells, where the top solar cell is monolithically integrated on a POLO-IBC cell, simplifies the fabrication of the tandem and facilitates the in-coupling of light into the bottom cell. Monolithic integration of a top solar cell on an interdigitated back-contact cell requires the bottom cell to have a third front contact, such that the rear contact of the top cell can be series-connected to the bottom cell. A required three-terminal IBC bottom cell and a top solar cell form the three-terminal (3T) tandem solar cell.

As describe in chapter 4, three-terminal tandem solar cells with the third terminal in-between of both sub-cell – a middle electrode – were demonstrated since the 1980s. Nagashima *et al.* [316, 321] proposed to use an interdigitated back-contact cell as the bottom cell for this purpose around the millennium. In the year 2015, the team at NREL initiated a fruitful and still ongoing collaboration with the author of this thesis on the topic of 3T tandem solar cells. The 3T IBC bottom cell for tandem applications was by that time unexplored in the literature (except for Nagashima’s work). Through the pioneering contributions of the NREL team in collaboration with the author of this thesis in the last few years, the 3T tandem solar cell has nowadays become popular and is currently studied by many research groups. In the following chapters, this novel² three-terminal bottom cell architecture is studied in detail. First, all possible permutations of a three-terminal tandem solar cell comprising a three-terminal bottom cell are summarized and a nomenclature for 3T tandem and bottom cells is established³. Two different types of bottom cells - the unijunction and the bipolar junction bottom cell - are required to implement all permutations. The operation of both types of bottom cells is studied by means of experiments and analytic models. Design rules are deduced for each cell type from the models and finally two attractive versions of a bottom cell are demonstrated - a high performance, lab-type bottom cell and a low-cost, industrially-feasible bottom cell.

²It was novel to the tandem community – especially to the perovskite/silicon tandem community – in 2016 and is now being adapted by an ever growing community.

³The taxonomy and nomenclature was developed by E. L. Warren in close collaboration with W. E. McMahon and the author of this thesis.

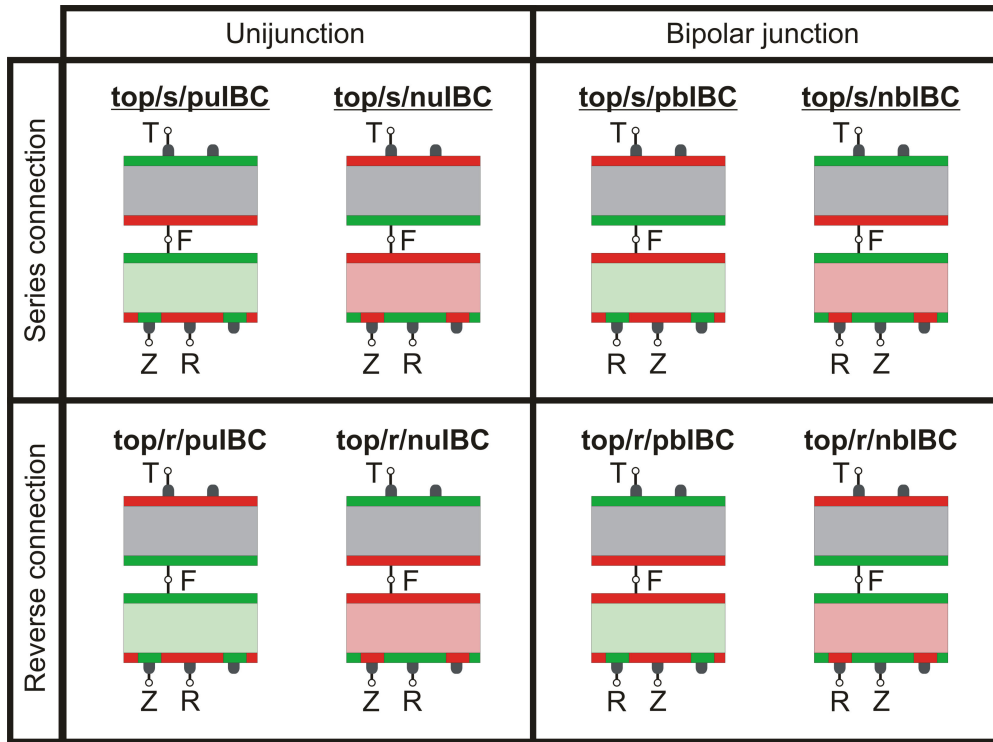


Figure 8.1.: Taxonomy and nomenclature of 3T tandem solar cells comprising 3T-IBC cells. Light red and light green colors indicate electron-dominated (n -type) and hole-dominated (p -type) absorber materials, respectively. Grey absorbers can be intrinsic or either p - or n -type. Red (green) contact layers represent electron (hole) selective contacts.

8.1. Taxonomy and nomenclature⁴

There are many potential ways to construct a tandem solar cell with three terminals from two different absorber materials. Different bottom cell architectures, absorber materials for top and bottom cells and different interconnection schemes between top and bottom cell can be permuted. Figure 8.1 summarizes all possible types of 3T tandem solar cells comprising an interdigitated back-contact bottom cell with three terminals.

8.1.1. Bottom solar cell

A 3T-IBC bottom cell needs an absorber (e.g. silicon) and three carrier-selective contacts. The carrier concentration for holes and electrons in the absorber at equilibrium can be of the same order of magnitude, then the absorber is intrinsic. But often the absorber in equilibrium is either conductive for electrons or for holes, because the majority carrier concentration

⁴The following section is based on a peer-review paper published in [294].

exceeds the minority carrier concentration significantly⁵. If the absorber is conductive for electrons, then the bottom cell is denoted to n -type IBC cell (red absorber in figure 8.1). If it is conductive for holes, it is referred to as p -type IBC cell (red absorber in figure 8.1). An i IBC bottom cell refers to a cell with an intrinsic absorber (not shown in figure 8.1).

The carrier-selective contact to the absorber at the front side of the bottom cell is an electron- or hole-selective contact and the rear side of the bottom cell accommodates one electron-selective contact and one hole-selective contact. One of the rear contacts (contact at node Z in figure 8.1) has the same polarity as the front contact and the other rear contact has the opposite polarity (contact at node R in figure 8.1). To construct a two-terminal both side-contacted bottom cell, one needs only the front contact with a particular polarity and the rear contact with the opposite polarity. The front contact is denoted as contact F for front and the rear contact with the opposite polarity is contact R for “root”. The rear contact with the same polarity as the front contact is superfluous for the operation of a two-terminal bottom cell. It is added to obtain a three-terminal bottom cell and therefore is denoted as the additional contact Z, where Z stands for the German word “zusätzlich” for additional.

Finally, one has to define the majority carrier type of the absorber and of the front contact to obtain a unique definition of the bottom cell. If the majority carrier type (polarity) of the front contact and the absorber is the same, then the front contact and the Z rear contact are selective for the majority carriers of the absorber and the root contact is selective for minority carriers of the absorber. In other words, contact F and Z are “majority carrier contacts” and contact R is a “minority carrier contact”⁶. A 3T-IBC cell, which exhibits two majority carrier contacts and a single minority carrier contact, is similar to a unijunction transistor. It is referred to as “unijunction bottom cell”. If the polarity of the front contact is opposite to that of the absorber, then contacts F and Z are minority carrier contacts and the root contact is the majority carrier contact. The 3T-IBC cell resembles a bipolar junction transistor architecture because of its single majority carrier contact and two minority carrier contacts, and is referred to as a “bipolar junction bottom cell”.

A unique and compact notation for the different bottom cell architectures facilitates the usage of a clear language. The proposed notation [p or n][u or b]IBC in Warren *et al.* [294] contains two properties of the bottom cell:

1. The type of the majority carrier in the absorber, where p identifies the holes and n the electrons as the majority carrier.
2. The number of minority carrier contacts, where u stands for unijunction with a single minority carrier contact and b is for bipolar junction with two minority carrier contacts.

Permuting the two properties, leads to four different bottom cell: pu IBC, nu IBC, pb IBC and nb IBC. A 3T-IBC bottom cell with a p -type absorber and a single minority carrier (electron selective) contact for example, as shown in the first column of figure 8.1, is then referred

⁵This classification according to absorber conductivity is useful for silicon, but not necessary for the physical understanding of 3T bottom cell.

⁶Note that the terms “majority” and “minority” carrier refer to the equilibrium carrier concentrations of the absorber.

to as *puIBC* bottom cell. The bottom cell from the last column of figure 8.1 with a *n*-type absorber and two minority carrier (hole selective) contacts, is referred to as *nbIBC* bottom cell.

If the absorber is intrinsic, no majority carriers exist and the notation needs an extension to uniquely describe the bottom cell. In this case, the polarity of the root contact R is added. A bottom cell with an intrinsic absorber and an electron-selective root contact R is denoted as $(nR)iIBC$.

8.1.2. Top solar cell

The top solar cell consist of an absorber material with a wide band gap enclosed by one electron-selective and one hole-selective contact⁷. In the compact notation, the top solar cell has a single descriptor like the placeholder “top” in figure 8.1 or the absorber material e.g. “perovskite” or “GaAs”.

8.1.3. Three-terminal tandem solar cell

As for any tandem solar cell, the bottom and top solar cell are optically connected in series to obtain a spectrum-splitting device, but the electrical interconnection of both sub-cells in a three-terminal tandem solar cell offers an additional possibility – the reverse connection – compared with an electrically series-connected two-terminal tandem solar cell. Figure 8.1 shows tandem solar cells with series-connected and reverse-connected sub-cells.

In a series-connected tandem solar cell, the hole-selective (electron-selective) rear contact of the top solar cell meets the electron-selective (hole-selective) front contact of the bottom cell at the midpoint (or focal point) F of the tandem. To provide an efficient carrier transport across this focal point, fast inter-band-recombination of electrons and holes has to be ensured by a tunnel or recombination junction [401–404].

If the top solar cell polarity is reversed, i.e. the cell is turned around, compared to the series-connected configuration, then an electron-selective (hole-selective) rear contact of the top cell meets another electron-selective (hole-selective) front contact of the bottom cell and efficient carrier transport across the focal point F is ensured, when the both electron-selective contacts form a low-resistive ohmic contact.

Finally, the full notation for a 3T tandem solar cell contains the descriptor for the top and the bottom solar cell and for the interconnection scheme, where “s” stands for series-connected and “r” for reverse-connected. For example, a 3T tandem cell comprising a GaInP top solar cell interconnected in series with a nuIBC bottom cell is referred to as GaInP/s/nuIBC.

8.1.4. Loading topology

The definition of the three different terminal nodes F, Z and R of a bottom cell and T, Z and R of the tandem cell facilitates the definition of voltages and currents of a three terminal

⁷Hypothetically, the top solar cell can have three terminals, but such top solar cells are not discussed herein.

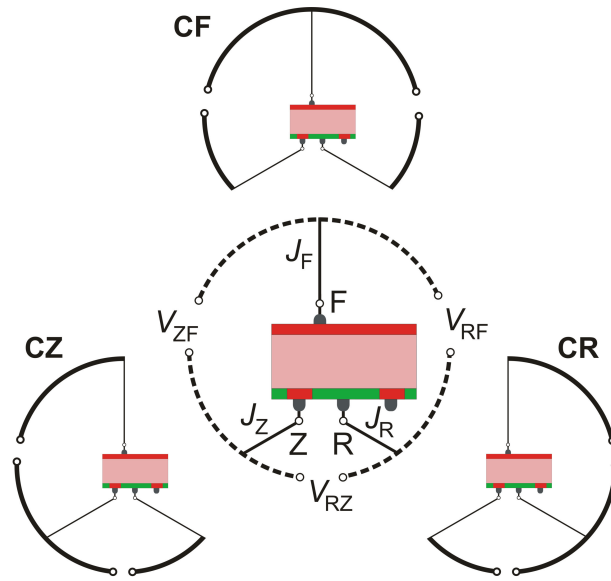


Figure 8.2.: Nomenclature of currents and voltages and the loading topology of a 3T bottom cell. Common Z (CZ), common R (CR) and common F (CF) denote loading topologies, where the contact Z, R or F is the common contact in the circuit.

device. As depicted in Figure 8.2 for a 3T bottom cell, the current density flowing in or out of each terminal F, R and Z is termed J_F , J_R and J_Z and the voltage between a pair of terminals F-Z, R-F and R-Z is V_{FZ} , V_{RF} and V_{RZ} .

For 3T devices, two of three terminal pairs are loaded. This is indicated by thick lines connecting the terminals of the bottom cell in figure 8.2. The resulting topology exhibit one common terminal between the loads. Figure 8.2 (smaller current wheels) shows the three possible topologies: common Z (CZ), common R (CR) and common F (CF)⁸. For example, the bottom cell in the following section is probed between terminals R and Z, and between R and F simultaneously. The common terminal of this topology is the root terminal R and this measurement configuration refers to CR.

8.2. Fabrication and characterization of 3T bottom cells

8.2.1. Cell fabrication process of the 3T unijunction bottom cell

Figure 8.3 shows the ion-implanted and inkjet-patterned interdigitated back contacted solar cells with POLO junctions for both polarities with an active cell area of $7.6 \text{ mm} \times 15.5 \text{ mm}$, which is prepared following the cell process described in section 7 and reference [155] and [157]. The p^+ POLO contact (R) and the n^+ POLO contact (Z) are separated by a $100 \mu\text{m}$ wide textured trench region and form an interdigitated pattern with a pitch of $952 \mu\text{m}$ on

⁸The notation follows that of bipolar junction transistors, where the topologies are common emitter, common base and common collector.

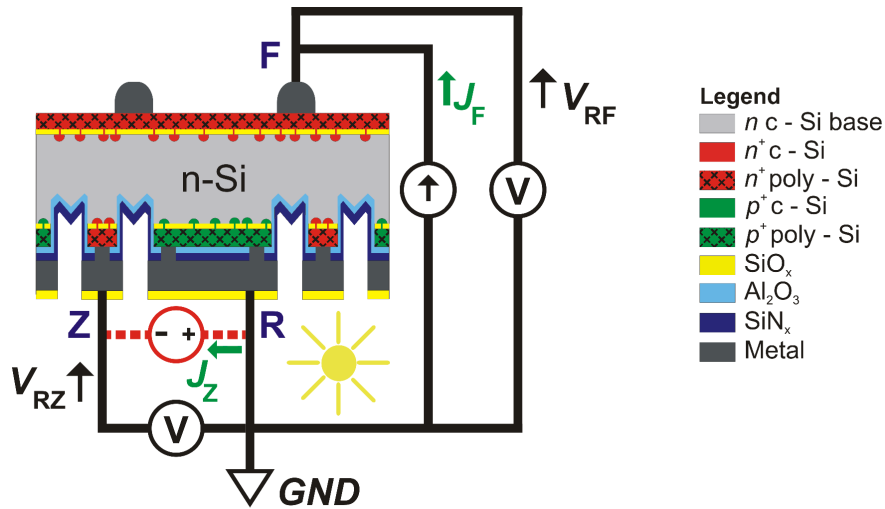


Figure 8.3.: Schematic cross-section of the unijunction three-terminal interdigitated back contact bottom cell (nuIBC) and measurement setup in common rear (CR) configuration

the rear side of a saw-damage etched $156 \text{ mm} \times 156 \text{ mm}$ n -type Czochralski silicon wafer with a base resistivity of $4 \Omega\text{cm}$ and a final thickness of $155 \mu\text{m}$. The applied p^+ POLO and n^+ POLO junctions exhibit low contact resistivity of around $1 \text{ m}\Omega\text{cm}^2$, while featuring excellent passivation qualities, resulting in a saturation current density $J_{C,poly}$ of 4 fA/cm^2 and 2 fA/cm^2 per side, respectively [157]. In order to permit a 3T operation of the bottom cell, a passivating and carrier-selective n^+ POLO majority carrier contact is applied to the front side of the cell. For measurement purposes, the n^+ POLO front contact receives an aluminum front side grid with a finger distance of $1778 \mu\text{m}$ and a finger width of $240 \mu\text{m}$ through a silicon shadow mask [405]. The rear side is finished according to section 7 and reference [157].

8.2.2. Cell fabrication process of the 3T bipolar junction bottom cell

A bipolar junction POLO-IBC Si bottom cells with an active cell area of $7.6 \text{ mm} \times 15.5 \text{ mm}$ is fabricated using a $300 \mu\text{m}$ -thick, p -type FZ-Si wafer with a nominal base resistivity of $200 \Omega\text{cm}$ and a bulk lifetime close to the intrinsic limit of approximately 100 ms after POLO junction formation [266]. Figure 8.4 shows the schematic cross-section of the cell. The processing of the ion-implanted and inkjet-patterned bottom cell mostly follows that of subsection 8.2.1 or reference [157], except that a p -type wafer is used instead of n -type one and the n^+ POLO contact at the front side is patterned. The full-area passivating n^+ POLO contact F at the front side and the n^+ counterdoped POLO contact Z at the rear side are now minority-carrier contacts and exhibit $J_{0,C}$ values of 13 fA/cm^2 and 5 fA/cm^2 , respectively. The p^+ POLO contact R on the rear side is the majority-carrier contact with a $J_{0,C}$ of 4 fA/cm^2 . The n^+ POLO contact (Z) and p^+ POLO contact (R) form an interdigitated pattern with a pitch of

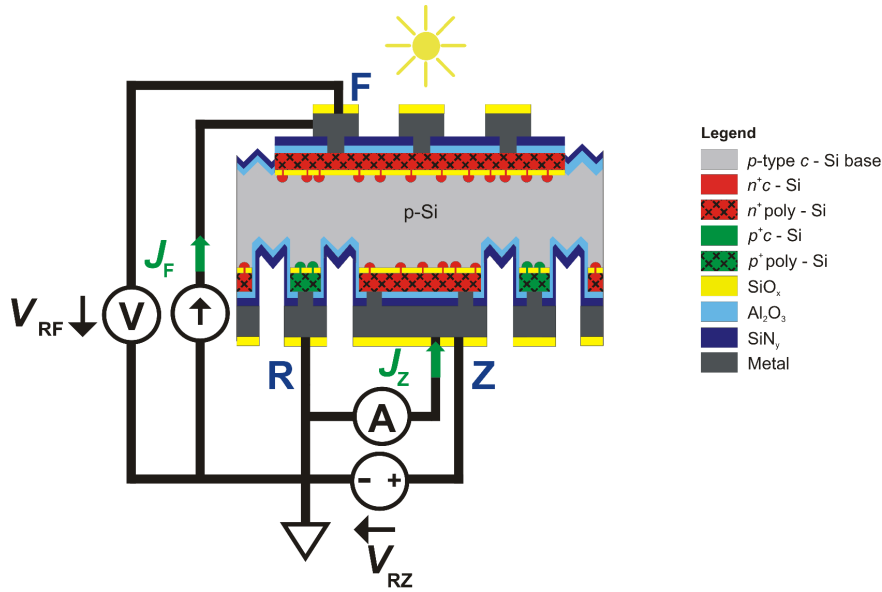


Figure 8.4.: Schematic cross-section of the bipolar junction three-terminal interdigitated back contact bottom cell (pbIBC) and measurement setup in CR configuration.

952 μm . The area fraction of the n^+ POLO contact Z amounts to about 50% and of the p^+ POLO contact R to 24%. A trench with a width of 120 μm separates both contact polarities. In order to avoid parasitic effects at the front contact, the n^+ POLO contact is patterned by inkjet-printing a hotmelt mask on the front side and wet-chemical etching during the trench patterning step. To passivate the region, where the n^+ POLO contact has been removed, a layer stack of Al_2O_3 and SiN_x is deposited on the full area of the front side. The dielectric layer stack on the n^+ POLO front contact is ablated locally to provide electrical contact with an area fraction of 10% to the evaporated aluminum layer. A SiO_x layer, which is sputtered on the front side, is patterned via laser ablation to yield a line pattern with a pitch of 300 μm and a line width of 100 μm . The remaining SiO_x protects the aluminum during the subsequent aluminum etch, which is required for the RISE contact separation on the rear side and produces a metal grid pattern on the front side.

8.2.3. Characterization

Figures 8.3 and 8.4 also show a schematic of the measurement setup. In order to exclude voltage drops across the setup, four-point probe measurements are conducted using a Süss PA 200 probe station and a Keithley 4200 parameter analyzer. The p^+ POLO root contact (R) is grounded, and currents and voltages are measured at each n^+ POLO contact (F or Z) using source measurement units with a measurement and source accuracy better than 0.05%. The illumination is applied by a halogen lamp through the texturized trench regions at the rear side for the unijunction bottom cell and to the front side for bipolar junction bottom cell. Without careful control and monitoring, the temperature of the cell can increase steadily

from 25 °C during a single J - V measurement due to radiative heating and insufficient heat sinking. A gaseous nitrogen stream acts as the heat sink for the cell and the measurement chuck. A thermocouple, which is in contact with the interdigitated rear side of the cell, measures the cells temperature. It is ensured that the temperature difference during data acquisition as well as within a set of J - V measurements at the same illumination level is smaller than 2 K.

The circuit between contact node R and contact node Z is defined as the RZ circuit, for which V_{RZ} is varied and J_Z is measured. The circuit between contact nodes F and R is defined as the FR circuit. The 2T current-voltage characteristic of the RZ (FR) circuit, thus between the contact R and the respective n^+ POLO contact Z (F) of the bottom cell, is measured as follows. While one circuit is swept, the current density in the other circuit is held constant. Thus, if the RZ circuit is probed, the current density J_F flowing into the front contact F is forced to a constant value, which emulates a series-connected top cell. Different values of J_F mimic different top cell materials with different band gaps, thicknesses, or variations in the irradiation spectrum. The illumination level is characterized by using the short-circuit current density $J_{Z,SC}$ for the unijunction cell and $J_{F,SC}$ for the bipolar junction cell, while the non-probe circuit was open ($J_F=0$ for the unijunction and $J_Z=0$ for the bipolar junction). The short-circuit current density $J_{Z,SC}$ or $J_{F,SC}$ is set to a value of 10 mA/cm² by adjusting the distance between lamp and cell. This photocurrent density mimics the current density in a GaInP/GaAs//Si tandem [398, 400, 406]. For other top cell materials with different band gaps, other photocurrent densities in the bottom cell might apply. However, for simplicity and without loss of generality all measurements in the following are conducted at the same illumination level.

The total power $P_{3T,total}$ is obtained as the sum of the powers extracted at the FR circuit $P_{3T,FR}$ and at the RZ circuit $P_{3T,RZ}$, thus by the sum of the products of the voltages V_{RF} and V_{RZ} and the corresponding current densities J_F and J_Z of the FR circuit and the RZ circuit. The maximum power point (MPP) is determined from the total 3T power in equation 8.1 rather than individually for each of the sub-circuits.

$$P_{3T,total} = J_F \cdot V_{RF} + J_Z \cdot V_{RZ} = P_{3T,FR} + P_{3T,RZ} \quad (8.1)$$

8.3. Operating principle of 3T bottom cells

The operation principles of unijunction and bipolar junction bottom cells are investigated experimentally in detail below. Even if both cell types appear differently and (in detail) have to be physically modeled differently, they still have a common operation principle in a 3T tandem solar cells.

Therefore, the first part of this section deals with the unijunction bottom cell and discussed the operation in detail. The second part presents the operation of a bipolar junction bottom cell, but in a less detailed discussion. It rather confirms that bipolar junction bottom cells operate in a similar manner as unijunction bottom cell in a 3T tandem.

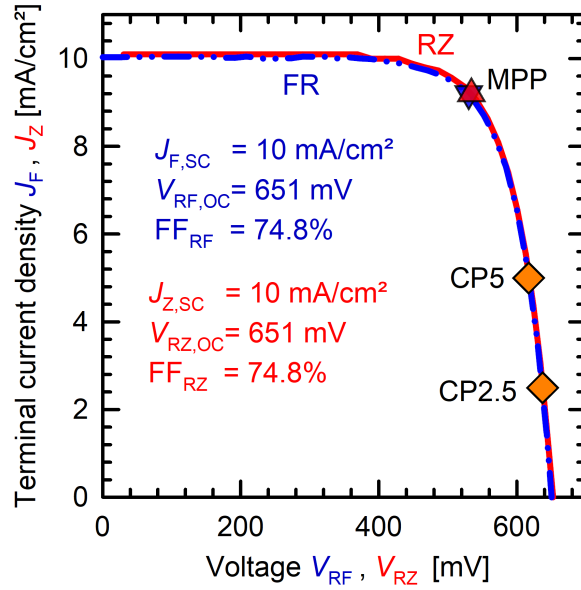


Figure 8.5.: Measured two-terminal J_Z-V_{RZ} (red line) and J_F-V_{RF} characteristic (blue line) at an illumination level corresponding to $J_{Z,SC} = 10 \text{ mA/cm}^2$. Red and blue triangles indicate the maximum power point of the RZ circuit and the FR circuit, respectively. Orange diamonds illustrate the operation points for a current-limited bottom cell (RZ circuit) with a current point (CP) at J_F of 2.5 mA/cm^2 (CP2.5) and 5 mA/cm^2 (CP5)

8.3.1. Unijunction bottom cell

The 3T IBC bottom cell for tandem application has been a rather unfamiliar type of solar cell and its $J-V$ characteristic along with the modes of operation differ significantly from commonly used 2T cells for single-junction and tandem applications [318]. Therefore, the 2T operation of a 3T IBC cell is explored first by using solely one of the majority carrier contacts and it is reviewed how the 2T-operated 3T IBC cell would operate in a 4T and 2T tandem to establish a benchmark for the subsequently introduced 3T operation.

Two-terminal operation

The 2T $J-V$ characteristic of the FR circuit and the RZ circuit is measured. The respective current density of the non-probed circuit is set to 0 mA/cm^2 . Figure 8.5 shows the matching 2T $J-V$ characteristic of the FR (blue line) and the RZ circuit (red line) with equal $J_{Z,SC}$ and $J_{F,SC}$ of 10 mA/cm^2 , equal open circuit voltages $V_{RZ,OC}$ and $V_{RF,OC}$ of 651 mV and equal fill factors FF_{RZ} and FF_{RF} of 74.8% . The maximum electrical power density $P_{2T,FR,mpp}$ extracted from the FR circuit amounts to 4.87 mW/cm^2 ($V_{RF,mpp} = 530 \text{ mV}$, $J_{F,mpp} = 9.2 \text{ mA/cm}^2$), which is in accordance with the maximum electrical power density $P_{2T,RZ,mpp}$ of 4.88 mW/cm^2 ($V_{RZ,mpp} = 534 \text{ mV}$, $J_{Z,mpp} = 9.2 \text{ mA/cm}^2$) extracted from the RZ circuit. In contrast to

simulated cells with diffused full-area metal contacts [317], the high performance⁹ of the investigated 3T IBC cell originates from the high contact selectivity of the POLO junctions [120, 127, 157] and facilitates the study of a nearly ideal 3T IBC cell with little parasitic effects. From the model that will be introduced in subsection 8.4.1, it follows that a suitable grid geometry and the use of low resistance POLO contacts (compared to simulations in Warren et al. [318]) result in comparable series resistances for the FR and RZ circuit and the matching J - V characteristic of the FR and RZ circuit. The scenario of measuring the FR circuit with a floating Z contact is similar to a 2T back-junction double-side contacted Si bottom cell and the scenario of measuring the RZ circuit with floating F contact resembles a 2T IBC Si bottom cell with a front surface field. Both bottom cell architectures were recently used in high efficiency 4T tandem cells [398, 406], where the bottom cell would extract the maximum power density $P_{2T,FR}$ or $P_{2T,RZ}$ at its own MPP independent of the top cell.

In a 2T tandem with series-connected sub-cells, where the n^+ POLO front contact (F) of the bottom cell is facing towards the top cell, the hole current density collected at the rear contact of the top cell has to correspond to the electron current density supplied at the front contact of the bottom cell and vice versa. The bottom cell operation complies with the familiar 2T operation modes of a tandem cell under current-matched and current-mismatched conditions [407]. Ideally, the current density from the top cell corresponds to $J_{F,2T,mpp}$ of an independently working bottom cell at MPP (blue triangle in figure 8.5) and the Si bottom cell delivers the same power density $P_{2T,FR,mpp}$ as in the independently working 4T tandem. This ideal situation of current-matching is only achievable with perfectly current-matched top cells for a particular solar spectrum, and excludes relevant cases such as GaInP, GaAs and methylammonium lead iodide (MAPI) perovskites and varying solar spectra. In the current-mismatched case of large and narrow top cell band gaps, the top cell or the bottom cell limits the current density of the tandem, respectively, and the power density of the 2T tandem cell is reduced. As an example of current-mismatched operation and as benchmark for the following description of 3T operation, two special operation points for a current-limited 2T bottom cell at a current point (CP) of J_F of 5 mA/cm² (CP5) and 2.5 mA/cm² (CP2.5) are shown in figure 8.5. These current points represent operating states of the bottom cell in a tandem, with a large band gap top cell and thus the low top cells current density limits the bottom cells performance. The bottom cell delivers less power compared to the operation at its overall maximum power point. Up to this point, the 3T IBC cell using solely two terminals and the resulting 4T and 2T tandems have been described using state-of-the-art solar cell models [60, 407, 408]. As soon as a third terminal (a second majority carrier contact) is added to a 2T Si cell, the cell and the operation of such a cell changes significantly [289, 311, 318].

Three-terminal operation

In order to study the 3T IBC cell under operation conditions similar to a tandem cell, a given operation point of the top cell (such as its maximum power point) is emulated by a

⁹Note that the illumination intensity of the cell is rather low and corresponds to the situation in a GaAs/Si tandem.

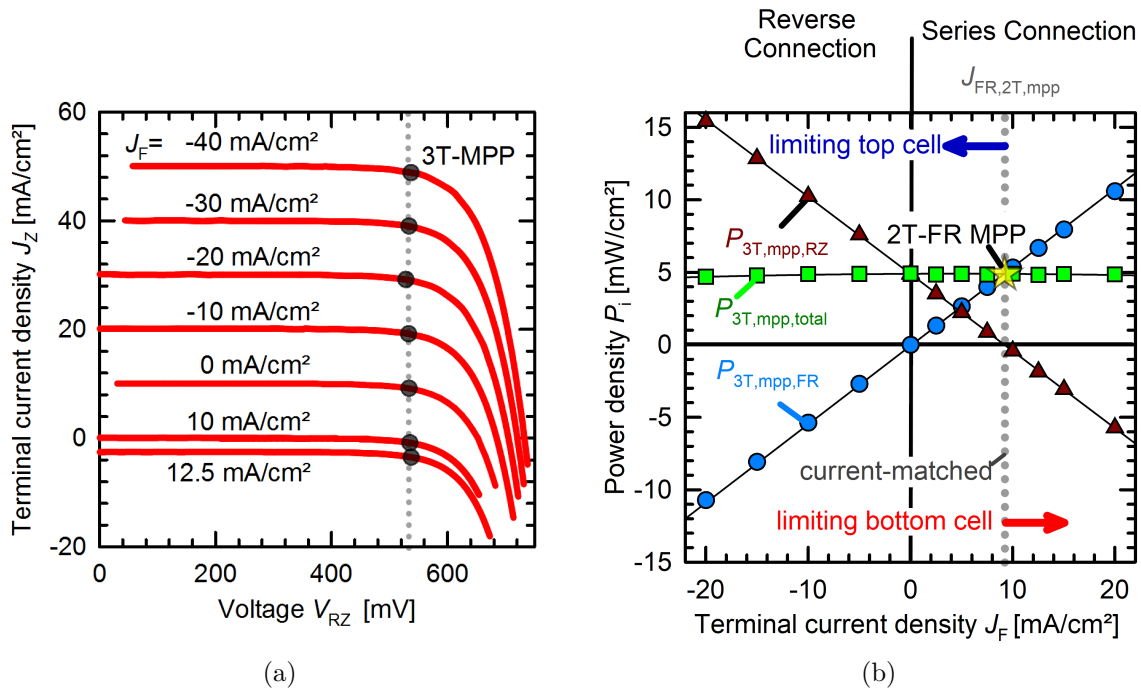


Figure 8.6.: (a) Measured J_z - V_{RZ} characteristics (red) for different J_F values at an illumination level corresponding to $J_{z,SC} = 10$ mA/cm² in two-terminal (2T) operation. Grey dotted line is a guide for the eye and indicates the maximum power point (MPP) voltage for the 2T operation ($J_F = 0$ mA/cm²). (b) Corresponding power densities at 3T-MPP for J_F value between -20 mA/cm² and 20 mA/cm²: The total three-terminal (3T) power density $P_{3T,mpp,total}$ (green squares) and the corresponding fraction of $P_{3T,mpp,total}$ contributed by the FR circuit $P_{3T,mpp,FR}$ (blue circles) and the RZ circuit $P_{3T,mpp,RZ}$ (brown triangles). The yellow star represents the maximum power point for 2T operation of the cell in either FR or RZ circuit.

constant current source. Since the FR circuit of the bottom cell would be series-connected to the top cell circuit in a 3T tandem, J_F in the FR circuit has to correspond to the current density of the top cell and thus J_F is forced to a certain constant current density. The Z contact is now used to inject or to extract majority carriers via the RZ circuit into or out of the bottom cell, which implies the CR loading configuration. The J - V characteristic of the RZ circuit is measured at different, but fixed J_F values. As in case of the two-terminal operation, a photocurrent density is generated, which corresponds to a $J_{z,SC}$ of 10 mA/cm² in the 2T-operated 3T cell. The resulting J - V curves for different J_F values are shown in figure 8.6a.

If $J_F = 0$ mA/cm², the J_z - V_{RZ} characteristics follows the J_z - V_{RZ} of the 2T-operated 3T-IBC cell from figure 8.5. Positive J_F shift the J - V characteristic of the RZ circuit to lower current densities and negative ones shift it up to higher current densities. The sum of the

current densities $J_{Z,SC}$ and J_F at short-circuit conditions is constant, which is consistent with Kirchhoff's current law. The 3T-MPP voltage of the RZ circuit for different applied J_F is nearly constant (grey dotted guide to the eye line in figure 8.6a).

The voltage of the RZ circuit (V_{RZ}) at 3T-MPP is similar, but not identical, to the voltage V_{RF} of the FR circuit for the investigated current densities J_F . This means that the n^+ doped rear root contact is nearly in equilibrium with the n^+ doped front contact via the n-type base. The electron quasi Fermi levels of both contacts are at almost the same position. A detailed discussion of an equivalent circuit model, the J - V characteristic and the origin of the voltage drop $V_{RF} - V_{RZ}$ is provided in section 8.4.1. Figure 8.6b shows the maximum electrical power density extracted from the RZ circuit ($P_{3T,mpp,RZ}$) and from the FR circuit ($P_{3T,mpp,FR}$), as well as the resulting total electrical power density $P_{3T,mpp,total}$ as a function of the current density J_F . All power densities for the 3T measurements were determined at the maximum of the total power density $P_{3T,total}$.

Depending on the magnitude and sign of J_F , four different operation modes of the bottom cell are possible. Figure 8.7 illustrates the current flows of electrons and holes in the investigated bottom cell and a hypothetical top cell, which is emulated by the constant current source. Three modes of operation for the series-connected subcells ($J_F > 0$) and a single one for reverse-connected ones ($J_F < 0$) are discussed in the following.

Current-matched operation of series-connected tandem For the current-matched scenario of the bottom cell in figure 8.7, J_F matches the photo-generated electron current density $J_{F,2T,mpp}$ in the bottom cell of 9.2 mA/cm^2 and the whole photo-generated electron and hole current in the bottom cell is collected at the front and root contact of the bottom cell, respectively. The bottom cell operates like it would be the case for a rear-junction double-side contacted Si bottom cell in a current-matched 2T tandem (grey dotted line in figure 8.6b). Since no surplus photo-generated electron current is left or missing in the bottom cell, no electrical power is left for the RZ circuit ($P_{3T,mpp,RZ}=0 \text{ mW/cm}^2$) and the additional contact Z is not required. The FR circuit of the cell extracts the entire power density $P_{3T,mpp,FR} = P_{3T,mpp,total}$ (blue circles in figure 8.6b) and the total power density extracted by the 3T bottom cell $P_{3T,mpp,total}$ (green squares in figure 8.6b) equals the maximum power density extracted by the current-matched 2T bottom cell $P_{2T,FR,mpp}$ (yellow star in figure 8.6b).

Operation in series-connected tandem with current-limiting top cell If the applied current density at the front contact J_F is smaller than $J_{F,2T,mpp}$, the scenario of a current-limiting top cell is emulated. The current density of the FR circuit is smaller than the photo-generated current density in the bottom cell and surplus electrons and holes remain in the bottom cell, if only the FR circuit is used. In a 3T bottom cell, the additional majority carrier contact Z enables the collection of the excess majority carriers (electrons) and the root contact now collects the surplus hole current density. As a consequence, the RZ circuit can extract the excess power density from the bottom cell, unlike the 2T case, where the excess power density dissipates within the cell. The power density of the FR circuit $P_{3T,mpp,FR}$ decreases with decreasing $J_F > 0$, but the power density extracted by the RZ

8.3. OPERATING PRINCIPLE OF 3T BOTTOM CELLS

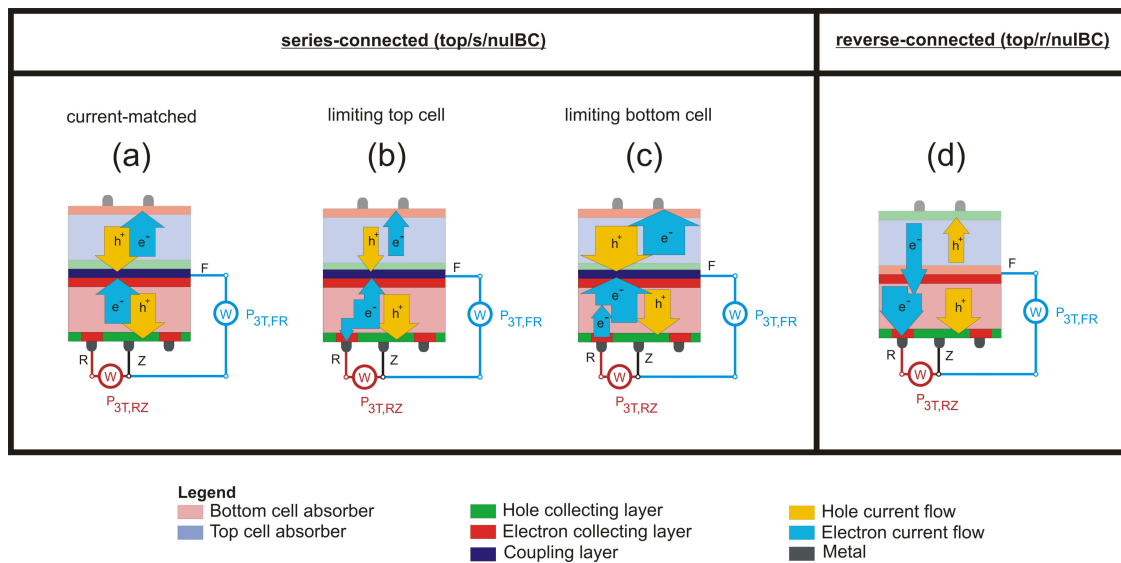


Figure 8.7.: Different operation regimes of a three-terminal interdigitated back contact (3T-IBC) bottom cell in a series-connected tandem cell (top/s/nuIBC) with current-matched subcells, with current-limiting top cell and with current-limiting bottom cell or in a reverse-connected tandem cell (top/r/nuIBC). Yellow arrows represent hole current flow and blue arrows electron current flow. Red and blue watt meters represent the calculation of the powers at the 3T-MPP from the $J-V$ measurements in figure 8.6a for the RZ and FR circuit.

circuit $P_{3T,mp\bar{p},RZ}$ (brown triangle in figure 8.6b) increases to almost the same extent. Finally, if a minor resistive effect is neglected, the net power density $P_{3T,mp\bar{p},total}$ is constant and equal to the current-matched case. The resistive effect will be discussed in more detail using an analytical model in subsection 8.4.1.

Operation in series-connected tandem with current-limiting bottom cell On the right hand side of the current matching line in figure 8.6b, J_F is larger than $J_{F,2T,mp\bar{p}}$ and thus a current limiting bottom cell is emulated (limiting bottom cell in figure 8.7). In contrast to the 2T tandem case, where the top cells current density and power extraction would be limited by the low electron current density of the bottom cell, no such loss occurs in the 3T case. The rear majority carrier contact Z in the 3T bottom cell enables efficient majority carrier (electron) injection into the bottom cell. The injected majority carrier current density at contact Z re-balances the electron current density at the front contact of the bottom cell to match the hole current density at the rear contact of the top cell. Now, the rear and front contact of the top cell would collect the entire photo-generated electron and hole current densities in the top cell. The top cell would operate at its maximum power point similar to a top cell in a 4T tandem. The injection of electrons at the contact Z appears as a negative extracted power density $P_{3T,mp\bar{p},RZ}$ in figure 8.6b, which is synonymous to power injection into the bottom cell by the RZ circuit. The power density extracted at the FR circuit $P_{3T,mp\bar{p},FR}$ increases with increasing J_F and is larger than the power density $P_{2T,mp\bar{p},FR}$ in the current-matched 2T case. Nevertheless, the net 3T bottom cell power density $P_{3T,mp\bar{p},total}$ remains approximately constant for all values of J_F investigated.

To enable this type of operation, the excess electron current density injected at contact Z has to be provided from the front contact T of the top cell or externally e.g. from the module string.

Operation in reverse-connected tandem If the current density J_F at the front majority carrier contact of the bottom cell is negative, then the reverse-connected tandem cell is emulated. The top cell is turned around in the reverse-connected tandem, which features a hole collecting contact T at the front side of the top cell, a hole collecting contact R on the rear side of the bottom cell and a common electron-collecting contact between top and bottom cell (reverse-connected in figure 8.7), instead of a coupling layer as in a series-connected tandem. A *pn-n-np* bipolar junction transistor-like structure forms by introducing the additional rear majority carrier contact Z [311, 316, 321]. The reverse-connected tandem cell is therefore unique for 3T tandem cells and does not have a working 2T equivalent. The front contact of the top cell collects the photo-generated holes and the rear contact of the top cell collects the electrons within the top cell. The collected electron current density by the rear contact of the top cell is then injected into the front majority carrier contact of the bottom cell and induces a negative extracted electron current density J_F . The rear majority carrier contact Z of the bottom cell collects the injected and photo-generated electrons and the rear root contact R collects the photo-generated holes in the bottom cell. In order to separate the holes of each cell and to provide efficient electron flow from the top into the bottom cell, hole-blocking and simultaneously electron-transparent layers is necessary at the common

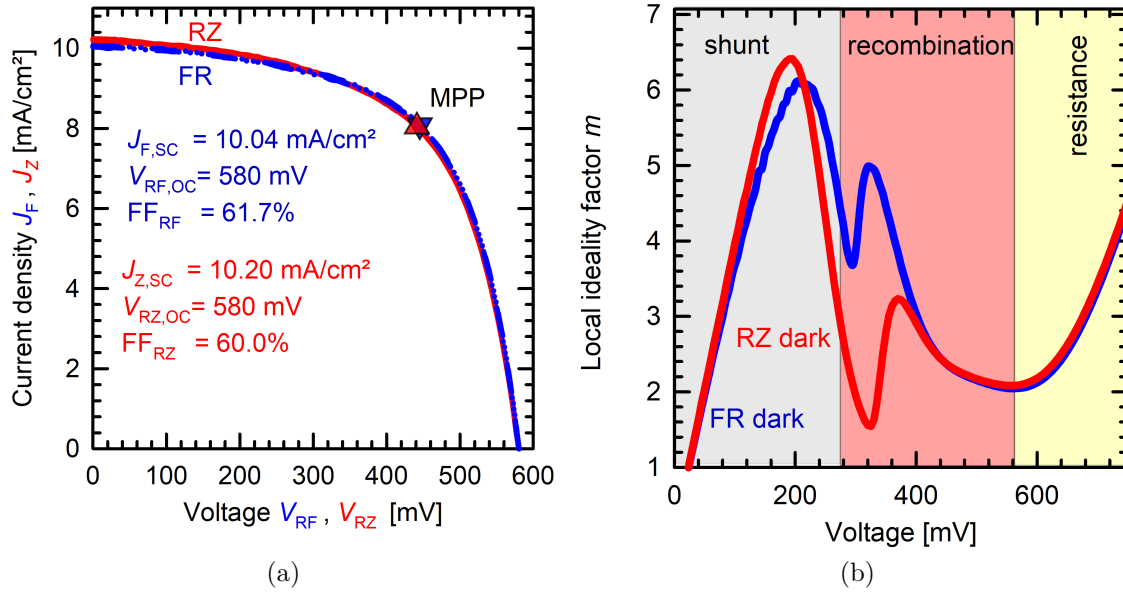


Figure 8.8.: (a) Measured two-terminal J_Z - V_{RZ} (red line) and J_F - V_{RF} characteristic (blue line) at an illumination level corresponding to $J_{F,SC} = 10$ mA/cm². Red and blue triangles indicate the maximum power point. (b) Local ideality factor of dark two-terminal J_Z - V_{RZ} (red line) and J_F - V_{RF} (blue line) characteristic.

contact at the center (focus F) of the tandem cell. Figure 8.6b shows the power densities of each sub-circuit in the bottom cell. Since the rear additional contact Z of the bottom cell collects the photo-generated electrons from the bottom cell and the injected electrons from the top cell, the extracted power density in the RZ circuit $P_{3T,mpp,RZ}$ exceeds the power density of the current-matched case $P_{2T,mpp,FR}$. The injected power at the front contact F appears as a negative extracted power density $P_{3T,mpp,FR}$ and the net power density of the 3T bottom cell has approximately a constant and maximum power output $P_{3T,mpp,total}$. However, due to large current densities J_Z , the resistive effect is more pronounced compared to the series-connected operations and reduces the net power density slightly.

In summary, it was demonstrated that, if resistive effects are neglected, the 3T bottom cell can be operated at a similar maximum power point independent of the magnitude and direction of the applied current density J_F at the front contact of the 3T bottom cell.

8.3.2. Bipolar junction bottom cell

Two-terminal operation

The 2T J - V characteristic of the FR and RZ circuit is measured, while the respective current density of the non-probed circuit is set to 0 mA/cm². The measurement of the RZ circuit is similar to a front floating emitter IBC cell [409] and that of the FR circuit similar to a floating rear emitter cell [410, 411]. Figure 8.8a reveals that for the device under investiga-

tion, the RZ circuit provides a similar maximum power density of $P_{2T,RZ,mpp}=3.55 \text{ mW/cm}^2$ ($V_{RZ,2T,mpp}=437 \text{ mV}$, $J_{Z,2T,mpp}=8.1 \text{ mA/cm}^2$) as for the FR circuit of $P_{2T,FR,mpp}=3.6 \text{ mW/cm}^2$ ($V_{RF,2T,mpp}=437 \text{ mV}$, $J_{F,2T,mpp}=8.2 \text{ mA/cm}^2$) and both J - V characteristics match well.

The moderate performance of the device is probably caused by resistance-limited recombination¹⁰ as suggested in figure 8.8b by the local ideality factor of the dark J - V characteristics [90]. At voltages below 300 mV, the dark characteristic is dominated by a finite ohmic shunt resistance of $5 \text{ k}\Omega\text{cm}^2$ and $11 \text{ k}\Omega\text{cm}^2$ for the dark FR and RZ circuit characteristic, respectively, and a hump shows up in the local ideality. At moderate voltages between 300 mV and 550 mV, a second hump is observed, which originates from resistance-limited recombination [90]. The origin of this second hump is most likely due to the following: The laser contact opening of the dielectric layer on top of the POLO junctions leads to an irregular poly-Si layer within the contact opening with a thickness down to less than 50 nm [156]. On the irregular poly-Si layer, a small amount of aluminum was observed to penetrate through the POLO junction with scanning electron microscopy imaging. The penetrated aluminum forms localized Schottky contacts to the lowly-doped p -type wafer and acts as resistance-limited recombination center. Furthermore, the penetration of aluminum through the floating n^+ POLO contact can cause floating junction shunting. Since the passivation of a floating junction relies on the band bending, i.e. a built-in voltage between the base and the floating junction, a shunted floating junction leads to a poor passivation of that junction and diminishes the fill factor and open-circuit voltage [90].

For voltages beyond 550 mV, the series resistance of $1 \Omega\text{cm}^2$ and $1.1 \Omega\text{cm}^2$ for the dark FR and RZ circuit characteristic, respectively, leads to an expected increase of the local ideality factor. A large series resistance of around $1 \Omega\text{cm}^2$ is expected from lateral majority-carrier (holes) transport in the highly resistive wafer base at low injection conditions and it can be concluded that only a small part of the series resistance stems from electron transport at the POLO junction or the metal grids. Due to the m - V characteristic, the 2T J - V can not be described by a two-diode model accurately.

The absolute performance of the examined cell is sufficient to demonstrate the working principle of a 3T bipolar junction bottom cell and to identify its limitations.

Three-terminal operation

As will become evident, the 3T operation is almost the same as for the unijunction bottom cell. Therefore, it is summarized only briefly.

Figure 8.9a depicts the measured J_Z - V_{RZ} characteristics for different J_F between -20 mA/cm^2 and 20 mA/cm^2 .

If $J_F = 0 \text{ mA/cm}^2$, the J_Z - V_{RZ} characteristics follows the J_Z - V_{RZ} of the 2T-operated 3T IBC cell. Positive J_F shift the J - V characteristic of the RZ circuit to more negative current densities and negative ones shift it up to more positive current densities. The 3T-MPP voltage of the RZ circuit has a minimum around 440 mV for a J_F of 5 mA/cm^2 and increases to about 490 mV for a J_F of $\pm 20 \text{ mA/cm}^2$. The voltage of the RZ circuit (V_{RZ}) is similar, but

¹⁰Resistance-limited recombination was discussed in the context of the parasitic poly-Si pn junction in figure 7.4.

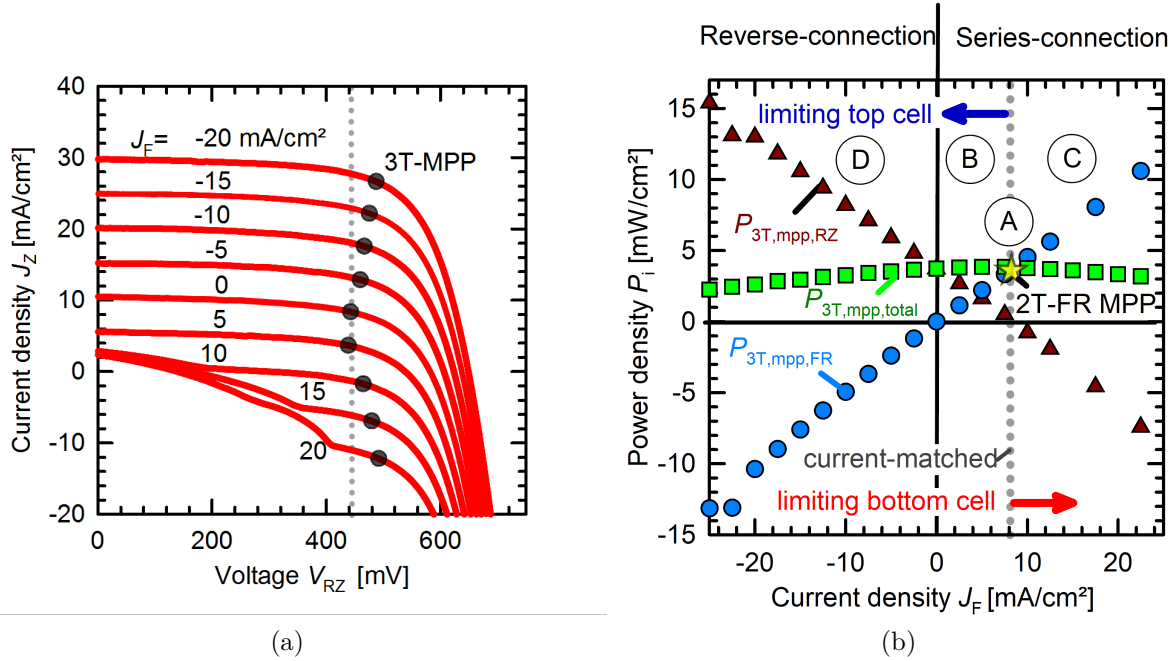


Figure 8.9.: (a) Measured J_Z - V_{RZ} characteristics (red) for different J_F values at an illumination level corresponding to $J_{Z,SC} = 10$ mA/cm² in two-terminal (2T) operation. Grey dotted line is a guide for the eye and indicates the maximum power point (MPP) voltage for the 2T operation ($J_F = 0$ mA/cm²). (b) Power densities for J_Z values between -25 mA/cm² and 22.5 mA/cm²: The total three-terminal (3T) power density $P_{3T, mpp, total}$ (green squares) and the corresponding fraction of $P_{3T, mpp, total}$ contributed by the FR circuit $P_{3T, mpp, FR}$ (blue circles) and the RZ circuit $P_{3T, mpp, RZ}$ (brown triangles). The yellow star represents the maximum power point for 2T operation of the FR circuit of the cell. Operation modes A, B, C, D correspond to figure (a), (b), (c), (d) in figure 8.10.

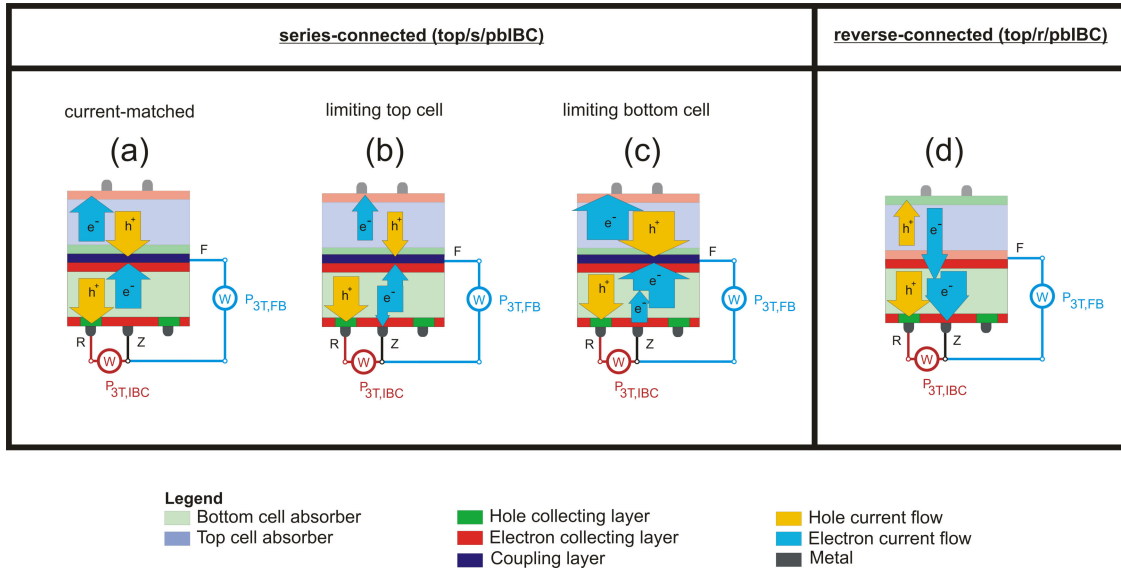


Figure 8.10.: Different operation regimes of a three-terminal interdigitated back contact (3T-IBC) bottom cell in a series-connected tandem cell (top/s/pbIBC) with current-matched subcells (a), with current-limiting top cell (b) and with current-limiting bottom cell (c) or in a reverse-connected tandem cell (top/r/pbIBC). Yellow arrows represent hole current flow and blue arrows electron current flow. Red and blue watt meters represent the calculation of the powers at the 3T-MPP from the J - V measurements in figure 8.9a for the RZ and FR circuit.

not identical, to the voltage V_{RF} of the FR circuit for the investigated current densities J_F . The origin of the voltage drop $V_{RF} - V_{RZ}$ is discussed within the framework of an equivalent circuit model in subsection 8.4.2. Figure 8.9b shows the maximum electrical power density extracted from the RZ circuit ($P_{3T, mpp, RZ}$) and from the FR circuit ($P_{3T, mpp, FR}$), as well as the resulting total electrical power density $P_{3T, mpp, total}$ as a function of the current density J_F . All power densities for the 3T measurements were determined at the maximum of the total power density $P_{3T, total}$.

Depending on the magnitude and sign of J_F , four different operation modes of the bottom cell are possible as already discussed for the unijunction bottom cell. Figure 8.7 illustrates the current flows of electrons and holes in the investigated bottom cell and a hypothetical top cell, which is emulated by the constant current source.

Current-matched operation of series-connected tandem If J_F matches the current density $J_{F, 2T, mpp} = 8.2 \text{ mA/cm}^2$ of the 2T-operated bottom cell at maximum power point, then the complete photo-generated electron current density is collected at the minority carrier contact F at the front side and no electrons are left for the rear minority carrier contact Z of the bottom cell (figure 8.10a). No electrical power is extracted from the RZ circuit, but the whole power is extracted from the FR circuit and equals that of the 2T reference case $P_{2T, FR, mpp}$.

Operation in series-connected tandem with current-limiting top cell If J_F is smaller than $J_{F,2T,mpp}$, the scenario of a current-limiting top cell (figure 8.10b) is emulated. The additional rear minority carrier contact Z enables the collection of the excess minority carriers (electrons), which are not collected by contact F. The power density of the FR circuit $P_{3T,mpp,FR}$ (blue circles) decreases and that of the RZ circuit $P_{3T,mpp,RZ}$ (brown triangles) increases to almost the same extent with decreasing J_F . First, the total power density increases slightly to a maximum power density at a J_F of 7.5 mA/cm². Then the total power density $P_{3T,mpp,total}$ decreases again for decreasing J_F .

Operation in series-connected tandem with current-limiting bottom cell If J_F is larger than $J_{F,2T,mpp}$, a current-limiting bottom cell is emulated (figure 8.10c). The additional rear minority carrier contact Z in the 3T bottom cell enables efficient minority carrier (electron) injection into the bottom cell and the injected minority carrier current density re-balances the electron current density at the front contact F of the bottom cell in such a way that the hole current density of the top cell is “matched”. The injection of electrons at the rear minority carrier contact appears as a negative extracted power density $P_{3T,mpp,RZ}$ in figure 8.9b, which is synonymous to power injection into the bottom cell by the RZ circuit. The power density extracted at the FR circuit $P_{3T,mpp,FR}$ increases with increasing J_F and is larger than the power density $P_{2T,FR,mpp}$ in the current-matched 2T case. The net 3T bottom cell power density $P_{3T,mpp,total}$ decreases slightly.

Operation in reverse-connected tandem For negative J_F , the operation of a reverse-connected tandem cell is emulated (figure 8.10d). The front contact of the top cell collects the photo-generated holes and the rear contact of the top cell collects the electrons within the top cell. The electron current density collected by the rear contact of the top cell is then injected via the minority carrier contact F at the front side into the bottom cell. The minority carrier contact Z at the rear side of the bottom cell collects the injected and photo-generated electrons and the majority carrier contact R collects the photo-generated holes in the bottom cell. The extracted power density in the RZ circuit $P_{3T,mpp,RZ}$ exceeds the power density $P_{2T,FR,mpp}$ of the current-matched case. The injected power density at contact F appears as a negative extracted power density $P_{3T,mpp,FR}$. The attainable total power density from the 3T bipolar junction bottom cell is lowered.

8.3.3. Summary of the common principles of operation

In the previous subsection, the similar operation principles for unijunction and bipolar junction bottom cell were discussed. Both bottom cells showed that they maintain their power output approximately constant independent of the current density applied from the top cell to the front contact. This is enabled by the fact that efficient transfer of charge carriers between the front contact F and contact Z is ensured. However, for the unijunction bottom cell majority carriers and for the bipolar junction bottom cell minority carriers are exchanged. Thus, the transport of charge carriers between the F and Z contact determines

how efficient the 3T operation is performed¹¹. In the following, detailed models for both cell architectures are presented and the transport between the front contact F and contact Z will be discussed.

8.4. Equivalent circuit model

The qualitative picture of a 3T-IBC cell, as presented in the previous section, is sufficient to describe the operation and the physics of a 3T-IBC cell in a simple and clear manner. The J - V characteristics were presented. The occurrence of a voltage difference between contact F and Z, and a power density loss was observed. This observation will now be discussed and explained in detail below.

8.4.1. Model of a unijunction bottom cell

In order to quantitatively model the J - V characteristic of a 3T bottom cell at each terminal, the 3T bottom cell is described by extending a simple and well-established two-diode solar cell model [412] to the 3T model shown in figure 8.11a. Using this extended model, the observed voltage difference $V_{ZF} = V_{RZ} - V_{RF}$ between the rear majority carrier contact Z and front majority carrier contact F together with the power density loss $\Delta P_{3T, mpp, total}$, which causes a parabolic shape of $P_{3T, mpp, total}$, is explained. The inner part of the circuit model (between nodes 1 and 2) is the two-terminal two-diode model. The two-diode model is composed of a current source providing a photo-generated current density J_{Ph} , diodes with an ideality factor of one and two with the corresponding diode current densities J_{D1} and J_{D2} , a series resistance R_S and shunt resistance R_{SH} . This part of the full model is characterized by the cells current density J_R at the root contact R and the cell voltage V_C . The cell voltage equals the diode voltage V_D reduced by a voltage drop across the series resistance R_S ¹². Equation 8.2 describes the relationship between the current density J_R and voltage V_C of the inner part of the model, the 2T cell, and is still valid for inner part of 3T cells.

$$\begin{aligned}
 J_R(V_C) &= J_{Ph} - J_{D1} - J_{D2} - J_{SH} \\
 &= J_{Ph} - J_{0,D1} \cdot \left(\exp \frac{q(V_C + J_R \cdot R_S)}{k_B T} - 1 \right) \\
 &\quad - J_{0,D2} \cdot \left(\exp \frac{q(V_C + J_R \cdot R_S)}{2k_B T} - 1 \right) - \frac{V_C + J_R \cdot R_S}{R_{SH}}
 \end{aligned} \tag{8.2}$$

$J_{0,D1}$ and $J_{0,D2}$ are the corresponding saturation current densities of diode 1 and 2. q is the elementary charge, k_B is the Boltzmann constant and T is the temperature. The two-terminal model is extended to a three-terminal model by introducing an additional majority carrier contact, the third terminal. The current path at node 1 in figure 8.11a is divided in two current paths, which connect the rear majority carrier contact Z and the front majority carrier contact F. Kirchhoffs point rule is applied to node 1 and the cells current density J_R

¹¹This fact becomes evident in the following modelling section.

¹²Note that the full series resistance of the 2T cell is $R_S + R_i$ with $i = F, Z$.

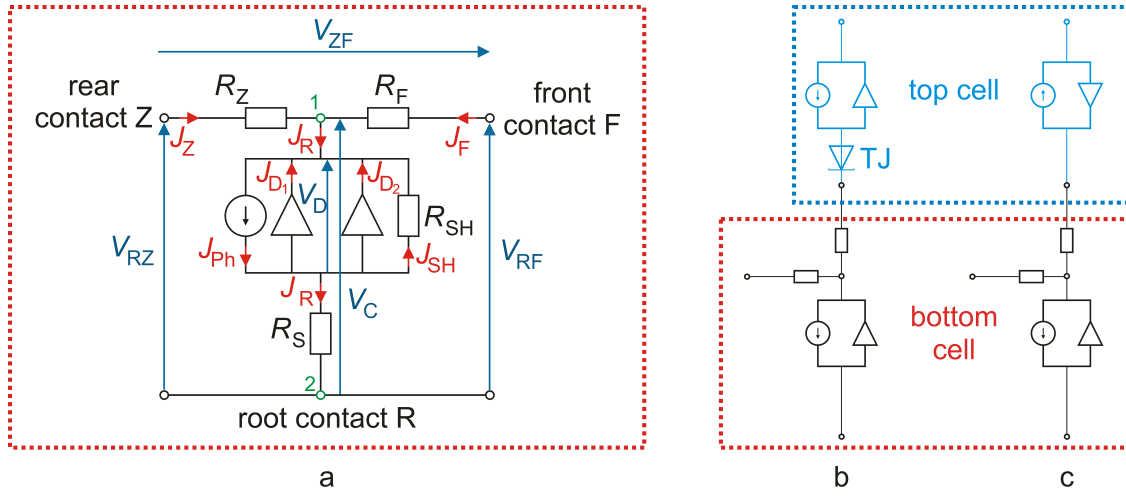


Figure 8.11.: (a) Detailed equivalent circuit model of a unijunction three-terminal (3T) bottom cell with two majority carrier contacts and a single minority carrier contact. The circuit model between nodes 1 and 2 is a 2T double diode model. (b,c) Model of a 3T tandem solar cell comprising a simplified equivalent circuit model of the 3T bottom cell series-connected (b) or reverse-connected (c) with a top solar cell.

decomposes into the sum of the current densities at the front majority carrier contact J_F and rear majority carrier contact J_Z as described in equation 8.3.

$$J_R = J_F + J_Z \quad (8.3)$$

The model introduced so far (with $R_Z = 0$ and $R_F = 0$) in figure 8.11a is intuitive and therefore commonly used for mid-contacted 3T tandem solar cells [93, 295, 298, 304, 306] as shown in figure 8.11b and 8.11c (with $R_Z = 0$ and $R_F = 0$). However, several authors [297, 300, 305, 413, 414] reported effects resulting from resistive coupling of top and bottom cell in a mid-contacted 3T cell architecture (as shown in figure 8.11b and 8.11c). This is consistent with the observation from the previous subsection for a 3T nuIBC bottom cell that a voltage difference $V_{ZF} = V_{RZ} - V_{RF}$ arises between the two majority carrier contacts accompanied by a power density loss $\Delta P_{3T, mpp, total}$. Thus, additional resistances are introduced, which induce a voltage drop proportional to the corresponding current densities: R_Z at the rear majority carrier contact Z and R_F at the front majority carrier contact F. In this case, the terminal voltage V_i is given by equation 8.4 as the cell voltage less the voltage drop across the terminal resistance R_i , where i is either F or Z and indicates the probed terminal.

$$V_i = V_C - J_i \cdot R_i \quad (8.4)$$

The unijunction 3T bottom cell's equivalent circuit model is now fully described by figure 8.11a and equations 8.2, 8.3 and 8.4.

In order to validate the equivalent circuit model, all model parameters are determined in the appendix A.4. Analytic equations are used to explain the arising voltage difference V_{ZF}

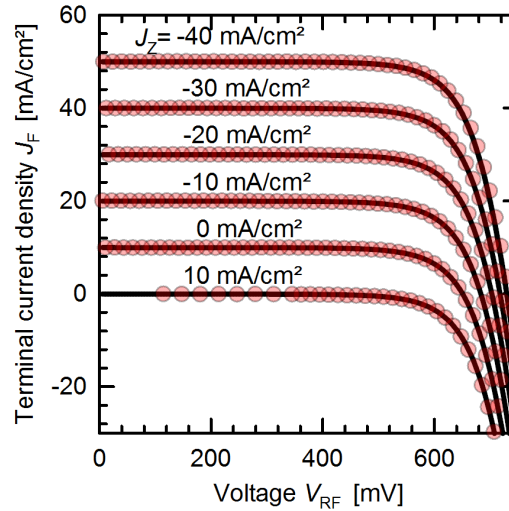


Figure 8.12.: Comparison of measured (red circles) and calculated (solid lines) J_F - V_{RF} characteristic for different J_Z .

and the parabolic power loss $\Delta P_{3T,mpptotal}$. Both result from Joule heating due to a current density flowing through the introduced resistances R_Z and R_F . The J_F value, where power density is maximized ($\Delta P_{3T,mpptotal}=0$), can be calculated as follows:

$$J_{F,3TPmax} = \frac{R_Z}{R_Z + R_F} \cdot J_{R,mppt} = J_{F,EP} \quad (8.5)$$

Equation 8.5, which describes the operation point, where power is maximized, is identical to equation A.17, which determines the equipotential between the two majority carrier contacts Z and F. Consequently, the power output is maximized for the equipotential case. This can be illustrated as follows. Since $V_{ZF,mppt} = 0$ mV for the equipotential case, R_Z and R_F are in parallel and the majority carrier current divides across the two resistors according to the current divider rule. The current flows along the path of least resistance and minimizes the resistive power loss. For the introduced resistances R_Z and R_F approximately the same value of $160 \text{ m}\Omega\text{cm}^2$ is found. Figure 8.12 compares the calculated and measured J - V characteristic using the determined resistances and shows a good agreement.

It is now interesting to discuss the origin and physical meaning of R_Z and R_F . Naturally, majority carrier transport resistances, which are distributed within the bottom cell, are considered as the origin. The lumped resistance value for the majority carrier transport is found by solving Poissons equation for the given geometries and sheet conductivities of the bottom cell by means of a finite element analysis in the appendix A.4. It is found that the lateral transport resistance within the poly-Si layer at the front side has about the same value as R_F and the lateral resistance within the wafer, which reflects the rear side geometry, has approximately the same value as R_Z . Therefore, R_F correlates with the sum of all resistances at the front side and R_Z to those at the rear side. For the ideal case, $R_Z = R_F = 0$ and requires at least an infinitely large conductivity within the wafer. This is not achievable for

a real device and the voltage difference $V_{ZF, mpp}$ between the two majority carrier contacts accompanied by the parabolic shape of $P_{3T, mpp, total}$ is an inherent property of unijunction 3T-IBC cells. However, for several scenarios e.g. small grid dimensions¹³ and large base conductivity¹⁴, the ideal case is approached.

Design guidelines for a unijunction bottom cell

From the equivalent circuit models of a 3T unijunction bottom cell and the detailed discussion of the introduced resistors R_F at the front and R_Z at the rear base contact, design guidelines can be deduced for the bottom cell of efficient 3T tandem cells.

For measurement purposes, the experimental 3T unijunction bottom cells discussed in previous subsections were fabricated with a front side metal grid. However, in a monolithic tandem cell, the front side metal grid will be replaced by a transparent full-area contact, between the top and bottom cell. The transparent full-area contact between top and bottom cell can be a tunnel junction for the series-connected tandem cell and at least a common Ohmic carrier-selective contact¹⁵ for the reverse-connected tandem cell. Replacing the grid by a full-area contact will eliminate lateral current flow at the front side of the bottom cell and thus the front side lateral resistance, which was the largest contributor to R_F . The full-area contact between top and bottom cell might add another resistive component to R_F , but it is anticipated that R_F is small in a well-designed 3T tandem solar cell.

Reverse-connected tandem solar cells

In a reverse-connected 3T tandem (figure 8.11c), current is injected from the top cell into the bottom cell through the front contact F of the bottom cell and the injected current density accompanied by the photo-generated current density in the bottom cell has to be collected at the rear contact Z of the bottom cell. Thus, J_Z is approximately constant with varying top cell band gaps and equal to the photo-generated current density in the Si bottom cell without a top cell ($\approx 44 \text{ mA/cm}^2$) [415, 416]. For wide top cell band gaps, J_F at the front contact of the bottom cell is small and the power dissipation at R_F is minor. The photo-generated current density in the bottom cell is large and the resistive power loss is governed by R_Z . For narrow top cell band gaps, J_F becomes larger and a significant amount of power is dissipated at the R_F resistor. The current density and the power loss at the rear contact Z remain almost constant. Due to the constant and large J_Z of approximately 44 mA/cm^2 (compared to lower J_{FR}), the power loss of a reversed-connected 3T bottom cell with a wide band gap cell ($>1.7\text{eV}$) is similar to a conventional IBC cell and the R_Z has to be minimized for highly

¹³E.g. if the pitch approaches the wafer thickness.

¹⁴If grid dimensions are small, then the current flow becomes approximately single dimensional and the resistance can be approximately calculated by multiplying the wafer thickness with the specific wafer resistance. For a $150 \mu\text{m}$ -thick wafer with a specific resistance of $1 \Omega\text{cm}$, the resistance is $15 \text{ m}\Omega\text{cm}^2$ and induces a voltage difference below 1 mV for a maximum current densities of 40 mA/cm^2 .

¹⁵This common Ohmic carrier-selective contact can be a single “layer” or any barrier in the energy band for the carriers to be blocked. The common contact prevents the exchange of one sort of carriers between both sub-cells. Two adjacent carrier selective contacts, e.g. n^+ POLO and the electron transport layer of a perovskite cell, would fulfil this function.

efficient 3T tandems. The R_F should be kept low for narrow band gap top cells.

In summary, bottom cells for highly efficient reverse-connected tandem cells should be designed similar to high efficiency IBC single junction solar cells with low R_Z values [156, 157, 396, 417]. Large-scale industrial-type IBC cells with a total series resistance of $0.4 \Omega\text{cm}^2$ and an efficiency of 25.2% as reported by Smith et al. [189] are an excellent choice for industrialization of reverse-connected tandem cells.

Series-connected tandem solar cell

A 3T unijunction bottom cell with a small $R_F = 0.1 \Omega\text{cm}^2$ and a large $R_Z = 1 \Omega\text{cm}^2$ in a series-connected tandem cell with a top cell around 1.7 eV (as shown in figure 8.11b) dissipates only a small amount of electrical power into heat power across the two resistors, since the current density at the front contact of the bottom cell is matched to the top cell current density ($\approx 22 \text{ mA/cm}^2$) [44, 416] and no surplus carriers have to be collected or injected at the highly resistive rear base contact. For wider band gap top cells, the photo-generated current density of the bottom cell exceeds that of the top cell. The power dissipation at the front contact of the bottom cell reduces while the rear base contact has to collect the excess current density in the bottom cell and the resistive gain at front side is compensated by the loss at the rear contact. For very high band gaps ($\gg 2 \text{ eV}$) the resistive loss is mostly governed by the rear contact, while the loss at front contact vanishes. This situation is comparable to that in a single junction IBC cell.

For top cells with a narrow band gap, the top cell current density exceeds the photo-generated bottom cell current density. The rear contact Z of the bottom cell injects the missing majority carriers to rebalance the current density mismatch at the front contact F of the bottom cell. Thus, the current density and the power dissipation increase at the R_F and R_Z resistors with decreasing top cell band gap. However, the current density at the front contact of the bottom cell is always larger than at the rear contact Z by the photo-generated current density. R_F is therefore more important than R_Z . As a consequence, it is necessary to minimize R_F and to ensure sufficiently low R_Z values of 3T bottom cells in a series-connected tandem solar cells with top cells with narrow band gaps ($\ll 1.7 \text{ eV}$). For tandem cells with a top cell band gap between 1.6 eV and 1.8 eV, a high R_Z of up to $10 \Omega\text{cm}^2$ is tolerable to keep the loss below 0.5%. For wide top cell band gaps the R_Z has to be low and R_F becomes less important.

To conclude, a bottom cell as designed for reverse-connected tandem cells would perform well in a series-connected tandem cell, but the design is not optimal in terms of fabrication complexity and performance. Bottom cells for series-connected tandem cells follow slightly different design rules. The bottom cell has to minimize the R_F resistance as for the reverse-connected case, but allows larger R_Z values. This relaxes the requirements for the design of the IBC grid and offers the potential to reduce the complexity and costs of cell production while maintaining acceptable R_Z values. One possible approach to optimize the design of a bottom cell for a series-connected 3T tandem is to start from the sample IBC cell in figure 8.3 and to reduce the contact fraction of the majority carrier contact contact Z, which would result in an increased contact and lateral resistance component of the R_Z . This simultaneously maximizes the emitter fraction and therefore avoids electrical shading effects. Additionally,

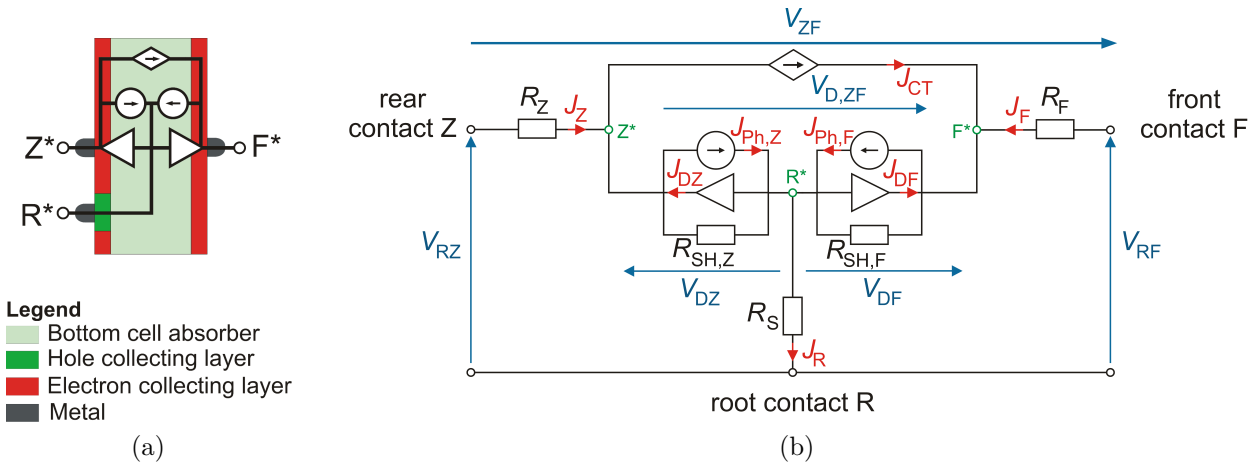


Figure 8.13.: (a) Schematic of the cross-section of a bipolar junction three-terminal bottom cell overlaid with the modified Ebers-Moll transport model. The asterisks in F^* , R^* and Z^* indicates the “inner” terminal node in figure 8.13b. (b) Detailed equivalent circuit model of a bipolar junction three-terminal bottom cell including shunt and series resistances.

the performance of the bottom cell might benefit from choosing a higher wafer resistivity due to lower defect and Auger recombination and lower free carrier absorption.

Given the fact that low contact fractions for the majority carrier contact Z are acceptable for series-connected 3T tandem cells, another approach would be to use a simple double-side contacted cell concepts similar to Peibst *et al.* [35], which may be extended to a 3T cell by inserting a small fraction (0.1-1%) of (non-passivating) majority carrier-type point contacts at the rear side of the cell with a millimeter scale distance between the contacts. Such contacts can be realized by laser-fired and bonding contacts [31, 418] in a two-level metallization scheme [419] and would provide a low-cost, but high efficiency approach for series-connected 3T tandem cells. The use of laser-fired and bonding contacts in a two-level metallization scheme would furthermore facilitate the interconnection into 2T modules.

8.4.2. Model of a bipolar junction bottom cell

In the previous section, the possible operation modes of a bipolar junction bottom cell were presented based on experimental observations. The voltage difference between both minority carrier contacts and the power dissipation observed in figure 8.9b ($P_{3T,mpp,total}$) is less intuitive compared to the unijunction bottom cell. In order to understand the physics behind the operation modes and the mechanisms associated with the power dissipation, an equivalent circuit model for a bipolar junction bottom cell is presented in the following.

Figure 8.13a shows the cross-section of a bipolar junction bottom cell (pbIBC), which is overlaid with the equivalent circuit model of a bipolar junction bottom cell. The detailed derivation of the circuit model from drift-diffusion model is presented in appendix A.5.1. Figure 8.13b extends this equivalent circuit model by incorporating a shunt resistance $R_{SH,i}$

and a series resistance R_i at each minority carrier contact $i = Z, F$ and a lumped series resistance R_S at the majority carrier contact R. If the shunt resistances are neglected, then the inner circuit model between the nodes Z^* , F^* and R^* simplifies to that in figure 8.13a. Figure 8.13a is used to motivate the equivalent circuit model and figure 8.13b contains the labels of each circuit element.

The bipolar junction bottom cell consists of a p -type absorber material, a majority carrier (hole) contact and two minority carrier (electron) contacts. The majority carrier (hole) contact is assumed to be a perfectly hole-selective ohmic contact and therefore a loss-free wire connects contact R^* in the circuit model. Each minority carrier contact forms a rectifying junction with the absorber and diodes DZ at contact Z^* and DF at contact F^* account for this fact in the equivalent circuit model. The voltage V_{DZ} or V_{DF} across the diode controls the minority carrier concentration in the absorber at the contact's boundary and thus the current density J_{DZ} or J_{DF} through the diode. Furthermore, a voltage difference $V_{D,ZF} = V_{DF} - V_{DZ}$ between the contacts F^* and Z^* results in a spatial gradient of minority carrier concentrations in the absorber from the contact with the higher potential to that with the lower potential. The resulting gradient of the chemical potential drives a diffusive transfer current density J_{CT} of minority carriers between both minority carrier contacts. This is represented with a voltage-controlled current source¹⁶. The obtained equivalent circuit model without illumination ($J_{Ph,Z} = J_{Ph,F} = 0$) is the well-known Ebers-Moll transport model for bipolar junction transistors [99].

To arrive at the final bipolar junction bottom cell model with illumination in figure 8.13a, constant current sources for the photo-generation in the absorber are superposed with the Ebers-Moll transport model. Superposition principle applies in this case because the obtained differential equations of the drift-diffusion model are linear (see appendix A.5.1) [408]. The corresponding model equations for the bipolar junction bottom cell in the simplest version (without shunt and series resistances) are as follows.

$$\begin{aligned}
 J_{CT} &= J_S \cdot [\exp(\frac{qV_{DF}}{k_B T}) - \exp(\frac{qV_{DZ}}{k_B T})] \\
 J_Z &= J_{Ph,Z} - J_{DZ} + J_{CT} = (1 - \Gamma) \cdot J_{Ph} - J_{0,DZ} \cdot [\exp(\frac{qV_{DZ}}{k_B T}) - 1] + J_{CT} \\
 J_F &= J_{Ph,F} - J_{DF} - J_{CT} = \Gamma \cdot J_{Ph} - J_{0,DF} \cdot [\exp(\frac{qV_{DF}}{k_B T}) - 1] - J_{CT} \\
 J_R &= J_Z + J_F = J_{Ph} - (J_{DZ} + J_{DF})
 \end{aligned} \tag{8.6}$$

J_S is denoted as the base transport coefficient¹⁷. $J_{0,DZ}$ and $J_{0,DF}$ are the saturation current densities of the diodes DZ and DF, respectively. $J_{Ph,Z}$ and $J_{Ph,F}$ are the photo-generated current densities at diodes DZ and DF, respectively. The total photo-generated current density J_{Ph} is the sum of $J_{Ph,Z}$ and $J_{Ph,F}$. The normalized photo-current density at the front terminal of the bottom cell $\Gamma = \frac{J_{Ph,F}}{J_{Ph}}$ is a number between 0 and 1, and describes the fraction

¹⁶rectangular current source symbol

¹⁷In the context of bipolar junction transistor models, J_S is often called (transport) saturation current density or intercept current density [99, 420–423]

8.4. EQUIVALENT CIRCUIT MODEL

of the total photo-generation, which contributes to the photo-generated current density at diode DF. Appendix A.5.2 provides a detailed discussion of Γ and concludes that Γ reflects the spatial distribution of photo-generated carriers through the generation profile. Γ can be calculated explicitly by numerical integration of tabulated data or analytic expressions of the generation profile¹⁸.

Note that the model in equation 8.6 is derived for low-level injection condition. However, Gummel's charge control relation [420, 421] and its extension [424] represent the most general relation for the transfer current density J_{CT} and provide an equivalent circuit model for high-level injection conditions (see appendix A.5.1). The obtained circuit model is almost the same as in figure 8.13b, but J_S is now voltage-dependent.

The model equations 8.6 can now be used to calculate the total power density $P_{3T,total}$ extracted from a 3T bipolar junction bottom cell by summing up the powers extracted at each minority carrier terminal.

$$\begin{aligned}
 P_{3T,total} &= J_Z \cdot V_{DZ} + J_F \cdot V_{DF} = P_{Ph} - P_D - P_{CT} \\
 P_{Ph} &= (1 - \Gamma) J_{Ph} \cdot (V_{DZ} + \frac{\Gamma}{1-\Gamma} \cdot V_{DF}) \\
 P_D &= J_{DZ} \cdot V_{DZ} + J_{DF} \cdot V_{DF} \\
 P_{CT} &= J_{CT} \cdot (V_{DF} - V_{DZ})
 \end{aligned}
 \tag{8.7}$$

Similar to a unijunction junction solar cell, the total power density includes a photo-generating term P_{Ph} and the diode recombination term P_D for the diodes DZ and DF. Additionally in a bipolar junction bottom cell, the transfer process of minority carriers¹⁹ between contact F* and contact Z* dissipates a power density P_{CT} . Conclusively, the $P_{3T,mpp,total}$ curve in figure 8.9b is expected to exhibit a point of operation at a current density $J_{F,EP}$, where $P_{3T,mpp,total}$ is maximum. This point of operation relies on minimizing the power dissipation and hence requires that contact Z* and F* are at the same potential to ensure that the transfer current density ($J_{CT} = 0$) and dissipative power density ($P_{CT} = 0$) vanish. For the latter conclusion, it is assumed that $J_{0,DZ}$ and $J_{0,DF}$ are similar.

Equipotential operation – $V_{ZF,mpp} = 0$

The fact that the power density $P_{3T,mpp,total}$ is maximized at equipotential operation ($V_{DZ,EP} = V_{DF,EP}$) was also found for the 3T unijunction bottom cell (equation A.20) and therefore applies as a general rule of thumb to 3T bottom cells. For example, if R_Z and R_F in figure 8.13b are taken into account, then another dissipative power density $P_{Res}(J_{CT})$ has to be added in equation 8.7. Now, $P_{Res} + P_{CT}$ is minimized²⁰ and J_{CT} is not necessarily zero.

¹⁸P. Stradins pointed out in a private communication that this statement is only true for a single dimensional cell. For a 2- and 3-dimensional model Γ will be modified by lateral transport.

¹⁹Note that this loss is not caused by recombination in the absorber, since the model equation were derived under the assumptions of an infinite minority carrier lifetime in the absorber.

²⁰Again, it is assumed that P_D does not change significantly with J_{CT} in the range of interest.

However, the equipotential operation ($V_{RZ,EP} = V_{RF,EP}$) still reflects the operation point, where $P_{3T,mpp,total}$ is maximized.

Since the 3T bipolar junction bottom cell in this section is designed such that R_Z and R_F are negligibly small, the effect of P_{Res} is neglected in the following and $J_{CT} = 0$ in case of equipotential operation. Under that conditions, the maximum power point voltage $V_{DZ,EP,mpp} = V_{DF,EP,mpp}$ for the equipotential case can be calculated from equations 8.6 by using a Taylor approximation as follows²¹.

$$V_{DF,EP,mpp} = V_{DZ,EP,mpp} = V_{EP,mpp} = \frac{k_B T}{q} [A_1 \cdot \ln \left(\frac{J_{Ph}}{J_{0,DZ} + J_{0,DF}} \right) - A_2] \quad (8.8)$$

If the Taylor approximation is performed around a voltage of 514 mV (corresponds to $\frac{qV_{EP,mpp}}{k_B T} = 20$), A_1 and A_2 are about 0.955 and 2, respectively. The Taylor approximation is also accurate for values between 440 mV and 720 mV within a relative error margin of 2.5%. For decent solar cells, diode saturation current densities $J_{0,DF}$ and $J_{0,DZ}$ between 20 fA/cm² and 50 fA/cm² for each of the DF and DZ diodes are typical. For a photo-current density of about 10 mA/cm², a voltage $V_{EP,mpp}$ between 575 mV and 600 mV for the equipotential case is expected. In contrast to this prediction, the experimental cell in figure 8.9a exhibits a voltage $V_{EP,mpp}$ of about 445 mV only. However, equation 8.8 does not include parasitic effects like non-ideal diode recombination, shunt or series resistance and the voltage value above 575 mV can be considered as an upper estimate. The current density $J_{F,EP,mpp}$ extracted from contact F* under equipotential operation is determined by a photo-generation current density and a diode recombination current density.

$$J_{F,EP,mpp} = \Gamma J_{Ph} - J_{0,DF} \cdot \left(\exp \frac{qV_{EP,mpp}}{k_B T} - 1 \right) \quad (8.9)$$

The exponential diode recombination defines the current density at the maximum power point as it would do for all type of solar cells (see section 2.3). The exponential recombination current density is typically small compared to the photo-generation current density and does not change considerably upon a deviation of the voltage from the equipotential operation. Therefore, in the case of equation 8.9, ΓJ_{Ph} determines the current density $J_{F,EP,mpp}$, where equipotential operation of the cell leads to a maximum in $P_{3T,mpp,total}$. Since Γ depends on the photo-generation profile within the cell, the optics of the cell and especially the illumination spectrum are important factors. If the front side of a Si bipolar junction bottom cell is illuminated with AM1.5G spectrum, most of the carriers are generated close to the front side and Γ is close to unity. For monochromatic illumination of a Si cell with a wavelength close to the absorption band-edge, an almost equal amount of carriers is generated at the front and rear side of the cell and Γ approaches $\frac{1}{2}$ for the case of homogeneous generation. Both cases are illustrated in figure A.14.

The investigated cell in figure 8.9b is illuminated from the front side with a tungsten-halogen lamp with a spectrum, which can be approximated with black-body radiation with a body temperature of about 3000 K [425]. A ray tracing simulation of the bipolar junction bottom

²¹The derivation of this equation can be found in the appendix A.5.3.

cell similar to that in appendix A.2.1 with the black-body spectrum yields the generation profile of the investigated cell and Γ is calculated to be about 0.84 by numerical evaluation of the integral in equation A.62. Conclusively, most of the photo-generated carriers are generated close to the front contact and $J_{F,EP,mpp}$ in figure 8.9b is close to the current density of the current-matched case, in which all photo-generated current is collected at the front junction.

Voltage $V_{ZF,mpp}$ in non-equipotential operation

For any operation state outside of the equipotential one, a minority-carrier transfer current density $J_{CT} \neq 0$ is required to flow between both diodes. The diode voltages are not equal anymore and a power density $P_{CT,mpp}$ is dissipated.

Figure 8.14a shows the evolving voltage difference $V_{ZF,mpp}$ as function of $J_{F,mpp}$. For the current density $J_{F,EP,mpp}$ of about 6.6 mA/cm², the voltage $V_{ZF,mpp}$ is zero and $J_{F,EP,mpp}$ can be used to calculate the transfer current density (blue x-axis at the top of figure 8.14) as²²

$$J_{F,EP,mpp} - J_{F,mpp} = J_{CT} + J_{0,DF} \cdot \left(\exp \frac{qV_{DF,mpp}}{k_B T} - \exp \frac{qV_{EP,mpp}}{k_B T} \right) \approx J_{CT}. \quad (8.10)$$

For small magnitudes of $J_{CT,mpp}$ close to equipotential operation in figure 8.14, $V_{ZF,mpp}$ appears to be a linear function of $J_{CT,mpp}$, but saturates logarithmically for larger magnitudes of $J_{CT,mpp}$.

In the framework of the equivalent circuit model, the following explicit equation for $V_{ZF,mpp}$ as function of $J_{CT,mpp}$ is obtained by rearranging the relationship between $J_{CT,mpp}$ and the diode voltages $V_{DZ,mpp}$ and $V_{DF,mpp}$ in equation 8.6.

$$V_{ZF,mpp} = V_{DF,mpp} - V_{DZ,mpp} = \frac{2k_B T}{q} \cdot \operatorname{arcsinh} \left[\frac{J_{CT,mpp}}{2 \cdot J_S \cdot \exp \frac{q(V_{DZ,mpp} + V_{DF,mpp})}{2k_B T}} \right] \quad (8.11)$$

The voltage $V_{FZ,mpp}$ depends on $J_{CT,mpp}$ through the inverse hyperbolic sine function, which is qualitatively in agreement (at least for small $J_{CT,mpp}$) with the experimental observation in figure 8.14a. The denominator of the argument of the inverse hyperbolic sine consists of J_S multiplied by an exponential function, whose exponent contains the average of the diode voltages $V_{DZ,mpp}$ and $V_{DF,mpp}$. As pointed out in appendix A.5.4, the average of the diode voltages approximately equals the equipotential voltage $V_{EP,mpp}$ as long as $qV_{ZF,mpp} \ll k_B T$. In that case, the average voltage represents the quasi-Fermi level splitting in the absorber and therefore the exponential function is a measure for the minority carrier concentration. Furthermore, equation 8.11 approximates to the following linear transport law for $qV_{ZF,mpp} \ll 2k_B T$.

$$V_{ZF,mpp} \approx \frac{k_B T}{q} \cdot \frac{J_{CT,mpp}}{J_S \cdot \exp \frac{qV_{EP,mpp}}{k_B T}} = R_{\text{diff}} \cdot J_{CT,mpp} \quad (8.12)$$

²²The approximation is quite accurate as long as $J_S \gg J_{0,DF}$ and $J_S \gg J_{0,DZ}$ in equation 8.6, which is required for a useful 3T bipolar junction cell. In this case the red part of equation 8.10 can be safely neglected.

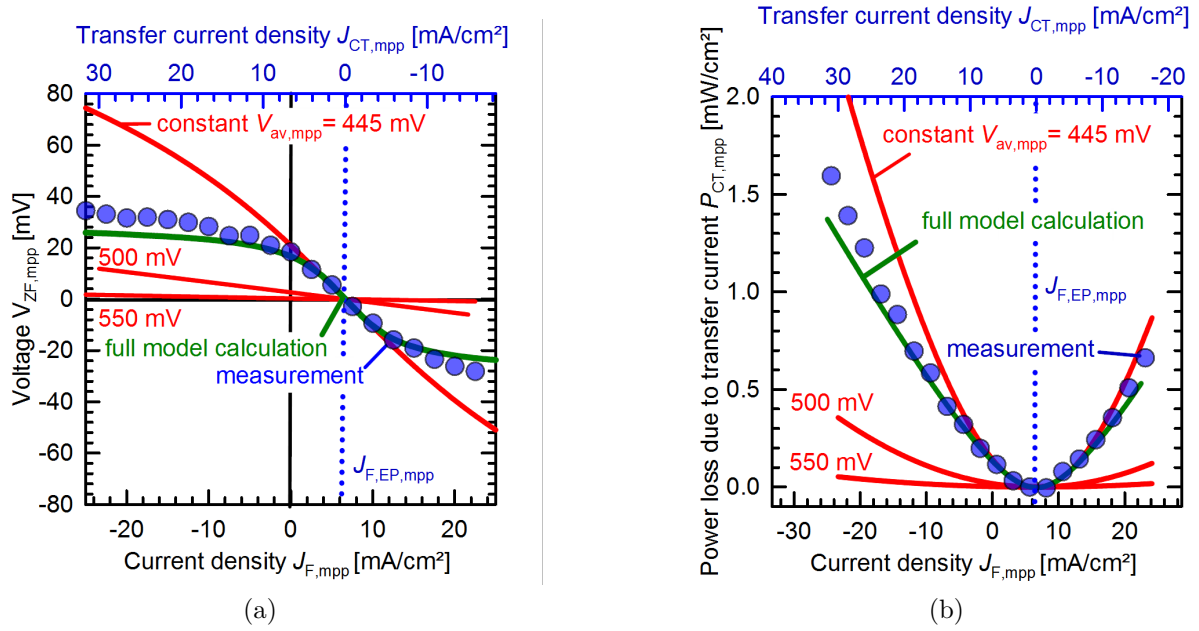


Figure 8.14.: (a) Measured and calculated voltage difference $V_{ZF,mpp} = V_{RF,mpp} - V_{RZ,mpp}$ between rear minority carrier contact Z and front contact F at the maximum total power point. (b) Comparison of experimentally determined and calculated power density loss $P_{CT,mpp}$ as a function of the transfer current density $J_{CT,mpp}$.

In this linear operation regime, a voltage difference between both minority carrier contacts drives a transfer current density proportional to a transport resistance $R_{diff}(V_{EP,mpp})$. This diffusion resistance R_{diff} is then defined as the resistance, which minority carrier experience, when they flow through a semiconductor [64].

$$R_{diff} = \frac{\frac{k_B T}{q}}{J_S \cdot \exp\left(\frac{qV_{EP,mpp}}{k_B T}\right)} \quad (8.13)$$

J_S for a p -type base with a thickness W_B , a minority carrier diffusion coefficient $D_{n,B}$, an equilibrium minority carrier concentration $n_{B,0}$ and with a sufficiently large minority carrier diffusion length calculates as follows (see also appendix A.5.1).

$$J_S = \frac{qD_{n,B}}{W_B} n_{B,0} \quad (8.14)$$

Using the definition of J_S and the Einstein relation between $D_{n,B}$ and minority carrier mobility $\mu_{n,B}$ in equation 8.13 yields a familiar form for the diffusion resistance.

$$R_{diff} = \frac{W_B}{q \cdot \mu_{n,B} \cdot n_{B,0} \cdot \exp\left(\frac{qV_{EP,mpp}}{k_B T}\right)} = \frac{W_B}{q \cdot \mu_{n,B} \cdot n_B} \quad (8.15)$$

The denominator of R_{diff} turns into the conductivity of the base for minority carriers, which is the product of the elementary charge q , minority carrier mobility $\mu_{n,B}$ and the minority

carrier density n_B .

The derived equation 8.11, 8.12 and 8.15 allow to calculate the voltage $V_{ZF,mpp}$ as a function of the transfer current density $J_{CT,mpp}$ from material properties and the equipotential voltage of the cell. For the cell in figure 8.14 with a wafer resistivity of $200 \Omega\text{cm}$, thus a dopant concentration of $6.7 \cdot 10^{13} \text{ cm}^{-3}$, the minority carrier concentration n_B amounts to $4.2 \cdot 10^{13} \text{ cm}^{-3}$ at an equipotential voltage of 445 mV and a temperature of 28°C . The diffusion resistance R_{diff} calculates to $3.25 \Omega\text{cm}^2$ from equation 8.15 with an electron mobility of $1378 \text{ cm}^2\text{V}^{-1}\text{s}^{-1}$ and a wafer thickness of $300 \mu\text{m}$.

The calculated voltage $V_{ZF,mpp}$ from equation 8.11 with the same input parameters and an assumed constant average voltage of 445 mV follows the linear relationship in equation 8.12 for $qV_{ZF,mpp} \ll \frac{1}{2}k_B T$. The calculation matches the experimental data in this linear regime well, which underlines the usefulness of the diffusive resistance picture.

The diffusion resistance is an intuitive representation of the ‘‘minority’’ carrier transport through the base and provides a simple way of understanding the operation principle of 3T bottom solar cells. In fact, equations 8.12 and 8.15 are not only valid for the low-level injection case, where the designation ‘‘minority carrier’’ has its justification, but can also be derived by using the (generalized) Gummel’s charge control relation [420, 424]²³. Since the charge control relation is also valid for high-level injection, it follows that the picture of a resistor from equations 8.12 and 8.15 also holds if the concentration of electrons and holes is similar.

For $qV_{ZF,mpp} > 2k_B T$, the calculation predicts a more than twice as high magnitude for $V_{ZF,mpp}$ as compared to the the experimentally determined one. The deviation results from the assumption that the average voltage $\frac{1}{2}(V_{DZ,mpp} + V_{DF,mpp}) \approx 445 \text{ mV}$ is constant for $J_{CT} > 0$. This assumption approximately holds for small values of $V_{ZF,mpp}$, but breaks down for larger values. When the full model from equations 8.6 and 8.7 with $J_{Ph} = 10 \text{ mA/cm}^2$, $\Gamma = 0.69$, $J_{0,DZ} = J_{0,DF} = 11 \text{ pA/cm}^2$ and $J_S = 320 \text{ pA/cm}^2$ is used to calculate the maximum power point, it turns out that the average voltage almost equals the equipotential voltage for $V_{ZF,mpp} \leq \pm 10 \text{ mV}$. Beyond $\pm 10 \text{ mV}$, the model with constant average voltage overestimates $V_{ZF,mpp}$, while the resulting $V_{ZF,mpp}$ from the full model as function of $J_{CT,mpp}$ agrees well with the experimental data in figure 8.14a.

Power density loss $P_{CT,mpp}$ in non-equipotential operation

The voltage $V_{ZF,mpp}$ drives a transport of minority carriers through the absorber and causes a power density loss $P_{CT,mpp}$. The power density loss $P_{CT,mpp}$ is calculated from the total power density $P_{3T,mpp,total}$ (figure 8.9b) by subtracting the absolute maximum of the total power density $P_{3T,mpp,total}(J_{CT,mpp} = 0)$ from $P_{3T,mpp,total}$. This implies the assumption that the complete loss results from the current transfer, such that the transfer current density $J_{CT,mpp}$ has to vanish in order to maximize the $P_{3T,mpp,total}$. The power density loss $P_{CT,mpp}$ is shown in figure 8.14b. For small $|J_{CT,mpp}|$ values around equipotential operation, the loss

²³In the case of Gummel’s charge control relation, J_{CT} still follows equation 8.6, but now J_S depends on the diode voltages V_{DZ} and V_{DF} , which control the base charge. In the equipotential case, J_S reaches some value $J_{S,EP}$ and as long as $V_{ZF} \ll V_{EP}$ and $qV_{ZF} \ll k_B T$, the contribution of biasing the junctions to the total base charge is negligible and J_S stays approximately constant.

grows quadratically with $|J_{CT,mpp}|$, which is consistent with irreversible thermodynamics for linear transport laws (as in equation 8.12) [45, chapter 16] and was discussed in the context of semiconductors by several authors [64, 69, 70, 394]. In this linear regime, the power density loss $P_{CT,mpp}$ can be calculated by multiplying the transfer current density $J_{CT,mpp}$ with the voltage $V_{ZF,mpp}$ from the linear transport law in equation 8.12.

$$P_{CT,mpp} = J_{CT,mpp} \cdot V_{ZF,mpp} \approx R_{diff} \cdot J_{CT,mpp}^2 \quad (8.16)$$

For the general case, equation 8.11 can be used to calculate $V_{ZF,mpp}$ as the input parameter for equation 8.12. Figure 8.14b (red solid line) depicts such a calculation for the same set of parameters, especially a constant average voltage $V_{EP,mpp}$ of 445 mV, as for the calculation of $V_{ZF,mpp}$ in figure 8.14a. As discussed for the calculation of $V_{ZF,mpp}$, the assumption of a constant average voltage $V_{EP,mpp} = \frac{1}{2}(V_{DF,mpp} + V_{DZ,mpp})$ is useful for the linear regime, but breaks down beyond this approximation. For this reason, the calculated $P_{CT,mpp}$ matches the experimental data close to the equipotential operation (small $|J_{CT,mpp}|$), but overestimates the loss for larger $|J_{CT,mpp}|$ values. In the latter case, the full model calculation, where $V_{DF,mpp}$ and $V_{DZ,mpp}$ are calculated numerically, yields a better agreement and demonstrates that the loss is inherently due to the operation of the bipolar junction bottom cell.

For well-designed bipolar junction bottom cells, it is necessary to keep the power density loss $P_{CT,mpp}$ small and therefore a well-designed bottom cell should operate close to the equipotential operation state, which renders the linear approximations from equations 8.12, 8.15 and 8.16 extremely valuable.

However, the experimental data shown in figure 8.14(b) refers to a bottom cell, which is far from being ideal and thus one expects the loss to be much smaller for better solar cells with higher $V_{EP,mpp}$. Figure 8.14(b) shows two examples with an average voltage $V_{EP,mpp}$ of 500 mV and 550 mV, which corresponds to cells with $J_{0,DF} = J_{0,DZ}$ of 870 fA/cm² and 110 fA/cm² according to equation 8.8, respectively. As expected the loss is strongly reduced and the diffusion resistance is around 0.397 Ωcm^2 and 0.055 Ωcm^2 for 500 mV and 550 mV, respectively. For the latter, the low resistance would hardly affect the performance of a bipolar junction bottom cell with relevant transfer current densities up to approximately 40 mA/cm².

Design guidelines

The investigation of the previous subsections show that the transfer of minority carriers through the wafer in a bipolar junction bottom cell can represent an important loss mechanism. In the framework of equations 8.15 and 8.16, the loss can be controlled by the diffusion resistance, which in turn depends on the properties of the wafer and the injection level at maximum power point. If the approximation in equation 8.8 and the relationship between the specific wafer resistivity $\rho_{B,0}$, majority carrier mobility $\mu_{p,B}$ and doping density is used, the following equation can be derived²⁴.

$$P_{CT,mpp} \approx \frac{\exp(A_2)}{q^2 \cdot \mu_{n,B} \cdot \mu_{p,B} \cdot n_i^2} \cdot \frac{(J_{0,DZ} + J_{0,DF})^{A_1}}{R_{Sheet,B}} \cdot \frac{J_{CT,mpp}^2}{(J_{ph,bottom})^{A_1}} \quad (8.17)$$

²⁴The derivation can be found in the appendix A.5.5.

8.4. EQUIVALENT CIRCUIT MODEL

For the Taylor approximation in equation 8.8 at $\frac{qV_{EP,mpp}}{k_B T} = 20$, $A_1 = 0.955$ and $A_2 = 2$. Equation 8.17 contains a product of three factors: The red factor is a constant, if constant carrier mobilities and a constant intrinsic carrier concentration are assumed²⁵, and has a value A_3 of $4.33 \cdot 10^{12} \Omega^2 \text{cm}^2$. The blue factor contains solar cell specific parameters – the saturation current densities of the two diodes and the sheet resistance of the wafer $R_{\text{Sheet,B}} = \frac{\rho_{B,0}}{W_B}$ under dark conditions. The last factor (black) contains information about the illumination conditions for the bottom and top solar cell. To relate the loss within the bottom cell to a particular top cell, one has to define how J_{CT} is related to the generation current density $J_{\text{ph,top}}$ and $J_{\text{ph,bottom}}$ in the top and bottom cell, respectively. As the simplest guess, the transfer current density can be expressed as the mismatch between the photo-generated current density of the top cell and the photo-generated current density at the front contact of the bottom cell $J_{CT,mpp} \approx |J_{\text{Ph,F}} \pm J_{\text{ph,top}}| = |\Gamma \cdot J_{\text{ph,bottom}} \pm J_{\text{ph,top}}|$, where the “–” and “+” refer to the series-connected and reverse-connected tandem cell configuration, respectively. For a silicon bottom cell with a perfectly transparent top cell (e.g. a top cell with a band gap of 4 eV), which is illuminated with AM1.5G spectrum, the total photo-generation current density for the bottom cell amounts to about $J_{\text{max}} = 44 \text{ mA/cm}^2$ [415]. If the band gap of the top cell decreases, the absorber of the top cell begins to absorb one part of the spectrum, which is lost for the bottom cell. For simplicity, it can be assumed that the photo-generation current densities add up to $J_{\text{max}} = J_{\text{ph,bottom}} + J_{\text{ph,top}}$. With that assumptions, $J_{CT,mpp} = J_{\text{max}} \cdot |\Gamma - (\Gamma \mp 1) \cdot \frac{J_{\text{ph,top}}}{J_{\text{max}}}|$ and $J_{\text{ph,bottom}} = J_{\text{max}} - J_{\text{ph,top}}$. By substituting $J_{CT,mpp}$ and $J_{\text{ph,bottom}}$ in equation 8.17, it reads

$$P_{CT,mpp} \approx A_3 \cdot \frac{(J_{0,DZ} + J_{0,DF})^{A_1}}{R_{\text{Sheet,B}}} \cdot J_{\text{max}}^{(2-A_1)} \cdot \frac{(\Gamma - \frac{(\Gamma \mp 1) \cdot J_{\text{ph,top}}}{J_{\text{max}}})^2}{(1 - \frac{J_{\text{ph,top}}}{J_{\text{max}}})^{A_1}} \quad (8.18)$$

The “+” and “–” signs of the “ \mp ” signs refer to the series-connected and reverse-connected tandem cell configurations, respectively. Equation 8.18 contains a product of four factors, where only three factors influence the design of bipolar 3T bottom cells. The first factor A_3 is approximately constant for a given temperature, the second factor (blue) contains the solar cell specific parameters and the third (black) one ($J_{\text{max}}^{(2-A_1)}$) contains the information on the illumination intensity. The last factor (orange) is denoted to as the current-mismatch loss factor

$$\chi = \frac{(\Gamma - \frac{(\Gamma \mp 1) \cdot J_{\text{ph,top}}}{J_{\text{max}}})^2}{(1 - \frac{J_{\text{ph,top}}}{J_{\text{max}}})^{A_1}}, \quad (8.19)$$

which describes the relative loss enhancement due to the current transfer through the bottom cell implied by the current-mismatch of the photo-generations.

Figure 8.15a shows the current-mismatch loss factor χ for a series- and reverse-connected tandem cell with different top cell band gaps²⁶. For simplicity, it is assumed that $\Gamma = 1$ applies to all tandem cells independent of the top cell band gap, which means that the photogeneration

²⁵This assumption is approximately valid for moderate doping and injection levels up to approximately $1 \cdot 10^{15} \text{ cm}^{-3}$. But even at carrier concentrations of $1 \cdot 10^{16} \text{ cm}^{-3}$ the electron mobility maintains approximately 84% and the intrinsic carrier concentration 92% of its initial value.

²⁶Details on the calculation procedure is found in the appendix A.5.6

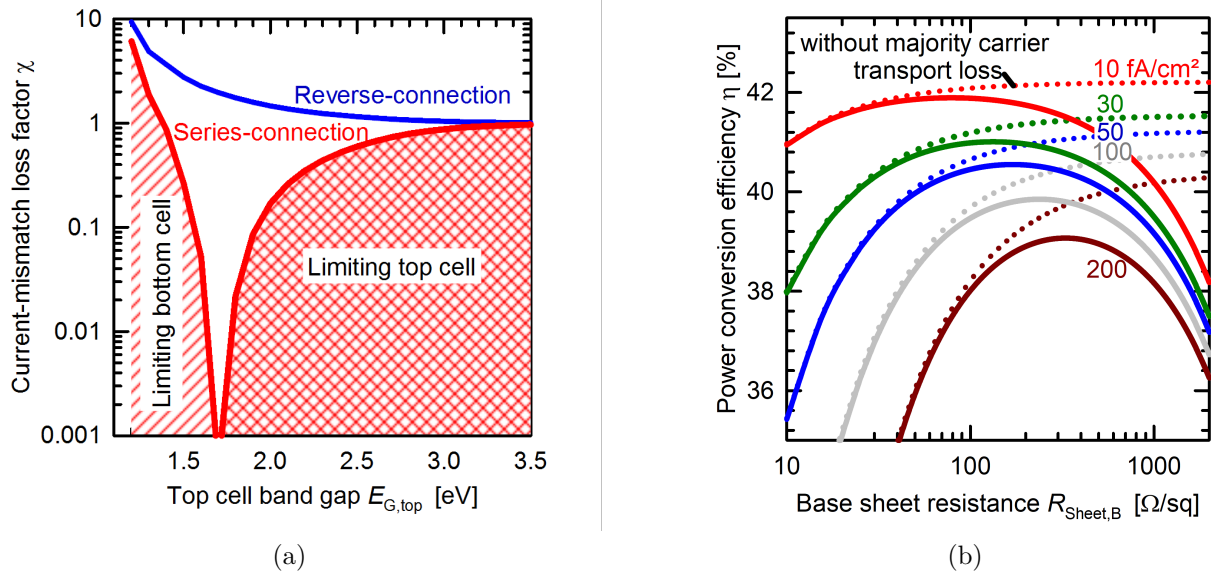


Figure 8.15.: (a) Current-mismatch loss factor as function of the top cell band gap for a Si bottom cell under AM1.5G spectrum. (b) Limiting efficiency for a reverse-connected 3T tandem cell comprising a top cell with a band gap of 1.8 eV ($\chi = 1.75$) and a bipolar junction IBC bottom cell with $J_{0,DZ} + J_{0,DF}$ between 10 fA/cm² and 200 fA/cm² and with a pitch of 2 mm. Solid and dotted lines represent the calculations with and without losses from lateral majority carrier transport.

exclusively takes place at the surface of front side of the bottom cell. While this is quite accurate for wide-band gap top cells, the assumption becomes inaccurate for narrow-band gap top cells and underestimates χ for the series-connected tandem and overestimates it for the reverse-connected tandem. For top cell band gaps exceeding 3.5 eV, χ equals $\Gamma^2 = 1$ in series- and reverse-connection, because the top cell is mostly transparent to AM1.5G spectrum and $J_{\text{ph,top}}$ vanishes. This case is equal to a 2T IBC cell under full-spectrum illumination, where the minority and majority carriers of the entire photo-generation current have to flow from the front side of the cell to the back.

If the band gap of the top cell decreases in a reverse-connected tandem cell, the transfer current density remains the same²⁷ as for 3.5 eV, but the photo-generation current density and hence the injection level in the bottom cell decreases. This leads to a larger resistance for minority carriers and a larger loss factor χ . In a series-connected tandem cell the injection level in the bottom cell decrease with decreasing band gap too, but now one part of the photo-generated current density is collected at the front side of the bottom cell to match the top cell's current density and the transfer current density is decreased. The loss factor χ is reduced until a band gap of 1.7 eV is reached, where top and bottom cell's current densities match and the transfer current density vanishes. For top cell band gaps below 1.7 eV, the photo-generation in the bottom cell decreases further and that of the top cell increases, such that the bottom cell would limit the current density of the tandem and a transfer current has to flow from the rear contact Z to the front contact. As the injection level decreases and the transfer current density increases simultaneously with narrower band gap, the loss factor rises steeply. From the loss factor, it can be expected that reverse-connected tandem cells, especially with a narrow band gap, exhibit a larger loss than the series-connected tandem cells. However, the power loss in equation 8.18 reveals that the loss can be minimized by choosing an appropriate base sheet resistance for given saturation current densities.

Reverse-connected tandem cell

Figure 8.15b shows the limiting efficiency for a reverse-connected tandem cell²⁸ comprising a Shockley-Queisser-limited top cell with a band gap of 1.8 eV [415]. The band gap is comparable to that of the GaInP top cell with an efficiency of 20% as used for the record 4T GaInP/Si tandem cell with an efficiency of 32.5% [406]. If lateral transport of majority carriers is neglected (dotted lines), the limiting efficiency for a bottom cell with $(J_{0,\text{DZ}} + J_{0,\text{DF}})$ of 10 fA/cm² saturates at 42.2% for a sheet resistance of several hundreds Ω/\square . For bottom cells with a sheet resistance far below 200 Ω/\square the efficiency is reduced due to dissipative minority carrier transport through the wafer. This same trend towards high base sheet resistances is also found for higher saturation current densities. If the lateral majority carrier transport for an IBC pitch of 2 mm is taken into account, a broad maximum efficiency of 41.9% is found for $(J_{0,\text{DZ}} + J_{0,\text{DF}})$ of 10 fA/cm² and a sheet resistance of between about 50 Ω/\square and 100 Ω/\square (red solid line). For higher saturation current densities the maximum efficiency

²⁷This is due to the definition $J_{\text{CT}} = J_{\text{max}} \cdot |\Gamma - (\Gamma - 1) \cdot \frac{J_{\text{ph,top}}}{J_{\text{max}}}|$ for the reverse-connected tandem cell. If $\Gamma = 1$, then $J_{\text{CT}} = J_{\text{max}}$ independent of the band gap down to the bottom cell band gap.

²⁸Details on the procedure for the calculation is found in the appendix A.5.7.

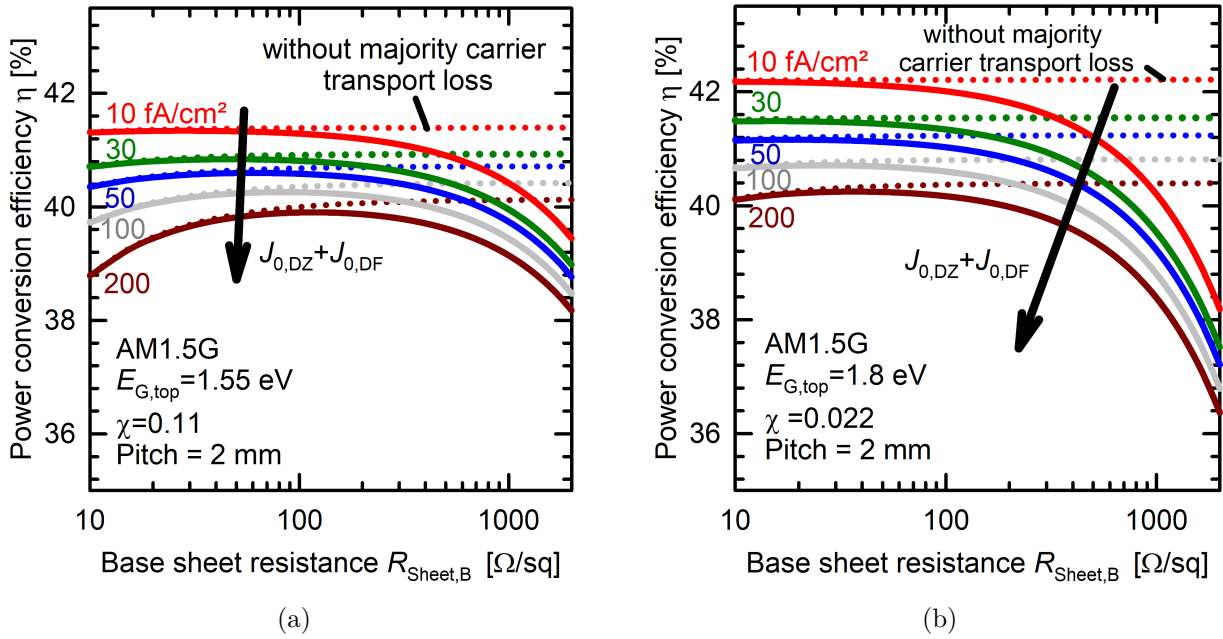


Figure 8.16.: Limiting efficiency for a series-connected 3T tandem cell comprising a top cell with a band gap of 1.55 eV (a) or 1.8 eV (b) and an IBC bottom cell with $J_{0,DZ} + J_{0,DF}$ between 10 fA/cm² and 200 fA/cm² and with a pitch of 2 mm.

decreases and the optimum sheet resistance is increased. The efficiency gap between the efficiency without considering transport losses²⁹ and the maximum efficiencies with transport loss can be used as a measure for the total loss and thus forms the basis to evaluate the potential for 3T bipolar junction tandem cells. For the example with an IBC grid with a pitch of 2 mm, the efficiency loss amounts to 0.3%_{abs.} for the bottom cell with the smallest saturation current density of 10 fA/cm² and 1.3%_{abs.} for the bottom cell with the largest saturation current density of 200 fA/cm². In conclusion, a well-designed reverse-connected tandem cell with a limiting top cell can operate with a small transport loss and therefore is an attractive architecture, especially if module integration [94, 95] and cell fabrication complexity (see 8.6) is considered.

Series-connected tandem cell

Figure 8.16a shows the limiting efficiency for a bottom cell-limited series-connected tandem cell comprising a top cell with a band gap of 1.55 eV³⁰, as it is used for the record lead halide perovskite solar cell with an efficiency of 25.2% [426, 427]. If lateral transport of majority carriers is neglected (dotted lines), the limiting efficiency for a tandem comprising a bottom cell with ($J_{0,DZ} + J_{0,DF}$) of 10 fA/cm² amounts to about 41.4% nearly independent of the sheet resistance, because the loss due to minority carrier transport is negligible. For bottom

²⁹This is simply the value from the calculation in the appendix A.5.7 without losses.

³⁰Details on the procedure for the calculation is found in the appendix A.5.7.

cells with a saturation current densities of 200 fA/cm^2 , the efficiency saturates at a value of 40.1% for sheet resistances above several hundred Ω/\square and decreases slightly for lower sheet resistances. If the lateral majority carrier transport for an IBC pitch of 2 mm is taken into account, a maximum efficiency of 41.3% is found for $(J_{0,\text{DZ}} + J_{0,\text{DF}})$ of 10 fA/cm^2 and a sheet resistance between $20 \text{ }\Omega/\square$ and $35 \text{ }\Omega/\square$ (red solid line). For a saturation current density of 200 fA/cm^2 , the maximum efficiency decreases to a value of 39.9% for an optimum sheet resistance between $60 \text{ }\Omega/\square$ and $230 \text{ }\Omega/\square$ (brown solid line).

The efficiency gap of the tandem cell with and without considering majority carrier transport amounts to $0.1\%_{\text{abs.}}$ and $0.25\%_{\text{abs.}}$ for low and high saturation current density, respectively. Finally, figure 8.16a shows the limiting efficiency of the third opportunity – the top cell-limited series-connected tandem cell comprising a top cell with a band gap of 1.8 eV. As expected from the current-mismatch loss factor χ of 0.022, the minority carrier transport loss in this configuration is the lowest, such that the efficiency for most of the investigated saturation current densities is almost constant with sheet resistance, when majority carrier transport is neglected (dotted lines). If majority carrier transport is included, then the maximum efficiency of 42.3% and a negligible efficiency loss is attained for the lowest sheet resistance and lowest saturation current density. For the highest saturation current density of 200 fA/cm^2 , an efficiency of 40.3% with an efficiency loss of 0.1% is predicted.

To summarize, equation 8.18 provides a simple and quick estimate of the power loss due to minority carrier transport in a 3T bipolar junction bottom cell for series- and reverse-connected tandem cells. The minority carrier transport loss is minimized for high sheet resistances. However, this would lead to a considerable majority carrier transport loss for finite IBC grid geometries. If the majority carrier transport is taken in to account, an optimum sheet resistance is found for each cell architecture, top cell band gap and saturation current density for given grid dimensions. This simple design guideline can serve as a the first rough estimate for the optimum sheet resistance and a maximum efficiency. Combining this approach with a Shockley-Queisser-limited top cell efficiencies demonstrates that a series- and reverse-connected 3T tandem cell featuring a well-designed bipolar junction bottom cell is able to achieve efficiencies close to 42% for relevant top cell band gaps.

8.5. High performance unijunction bottom cell

The 3T unijunction bottom cell with a planar n^+ POLO front contact from section 8.2.1 is the simplest implementation of a 3T unijunction bottom cell and requires only small modification to the POLO-IBC cell process developed in chapter 7. Although the solar cell is good enough to investigate the physics and to demonstrate a prototype of a 3T tandem, it is hardly possible to achieve highest efficiencies. In the following, several shortcomings of the bottom cell are addressed and a high performance 3T unijunction bottom cell is developed.

8.5.1. Cell fabrication process

The high performance 3T bottom cells are fabricated on 6-inch n -type FZ wafers with a resistivity of $1.7 \text{ }\Omega\text{cm}$ and a thickness of $250 \text{ }\mu\text{m}$ following the process flow of section 8.2.1

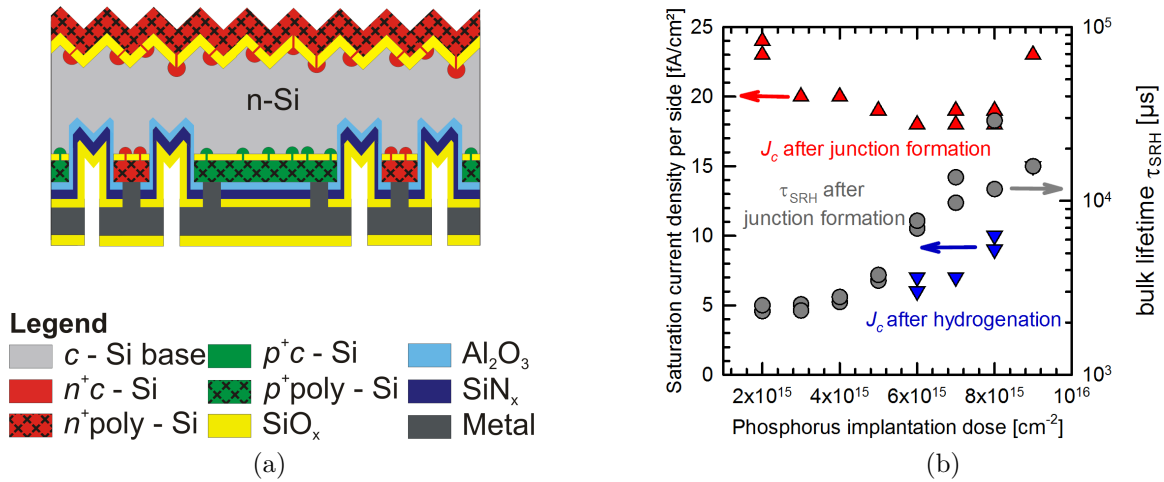


Figure 8.17.: (a) Schematic cross-section of a high performance 3T unijunction bottom cell. (b) Saturation current density of the n^+ POLO junction on a textured surface for varying phosphorus implantation doses and the corresponding bulk lifetime of the sample after junction formation.

exactly, except that a textured n^+ POLO front side and an improved dielectric stack at the rear side are implemented. The latter enables an improved and damage-free laser contact opening process of PECVD-deposited 200 nm-thick SiO_x layers, which greatly enhances the infrared response of the solar cells. A schematic cross-section of the finished 3T bottom cell is shown in figure 8.17a.

Implementation of a textured n^+ POLO front side

In order to implement a textured n^+ POLO contact on the front side, the front side of the wafer is textured, while the rear side is protected by a SiN_x layer. After removing the SiN_x layer and RCA cleaning, a 2.2 nm-thick³¹ interfacial silicon oxide grows in an oxidation furnace, which is capped by intrinsic a-Si in a LPCVD furnace. The rear side is doped by masked ion implantation as described in section 7.

Since the textured n^+ POLO contact on the front side is used for the first time in a POLO-IBC cell process, the implantation parameters are optimized on Cz n -type samples. A phosphorus implantation dose between $2 \cdot 10^{15} \text{ cm}^{-2}$ and $9 \cdot 10^{15} \text{ cm}^{-2}$ is implanted into a 225 nm-thick a-Si layer on both side textured samples. After oxidation and junction formation in a tube furnace, photo-conductance decay measurements are performed and the saturation current density and bulk lifetime are extracted according to Kane and Swanson [101]. Figure 8.17b shows an increase of bulk lifetime³² (grey circles) from approximately 2 ms for the lowest implantation dose to above 20 ms for the higher doses, which is consistent with the gettering effect observed among others by Wong *et al.* [428] and Krügener *et al.* [266]. The saturation

³¹The oxide thickness was measure on a polished reference wafer by using ellipsometry.

³²Bulk lifetime was determined from the intercept of the Kane&Swanson analysis.

current density for the POLO junction after formation (red triangles) decreases with increasing implantation dose until a minimum of about 18 fA/cm^2 is reached for implantation doses between $6 \cdot 10^{15} \text{ cm}^{-2}$ and $8 \cdot 10^{15} \text{ cm}^{-2}$. The saturation current density is further decreased significantly to a minimum of 6 fA/cm^2 after hydrogenation with a hydrogen-rich SiN_x layer. The implantation dose of $7 \cdot 10^{15} \text{ cm}^{-2}$ for the cell is chosen, which yields the highest bulk lifetime and a low saturation current density after hydrogenation.

The POLO junctions are formed and the trench separation is performed following chapter 7.

Improved laser contact opening process

As a next step in the process flow in chapter 7, the trench region on rear side is passivated by an AlO_x layer, which is covered by a protective SiN_y layer. In a subsequent laser ablation process, this dielectric stack has to be removed locally on the POLO junctions to enable electrical contact to subsequently deposited aluminium layer. During the laser ablation process a part of the poly-Si is “evaporated” to mechanically remove the UV-transparent dielectric layers above by the pressure built up. Thus, this type of ablation process restricts the layer thickness and type of the used dielectric layers on the rear side and always reduces the poly-Si layer thickness [156], which can lead to a reduced passivation of the POLO junction and local shunting (e.g. compare with subsection 8.3.2). In order to achieve the highest performance, it is essential to avoid any degradation of the POLO junction and to maximize the infrared response of the solar cell through the use of thick dielectric layers [429, 430].

For this purpose, a slightly different laser process is developed in this thesis, which uses a 20 nm-thick AlO_x passivation layer with a thin lift-off-mediating SiN_y layer and an infrared-response-enhancing thick SiO_z layer. The optical properties of this dielectric layer stack are chosen such that the infrared response is optimized and a damage-free laser ablation is possible. According to simple raytracing simulations around a wavelength of 355 nm, a 30 nm-thin SiN_y layer with a refractive index of 2.4 covered by a 200 nm-thick SiO_z layer leads to an absorption of more than 50% of the UV intensity in the thin lift-off-mediating SiN_y layer and less than about 30% in the poly-Si layer³³. In contrast to the laser ablation processes used previously, the SiN_y layer is consumed during the ablation process instead of the poly-Si layer, which enables one to lift-off a thick SiO_z layer and simultaneously leave the POLO junction unaffected by the incident laser beam. Figure 8.18a shows a tilted top view SEM image of the LCO before evaporation of aluminium and figure 8.18b depicts the SEM image of the cross-section of the LCO after evaporation of aluminium. A sharp tear-off edge of the thick SiO_z layer (red box in figure 8.18b) marks the edge of the contact opening and indicates that the SiO_z is indirectly ablated by a mechanical lift-off process. Due to the Gaussian distribution of fluence and the direct ablation of the SiN_y layer, the contact opening accommodates three regions:

- In the inner circle of the contact opening (blue box in figure 8.18b), the laser fluence is sufficient to remove the SiN_y layer completely and leaves a smooth poly-Si surface,

³³The author is aware that a raytracing simulation is not able to simulate a laser process accurately. However, it is used here as rough guess to adjust the layer thicknesses.

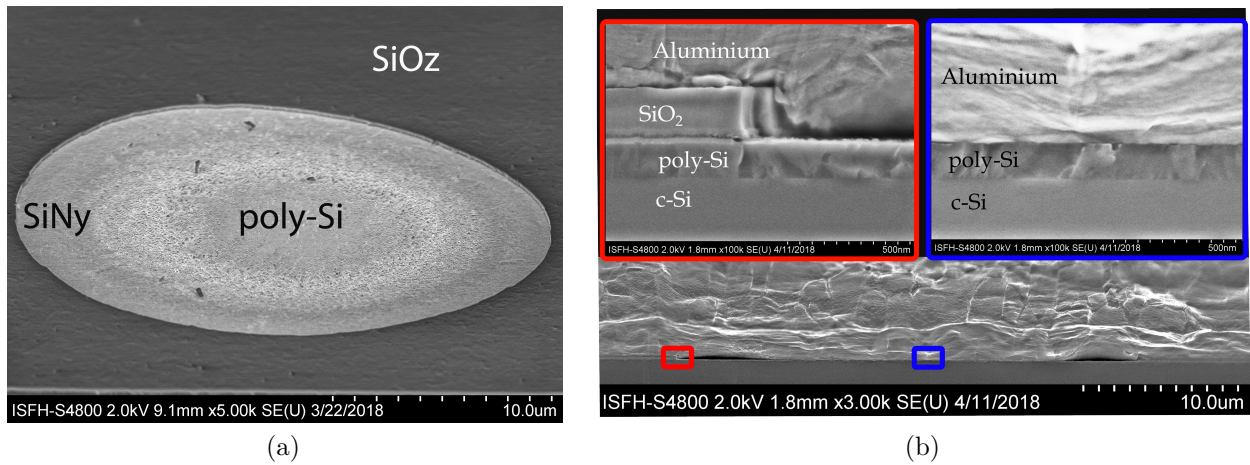


Figure 8.18.: (a) Tilted top view SEM image of a laser contact opening before evaporating aluminium. (b) SEM image of the cross-section of the laser contact opening after evaporating aluminium. Red and blue boxes detail the edge and the center of the LCO, respectively.

which is probably still covered with the AlO_x layer. The possibly remaining AlO_x layer is removed by a short single-side etching in a 1% HF solution, which is anyhow performed before evaporating the aluminium.

- In the outer circle, however, the fluence is not sufficient to completely remove the SiN_y layer and therefore leaves a thinned SiN_y layer with nanometer roughness in this region.
- Between these two regions there is a transition region where the SiN_y layer is no longer closed and is probably lifted off during the short HF etching.

From the SEM cross-section in figure 8.18b, one would expect that the POLO junction is not affected by the laser ablation process and that a reasonable electrical contact forms between poly-Si and aluminium. Indeed, lifetime data from infrared lifetime mapping [431] supports this conclusion, which shows identical lifetimes before and after laser ablation (not shown here). The contact resistance is not measured separately, but can be estimated from the series resistance in figure 8.19a of the obtained solar cell. If the series resistances of the solar cells with approximately the same geometry, but a varying contact opening area fraction, is plotted versus the inverse of the area fraction, then the slope of the resulting line corresponds to the contact resistance. The slope of the fitted line to blue diamonds is $1.075 \pm 0.38 \text{ m}\Omega\text{cm}^2$ and that fitted to the red circles is $0.38 \pm 0.66 \text{ m}\Omega\text{cm}^2$. This simple estimate suggests that the contact resistance is of the order of or below $1 \text{ m}\Omega\text{cm}^2$.

The developed laser contact opening process is applied to the precursors of the high performance 3T unijunction bottom cells and the cells are finished according to chapter 6. During the passivation of the rear side, the front side received a 20 nm-thick AlO_x layer to improved the POLO junction properties by hydrogenation. The AlO_x layer is removed after finishing the cell process.

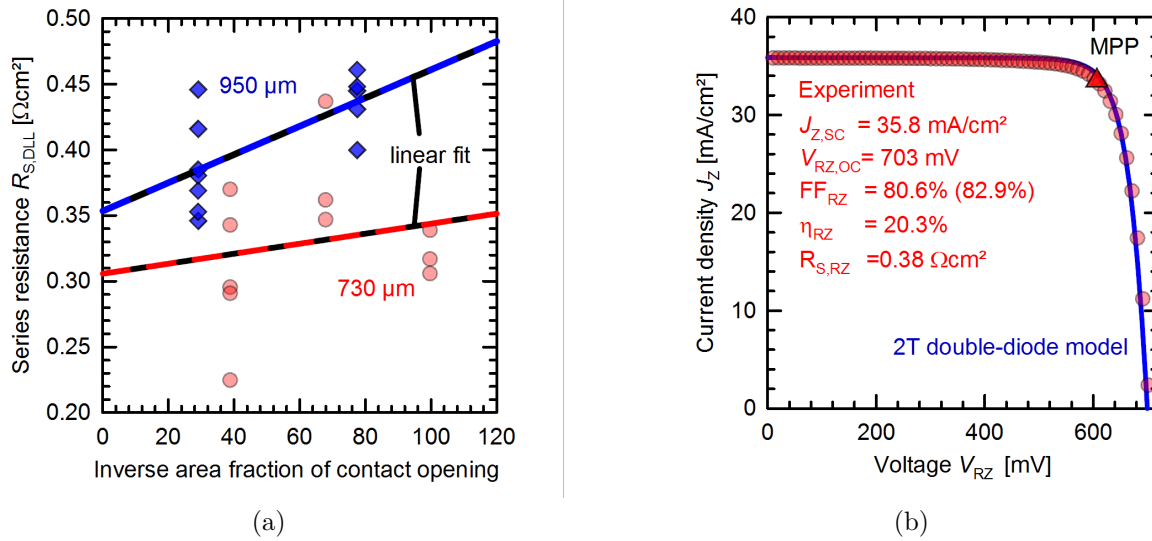


Figure 8.19.: (a) Series resistance of 15 cells with a pitch of 730 μm (red circles) and 11 cells with a pitch of 950 μm (blue circles) with a variation of the contact opening area fraction. Red and blue lines represent linear fits to the red and blue data points. (b) Two-terminal J - V characteristic of the best 4 cm^2 high performance 3T unijunction bottom cells of 27 cells on a single wafer.

8.5.2. Cell performance

The 2T J - V characteristic of the finished solar cells is recorded using LOANA solar cell analysis system from pv-tools under one-sun illumination, but with the calibration to the cell from chapter 7 due to the lack of a calibrated 3T unijunction bottom cell with a textured front side. The J_z - V_{RZ} characteristic of the best solar cell obtained from 27 solar cell on a single wafer is shown in figure 8.19b. The solar cell exhibits a $J_{Z,SC}$ of 35.8 mA/cm^2 , a $V_{RZ,OC}$ of 703 mV, a fill factor of 80.6% and a resulting efficiency of 20.3%. Since the solar cell accommodates a thick parasitically absorbing poly-Si layer instead of an anti-reflection coating on the front side, it is expected that the $J_{Z,SC}$ is strongly reduced under one-sun condition. Under the operation in a tandem solar cell, however, the front side optics of the bottom cell will improve significantly and the parasitic absorption of the approx. 100 nm-thick poly-Si layer is then mainly restricted to free-carrier absorption.

The open-circuit voltage is limited by the saturation current density $J_{Z,01}$ of approximately 40 fA/cm^2 from recombination with an ideality factor of unity. The saturation current density is composed of the following contributions: 5 fA/cm^2 from band-to-band and Auger recombination in the wafer, between 15-20 fA/cm^2 from bulk SRH recombination and the remaining 15-20 fA/cm^2 are due to the POLO junctions on the front and rear side and the trench passivation. The pseudo fill factor of 82.9% as extracted from $J_{Z,SC}$ - $V_{RZ,OC}$ indicates a neat recombination behavior around the maximum power point with a local ideality factor of about 1.2 at 600 mV. However, the J_z - V_{RZ} characteristic under illumination exhibits a

strongly enhanced parasitic recombination compared to the $J_{Z,SC}-V_{RZ,OC}$ characteristic, such that a local ideality factor above 1.6 at 600 mV is observed. This parasitic recombination together with a series resistance of $0.38 \Omega\text{cm}^2$ reduces the fill factor to a value of 80.6%. The reason for the degradation of the recombination behavior is unclear and needs further investigation.

To better classify the results, a 2T double-diode model is fitted to the $J-V$ data and the efficiency of the cell is simulated with a short circuit current density of 41.5 mA/cm^2 as in the POLO-IBC cell in chapter 7 and with a short-circuit current density of 24.2 mA/cm^2 as in the bottom solar cell of the GaInP//Si tandem solar cell reported in reference [398]. For the former scenario, an efficiency of 24.1% is predicted, which is comparable with the efficiency of the POLO-IBC cell of 24.25% from chapter 7. For the scenario in a GaInP//Si tandem cell, a bottom cell efficiency of 13.8% is predicted, which is 1.3%abs. better than that reported in reference [398] and would enable a GaInP/Si tandem cell with an efficiency of 32.9%, which is better than the current world record of 32.8% for a mechanically stacked GaAs//Si dual-junction cell [406]. Actually, POLO-IBC bottom cells with a similar rear side processing as the high performance 3T bottom cell, but an $\text{AlO}_x/\text{SiN}_y$ front side passivation, have been integrated in 4T GaAs//Si tandem cells with an efficiency of 32.6%, which is close to the current world record [399, 400]. To conclude, the developed high performance 3T unijunction bottom cell is a promising basis for a 3T tandem solar cell with an efficiency close to or even beyond 33%.

8.6. Simplified PERC-like three-terminal bipolar junction bottom cells

The fabrication process of the high performance unijunction IBC bottom cells with POLO junctions from the previous subsection is much more complex than that of a Passivated Rear and Emitter cell (PERC) and might compromise the competitiveness of 3T tandem cells [432]. Fortunately, for the bipolar junction bottom cell architecture, an elegant and simplified PERC-like 3T bottom cell process, which features local Al back surface field (BSF) contacts similar to the recently proposed two-terminal (2T) bottom cell [376] and IBC single junction cell [349, 433], can be constructed. The lean cell fabrication process is introduced and demonstrated in the following subsection.

8.6.1. Cell fabrication process

As discussed in section 8.1, two different tandems are possible with a p -type bottom cell – a series-connected tandem “top/s/pbIBC tandem” and a reverse-connected tandem “top/r/pIBC”. The former requires a tunnel recombination junction on the front side of the bottom cell and the latter does not. As a consequence, two slightly different process flows – one with a tunnel junction (figure 8.20, denoted as top/s/pbIBC cell), and another without a p^+/n^+ poly-Si tunnel junction (figure 8.21, denoted as top/r/pbIBC cell) – are demonstrated in the following.

8.6. SIMPLIFIED PERC-LIKE THREE-TERMINAL BIPOLAR JUNCTION BOTTOM CELLS

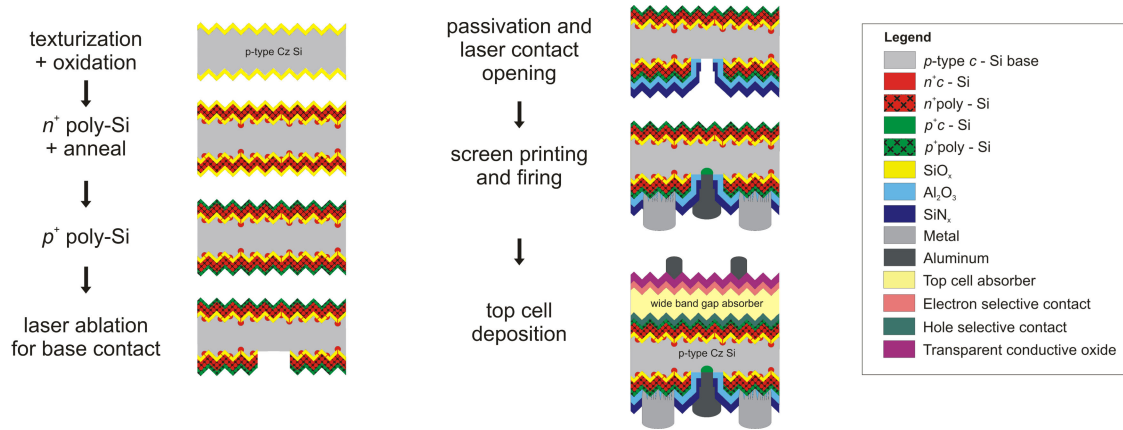


Figure 8.20.: Fabrication process for a series-connected 3T tandem featuring a PERC-like bipolar junction bottom cell (top/r/bpIBC) with a p^+/n^+ poly-Si tunnel junction.

top/s/pbIBC cell process

Bipolar junction bottom cells with an active cell area of 4 cm^2 are fabricated on $156 \text{ mm} \times 156 \text{ mm}$ pseudo-square, boron-doped p -type Czochralski (Cz) wafers with a resistivity of $20 \Omega\text{cm}$ and an as-cut thickness of $180 \mu\text{m}$ by using tools and processes common for industrial PERC cells. The wafers are pre-cleaned (pseudo-SC1), saw damage etched and both-side textured in RENA's down-sized industrial cleaning tool "Batchlab" [434]. After a subsequent RCA cleaning, an approximately 1.6 nm -thick interfacial silicon oxide is grown in de-ionized water with diluted ozone in the Batchlab tool. In-situ phosphorus-doped amorphous Si is deposited on top of the interfacial silicon oxide on both sides of the wafer in a LPCVD furnace (E2000) from Centrotherm. A layer thickness of 200 nm is chosen here to ensure compatibility with the fire-through metallization process developed elsewhere [433]. Since the screen-printed metallization of POLO contacts is rapidly evolving [433, 435–440], it can be speculated that also thinner poly-Si layers can be contacted with fire-through pastes in the future.

After LPCVD deposition, the POLO junction forms during a high-temperature furnace annealing³⁴ at $880 \text{ }^\circ\text{C}$ in a dry N_2 atmosphere. The LPCVD deposition and furnace annealing replace the POCl_3 diffusion process for the emitter formation of PERC cells [442].

The silicon oxide, which has parasitically grown during junction formation, is removed with hydrofluoric acid directly before a second 35 nm -thin highly boron-doped poly-Si layer is deposited on the n^+ poly-Si layer using LPCVD. The p^+ poly-Si layer serves as an Esaki-like interband tunnel junction (TJ) with the n^+ poly-Si [376, 443] on the front and rear side of the cell³⁵.

The poly-Si layers on the rear side are locally laser ablated to define the majority-carrier contact region with a hyper rapid 50 laser from Coherent with a pulse length of 10 ps and a wavelength of 532 nm . Since the lab-type 4 cm^2 cells are cleaved at the end of the cell

³⁴The prolong furnace annealing can potentially be replaced by a fast firing step [244, 255, 441].

³⁵The p^+/n^+ poly-Si TJ on the rear side of the cell does not affect the device operation [444].

processing, it is necessary to remove the n^+ POLO junction from the front side outside of the active cell area by laser ablation. The induced laser damage on both sides is removed in a KOH-based etching solution, where the highly boron-doped poly-Si layer of the TJ acts as a protective etching barrier for the POLO contact. The base contact region and the front side is then passivated using an aluminum oxide/silicon nitride dielectric stack. This layer stack is removed locally from the n^+ POLO junction in the active cell area on the front side using an inkjet printed mask and HF etching³⁶. An aluminum oxide is deposited on the front side again to act as hydrogenation source during the co-firing step. To enable the formation of a local aluminium back-surface field (Al-BSF) contact as the majority-carrier contact to the base, the dielectric layers on the rear side are opened locally by laser ablation with the hyper rapid 50 laser from coherent with a wavelength of 532 nm. Silver and aluminum pastes are screen-printed on the POLO contact and the base region, respectively, and co-fired in an industrial conveyor-belt firing furnace from Centrotherm. During the firing step, the Ag paste penetrates through the aluminum oxide/silicon nitride dielectric stack and enables the contact formation of the Ag paste to the poly-Si layer. Simultaneously, Al alloys with Si within the contact opening and forms a local Al-doped region below the contact (Al-BSF) [445–448].

The top cell (e.g. based on perovskites or III-V semiconductors) is then intended to be deposited on top of the poly-Si layer on the front side of the bottom cell.

top/r/pbIBC cell process

The process sequence for the bottom cells without a poly-Si TJ is shown in figure 8.20 and follows that of the bottom cells with poly-Si TJ from figure 8.21, except that the p^+ poly-Si LPCVD deposition step and the prior oxide removal with HF is omitted. In order to provide an alternative for the omitted p^+ poly-Si layer, which acts as a protective etch barrier against the laser damage removal, the n^+ POLO junction forms during a pyrogenic oxidation at 860 °C. This yields a silicon dioxide layer with a thickness of approximately 70 nm, which is sufficient to protect the n^+ POLO junction for several minutes during the KOH-based damage etch removal. The remaining protective SiO₂ layer is removed with HF afterwards. The cells are finished following the remaining sequence of bottom cell with TJ after damage etch removal.

Novel process steps

Both process flows for a simplified PERC-like 3T bipolar junction bottom cell contain several novel process steps compared to the PERC cell technology.

1. A n^+ POLO junction is fabricated on a textured wafer surface instead of a homojunction emitter. As pointed out in section 4.2, the fabrication of such junctions with several different techniques was developed by many research groups and the process used herein was reported elsewhere [36, 433]. A dark saturation current-density per side

³⁶This is only necessary due to the small size of the cell to avoid enhanced minority carrier transport from the active cell area to the defective cell edges.

8.6. SIMPLIFIED PERC-LIKE THREE-TERMINAL BIPOLAR JUNCTION BOTTOM CELLS

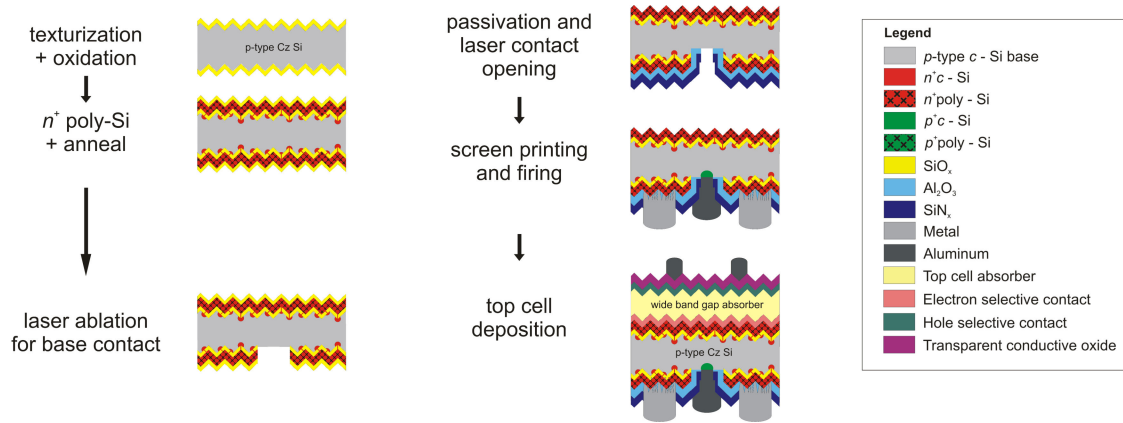


Figure 8.21.: Fabrication process for a reverse connected 3T tandem featuring a PERC-like bipolar junction bottom cell (top/r/bpIBC).

of between 20 fA/cm^2 and 50 fA/cm^2 is achieved on $5 \Omega\text{cm}$ n -type CZ reference wafers after the corresponding dry formation annealing at 880°C and pyrogenic oxidation at 860°C by using the slope method according to Kane and Swanson [101]. This is significantly higher than the value of 10 fA/cm^2 after forming gas anneal (2.4 fA/cm^2 after hydrogenation) reported by Peibst *et al.* [36] for a similar POLO junction with 1.7 nm -thick interfacial silicon oxide and a 20 nm -thick in-situ doped n^+ poly-Si formed on a textured wafer at 900°C . However, it is expected that the saturation current density of the junctions reported here is significantly improved after the co-firing step with the hydrogen-containing $\text{AlO}_x/\text{SiN}_y$ passivation layers.

2. For a low-resistive Esaki-like p^+/n^+ poly-Si TJ an abrupt pn -junctions with degenerated p -type and n -type layers is vital. Peibst *et al.* have reported on Sentaurus Device simulations of similar tunnel junctions as reported herein with measured doping profiles and a minority carrier lifetime of 50 ps as input parameter. The simulated TJ yielded a resistivity of only about $3 \text{ m}\Omega\text{cm}^2$.

In this thesis, the p^+ poly-Si is deposited at 640°C as a polycrystalline film with an active boron concentration above $2 \cdot 10^{20} \text{ cm}^{-3}$. The active phosphorous concentration of the n^+ poly-Si layer exceeds $2 \cdot 10^{20} \text{ cm}^{-3}$. Thus, it is expected that the TJ exhibits low resistivity. Indeed, the experimentally determined current-voltage characteristics are linear for small voltages, but the resistivity of the aimed LPCVD-fabricated tunnel junction amounts to about $450 \text{ m}\Omega\text{cm}^2$. It can be speculated that the pn poly-Si junction is slightly graded due to a delayed incorporation of boron into the layer, which can be prevented by optimizing the deposition process³⁷.

Recently, Luderer *et al.* have demonstrated similar tunnel junctions with resistivity below $10 \text{ m}\Omega\text{cm}^2$ by using PECVD [443].

3. The process step for the base contact definition and the subsequent damage etch removal

³⁷At the time of submitting this thesis to the referees in May 2021, the team lead by the author (project 27Plus6) has achieved resistivities of the order of $10 \text{ m}\Omega\text{cm}^2$ after optimizing the LPCVD process at ISFH.

is outlined in the next subsection.

4. The used screen printing and co-firing process was developed by Haase *et al.* [433].

8.6.2. Base contact definition

After the n^+ POLO junction is formed in figure 8.20 and the p^+/n^+ TJ is created in figure 8.21, the cell precursor features two full-area minority carrier-selective electron contacts and a majority carrier-selective contact has to be created to the c-Si wafer for a proper operation of the solar cell. In both process flows, the poly-Si layers are removed locally on the rear side and an Al-BSF serves as the majority carrier-selective contact. Several potentially industrial feasible techniques like screen/ inkjet printing of Si etchants or laser ablation can be used [367, 449–451].

In the following, laser patterning was performed with a hyper rapid 50 ps-laser from coherent. Two laser wavelengths – 532 nm (denoted as “green laser”) and 355 nm (denoted as “UV laser”) – are compared for the ablation process. A pattern of lines with a laser spot distance of 5 μm within a line and a distance of 20 μm between the lines is used to ablate the poly-Si from the wafer.

The ablation process is applied to one side of a symmetric sample as obtained after p^+ poly-Si deposition³⁸ in figure 8.21. In order to blind out effects related to bulk defects of p -type Cz wafers, n -type Cz wafers with a resistivity of 5 Ωcm are used. The lifetime of the samples before laser ablation of about 1.4 ms at an excess carrier density of $1 \cdot 10^{15}\text{cm}^{-3}$ is limited by the POLO junction with a saturation current density of 30 fA/cm².

Protective p^+ poly-Si etch barrier in KOH

If the laser ablation is applied to a textured surface, the laser irradiation interferes with the scattered laser light and leads to a spatially non-uniform distribution of the laser fluence. Knorz *et al.* [452] have found that increased ablation occurs at the baseline between pyramids and at the tip and at the edges of the pyramid. The side facets of the pyramids are mostly unaffected by laser irradiation [452]. Thus, the laser ablation process on a textured surface inherently causes severe damage to the pyramids and diminishes the surface passivation [452, 453]. For this reason, the laser damage has to be removed from the c-Si wafer and the surface has to be re-passivated by an $\text{AlO}_x/\text{SiN}_y$ layer stack. During the damage etch removal in KOH, the p^+ poly-Si should act as a protective etch barrier layer for the n^+ POLO junction. In order to study the stability of the p^+ poly-Si layer in KOH, the same symmetric samples as for the single-side laser ablation were etched in KOH with different concentrations. Figure 8.22a summarizes the lifetimes of the samples before etching and after etching for 30 s, 1 min and 2 min. The lifetime at $\Delta n = 1 \cdot 10^{15}\text{cm}^{-3}$ before etching exceeds 1 ms for all samples. If ISFH’s standard protocol for damage etch removal with a KOH concentration of 50% at 90 °C and a resulting etch rate for c-Si of about 1.5 $\mu\text{m}/\text{min}$ per side is applied, a strong

³⁸Ablation experiments for the samples without TJ as in figure 8.20 were performed too and yielded qualitatively the same results as for the samples with TJ. Therefore, only the results of the samples with TJ are described.

8.6. SIMPLIFIED PERC-LIKE THREE-TERMINAL BIPOLAR JUNCTION BOTTOM CELLS

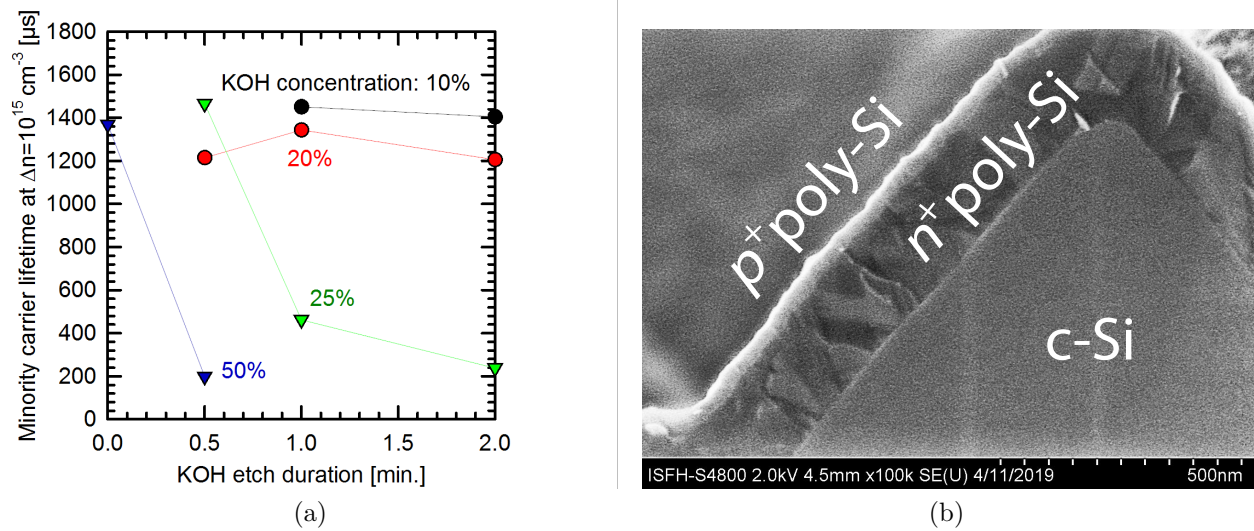


Figure 8.22.: (a) Stability of the 35 nm-thick p^+ poly-Si layer as etch barrier in KOH with different concentrations. (b) Scanning electron micrograph of the p^+/n^+ poly-Si/c-Si sample after etching for 2 min in KOH with a concentration of 10%.

decrease of the lifetime after 30 s is observed. Scanning electron microscopy imaging reveals that the p^+ poly-Si layer is removed completely and the thickness of the n^+ poly-Si layer is reduced significantly, such that the n^+ POLO junction does not cover the whole surface of the wafer and leaves parts of the wafer surface unpassivated. Given the initial thickness of the p^+ poly-Si layer of 35 nm, an upper bound for the etch rate of 70 nm/min and a rate selectivity of approximately 20 is estimated. For a damage etch removal with a reduced KOH concentration of 25% at 75 °C and a resulting etch rate for c-Si of about 1.4 $\mu\text{m}/\text{min}$ per side, the lifetime is maintained after 30 s, but decreases strongly for an etch duration of 1 min and 2 min. The estimate for the etch rate and rate selectivity amounts to 35 nm/min and 40, respectively. Finally, for a KOH concentration of 20% and 10% at 75 °C and a resulting etch rate for c-Si of between 1 $\mu\text{m}/\text{min}$ and 1.5 $\mu\text{m}/\text{min}$, the lifetime is maintained up to 2 min, which indicates that the 35 nm-thick p^+ poly-Si layer successfully protects the n^+ POLO junction underneath. Indeed, figure 8.22b confirms this fact for the sample after etching in 10% KOH solution for 2 min, where the p^+ poly-Si layer thickness remains at around 30 nm and leads to the conclusion that for each nanometer of p^+ poly-Si, several hundreds of nanometers of c-Si can be removed. The p^+ poly-Si layer acts as an etch stop in 10% KOH solution and can be used as protective barrier layer for laser damage etch removal. The dependence of the rate selectivity of lowly boron-doped c-Si versus highly boron-doped c-Si on KOH concentration was studied by Seidel *et al.* [454] and is in good agreement with the findings for the rate selectivity of lowly boron-doped c-Si versus highly boron-doped poly-Si in this thesis.

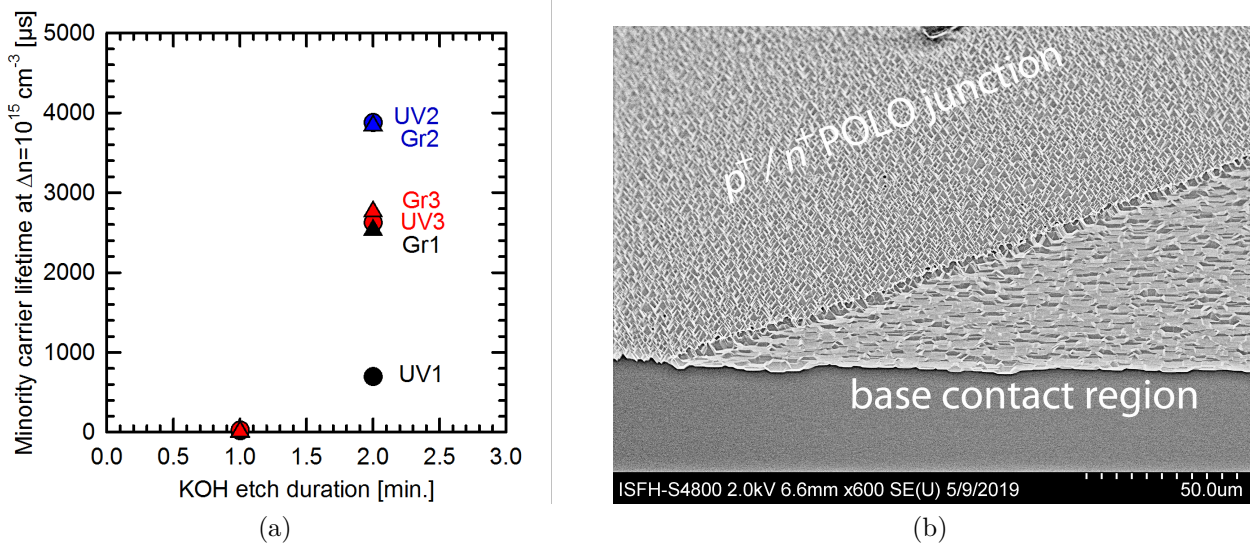


Figure 8.23.: (a) Minority carrier lifetime of laser ablated samples after damage etch removal in 10% KOH and passivation with AlO_x . Circles and triangles correspond to the laser ablation process with the UV and green laser, respectively. (b) Scanning electron micrograph of a bottom cell precursor with TJ after laser ablation of the base contact region and damage etch removal.

Laser ablation and damage etch removal

The poly-Si layers on one side of the lifetime samples are ablated by using either a UV or green laser beam with three different pulse energies – 30%, 35% and 45% of the maximum pulse energy of $16 \mu\text{J}$ for the UV beam and $26 \mu\text{J}$ for the green beam. After laser ablation, the lifetime of the samples drops from more than 1 ms to a small value³⁹ for all investigated laser parameters due to a severe damage of the surface. Next, the samples are etched in 10% KOH solution for 1 min or 2 min and are subsequently passivated with AlO_x . Figure 8.23a depicts the lifetimes of the samples after damage etch removal and passivation. It is evident that the 1 min-damage etch removal is not sufficient to remove the damage and to recover the lifetime for any set of laser parameters. On the other hand, the 2 min-damage etch recovers the lifetime up to nearly 4 ms, which exceeds the initial lifetime of about 1.4 ms. This results from an improved passivation of the laser ablated and AlO_x -passivated surface compared to the previously n^+ POLO passivated surface and suggest that the laser ablated surface is almost damage-free after a 2 min-damage etch removal for all laser parameters, except the UV laser ablation process with the lowest pulse energy. The pulse energy of the latter is too low to remove the p^+ poly-Si completely, which locally prevents the damage etch removal and yields a poorer surface passivation.

In summary, the ablation process with the UV laser with a pulse energy of $5.7 \mu\text{J}$ (UV2 in

³⁹The sample was not measured directly after laser ablation. However, the lifetime after 1 min KOH damage etch and passivation with AlO_x is below $50 \mu\text{s}$. Therefore, it can be concluded that the lifetime of the sample without damage etch removal and passivation is even lower than that.

8.6. SIMPLIFIED PERC-LIKE THREE-TERMINAL BIPOLAR JUNCTION BOTTOM CELLS

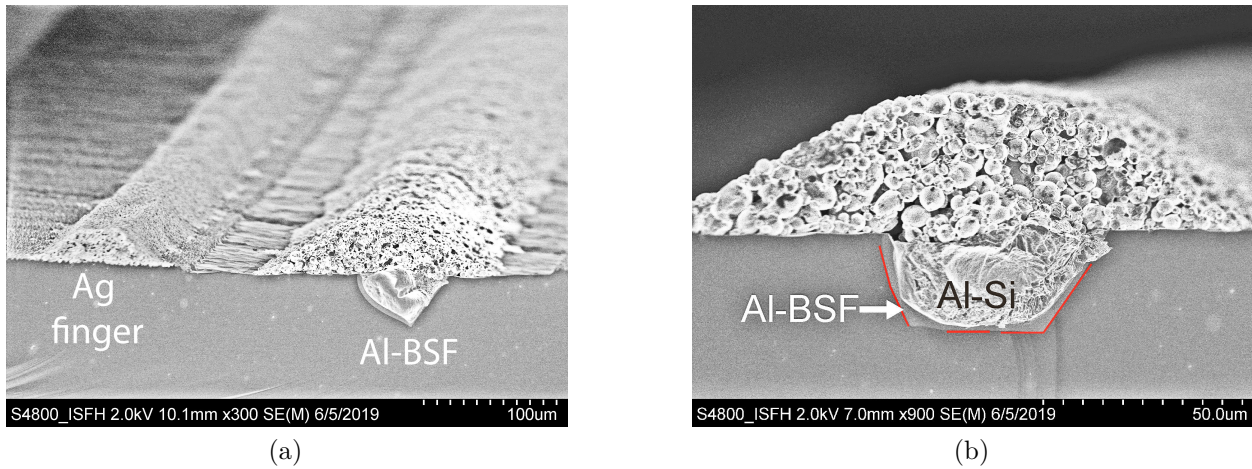


Figure 8.24.: Scanning electron micrograph of the rear side of a finished bottom cell without TJ. (a) Interdigitated screen printed Ag and Al contacts. (b) Al-BSF contact with an Al-doped BSF. Red lines indicate the border between c-Si wafer and the Al-doped BSF region.

figure 8.23a) and with the green laser with a pulse energy of $9.1 \mu\text{J}$ (Gr2 in figure 8.23a) completely remove the p^+ poly-Si etch barrier and a subsequent 2 min-damage etch removal in 10% KOH solution recovers the lifetime of the ablated region, while the p^+ poly-Si layer in the non-ablated region acts as a protective etch barrier and conserves the n^+ POLO junction passivation. The scanning electron micrograph in figure 8.23b illustrates the two regions of the bottom cell with TJ – the p^+/n^+ POLO junction region and the laser ablated and damage etched base contact region. While the p^+/n^+ POLO junction region maintains the textured morphology, the base contact region is planarized by the laser ablation and damage etch removal, which is beneficial for the passivation and Al-BSF formation.

For the processing of the cells in the following subsection as shown figure 8.25a, the ablation process with the green laser in combination with a 2 min-damage etch removal is used. In principle, even a nanosecond laser is acceptable, because it has been experimentally found to yield similar results as for the picosecond laser⁴⁰. Furthermore, the etch duration of 2 min can be decreased by a factor of three by increasing the temperature of the KOH solution from 75°C to 95°C . The selectivity of the etch process should be maintained as long as the KOH concentration is low as found by Seidel *et al.* [454]. The temperature of 75°C was chosen here to have a sufficiently long etch duration for a better control of the etch process in the lab.

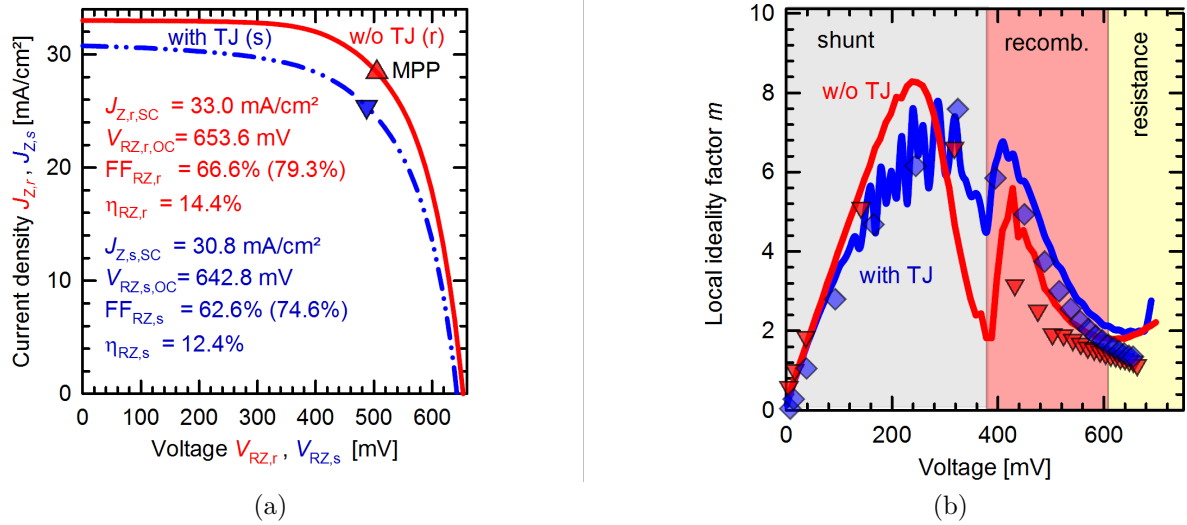


Figure 8.25.: (a) Two-terminal current-voltage $J_{Z,i}$ - $V_{RZ,i}$ characteristic of the screen printed 3T bipolar junction bottom cell with (i=s, blue dash-dotted line) and without (i=r, red solid line) TJ as measured between the rear contacts R and Z under one-sun illumination. The front contact is floating. (b) The corresponding m - V characteristic from the dark $J_{Z,i}$ - $V_{RZ,i}$ (solid lines) and $J_{Z,i,SC}$ - $V_{RZ,i,OC}$ characteristics (diamonds and triangles).

Al-BSF formation

After ablation and damage etch removal, the bottom cell's rear side is passivated with an $\text{AlO}_x/\text{SiN}_y$ layer stack. A dashed line is ablated locally in the passivation on the base contact region to enable the formation of a local Al-BSF formation. The area fraction of the local contact opening amounts to 0.9% for a pitch of 1 mm. Silver is screen printed on the n^+ POLO contact and Al on the base region. Finally, the cells are co-fired at a set peak temperature of 790 °C. Figure 8.24a shows a cross-section scanning electron micrograph of the rear side of the bottom cell and figure 8.24b details the Al-BSF contact after co-firing. An Al-doped BSF region with a thickness between below 1 μm and 3 μm around the contact (light grey region around the bright Al-Si alloyed region) is clearly visible in figure 8.24b, which is slightly shallower than the Al-BSF contacts of PERC+ cells [447, 455] due to a narrower contact line width of 30 μm [456, 457] and should yield a slightly higher saturation current density.

8.6.3. Cell performance

The final solar cells are characterized directly after co-firing⁴¹ using the LOANA solar cell analysis system from pv-tools. Figure 8.25a shows the 2T $J_{Z,i}$ - $V_{RZ,i}$ characteristic of a bottom cell with and without TJ with a floating front contact.

The bottom cell without a TJ (red solid line in figure 8.25a) exhibits a short-circuit current density of 33 mA/cm², an open circuit voltage of 653.6 mV, a fill factor of 66.6% and an efficiency of 14.4%. The reduced $J_{Z,r,SC}$ compared to single junction solar cells (section 7) results from high front side reflection and parasitic absorption of the thick n^+ poly-Si layers of the bottom cell without an anti-reflection coating. The open-circuit voltage is lower by more than 30 mV compare to a Quokka simulation with an assumed saturation current density of 500 fA/cm² [447] for the Al-BSF contact. The slightly shallower BSF and spiking of Al through the AlO_x/SiN_y passivation could be two sources for the reduced open-circuit voltage. The high wafer resistivity of 20 Ωcm paired with a cell pitch of 1 mm causes a considerable lateral transport resistance for majority carriers, thus a high series resistance of more than 3 Ωcm², and results in a loss of more than 10%_{abs.} of the fill factor compared to the pseudo fill factor of 79.3%. The series resistance of approximately 3.3 Ωcm² is consistent with the Quokka simulation, where contact resistances are assumed to be negligible. However, further investigation are required to confirm a low contact resistance.

Furthermore, the pseudo fill factor is approximately 4%_{abs.} lower than the maximum pseudo fill factor of 83.9% as calculated according to Green *et al.* [91] with an ideality factor of unity and the measured open-circuit voltage. This difference attributes to a non-ideal recombination behavior and thus a local ideality factor larger than unity. The local ideality factor of the dark characteristic in figure 8.25b rise at around 380 mV, peaks at 430 mV and decreases again beyond 430 mV. This hump is also present in the m - V characteristic from $J_{Z,r,SC}$ - $V_{RZ,r,OC}$ characteristic and is responsible for an ideality factor larger than unity at the the maximum power point voltage. Such a hump can have different origins, but the most likely sources are resistance-limited recombination or recombination rate saturation [115, 458–460]. Moreover, a shunted floating junction on the front side of the bottom cell can cause similar non-idealities, but it is unlikely that this junction is shunted e.g. through metal spiking, because the junction is not contacted by a metal grid at this stage. Anyway, the clarification of the source for the non-ideality needs more work and should be addressed in the future.

The bottom cells with a TJ show a similar current-voltage characteristic as the bottom cells without it. Since the former cells have an extra p^+ poly-Si layer and a thicker n^+ poly-Si layer, which parasitically absorbs a part of the illumination, the $J_{Z,s,SC}$ is reduced further compared to the latter cells. The open-circuit voltage of 642.8 mV is also smaller by more than 10 mV. As evident from figure 8.25b, the ideality of the cells with TJ is slightly increased compare to the cells without a TJ, which results in a diminished pFF of 74.6%. The FF is further reduced by a series resistance of 3.7 Ωcm² and leads to an efficiency of 12.4%. The

⁴⁰The experimental result for the nanosecond laser were performed in a separated study and they are not included in this thesis.

⁴¹Since boron-doped CZ wafer are used, a permanent deactivation of the boron-oxygen defect might be beneficial for the cell performance. However, all measurements were performed without deactivation.

performance difference between both bottom cell types is assumed to be due to variations of the non-optimized cell processes rather than due to a fundamental reason.

Conclusively, the obtained cell results ($V_{RZ,i,OC} \approx 650$ mV, $\text{pFF}_{RZ,i}$ up to 79.3%) of the very first batch of such solar cells demonstrate that the proposed cell processes in figure 8.21 and 8.20 works on a reasonable level. A detailed discussion of the 3T operation is found in the appendix A.5.8.

8.7. Chapter summary

In this chapter, the 3T-IBC bottom cell was examined in detail. First, a taxonomy of 3T tandem solar cells and the associated nomenclature and loading topology was introduced. A distinction was made between series-connected and reverse-connected tandem solar cells. Furthermore, two IBC bottom cell architectures are distinguished. A uni-junction bottom solar cell contains a single (uni) minority carrier contact and two majority carrier contacts. A bipolar junction bottom solar cell has two minority carrier contacts and a single majority carrier contact.

Both 3T bottom cell architectures were fabricated base on a modified POLO-IBC fabrication process from section 7 and the working principle was investigated by means of J - V measurements of illuminated devices and analytical modelling. The experiments reveal that the third contact of a 3T unijunction and bipolar junction bottom cell enables the collection or injection of additional minority-carriers from or into the bottom cell, and therefore additional carriers from the bottom cell or top cell can be collected compare to a 2T tandem cell. In the ideal case, the power output of such a 3T bottom cell is almost independent of the current density applied from the top cell and no current-matching is needed.

To enable a deeper understanding of the operation of a 3T IBC cell and to ascertain the origin of a minor power loss and a voltage drop between the contact of the same carrier-type of the bottom cell, a simple analytical equivalent circuit model is proposed for each architecture, the unijunction and bipolar junction bottom cell. The proposed analytical models were compared with the experimental data and predict the experimental findings. Design rules are derived from the verified models for both bottom cell types in different operation modes and it is calculated that a well-design series- and reverse-connected 3T tandem cell comprising a unijunction or bipolar junction bottom cell with a total saturation current density of 10 fA/cm^{42} and a current-mismatched Shockley-Queisser-limited top cell with a band gap of 1.55 eV (e.g. lead halide perovskite) or 1.8 eV (e.g. GaInP) is able to attain an efficiency close to 42% and beyond⁴³.

Next, a high performance 3T unijunction cell with a textured n^+ POLO front contact and

⁴²This corresponds to a single-junction IBC cell with an efficiency of approximately 27%, which is considerably lower than for a detailed-balance-limited or Auger-limited cell with an efficiency of more than 32% [415] and 29.6% [28], respectively.

⁴³In fact, the tandem efficiency close to 42% was calculated for a tandem comprising a bipolar junction bottom cell. However, it was shown that the unijunction bottom cell operates almost loss-free compared to the bipolar junction bottom cell and therefore it can be concluded that a tandem with a unijunction bottom cell is as efficient as with a bipolar junction bottom cell.

an improved laser contact opening process is developed, which allows to implement thick dielectric layers on the rear side of a POLO-IBC cell for an enhanced IR-response of the cell. The resulting 3T unijunction bottom cell exhibits an efficiency of 20.3% under full-spectrum illumination. When using such a bottom cell in a 3T tandem cell with a GaInP, GaAs [398, 399, 406] or a record lead halide perovskite [426, 427] top cell, it is expected that a 3T tandem efficiency between 32-33% is within reach.

Finally, a simplified screen printed PERC-like 3T bipolar junction bottom cell is proposed for a cost-effective and potentially high performance 3T tandem cell. The corresponding elegant fabrication process and novel process steps are developed and the feasibility to fabricate such a bottom cell with industrially relevant tools is demonstrated. In a first non-optimized cell batch, an one-sun efficiency of already 12.4% and 14.4% is achieved for a bottom cell with and without an integrated p^+/n^+ poly-Si tunnel junction, respectively. It can be projected that the optimization of single process steps and by following the derived design guidelines will yield a low-cost PERC-like 3T bottom cell with an efficiency approaching that of the high performance 3T unijunction bottom cell. This path is a promising and attractive way to reuse the installed production capacity of the dominating PERC-technology in a cost-effective tandem solar cell with maximum energy yield production.

9. Three-terminal GaInP//Si tandem cell demonstrator

The following chapter is based on a peer-review paper published in Schnabel *et al.* [293], which was for the first time presented at the 2018 Material Research Society Spring Meeting and Exhibit in Phoenix, Arizona, USA [292].

M. Schnabel and H. Schulte-Huxel developed the cell fabrication process of the GaInP top cell on top of the bottom cell and fabricated the tandem cell at NREL. The author designed and partly fabricated the bottom cells at ISFH.

After studying the carrier-selectivity of a contact and the properties of such a carrier-selective POLO junction, the POLO-IBC cell was developed. A modified POLO-IBC cell with a third POLO front contact enabled an in-depth investigation of 3T-POLO-IBC bottom cells in chapter 8 with the focus on the integration in 3T tandem solar cells. It was found that a 3T POLO-IBC bottom cell allows to make a 3T tandem solar cell from current-mismatched sub-cells, which is as efficient as an independently operating 4T tandem solar cell.

Finally, as the title of this thesis “Three-terminal tandem solar cells enabled by back-contacted bottom cells featuring polysilicon based junctions” suggests, all ingredients of the previous chapters are brought together to demonstrate a 3T GaInP//Si tandem solar cell, which is enabled by the development of the back-contacted bottom solar cell with passivating and carrier-selective polysilicon-based contacts. The reported GaInP//Si POLO-IBC tandem solar cell demonstrator by Schnabel *et al.* [280, 292, 293] is the first published 3T tandem solar cell featuring an IBC bottom solar cell and proves the findings of chapter 8 in a full tandem device.

9.1. Fabrication of the demonstrator

The 3T tandem demonstrator device is fabricated by bonding a separately prepared GaInP cell precursor to a finished 3T unijunction POLO-IBC cell by means of a transparent conductive adhesive (TCA) [461]. Subsequently, the top cell processing is completed on top of the POLO-IBC cells. The a schematic cross-section of the final 3T GaInP//Si POLO-IBC cell is shown in figure 9.1a.

The rear-heterojunction GaInP cell [462] precursor was epitaxially grown inverted on a GaAs substrate by metal organic chemical vapor phase epitaxy (MOVPE) following reference [406, 463, 464]. The fabrication of the used 3T unijunction POLO-IBC cell follows the process

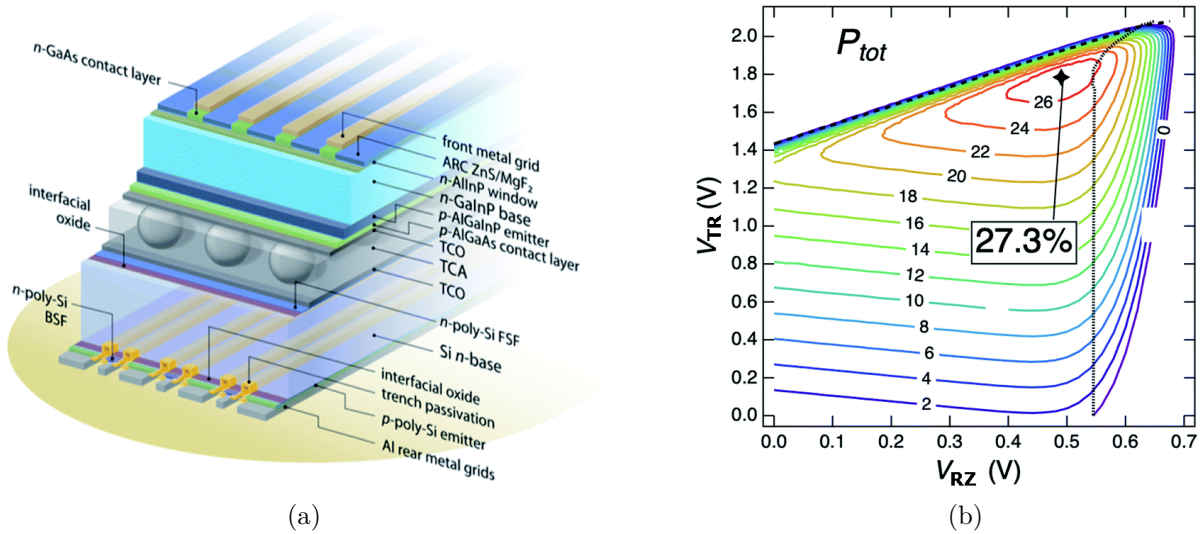


Figure 9.1.: (a) Schematic cross-section of the TCA-bonded 3T GaInP//Si POLO-IBC cell. (b) Total power density P_{tot} represented as a heat map of the two terminal voltages V_{TR} and V_{RZ} . [Adapted from Schnabel *et al.* [293] with permission from The Royal Society of Chemistry.]

sequence described in section 8.2.1, but without implementing a metal grid on the planar n^+ POLO front side contact. Since the top cell processing is completed after bonding top and bottom cell, the rear side of the bottom cell has to be protected against the aggressive wet chemistry with two layers of Fujifilm SC-900 photoresist, which is removed with toluene after completing the cell processing.

Before bonding top and bottom cell, the bonding interfaces – the bottom of the GaInP top cell and the n^+ POLO front side of the bottom cell – are coated with a 95 nm-thick indium tin oxide (ITO) layer [293] to ensure a low-resistive contact to the TCA composite layer. The TCA is composed of silver-coated poly(methyl methacrylate) (PMMA) spheres embedded in epoxy. In order to bond top and bottom cell, the TCA is applied to the ITO-coated surfaces of the top and bottom cell and the GaInP/TCA/POLO-IBC stack is laminated.

After bonding, the GaAs substrate is etched off from the top cell and a photo-lithographically defined Ni/Au grid is plated on the front n -GaAs contact layer of the GaInP top cell and the cell area is defined by a mesa etch. The GaAs contact layer is removed between the grid fingers and a MgF₂/ZnS antireflection coating is deposited on the front side of the GaInP top cell.

9.2. Performance of the demonstrator

The illuminated current-voltage characteristic of the 3T GaInP//Si tandem cell was recorded on a class A adjustable solar simulator with calibrated reference cells. The illumination intensity in each sub-cell was adjusted to AM1.5G conditions by means of an LED array and

a Xenon lamp. A detailed discussion of the measurement procedure is found in Schnabel *et al.* [293] and a detailed study on the measurement procedure of 3T tandem cell is found in Geisz *et al.* [336].

The 3T tandem cell is measured in two different arrangements. The 2T J_T - V_{TR} is acquired between the front contact of the top cell and the p^+ POLO contact of the bottom cell, while the n^+ POLO contact Z on the rear side of the bottom cell was floating ($J_Z = 0$). The 2T measurement yields an open circuit voltage $V_{TR,OC}$ of 2053 ± 30 mV, a short-circuit current density $J_{T,SC}$ of 14.9 ± 0.5 mA/cm², a fill factor FF_{TR} of $86.3 \pm 0.5\%$ and an efficiency η_{TR} of $26.4 \pm 1.0\%$.

For the 3T measurement, the J_T - V_{TR} of the TR circuit depends on the state of the circuit between the IBC contacts. The characteristic of both circuits has to be acquired simultaneously for an accurate measurement. However, the mpp voltages of the top and bottom cell during 3T operation can be estimated. If the J_T - V_{TZ} characteristic between contact T and Z is measured, while the RZ circuit is open ($J_R = 0$), one can measure the “top cell” through the bottom cell. Bauer [414] pointed out, that if the RZ circuit is shorted, an artifact can lead to an error. If the J_R - V_{RZ} characteristic of the RZ circuit is measured, while the TR circuit is held at the determined maximum power point voltage $V_{TZ,mpp}$, the “bottom cell” is measured in a similar situation as in the 3T tandem. Both mpp voltages should be close to the mpp voltages of the maximum power point of the total 3T power [414]. However, for an accurate measurement the voltages should be scanned around the estimated voltages. Therefore, for the 3T measurement, a pair of voltages V_{TR} and V_{RZ} is applied by using two sourcemeters and the respective current densities J_T and J_Z are measured. By multiplying the current densities and voltages, the respective power densities extracted from each circuit can be determined. The power densities of both circuits add up to the total 3T power density P_{tot} . Figure 9.1b shows the P_{tot} - V_{TR} - V_{RZ} characteristic of the 3T tandem device plotted as a power density heat map. From the heat map, the operation point of the 3T tandem cell with maximum power output can be found at $V_{TR,mpp}$ of 1785 ± 30 mV and $V_{RZ,mpp}$ of 490 ± 10 mV, where the TR circuit contributes $25.4 \pm 0.9\%$ and the RZ circuit $1.9 \pm 0.1\%$ to the total 3T efficiency of $27.3 \pm 1.0\%$.

The net efficiency gain for the 3T operation is $0.9 \pm 0.2\%_{abs.}$ compared to the top cell limiting 2T operation and confirms the findings of chapter 8, that a 3T tandem cell comprising a 3T IBC cell can be operated more efficiently than a current-mismatch 2T tandem cell. The efficiency gain of only $0.9\%_{abs.}$ is expected, because the current-mismatch of the POLO-IBC cell with a planar n^+ POLO front contact and the GaInP top cell is small. However, for 3T tandem cells with a stronger mismatch (e.g. with GaAs top cell), a much higher efficiency gain of about $10\%_{abs.}$ was observed [324].

Although an efficiency of 27.3% for a simple demonstrator device is already impressive, it is far below the record efficiency of 32.5% for a 4T GaInP//Si tandem cell [406]. This is partly due to the non-optimized bottom cell [280], which was improved in section 8.5 to obtain a high performance 3T unijunction bottom cell. This raises optimism that a more than 33%-efficient 3T tandem solar cell will be achieved in the future.

10. Summary

The aim of the present thesis was to investigate three-terminal interdigitated back-contact bottom cells with passivating and carrier-selective POLO junctions, which allow the realization of 3T tandem solar cells. For this purpose, the three building blocks of a 3T-POLO-IBC cell, which are based on each other, were examined: the passivating and carrier-selective POLO junction, the integration of POLO junctions on the rear side of an IBC cell and the physics of a three-terminal IBC cell. Finally, the first 3T tandem solar cell comprising a back-contacted solar cell is demonstrated.

As the POLO junction is a passivating and carrier-selective contact, the process of carrier extraction at such a contact to an absorber is studied from theoretical point of view. The selectivity of a contact is defined on the basis of (reaction) kinetic considerations at the contact in terms of the rate ratio of desired processes to undesired processes. The extraction efficiency of charge carriers at the contact is derived as the ratio of the external voltage versus the internal voltage from a thermodynamic point of view. To emphasize the unifying nature of the definitions in this thesis, the existing literature definitions are calculated from the definitions in this thesis. The selectivity and extraction efficiency are correlated and the efficiency of a solar cell with given contact selectivity is calculated accordingly.

After the detailed theoretical investigation of selectivity, the properties of n^+ and p^+ POLO junctions are studied and low saturation current densities between 2 fA/cm^2 and 18 fA/cm^2 and simultaneously junction resistivity between $0.4 \text{ m}\Omega\text{cm}^2$ and $10 \text{ m}\Omega\text{cm}^2$ are observed. The resulting logarithmic selectivity according to Brendel and Peibst [120] of POLO junctions exhibits values larger than 15.

For the next building block, a photolithography-free fabrication process flow for an interdigitated back-contact cell with POLO junction for both polarities was presented, the challenges of integrating polysilicon-based contacts on the rear side and the properties of the resulting POLO-IBC cell were discussed. The implementation of p^+ and n^+ doped poly-Si on the rear side of the cell, results in a parasitic p^+n^+ graded junction within the poly-Si and reduces the performance of the POLO-IBC cell significantly. Therefore, the parasitic junction was removed during the cell fabrication process by implementing a trench separation of the n^+ and p^+ doped poly-Si regions, which yielded a POLO-IBC cell with a certified power conversion efficiency of 24.25%. A detailed analysis of the optics and the recombination behavior of the cell along with Quokka simulations were presented. When the determined contact resistances are used for the simulation a good agreement with experimental device characteristic is achieved. This supports the findings that POLO junctions offer excellent recombination and majority carrier transport properties and it is anticipated that the practical efficiency limit for POLO-IBC cell is above 27%.

For the final building block, a third POLO contact was added to the POLO-IBC cell and the

3T-IBC bottom cell was examined in detail. A taxonomy of 3T tandem solar cells and the associated nomenclature was presented and two different 3T-IBC bottom cell architectures are distinguished. A unijunction bottom solar cell contains a single (uni) minority carrier contact and two majority carrier contacts. A bipolar junction bottom solar cell has two minority carrier contacts and a single majority carrier contact.

Both 3T bottom cell architectures were fabricated base on a modified POLO-IBC fabrication process. The working principle and loss mechanisms were investigated by means of J - V measurements of illuminated devices and analytical modelling. The experiments reveal that the third contact of a 3T unijunction and bipolar junction bottom cell enables the collection or injection of additional minority or majority carriers from or into the bottom cell. In the ideal case, the power output of such a 3T bottom cell is almost independent of the current density applied from the top cell and no current-matching is required.

For a deeper understanding of the operation of a 3T IBC cell, simple analytical equivalent circuit models are proposed and evaluated for the unijunction and bipolar junction bottom cells. Design rules are derived from the verified models and it is predicted that a well-design series- and reverse-connected 3T tandem cell comprising a unijunction or bipolar junction bottom cell and a current-mismatched top cell with a band gap of 1.55 eV (e.g. lead halide perovskite) or 1.8 eV (e.g. GaInP) is able to attain an efficiency close to 42%. Finally, a high performance 3T unijunction cell with a textured n^+ POLO front contact with an efficiency of 20.3% and a simplified screen printed PERC-like 3T bipolar junction bottom cell with 14.4% under full-spectrum illumination is developed. It can be projected that the optimization of single process steps and by following the derived design guidelines will yield a low-cost PERC-like 3T bottom cell with an efficiency approaching that of the high performance 3T unijunction bottom cell. This path is a promising and attractive way to reuse the installed production capacity of the dominating PERC-technology in a cost-effective tandem solar cell with maximum energy yield production.

Finally, the first 3T GaInP//POLO-IBC tandem cell demonstrator with an efficiency of 27.3% is fabricated and a net efficiency gain of 0.9% is demonstrated with respect to the 2T operation of the 3T tandem cell.

Bibliography

- ¹O. Hoegh-Guldberg, D. Jacob, M. Taylor, T. Guillén Bolaños, M. Bindi, S. Brown, I. A. Camilloni, A. Diedhiou, R. Djalante, K. Ebi, F. Engelbrecht, J. Guiot, Y. Hijioka, S. Mehrotra, C. W. Hope, A. J. Payne, H.-O. Pörtner, S. I. Seneviratne, A. Thomas, R. Warren, and G. Zhou, “The human imperative of stabilizing global climate change at 1.5°C,” *Science* **365**, 10.1126/science.aaw6974 (2019).
- ²T. M. Lenton, J. Rockström, O. Gaffney, S. Rahmstorf, K. Richardson, W. Steffen, and H. J. Schellnhuber, “Climate tipping points - too risky to bet against,” *Nature* **575** (2019).
- ³J. Rockström, O. Gaffney, J. Rogelj, M. Meinshausen, N. Nakicenovic, and H. J. Schellnhuber, “A roadmap for rapid decarbonization,” *Science* **355**, 1269–1271 (2017).
- ⁴C. S. Stoughton, “The tragedy of climate change,” PhD thesis (UC Irvine, 2020).
- ⁵D. Gerten, V. Heck, J. Jägermeyr, B. L. Bodirsky, I. Fetzer, M. Jalava, M. Kummu, W. Lucht, J. Rockström, S. Schaphoff, et al., “Feeding ten billion people is possible within four terrestrial planetary boundaries,” *Nature Sustainability* **3**, 200–208 (2020).
- ⁶V. Krey, G. Luderer, L. Clarke, and E. Kriegler, “Getting from here to there—energy technology transformation pathways in the emf27 scenarios,” *Climatic change* **123**, 369–382 (2014).
- ⁷S. Gota, C. Huizenga, K. Peet, N. Medimorec, and S. Bakker, “Decarbonising transport to achieve paris agreement targets,” *Energy Efficiency* **12**, 363–386 (2019).
- ⁸R. Zhang and S. Fujimori, “The role of transport electrification in global climate change mitigation scenarios,” *Environmental Research Letters* **15**, 034019 (2020).
- ⁹H. N. Psaraftis, “Decarbonization of maritime transport: to be or not to be?” *Maritime Economics & Logistics* **21**, 353–371 (2019).
- ¹⁰J. H. Wesseling, S. Lechtenböhrer, M. Åhman, L. J. Nilsson, E. Worrell, and L. Coenen, “The transition of energy intensive processing industries towards deep decarbonization: characteristics and implications for future research,” *Renewable and Sustainable Energy Reviews* **79**, 1303–1313 (2017).
- ¹¹Z. J. Schiffer and K. Manthiram, “Electrification and decarbonization of the chemical industry,” *Joule* **1**, 10–14 (2017).
- ¹²N. M. Haegel, R. Margolis, T. Buonassisi, D. Feldman, A. Froitzheim, R. Garabedian, M. Green, S. Glunz, H.-M. Henning, B. Holder, I. Kaizuka, B. Kroposki, K. Matsubara, S. Niki, K. Sakurai, R. A. Schindler, W. Tumas, E. R. Weber, G. Wilson, M. Woodhouse, and S. Kurtz, “Terawatt-scale photovoltaics: trajectories and challenges,” *Science* **356**, 141–143 (2017).

- ¹³N. M. Haegel, H. Atwater, T. Barnes, C. Breyer, A. Burrell, Y.-M. Chiang, S. De Wolf, B. Dimmler, D. Feldman, S. Glunz, J. C. Goldschmidt, D. Hochschild, R. Inzunza, I. Kaizuka, B. Kroposki, S. Kurtz, S. Leu, R. Margolis, K. Matsubara, A. Metz, W. K. Metzger, M. Morjaria, S. Niki, S. Nowak, I. M. Peters, S. Philipps, T. Reindl, A. Richter, D. Rose, K. Sakurai, R. Schlatmann, M. Shikano, W. Sinke, R. Sinton, B. Stanbery, M. Topic, W. Tumas, Y. Ueda, J. van de Lagemaat, P. Verlinden, M. Vetter, E. Warren, M. Werner, M. Yamaguchi, and A. W. Bett, “Terawatt-scale photovoltaics: transform global energy,” *Science* **364**, 836–838 (2019).
- ¹⁴F. Creutzig, P. Agoston, J. C. Goldschmidt, G. Luderer, G. Nemet, and R. C. Pietzcker, “The underestimated potential of solar energy to mitigate climate change,” *Nature Energy* **2**, 17140 (2017).
- ¹⁵D. B. Needleman, J. R. Poindexter, R. C. Kurchin, I. Marius Peters, G. Wilson, and T. Buonassisi, “Economically sustainable scaling of photovoltaics to meet climate targets,” *Energy Environ. Sci.* **9**, 2122–2129 (2016).
- ¹⁶J. Jean, P. R. Brown, R. L. Jaffe, T. Buonassisi, and V. Bulovi, “Pathways for solar photovoltaics,” *Energy Environ. Sci.* **8**, 1200–1219 (2015).
- ¹⁷S. Kurtz, N. Haegel, R. Sinton, and R. Margolis, “A new era for solar,” *Nature photonics* **11**, 3–5 (2017).
- ¹⁸D. M. Chapin, C. S. Fuller, and G. L. Pearson, “A new silicon p-n junction photocell for converting solar radiation into electrical power,” *Journal of Applied Physics* **25**, 676–677 (1954).
- ¹⁹A. Jäger-Waldau, “Snapshot of photovoltaics - february 2020,” *Energies* **13**, 930 (2020).
- ²⁰International Energy Agency - Photovoltaic Power Systems Programme, *Snapshot of global pv markets 2020, report iea-pvps t1-37:2020*, (2020).
- ²¹A. Louwen and W. van Sark, “Chapter 5 - photovoltaic solar energy,” in *Technological learning in the transition to a low-carbon energy system*, edited by M. Junginger and A. Louwen (Academic Press, 2020), pp. 65–86.
- ²²R. M. Swanson, “A vision for crystalline silicon photovoltaics,” *Progress in Photovoltaics: Research and Applications* **14**, 443–453 (2006).
- ²³G. F. Nemet, “Beyond the learning curve: factors influencing cost reductions in photovoltaics,” *Energy Policy* **34**, 3218–3232 (2006).
- ²⁴U. Pillai, “Drivers of cost reduction in solar photovoltaics,” *Energy Economics* **50**, 286–293 (2015).
- ²⁵D. M. Powell, R. Fu, K. Horowitz, P. A. Basore, M. Woodhouse, and T. Buonassisi, “The capital intensity of photovoltaics manufacturing: barrier to scale and opportunity for innovation,” *Energy & Environmental Science* **8**, 3395–3408 (2015).
- ²⁶H. Ding, D. Zhou, G. Liu, and P. Zhou, “Cost reduction or electricity penetration: government r&d-induced pv development and future policy schemes,” *Renewable and Sustainable Energy Reviews* **124**, 109752 (2020).

-
- ²⁷Fraunhofer ISE (2015): *Current and Future Cost of Photovoltaics. Long-term Scenarios for Market Development, System Prices and LCOE of Utility-Scale PV Systems. Study on behalf of Agora Energiewende* ().
- ²⁸S. Schafer and R. Brendel, “Accurate Calculation of the Absorptance Enhances Efficiency Limit of Crystalline Silicon Solar Cells With Lambertian Light Trapping,” *IEEE Journal of Photovoltaics*, 1–3 (2018).
- ²⁹B. A. Veith-Wolf, S. Schäfer, R. Brendel, and J. Schmidt, “Reassessment of intrinsic lifetime limit in n-type crystalline silicon and implication on maximum solar cell efficiency,” *Solar Energy Materials and Solar Cells* **186**, 194–199 (2018).
- ³⁰X. Zhang, W. Liu, Y. Chen, S. Chen, G. Xu, Y. Hu, Y. Yang, D. Chen, Y. Chen, P. P. Altermatt, P. J. Verlinden, and Z. Feng, “A roadmap towards 24%-efficiency PERC cells based on screen printing for mass production,” in *37th European Photovoltaic Solar Energy Conference and Exhibition* (2020), pp. 233–237.
- ³¹J. H. Petermann, “Prozessentwicklung & Verlustanalysen für dünne monokristalline Siliziumsolarzellen und deren Prozessierung auf Modullevel,” PhD thesis (Gottfried Wilhelm Leibniz Universität Hannover, 2014).
- ³²R. Peibst, C. Kruse, S. Schäfer, V. Mertens, S. Bordihn, T. Dullweber, F. Haase, C. Hollemann, B. Lim, B. Min, R. Niepelt, H. Schulte-Huxel, and R. Brendel, “For none, one, or two polarities how do p-n junctions fit best into industrial silicon solar cells?” *Progress in Photovoltaics: Research and Applications* **28**, 503–516 (2020).
- ³³J. Melskens, B. W. van de Loo, B. Macco, L. E. Black, S. Smit, and W. Kessels, “Passivating contacts for crystalline silicon solar cells: from concepts and materials to prospects,” *IEEE Journal of Photovoltaics* **8**, 373–388 (2018).
- ³⁴T. G. Allen, J. Bullock, X. Yang, A. Javey, and S. De Wolf, “Passivating contacts for crystalline silicon solar cells,” *Nature Energy*, 1–15 (2019).
- ³⁵R. Peibst, Y. Larionova, S. Reiter, T. F. Wietler, N. Orłowski, S. Schäfer, B. Min, M. Stratmann, D. Tetzlaff, J. Krügener, U. Höhne, J. D. Kähler, H. Mehlich, S. Frigge, and R. Brendel, “Building Blocks for Industrial, Screen-Printed Double-Side Contacted POLO Cells With Highly Transparent ZnO:Al Layers,” *IEEE Journal of Photovoltaics* **8**, 719–725 (2018).
- ³⁶R. Peibst, Y. Larionova, S. Reiter, M. Turcu, R. Brendel, D. Tetzlaff, J. Krügener, T. Wietler, U. Höhne, J. Kähler, et al., “Implementation of n+ and p+ poly junctions on front and rear side of double-side contacted industrial silicon solar cells,” in *32nd European photovoltaic solar energy conference and exhibition* (2016), pp. 323–327.
- ³⁷E. Jackson, “Areas for improvement of the semiconductor solar energy converter,” in *Transactions of the conference on the use of solar energy* (1955).
- ³⁸M. A. Green, Y. Hishikawa, E. D. Dunlop, D. H. Levi, J. Hohl-Ebinger, and A. W. Ho-Baillie, “Solar cell efficiency tables (version 51),” *Progress in Photovoltaics: Research and Applications* **26**, 3–12 (2018).

- ³⁹K. Sasaki, T. Agui, K. Nakaido, N. Takahashi, R. Onitsuka, and T. Takamoto, “Development of InGaP/GaAs/InGaAs inverted triple junction concentrator solar cells,” in AIP conference proceedings, Vol. 1556 (American Institute of Physics, 2013), pp. 22–25.
- ⁴⁰J. F. Geisz, R. M. France, K. L. Schulte, M. A. Steiner, A. G. Norman, H. L. Guthrey, M. R. Young, T. Song, and T. Moriarty, “Six-junction III–V solar cells with 47.1% conversion efficiency under 143 Suns concentration,” *Nature Energy* **5**, 326–335 (2020).
- ⁴¹M. A. Green, “Silicon wafer-based tandem cells: the ultimate photovoltaic solution?” In *Physics, simulation, and photonic engineering of photovoltaic devices iii*, Vol. 8981 (International Society for Optics and Photonics, 2014), p. 89810L.
- ⁴²J. Werner, B. Niesen, and C. Ballif, “Perovskite/Silicon Tandem Solar Cells: Marriage of Convenience or True Love Story? - An Overview,” *Advanced Materials Interfaces*, 1700731 (2017).
- ⁴³M. Nell and A. Barnett, “The spectral p-n junction model for tandem solar-cell design,” *IEEE Transactions on Electron Devices* **34**, 257–266 (1987).
- ⁴⁴A. D. Vos, “Detailed balance limit of the efficiency of tandem solar cells,” *Journal of Physics D: Applied Physics* **13**, 839–846 (1980).
- ⁴⁵D. Kondepudi and I. Prigogine, *Modern Thermodynamics From Heat Engines to Dissipative Structures*, Second Edition (John Wiley & Sons, Ltd, 2015).
- ⁴⁶S. R. De Groot and P. Mazur, *Non-equilibrium thermodynamics* (Courier Corporation, 2013).
- ⁴⁷S. Carnot, *Reflections on the motive power of heat and on machines fitted to develop that power* (J. Wiley, 1890).
- ⁴⁸B. Andresen, R. S. Berry, A. Nitzan, and P. Salamon, “Thermodynamics in finite time. i. the step-carnot cycle,” *Physical Review A* **15**, 2086 (1977).
- ⁴⁹M. H. Rubin, “Figures of merit for energy conversion processes,” *American Journal of Physics* **46**, 637–639 (1978).
- ⁵⁰L. S. Garcia-Colin and J. R. Uribe, “Extended Irreversible Thermodynamics Beyond the Linear Regime: A Critical Overview,” **16**, 89–128 (1991).
- ⁵¹M. H. Rubin, “Optimal configuration of a class of irreversible heat engines. i,” *Physical Review A* **19**, 1272 (1979).
- ⁵²M. H. Rubin, “Optimal configuration of a class of irreversible heat engines. ii,” *Physical Review A* **19**, 1277 (1979).
- ⁵³I. Novikov, “The efficiency of atomic power stations (a review),” *Journal of Nuclear Energy* (1954) **7**, 125–128 (1958).
- ⁵⁴F. L. Curzon and B. Ahlborn, “Efficiency of a carnot engine at maximum power output,” *American Journal of Physics* **43**, 22–24 (1975).
- ⁵⁵K. H. Hoffmann, “An introduction to endoreversible thermodynamics,” in *Proceedings of the international conference and summer school on thermal theories of continua: survey and developments* (2005).

-
- ⁵⁶P. Chambadal, “Le choix du cycle thermique dans une usine génératrice nucléaire,” French, *Revue Générale de l’Electricité* **67**, 332–345 (1958).
- ⁵⁷M. Esposito, R. Kawai, K. Lindenberg, and C. Van den Broeck, “Efficiency at maximum power of low-dissipation carnot engines,” *Physical Review Letters* **105**, 150603 (2010).
- ⁵⁸G. Busch, “Early history of the physics and chemistry of semiconductors—from doubts to fact in a hundred years,” *European Journal of Physics* **10**, 254 (1989).
- ⁵⁹W. Shockley, *Electrons and holes in semiconductors: with applications to transistor electronics*, Bell Telephone Laboratories series (Van Nostrand, 1950).
- ⁶⁰W. Shockley, “The Theory of p-n Junctions in Semiconductors and p-n Junction Transistors,” *Bell System Technical Journal* **28**, 435–489 (1949).
- ⁶¹S. M. Sze, *Semiconductor devices: physics and technology* (Wiley, 1985).
- ⁶²R. F. Pierret and G. W. Neudeck, *Advanced semiconductor fundamentals*, Vol. 6 (Addison-Wesley Reading, MA, 1987).
- ⁶³M. Shur, *Physics of semiconductor devices*, Prentice-Hall series in solid state physical electronics (Prentice Hall, 1990).
- ⁶⁴P. Würfel, *Physik der Solarzellen* (Spektrum, Akad. Verlag, 2000).
- ⁶⁵J. S. Blakemore, *Semiconductor statistics* (Courier Corporation, 2002).
- ⁶⁶J. Nelson, *The physics of solar cells* (World Scientific Publishing Company, 2003).
- ⁶⁷A. B. Sproul and M. A. Green, “Intrinsic carrier concentration and minority carrier mobility of silicon from 77 to 300 k,” *Journal of Applied Physics* **73**, 1214–1225 (1993).
- ⁶⁸P. P. Altermatt, A. Schenk, F. Geelhaar, and G. Heiser, “Reassessment of the intrinsic carrier density in crystalline silicon in view of band-gap narrowing,” *Journal of Applied Physics* **93**, 1598–1604 (2003).
- ⁶⁹J. E. Parrott, “Transport theory of semiconductor energy conversion,” *Journal of Applied Physics* **53**, 9105–9111 (1982).
- ⁷⁰J. Parrott, “Thermodynamic theory of transport processes in semiconductors,” *IEEE Transactions on Electron Devices* **43**, 809–826 (1996).
- ⁷¹U. Lindelfelt, “Heat generation in semiconductor devices,” *Journal of Applied Physics* **75**, 942–957 (1994).
- ⁷²W. Shockley and W. T. Read, “Statistics of the Recombinations of Holes and Electrons,” *Physical Review* **87**, 835–842 (1952).
- ⁷³H. A. Müser, “Thermodynamische Behandlung von Elektronenprozessen in Halbleiter-Randschichten,” *Zeitschrift für Physik* **148**, 380–390 (1957).
- ⁷⁴A. Rose, “Photovoltaic Effect Derived from the Carnot Cycle,” *Journal of Applied Physics* **31**, 1640–1641 (1960).
- ⁷⁵R. T. Ross and T.-L. Hsiao, “Limits on the yield of photochemical solar energy conversion,” *Journal of Applied Physics* **48**, 4783–4785 (1977).

- ⁷⁶W. Ruppel and P. Würfel, “Upper limit for the conversion of solar energy,” *IEEE Transactions on Electron Devices* **27**, 877–882 (1980).
- ⁷⁷A. De Vos and H. Pauwels, “On the thermodynamic limit of photovoltaic energy conversion,” *Applied physics* **25**, 119–125 (1981).
- ⁷⁸P. Baruch, C. Picard, and R. Swanson, “Thermodynamical limits to photovoltaic solar energy conversion efficiency,” in *Proceedings of the 3rd European Photovoltaic Solar Energy Conference* (1981), p. 927.
- ⁷⁹P. Baruch and J. E. Parrott, “A thermodynamic cycle for photovoltaic energy conversion,” *Journal of Physics D: Applied Physics* **23**, 739–743 (1990).
- ⁸⁰T. Markvart and P. Landsberg, “Thermodynamics and reciprocity of solar energy conversion,” *Physica E: Low-dimensional Systems and Nanostructures* **14**, 71–77 (2002).
- ⁸¹A. Cuevas, T. Allen, J. Bullock, Yimao Wan, Di, and Xinyu Zhang, “Skin care for healthy silicon solar cells,” in *2015 IEEE 42nd Photovoltaic Specialist Conference (PVSC)* (2015), pp. 1–6.
- ⁸²A. Cuevas, “The recombination parameter j_0 ,” *Energy Procedia* **55**, 53–62 (2014).
- ⁸³K. Van Vliet, “High injection theories of the p- n junction in the charge neutrality approximation,” *Solid-State Electronics* **9**, 185–201 (1966).
- ⁸⁴N. H. Fletcher, “General Semiconductor Junction Relations,” *Journal of Electronics and Control* **2**, 609–610 (1957).
- ⁸⁵R. Corkish and M. A. Green, “Junction recombination current in abrupt junction diodes under forward bias,” *Journal of Applied Physics* **80**, 3083–3090 (1996).
- ⁸⁶S. Choo, “Space-charge recombination in a forward-biased diffused p-n junction,” *Solid-State Electronics* **14**, 1201–1208 (1971).
- ⁸⁷P. J. Anderson and M. J. Buckingham, “Theory of depletion-layer recombination in silicon p–n junctions,” *Electronics Letters* **13**, 496–498 (1977).
- ⁸⁸C.-T. Sah, R. Noyce, and W. Shockley, “Carrier Generation and Recombination in P-N Junctions and P-N Junction Characteristics,” in *Proceedings of the IRE*, Vol. 45, 9 (Sept. 1957), pp. 1228–1243.
- ⁸⁹A. Nussbaum, “Generation-recombination characteristic behavior of silicon diodes,” *Physica Status Solidi (a)* **19**, 441–450 (1973).
- ⁹⁰K. R. McIntosh, P. P. Altermatt, and G. Heiser, “Depletion-region recombination in silicon solar cells: When does $m_{DR} = 2$?” In *Proceedings of the 16th European photovoltaic solar energy conference* (2000), pp. 251–254.
- ⁹¹M. A. Green, “Solar cell fill factors: general graph and empirical expressions,” *Solid-State Electronics* **24**, 788–789 (1981).
- ⁹²K. T. VanSant, J. Simon, J. F. Geisz, E. L. Warren, K. L. Schulte, A. J. Ptak, M. S. Young, M. Rienäcker, H. Schulte-Huxel, R. Peibst, et al., “Toward low-cost 4-terminal GaAs//Si tandem solar cells,” *ACS Applied Energy Materials* **2**, 2375–2380 (2019).

- ⁹³J. M. Gee, “A comparison of different module configurations for multi-band-gap solar cells,” *Solar Cells* **24**, 147–155 (1988).
- ⁹⁴H. Schulte-Huxel, D. J. Friedman, and A. C. Tamboli, “String-Level Modeling of Two, Three, and Four Terminal Si-Based Tandem Modules,” *IEEE Journal of Photovoltaics* **8**, 1370–1375 (2018).
- ⁹⁵H. Schulte-Huxel, T. J. Silverman, M. G. Deceglie, D. J. Friedman, and A. C. Tamboli, “Energy Yield Analysis of Multiterminal Si-Based Tandem Solar Cells,” *IEEE Journal of Photovoltaics* **8**, 1376–1383 (2018).
- ⁹⁶S. MacAlpine, D. C. Bobela, S. Kurtz, M. P. Lumb, K. J. Schmieder, J. E. Moore, R. J. Walters, and K. Alberi, “Simulated potential for enhanced performance of mechanically stacked hybrid IIIV/Si tandem photovoltaic modules using DCDC converters,” *Journal of Photonics for Energy* **7**, 1 (2017).
- ⁹⁷J. Bardeen and W. H. Brattain, “The transistor, a semi-conductor triode,” *Phys. Rev.* **74**, 230–231 (1948).
- ⁹⁸I. M. Ross, “The invention of the transistor,” *Proceedings of the IEEE* **86**, 7–28 (1998).
- ⁹⁹J. Ebers and J. Moll, “Large-Signal Behavior of Junction Transistors,” *Proceedings of the IRE* **42**, 1761–1772 (1954).
- ¹⁰⁰D. T. Stevenson and R. J. Keyes, “Measurement of carrier lifetimes in germanium and silicon,” *Journal of Applied Physics* **26**, 190–195 (1955).
- ¹⁰¹D. E. Kane and R. M. Swanson, “Measurement of the emitter saturation current by a contactless photoconductivity decay method,” in *IEEE Photovoltaic Specialists Conference* (1985).
- ¹⁰²R. Sinton and A. Cuevas, “A quasi-steady-state open-circuit voltage method for solar cell characterization,” in *Proceedings of the 16th European Photovoltaic Solar Energy Conference* (2000), p. 1152.
- ¹⁰³K. Bothe, “Oxygen-related trapping and recombination centres in boron-doped crystalline silicon,” PhD thesis (Leibniz Universität Hannover, 2006).
- ¹⁰⁴H. Mäckel and K. Varner, “On the determination of the emitter saturation current density from lifetime measurements of silicon devices,” *Progress in Photovoltaics: Research and Applications* **21**, 850–866 (2013).
- ¹⁰⁵K. R. McIntosh and L. E. Black, “On effective surface recombination parameters,” *Journal of Applied Physics* **116**, 014503 (2014).
- ¹⁰⁶A. Kimmerle, J. Greulich, and A. Wolf, “Carrier-diffusion corrected J0-analysis of charge carrier lifetime measurements for increased consistency,” *Solar Energy Materials and Solar Cells* **142**, 116–122 (2015).
- ¹⁰⁷J. del Alamo and R. Swanson, “The physics and modeling of heavily doped emitters,” *IEEE Transactions on Electron Devices* **31**, 1878–1888 (1984).
- ¹⁰⁸R. T. Tung, “The physics and chemistry of the schottky barrier height,” *Applied Physics Reviews* **1**, 011304 (2014).

- ¹⁰⁹R. Singh, M. Green, and K. Rajkanan, "Review of conductor-insulator-semiconductor (cis) solar cells," *Solar Cells* **3**, 95–148 (1981).
- ¹¹⁰S. J. Fonash, "Photovoltaic devices," *Critical Reviews in Solid State and Materials Sciences* **9**, 107–209 (1980).
- ¹¹¹D. Schroder and D. Meier, "Solar cell contact resistanceA review," *IEEE Transactions on Electron Devices* **31**, 637–647 (1984).
- ¹¹²S. Fonash, *Solar cell device physics* (Academic Press, Inc., New York, NY, 1981).
- ¹¹³A. Fahrenbruch and R. Bube, *Fundamentals of solar cells: photovoltaic solar energy conversion* (Elsevier, 2012).
- ¹¹⁴S. Eidelloth and R. Brendel, "Analytical Theory for Extracting Specific Contact Resistances of Thick Samples From the Transmission Line Method," *English, IEEE Electron Device Letters* **35**, 9–11 (2014).
- ¹¹⁵K. R. McIntosh, "Lumps, humps and bumps: three detrimental effects in the current-voltage curve of silicon solar cells," PhD thesis (University of New South Wales, 2001).
- ¹¹⁶U. Würfel, A. Cuevas, and P. Würfel, "Charge Carrier Separation in Solar Cells," *IEEE Journal of Photovoltaics* **5**, 461–469 (2015).
- ¹¹⁷P. Koswatta, "Quantifying Carrier Selective Contacts in Solar Cells," PhD thesis (Arizona State University, 2016).
- ¹¹⁸S. Smit, "Passivating selective contacts for silicon photovoltaics : Solar cells designed by physics," PhD thesis (Eindhoven University of Technology, 2016).
- ¹¹⁹C. D. Weber, D. P. Stay, and M. C. Lonergan, "Effects of Polyfluorene Polyelectrolyte Interfacial Layers on Selectivity and Recombination Measured Using the Interdigitated Back-Contact Solar Cell," *The Journal of Physical Chemistry C* **120**, 19951–19960 (2016).
- ¹²⁰R. Brendel and R. Peibst, "Contact Selectivity and Efficiency in Crystalline Silicon Photovoltaics," *IEEE Journal of Photovoltaics*, 10.1109/JPHOTOV.2016.2598267 (2016).
- ¹²¹M. Bivour, C. Messmer, L. Neusel, F. Zähringer, J. Schön, S. W. Glunz, and M. Hermle, "Principles of carrier-selective contacts based on induced junctions," in *33rd European Photovoltaic Solar Energy Conference and Exhibition* (2017), pp. 348–352.
- ¹²²S. Glunz, M. Bivour, C. Messmer, F. Feldmann, R. Muller, C. Reichel, A. Richter, F. Schindler, J. Benick, and M. Hermle, "Passivating and Carrier-selective Contacts - Basic Requirements and Implementation," in *IEEE 44th Photovoltaic Specialist Conference (PVSC)* (June 2017), pp. 2064–2069.
- ¹²³E. T. Roe, K. E. Egelhofer, and M. C. Lonergan, "Limits of Contact Selectivity/Recombination on the Open-Circuit Voltage of a Photovoltaic," *ACS Applied Energy Materials* **1**, acaem.7b00179 (2018).
- ¹²⁴A. Onno, C. Chen, P. Koswatta, M. Boccard, and Z. C. Holman, "Passivation, conductivity, and selectivity in solar cell contacts: concepts and simulations based on a unified partial-resistances framework," *Journal of Applied Physics* **126**, 183103 (2019).

- ¹²⁵D. Pysch, C. Meinhard, M. Hermle, and S. W. Glunz, “Development and understanding of the intrinsic and doped amorphous emitter- layer stacks for silicon heterojunction solar cells,” in 25th European Photovoltaic Solar Energy Conference and Exhibition / 5th World Conference on Photovoltaic Energy Conversion, 6-10 September 2010, Valencia, Spain, September (2010), pp. 1820–1823.
- ¹²⁶D. Pysch, C. Meinhard, N.-P. Harder, M. Hermle, and S. W. Glunz, “Analysis and optimization approach for the doped amorphous layers of silicon heterojunction solar cells,” *Journal of Applied Physics* **110**, 94516 (2011).
- ¹²⁷R. Brendel, M. Rienaeker, and R. Peibst, “A Quantitative Measure for the Carrier Selectivity of Contacts To Solar Cells,” 32nd European Photovoltaic Solar Energy Conference and Exhibition, 2–6 (2016).
- ¹²⁸M. X. Tan, C. Kenyon, O. Krüger, and N. S. Lewis, “Behavior of Si photoelectrodes under high level injection conditions. 1. Steady-state current-voltage properties and quasi-Fermi level positions under illumination,” *The Journal of Physical Chemistry B* **101**, 2830–2839 (1997).
- ¹²⁹E. T. Roe, K. E. Egelhofer, and M. C. Lonergan, “Exchange current density model for the contact-determined current-voltage behavior of solar cells,” *Journal of Applied Physics* **225302** (2019).
- ¹³⁰D. Matthews, P. Infelta, and M. Grätzel, “Calculation of the photocurrent-potential characteristic for regenerative, sensitized semiconductor electrodes,” *Solar Energy Materials and Solar Cells* **44**, 119–155 (1996).
- ¹³¹J. Nelson, J. Kirkpatrick, and P. Ravirajan, “Factors limiting the efficiency of molecular photovoltaic devices,” *Physical Review B* **69**, 035337 (2004).
- ¹³²R. A. J. Janssen and J. Nelson, “Factors Limiting Device Efficiency in Organic Photovoltaics,” *Advanced Materials* **25**, 1847–1858 (2013).
- ¹³³R. W. Gurney, “The Quantum Mechanics of Electrolysis,” *Proceedings of the Royal Society A: Mathematical, Physical and Engineering Sciences* **134**, 137–154 (1931).
- ¹³⁴R. W. Gurney, *Ions in solution* (The University Press, Cambridge, 1936).
- ¹³⁵R. A. Marcus, “On the theory of oxidation-reduction reactions involving electron transfer. I,” *The Journal of Chemical Physics* **24**, 966–978 (1956).
- ¹³⁶H. Gerischer, “Über den Ablauf von Redoxreaktionen an Metallen und an Halbleitern,” *Zeitschrift für Physikalische Chemie* **26**, 223–247 (1960).
- ¹³⁷H. Gerischer, “Über den Ablauf von Redoxreaktionen an Metallen und an Halbleitern,” *Zeitschrift für Physikalische Chemie* **27**, 48–79 (1961).
- ¹³⁸D. Matthews, “The Absence of a Marcus Inversion Region for Electron Transfer at the Metal-Redox Electrolyte Interface,” *Australian Journal of Chemistry* **47**, 2171 (1994).
- ¹³⁹W. Shockley, G. L. Pearson, and J. R. Haynes, “Hole injection in germanium quantitative studies and filamentary transistors,” *The Bell System Technical Journal* **28**, 344–366 (1949).

- ¹⁴⁰H. Kroemer, “Theory of a wide-gap emitter for transistors,” *Proceedings of the IRE* **45**, 1535–1537 (1957).
- ¹⁴¹H. de Graaff and J. de Groot, “The SIS tunnel emitter: A theory for emitters with thin interface layers,” *IEEE Transactions on Electron Devices* **26**, 1771–1776 (1979).
- ¹⁴²A. Neugroschel, M. Arienzo, Y. Komem, and R. Isaac, “Experimental study of the minority-carrier transport at the polysilicon-monosilicon interface,” *IEEE Transactions on Electron Devices* **32**, 807–816 (1985).
- ¹⁴³A. Yu and E. Snow, “Minority carrier injection of metal-silicon contacts,” *Solid-State Electronics* **12**, 155–160 (1969).
- ¹⁴⁴H. Card and E. Rhoderick, “The effect of an interfacial layer on minority carrier injection in forward-biased silicon Schottky diodes,” *Solid-State Electronics* **16**, 365–374 (1973).
- ¹⁴⁵F. Feldmann, “Carrier-selective contacts for high-efficiency Si solar cells,” PhD thesis (Universität Freiburg, 2015).
- ¹⁴⁶M. Stolterfoht, P. Caprioglio, C. M. Wolff, J. A. Márquez Prieto, J. Nordmann, S. Zhang, D. Rothhardt, U. Hörmann, Y. Amir, A. Redinger, L. Kegelman, F. Zu, S. Albrecht, N. Koch, T. Kirchartz, M. Saliba, T. Unold, and D. Neher, “The impact of energy alignment and interfacial recombination on the open-circuit voltage of perovskite solar cells,” *Energy & Environmental Science* (2019).
- ¹⁴⁷W. Shockley, A. Goetzberger and R. M. Scarlett, *Theory and experiments on current transfer from alloyed contact to diffused layer, in Appendix B of Research and investigation of inverse epitaxial UHF power transistors, Shockley Res. Lab., Palo Alto, CA USA, Tech. Rep. AFALL TDR 64-207*, tech. rep. (1964).
- ¹⁴⁸H. Berger, “Models for contacts to planar devices,” *Solid-State Electronics* **15**, 145–158 (1972).
- ¹⁴⁹H. Murrmann and D. Widmann, “Messung des Übergangswiderstandes zwischen Metall und Diffusionsschicht in Si-Planarelementen,” *Solid-State Electronics* **12**, 879–886 (1969).
- ¹⁵⁰R. Cox and H. Strack, “Ohmic contacts for GaAs devices,” *Solid-State Electronics* **10**, 1213–1218 (1967).
- ¹⁵¹D. L. Young, W. Nemeth, S. Grover, A. Norman, H.-C. Yuan, B. G. Lee, V. LaSalvia, and P. Stradins, “Carrier selective, passivated contacts for high efficiency silicon solar cells based on transparent conducting oxides,” *Energy Procedia* **55**, Proceedings of the 4th International Conference on Crystalline Silicon Photovoltaics (SiliconPV 2014), 733–740 (2014).
- ¹⁵²J. Bullock, C. Samundsett, A. Cuevas, D. Yan, Y. Wan, and T. Allen, “Proof-of-Concept p-Type Silicon Solar Cells With Molybdenum Oxide Local Rear Contacts,” *IEEE Journal of Photovoltaics* **5**, 1591–1594 (2015).
- ¹⁵³U. Rau and T. Kirchartz, “Charge Carrier Collection and Contact Selectivity in Solar Cells,” *Advanced Materials Interfaces*, 1900252 (2019).

- ¹⁵⁴R. Peibst, U. Romer, Y. Larionova, H. Schulte-Huxel, T. Ohrdes, M. Haberle, B. Lim, J. Krugener, D. Stichtenoth, T. Wutherich, C. Schollhorn, J. Graff, and R. Brendel, “Building blocks for back-junction back-contacted cells and modules with ion-implanted poly-Si junctions,” in 2014 IEEE 40th Photovoltaic Specialist Conference (PVSC) (June 2014), pp. 0852–0856.
- ¹⁵⁵M. Rienäcker, A. Merkle, U. Römer, H. Kohlenberg, J. Krügener, R. Brendel, and R. Peibst, “Recombination Behavior of Photolithography-free Back Junction Back Contact Solar Cells with Carrier-selective Polysilicon on Oxide Junctions for Both Polarities,” *Energy Procedia* **92**, 412–418 (2016).
- ¹⁵⁶F. Haase, C. Hollemann, S. Schäfer, A. Merkle, M. Rienäcker, J. Krügener, R. Brendel, and R. Peibst, “Laser contact openings for local poly-Si-metal contacts enabling 26.1%-efficient POLO-IBC solar cells,” *Solar Energy Materials and Solar Cells* **186**, 184–193 (2018).
- ¹⁵⁷M. Rienäcker, M. Bossmeyer, A. Merkle, U. Römer, F. Haase, J. Krügener, R. Brendel, and R. Peibst, “Junction resistivity of carrier-selective polysilicon on oxide junctions and its impact on solar cell performance,” *IEEE Journal of Photovoltaics* **7**, 11–18 (2017).
- ¹⁵⁸T. F. Wietler, D. Tetzlaff, J. Krügener, M. Rienäcker, F. Haase, Y. Larionova, R. Brendel, and R. Peibst, “Pinhole density and contact resistivity of carrier selective junctions with polycrystalline silicon on oxide,” *Applied Physics Letters* **110**, 253902 (2017).
- ¹⁵⁹N. Folchert, M. Rienäcker, A. Yeo, B. Min, R. Peibst, and R. Brendel, “Temperature-dependent contact resistance of carrier selective Poly-Si on oxide junctions,” *Solar Energy Materials and Solar Cells* **185**, 425–430 (2018).
- ¹⁶⁰M. Takagi, K. Nakayama, C. Tevada, and H. Kamioko, “Improvement of shallow base transistor technology by using a doped polysilicon diffusion source,” *J. Jpn. Soc. Appl. Phys* **42**, 101–109 (1972).
- ¹⁶¹J. Graul, A. Glasl, and H. Murrmann, “Ion implanted bipolar high performance transistors with polysil emitter,” in 1975 International Electron Devices Meeting (1975), pp. 450–454.
- ¹⁶²J. Graul, A. Glasl, and H. Murrmann, “High-performance transistors with arsenic-implanted polysil emitters,” *IEEE Journal of Solid-State Circuits* **11**, 491–495 (1976).
- ¹⁶³Z. Lieblich and A. Bar-Lev, “A polysilicon-Silicon n-p junction,” *IEEE Transactions on Electron Devices* **24**, 1025–1031 (1977).
- ¹⁶⁴T. Matsushita, N. Ohuchi, H. Hayashi, and H. Yamoto, “A silicon heterojunction transistor,” *Applied Physics Letters* **35**, 549–550 (1979).
- ¹⁶⁵N. Oh-uchi, H. Hayashi, H. Yamoto, and T. Matsushita, “A new silicon heterojunction transistor using the doped SIPOS,” in International Electron Devices Meeting (1979), pp. 522–525.
- ¹⁶⁶T. Ning and R. Isaac, “Effect of emitter contact on current gain of silicon bipolar devices,” *IEEE Transactions on Electron Devices* **27**, 2051–2055 (1980).
- ¹⁶⁷G. Patton, J. Bravman, and J. Plummer, “Impact of processing parameters on base current in polysilicon contacted bipolar transistors,” in International Electron Devices Meeting (1985), pp. 30–33.

- ¹⁶⁸Y. Kwark and R. Swanson, "N-type SIPOS and poly-silicon emitters," *Solid-State Electronics* **30**, 1121–1125 (1987).
- ¹⁶⁹G. R. Wolstenholme, N. Jorgensen, P. Ashburn, and G. R. Booker, "An investigation of the thermal stability of the interfacial oxide in polycrystalline silicon emitter bipolar transistors by comparing device results with highresolution electron microscopy observations," *Journal of Applied Physics* **61**, 225–233 (1987).
- ¹⁷⁰J. Egley and J. Gray, "Demonstration of the importance of the oxide breakup in polysilicon-contacted-emitter modeling," *IEEE Transactions on Electron Devices* **38**, 2112–2117 (1991).
- ¹⁷¹I. Post, P. Ashburn, and G. Wolstenholme, "Polysilicon emitters for bipolar transistors: a review and re-evaluation of theory and experiment," *IEEE Transactions on Electron Devices* **39**, 1717–1731 (1992).
- ¹⁷²P. V. Halen, D. S. Camporese, and D. L. Pulfrey, "The emitter-injection efficiency and emitter effective surface-recombination velocity in polysilicon emitter transistors," *Canadian Journal of Physics* **63**, 693–694 (1985).
- ¹⁷³T. H. Ning, "History and future perspective of the modern silicon bipolar transistor," *IEEE Transactions on Electron Devices* **48**, 2485–2491 (2001).
- ¹⁷⁴J. Fossum and M. Shibib, "A minority-carrier transport model for polysilicon contacts to silicon bipolar devices, including solar cells," in *International Electron Devices Meeting* (1980), pp. 280–283.
- ¹⁷⁵R. J. Van Overstraeten, "Advances in silicon solar cell processing," in *Conference Record of the IEEE Photovoltaic Specialists Conference* (1981), pp. 372–376.
- ¹⁷⁶M. Green and A. Blakers, "Advantages of metal-insulator-semiconductor structures for silicon solar cells," *Solar Cells* **8**, 3–16 (1983).
- ¹⁷⁷E. Yablonovitch, R. M. Swanson, and Y. H. Kwark, "An n-SIPOS: p-SIPOS homojunction and a SIPOS-Si-SIPOS double heterostructure," in *17th Photovoltaic Specialists Conference* (1984), pp. 1146–1148.
- ¹⁷⁸N. Tarr, "A polysilicon emitter solar cell," *IEEE Electron Device Letters* **6**, 655–658 (1985).
- ¹⁷⁹E. Yablonovitch, T. Gmitter, R. M. Swanson, and Y. H. Kwark, "A 720 mV open circuit voltage $\text{SiO}_x : \text{cSi:SiO}_x$ double heterostructure solar cell," *Applied Physics Letters* **47**, 1211–1213 (1985).
- ¹⁸⁰F. Lindholm, A. Neugroschel, M. Arienzo, and P. Iles, "Heavily doped polysilicon-contact solar cells," *IEEE Electron Device Letters* **6**, 363–365 (1985).
- ¹⁸¹J. Y. Gan and R. M. Swanson, "Polysilicon emitters for silicon concentrator solar cells," in *IEEE Conference on Photovoltaic Specialists* (May 1990), pp. 245–250.
- ¹⁸²G. Papadopoulos, L. P. Boivin, and N. G. Tarr, "Development and characterization of polysilicon emitter solar cells," *Canadian Journal of Physics* **69**, 479–482 (1991).
- ¹⁸³A. Tilak and K. Bhat, "Electrical and photovoltaic characteristics of poly-emitter solar cells," *Thin Solid Films* **312**, 273–279 (1998).

- ¹⁸⁴L. Castañer, S. Silvestre, J. Carter, D. Parton, and P. Ashburn, "Effects of fluorine in silicon solar cells with polysilicon contacts," *Solar Energy Materials and Solar Cells* **53**, 115–129 (1998).
- ¹⁸⁵A. Zouari, A. Trabelsi, and A. Ben Arab, "Simple analytical solution and efficiency improvement of polysilicon emitter solar cells," *Solar Energy Materials and Solar Cells* **92**, 313–322 (2008).
- ¹⁸⁶P. Borden, L. Xu, B. McDougall, C. P. Chang, D. Pysch, P. Voisin, and S. W. Glunz, "Polysilicon tunnel junctions as alternates to diffused junctions," in *Proceedings of the 23rd European Photovoltaic Solar Energy Conference (WIP Renewable Energies Valencia, Spain, 2008)*, pp. 1149–1152.
- ¹⁸⁷M. A. Green, "The path to 25% silicon solar cell efficiency: History of silicon cell evolution," *Progress in Photovoltaics: Research and Applications* **17**, 183–189 (2009).
- ¹⁸⁸P. J. Cousins, D. D. Smith, H.-C. Luan, J. Manning, T. D. Dennis, A. Waldhauer, K. E. Wilson, G. Harley, and W. P. Mulligan, "Generation 3: Improved performance at lower cost," in *35th IEEE Photovoltaic Specialists Conference* (2010), pp. 000275–000278.
- ¹⁸⁹D. D. Smith, G. Reich, M. Baldrias, M. Reich, N. Boitnott, and G. Bunea, "Silicon solar cells with total area efficiency above 25 %," in *IEEE 43rd Photovoltaic Specialists Conference (PVSC)* (2016), pp. 3351–3355.
- ¹⁹⁰R. M. Swanson and J.-Y. Gan, "Method of fabricating polysilicon emitters for solar cells," US Patent 5,057,439 (2018).
- ¹⁹¹R. Swanson, "Approaching the 29% limit efficiency of silicon solar cells," *Conference Record of the Thirty-first IEEE Photovoltaic Specialists Conference*, 2005., 889–894 (2005).
- ¹⁹²R. M. Swanson, "Back side contact solar cell with doped polysilicon regions," US Patent 7,468,485 (2008).
- ¹⁹³D. De Ceuster, P. J. Cousins, and D. D. Smith, "Trench process and structure for backside contact solar cells with polysilicon doped regions," US Patent 7,851,698 (2010).
- ¹⁹⁴P. J. Cousins, "Solar cell having doped semiconductor heterojunction contacts," US Patent 7,737,357 (2010).
- ¹⁹⁵D. D. Smith, "Backside contact solar cell with formed polysilicon doped regions," US Patent 8,242,354 (2012).
- ¹⁹⁶R. I. M. Seung and D. D. Smith, "Spacer formation in a solar cell using oxygen ion implantation," US Patent App. 13/631,457 (2014).
- ¹⁹⁷P. J. Cousins, D. D. Smith, and S. B. Rim, "Hybrid polysilicon heterojunction back contact cell," US Patent 8,679,889 (2014).
- ¹⁹⁸S. B. Rim and D. D. Smith, "Built-in bypass diode," US Patent App. 14/136,719 (2015).
- ¹⁹⁹T. Weidman and D. D. Smith, "Solar cell emitter region fabrication using ion implantation," US Patent 9,401,450 (2016).

- ²⁰⁰F. Feldmann, M. Bivour, C. Reichel, M. Hermle, and S. W. Glunz, “Passivated rear contacts for high-efficiency n-type Si solar cells providing high interface passivation quality and excellent transport characteristics,” *Solar Energy Materials and Solar Cells* **120**, 270–274 (2014).
- ²⁰¹F. Feldmann, M. Bivour, C. Reichel, M. Hermle, and S. W. Glunz, “A Passivated Rear Contact for High-Efficiency n-Type Si Solar Cells Enabling High Voc’s and FF>82,” in 28th European Photovoltaic Solar Energy Conference and Exhibition (2013), pp. 988–992.
- ²⁰²F. Feldmann, M. Simon, M. Bivour, C. Reichel, M. Hermle, and S. W. Glunz, “Carrier-selective contacts for Si solar cells,” *Applied Physics Letters* **104**, 181105 (2014).
- ²⁰³R. Brendel, T. Dullweber, R. Gogolin, H. Hannebauer, N.-P. Harder, J. Hensen, S. Kajari-Schröder, R. Peibst, J. Petermann, U. Römer, J. Schmidt, H. Schulte-Huxel, and V. Steckenreiter, “Recent Progress and Options for Future Crystalline Silicon Solar Cells,” in 28th European Photovoltaic Solar Energy Conference and Exhibition (2013), pp. 676–690.
- ²⁰⁴U. Römer, R. Peibst, T. Ohrdes, B. Lim, J. Krügener, E. Bugiel, T. Wietler, and R. Brendel, “Recombination behavior and contact resistance of n+ and p+ poly-crystalline Si/mono-crystalline Si junctions,” *Solar Energy Materials and Solar Cells* **131**, 85–91 (2014).
- ²⁰⁵R. Peibst, U. Römer, K. R. Hofmann, B. Lim, T. F. Wietler, J. Krügener, N. Harder, and R. Brendel, “A Simple Model Describing the Symmetric I-V Characteristics of p Polycrystalline Si/ n Monocrystalline Si, and n Polycrystalline Si/ p Monocrystalline Si Junctions,” *IEEE Journal of Photovoltaics* **4**, 841–850 (2014).
- ²⁰⁶B. Nemeth, D. L. Young, H.-C. Yuan, V. LaSalvia, A. G. Norman, M. Page, B. G. Lee, and P. Stradins, “Low temperature Si/SiO_x pc-Si passivated contacts to n-type Si solar cells,” in IEEE 40th Photovoltaic Specialist Conference (PVSC) (2014), pp. 3448–3452.
- ²⁰⁷J. B. Heng, J. Fu, B. Kong, Y. Chae, W. Wang, Z. Xie, A. Reddy, K. Lam, C. Beitel, C. Liao, C. Erben, Z. Huang, and Z. Xu, “>23% High-Efficiency Tunnel Oxide Junction Bifacial Solar Cell With Electroplated Cu Gridlines,” *IEEE Journal of Photovoltaics* **5**, 82–86 (2015).
- ²⁰⁸Yuguo Tao, E. L. Chang, A. Upadhyaya, B. Roundaville, Young-Woo Ok, K. Madani, Chia-Wei Chen, K. Tate, V. Upadhyaya, F. Zimbardi, J. Keane, A. Payne, and A. Rohatgi, “730 mV implied Voc enabled by tunnel oxide passivated contact with PECVD grown and crystallized n+ polycrystalline Si,” in 2015 IEEE 42nd Photovoltaic Specialist Conference (PVSC) (June 2015), pp. 1–5.
- ²⁰⁹D. Yan, A. Cuevas, J. Bullock, Y. Wan, and C. Samundsett, “Phosphorus-diffused polysilicon contacts for solar cells,” *Solar Energy Materials and Solar Cells* **142**, 75–82 (2015).
- ²¹⁰M. Lenes, M. K. Stodolny, Y. Wu, B. Geerligs, and J. R. M. Luchies, “LPCVD doped poly passivated contacts for Si-cell technology,” in Oral presentation in PV Asia Scientific Conference (2015).

- ²¹¹G. Yang, A. Ingenito, N. van Hameren, O. Isabella, and M. Zeman, “Design and application of ion-implanted polySi passivating contacts for interdigitated back contact c-Si solar cells,” *Applied Physics Letters* **108**, 033903 (2016).
- ²¹²M. Stodolny, M. Lenes, Y. Wu, G. Janssen, I. Romijn, J. Luchies, and L. Geerligs, “n-Type polysilicon passivating contact for industrial bifacial n-type solar cells,” *Solar Energy Materials and Solar Cells* **158**, 24–28 (2016).
- ²¹³J. Stuckelberger, G. Nogay, P. Wyss, Q. Jeangros, C. Allebé, F. Debrot, X. Niquille, M. Ledinsky, A. Fejfar, M. Despeisse, F.-J. Haug, P. Löper, and C. Ballif, “Passivating electron contact based on highly crystalline nanostructured silicon oxide layers for silicon solar cells,” *Solar Energy Materials and Solar Cells* **158**, 2–10 (2016).
- ²¹⁴S. Choi, K. H. Min, M. S. Jeong, J. I. Lee, M. G. Kang, H.-E. Song, Y. Kang, H.-S. Lee, D. Kim, and K.-H. Kim, “Structural evolution of tunneling oxide passivating contact upon thermal annealing,” *Scientific Reports* **7**, 12853 (2017).
- ²¹⁵H. Kim, S. Bae, K.-s. Ji, S. M. Kim, J. W. Yang, C. H. Lee, K. D. Lee, S. Kim, Y. Kang, H.-S. Lee, and D. Kim, “Passivation properties of tunnel oxide layer in passivated contact silicon solar cells,” *Applied Surface Science* **409**, 140–148 (2017).
- ²¹⁶K. Tao, Q. Li, C. Hou, S. Jiang, J. Wang, R. Jia, Y. Sun, Y. Li, Z. Jin, and X. Liu, “Application of a-Si/ μ c-Si hybrid layer in tunnel oxide passivated contact n-type silicon solar cells,” *Solar Energy* **144**, 735–739 (2017).
- ²¹⁷A. Morisset, R. Cabal, B. Grange, C. Marchat, J. Alvarez, M.-E. Gueunier-Farret, S. Dubois, and J.-P. Kleider, “Conductivity and Surface Passivation Properties of Boron-Doped Poly-Silicon Passivated Contacts for c-Si Solar Cells,” *physica status solidi (a)*, 1800603 (2018).
- ²¹⁸Y. Yang, P. P. Altermatt, Y. Cui, Y. Hu, D. Chen, L. Chen, G. Xu, X. Zhang, Y. Chen, P. Hamer, R. S. Bonilla, Z. Feng, and P. J. Verlinden, “Effect of carrier-induced hydrogenation on the passivation of the poly-Si/SiO_x/c-Si interface,” in *AIP Conference Proceedings*, Vol. 1999, 1 (Aug. 2018), p. 040026.
- ²¹⁹K. Nishimura, Y. Yashiki, T. Morioka, Y. Kobayashi, T. Watahiki, and H. Tokioka, “N-type silicon solar cell with rear tunnel oxide combined with rear screen-printed electrodes,” *Japanese Journal of Applied Physics* **57**, 08RB16 (2018).
- ²²⁰S. Masuda, K. Gotoh, I. Takahashi, K. Nakamura, Y. Ohshita, and N. Usami, “Impact of boron incorporation on properties of silicon solar cells employing p-type polycrystalline silicon grown by aluminum-induced crystallization,” *Japanese Journal of Applied Physics* **57**, 08RB12 (2018).
- ²²¹N. Nandakumar, J. Rodriguez, T. Kluge, T. Große, L. Fondop, P. Padhamnath, N. Balaji, M. König, and S. Duttgupta, “Approaching 23% with largearea monoPoly cells using screenprinted and fired rear passivating contacts fabricated by inline PECVD,” *Progress in Photovoltaics: Research and Applications*, pip.3097 (2018).

- ²²²P. Padhamnath, N. Nandakumar, B. J. Kitz, N. Balaji, M.-J. Naval, V. Shanmugam, and S. Duttagupta, “High-Quality Doped Polycrystalline Silicon Using Low-Pressure Chemical Vapor Deposition (LPCVD),” *Energy Procedia* **150**, 9–14 (2018).
- ²²³J. Lossen, J. HoSS, S. Eisert, D. Amkreutz, M. Muske, J. Plentz, and G. Andrä, “Electron Beam Evaporation of Silicon for Poly-Silicon/SiO₂ Passivated Contacts,” in *35th European Photovoltaic Solar Energy Conference and Exhibition* (2018), pp. 418–421.
- ²²⁴D. Yan, A. Cuevas, J. I. Michel, C. Zhang, Y. Wan, X. Zhang, and J. Bullock, “Polysilicon passivated junctions: the next technology for silicon solar cells?” *Joule* (2021).
- ²²⁵D. Chen, Y. Chen, Z. Wang, J. Gong, C. Liu, Y. Zou, Y. He, Y. Wang, L. Yuan, W. Lin, R. Xia, L. Yin, X. Zhang, G. Xu, Y. Yang, H. Shen, Z. Feng, P. P. Altermatt, and P. J. Verlinden, “24.58% total area efficiency of screen-printed, large area industrial silicon solar cells with the tunnel oxide passivated contacts (i-topcon) design,” *Solar Energy Materials and Solar Cells* **206**, 110258 (2020).
- ²²⁶“Jinkosolar has n-type mono cell verified at record 24.90% conversion efficiency,” <https://jinkosolar.eu> (2021).
- ²²⁷R. Peibst, U. Römer, Y. Larionova, M. Rienäcker, A. Merkle, N. Folchert, S. Reiter, M. Turcu, B. Min, J. Krügener, D. Tetzlaff, E. Bugiel, T. Wietler, and R. Brendel, “Working principle of carrier selective poly-Si/c-Si junctions: Is tunnelling the whole story?” *Solar Energy Materials and Solar Cells* **158**, Proceedings of the 6th International Conference on Silicon Photovoltaics, 60–67 (2016).
- ²²⁸K. Lancaster, S. GroSSer, F. Feldmann, V. Naumann, and C. Hagendorf, “Study of Pinhole Conductivity at Passivated Carrier-selected Contacts of Silicon Solar Cells,” *Energy Procedia* **92**, 116–121 (2016).
- ²²⁹D. Tetzlaff, J. Krügener, Y. Larionova, S. Reiter, M. Turcu, R. Peibst, U. Höhne, J.-D. Kähler, and T. Wietler, “Evolution of oxide disruptions: The (W)hole story about poly-Si/c-Si passivating contacts,” in *IEEE 43rd Photovoltaic Specialists Conference (PVSC)* (2016), pp. 0221–0224.
- ²³⁰A. Moldovan, F. Feldmann, G. Krugel, M. Zimmer, J. Rentsch, M. Hermle, A. Roth-Fölsch, K. Kaufmann, and C. Hagendorf, “Simple Cleaning and Conditioning of Silicon Surfaces with UV/Ozone Sources,” *Energy Procedia* **55**, 834–844 (2014).
- ²³¹J. Tong, X. Wang, Z. Ouyang, and A. Lennon, “Ultra-thin Tunnel Oxides Formed by Field-induced Anodisation for Carrier-selective Contacts,” *Energy Procedia* **77**, 840–847 (2015).
- ²³²M. Jeon, J. Kang, G. Shim, S. Ahn, N. Balaji, C. Park, Y.-J. Lee, and J. Yi, “Passivation effect of tunnel oxide grown by N₂O plasma for c-Si solar cell applications,” *Vacuum* **141**, 152–156 (2017).

- ²³³Y. Huang, M. Liao, Z. Wang, X. Guo, C. Jiang, Q. Yang, Z. Yuan, D. Huang, J. Yang, X. Zhang, Q. Wang, H. Jin, M. Al-Jassim, C. Shou, Y. Zeng, B. Yan, and J. Ye, "Ultrathin silicon oxide prepared by in-line plasma-assisted N₂O oxidation (PANO) and the application for n-type polysilicon passivated contact," *Solar Energy Materials and Solar Cells* **208**, 110389 (2020).
- ²³⁴A. Alzahrani, T. G. Allen, M. De Bastiani, E. Van Kerschaver, G. T. Harrison, W. Liu, and S. De Wolf, "In situ plasma-grown silicon-oxide for polysilicon passivating contacts," *Advanced Materials Interfaces* **7**, 2000589 (2020).
- ²³⁵H. Kobayashi, K. Imamura, W.-B. Kim, S.-S. Im, and Asuha, "Nitric acid oxidation of Si (NAOS) method for low temperature fabrication of SiO₂/Si and SiO₂/SiC structures," in *Proceedings of the 6th International Workshop on Semiconductor Surface Passivation SSP 2009*, Vol. 256, 19 (2010), pp. 5744–5756.
- ²³⁶H. Tong, M. Liao, Z. Zhang, Y. Wan, D. Wang, C. Quan, L. Cai, P. Gao, W. Guo, H. Lin, C. Shou, Y. Zeng, B. Yan, and J. Ye, "A strong-oxidizing mixed acid derived high-quality silicon oxide tunneling layer for polysilicon passivated contact silicon solar cell," *Solar Energy Materials and Solar Cells* **188**, 149–155 (2018).
- ²³⁷Y. Larionova, R. Peibst, M. Turcu, S. Reiter, R. Brendel, D. Tetzlaff, J. Krügener, T. Wietler, U. Höhne, and J.-D. Kähler, "Optimization of p+ poly-Si/c-Si junctions on wet-chemically grown interfacial oxides and on different wafer morphologies," in *Proc. of 32nd European Photovoltaic Solar Energy Conference and Exhibition* (2016).
- ²³⁸A. Moldovan, F. Feldmann, M. Zimmer, J. Rentsch, J. Benick, and M. Hermle, "Tunnel oxide passivated carrier-selective contacts based on ultra-thin sio₂ layers," *Solar Energy Materials and Solar Cells* **142**, Proceedings of the 5th International Conference on Crystalline Silicon Photovoltaics (SiliconPV 2015), 123–127 (2015).
- ²³⁹A. Moldovan, "Ozonbasierte Reinigungs- und Konditionierungsverfahren für die Herstellung hocheffizienter Silizium Solarzellen," PhD thesis (Albert-Ludwig-Universität Freiburg, 2015).
- ²⁴⁰U. Römer, "Polycrystalline silicon/monocrystalline silicon junctions and their application as passivated contacts for si solar cells," PhD thesis (Gottfried Wilhelm Leibniz Universität Hannover, 2015).
- ²⁴¹D. Yan, A. Cuevas, Y. Wan, and J. Bullock, "Silicon nitride/silicon oxide interlayers for solar cell passivating contacts based on PECVD amorphous silicon," *physica status solidi (RRL) - Rapid Research Letters* **9**, 617–621 (2015).
- ²⁴²W. D. Eades and R. M. Swanson, "Calculation of surface generation and recombination velocities at the Si-SiO₂ interface," *Journal of Applied Physics* **58**, 4267 (1985).
- ²⁴³K. C. Fong, T. C. Kho, W. Liang, T. K. Chong, M. Ernst, D. Walter, M. Stocks, E. Franklin, K. McIntosh, and A. Blakers, "Phosphorus diffused LPCVD polysilicon passivated contacts with in-situ low pressure oxidation," *Solar Energy Materials and Solar Cells* **186**, 236–242 (2018).

- ²⁴⁴A. Merkle, S. Seren, H. Knauss, B. Min, J. Steffens, B. Terheiden, R. Brendel, and R. Peibst, “Atmospheric Pressure Chemical Vapor Deposition of In-Situ Doped Amorphous Silicon Layers for Passivating Contacts,” in 35th European Photovoltaic Solar Energy Conference and Exhibition (2018), pp. 785–791.
- ²⁴⁵G. Yang, P. Guo, P. Procel, A. Weeber, O. Isabella, and M. Zeman, “Poly-crystalline silicon-oxide films as carrier-selective passivating contacts for c-Si solar cells,” *Applied Physics Letters* **112**, 193904 (2018).
- ²⁴⁶H. Park, H. Park, S. J. Park, S. Bae, H. Kim, J. W. Yang, J. Y. Hyun, C. H. Lee, S. H. Shin, Y. Kang, H.-S. Lee, and D. Kim, “Passivation quality control in poly-Si/SiO_x/c-Si passivated contact solar cells with 734 mV implied open circuit voltage,” *Solar Energy Materials and Solar Cells* **189**, 21–26 (2019).
- ²⁴⁷D. Yan, A. Cuevas, S. P. Phang, Y. Wan, and D. Macdonald, “23% efficient p-type crystalline silicon solar cells with hole-selective passivating contacts based on physical vapor deposition of doped silicon films,” *Appl. Phys. Lett* **113**, 61603 (2018).
- ²⁴⁸F. Kiefer, N. Wehmeier, T. Brendemühl, L. Mettner, F. Haase, M. Holthausen, C. Daeschlein, O. Wunnicke, C. Mader, and S. Kajari-Schröder, *Inkjet Printing as a New Method for the Preparation of POLO Contacts*, 2018 MRS Fall Meeting & Exhibit, Boston, MA, USA, Nov. 28, 2018.
- ²⁴⁹J. A. Aguiar, D. Young, B. Lee, W. Nemeth, S. Harvey, T. Aoki, M. Al-Jassim, and P. Stradins, “Atomic scale understanding of poly-Si/SiO₂/c-Si passivated contacts: Passivation degradation due to metallization,” in IEEE 43rd Photovoltaic Specialists Conference (PVSC) (2016), pp. 3667–3670.
- ²⁵⁰J. Temmler, J.-I. Polzin, F. Feldmann, L. Kraus, B. Kaffle, S. Mack, A. Moldovan, M. Hermle, and J. Rentsch, “Inline PECVD Deposition of Poly-Si-Based Tunnel Oxide Passivating Contacts,” *physica status solidi (a)* **215**, 1800449 (2018).
- ²⁵¹G. Nogay, J. Stuckelberger, P. Wyss, E. Rucavado, C. Allebé, T. Koida, M. Morales-Masis, M. Despeisse, F.-J. Haug, P. Löper, and C. Ballif, “Interplay of annealing temperature and doping in hole selective rear contacts based on silicon-rich silicon-carbide thin films,” *Solar Energy Materials and Solar Cells* **173**, 18–24 (2017).
- ²⁵²D. Yan, A. Cuevas, Y. Wan, and J. Bullock, “Silicon nitride/silicon oxide interlayers for solar cell passivating contacts based on PECVD amorphous silicon,” *physica status solidi (RRL) - Rapid Research Letters* **9**, 617–621 (2015).
- ²⁵³D. Yan, S. P. Phang, Y. Wan, C. Samundsett, D. Macdonald, and A. Cuevas, “High efficiency n-type silicon solar cells with passivating contacts based on PECVD silicon films doped by phosphorus diffusion,” *Solar Energy Materials and Solar Cells* **193**, 80–84 (2019).
- ²⁵⁴G. Nogay, A. Ingenito, E. Rucavado, Q. Jeangros, J. Stuckelberger, P. Wyss, M. Morales-Masis, F.-J. Haug, P. Loper, and C. Ballif, “Crystalline Silicon Solar Cells With Coannealed Electron- and Hole-Selective SiC Passivating Contacts,” *IEEE Journal of Photovoltaics* **8**, 1478–1485 (2018).

- ²⁵⁵A. Ingenito, G. Nogay, J. Stuckelberger, P. Wyss, L. Gnocchi, C. Allebe, J. Horzel, M. Despeisse, F.-J. Haug, P. Loper, and C. Ballif, “Phosphorous-Doped Silicon Carbide as Front-Side Full-Area Passivating Contact for Double-Side Contacted c-Si Solar Cells,” *IEEE Journal of Photovoltaics*, 1–9 (2018).
- ²⁵⁶S. Reiter, N. Koper, R. Reineke-Koch, Y. Larionova, M. Turcu, J. Krügener, D. Tetzlaff, T. Wietler, U. Höhne, J.-D. Kähler, and R. Peibst, “Parasitic Absorption in Polycrystalline Si-layers for Carrier-selective Front Junctions,” *Energy Procedia* **92**, 199–204 (2016).
- ²⁵⁷B. Min, M. R. Vogt, T. Wietler, R. Reineke-Koch, B. Wolpensinger, E. Köhnen, D. Tetzlaff, C. Schinke, R. Brendel, and R. Peibst, “Increasing the photo-generated current in solar cells with passivating contacts by reducing the poly-Si deposition temperature,” in *Aip conference proceedings*, Vol. 1999, 1 (Aug. 2018), p. 040015.
- ²⁵⁸R. Santbergen, G. Yang, P. Procel, G. Limodio, A. Weeber, O. Isabella, and M. Zeman, “Optical Analysis of Poly-Si and Poly-SiOx Carrier-Selective Passivating Contacts for c-Si Solar Cells,” in *Light, Energy and the Environment* (Nov. 2017), PW3A.5.
- ²⁵⁹Y. Wu, M. K. Stodolny, L. Geerligs, M. Lenes, and J.-M. Luchies, “In-situ Doping and Local Overcompensation of High Performance LPCVD Polysilicon Passivated Contacts as Approach to Industrial IBC Cells,” *Energy Procedia* **92**, 427–433 (2016).
- ²⁶⁰D. Yan, A. Cuevas, Y. Wan, and J. Bullock, “Passivating contacts for silicon solar cells based on boron-diffused recrystallized amorphous silicon and thin dielectric interlayers,” *Solar Energy Materials and Solar Cells* **152**, 73–79 (2016).
- ²⁶¹F. Feldmann, R. Müller, C. Reichel, and M. Hermle, “Ion implantation into amorphous Si layers to form carrier-selective contacts for Si solar cells,” *physica status solidi (RRL) - Rapid Research Letters* **08**, 767–770 (2014).
- ²⁶²U. Römer, R. Peibst, T. Ohrdes, B. Lim, J. Krügener, T. Wietler, and R. Brendel, “Ion Implantation for Poly-Si Passivated Back-Junction Back-Contacted Solar Cells,” *IEEE Journal of Photovoltaics* **5**, 507–514 (2015).
- ²⁶³A. D. Upadhyaya, Young Woo Ok, E. Chang, V. Upadhyaya, K. Madani, K. Tate, Eunhwan Cho, B. Rounsaville, V. Chandrasekaran, V. Yelundur, A. Gupta, and A. Rohatgi, “Ion implanted screen printed N-type solar cell with tunnel oxide passivated back contact,” in *IEEE 42nd Photovoltaic Specialist Conference (PVSC)* (June 2015), pp. 1–3.
- ²⁶⁴D. L. Young, W. Nemeth, V. LaSalvia, R. Reedy, N. Bateman, and P. Stradins, “Ion implanted passivated contacts for interdigitated back contacted solar cells,” in *IEEE 42nd Photovoltaic Specialist Conference (PVSC)* (June 2015), pp. 1–5.
- ²⁶⁵D. L. Young, B. G. Lee, D. Fogel, W. Nemeth, V. LaSalvia, S. Theingi, M. Page, M. Young, C. Perkins, and P. Stradins, “Gallium-Doped Poly-Si:Ga/SiO₂ Passivated Emitters to n-Cz Wafers With $iV_{OC} > 730$ mV,” *IEEE Journal of Photovoltaics* **7**, 1640–1645 (2017).
- ²⁶⁶J. Krügener, Y. Larionova, D. Tetzlaff, B. Wolpensinger, S. Reiter, M. Turcu, R. Peibst, J.-D. Kähler, and T. Wietler, “Dopant diffusion from p₊-poly-Si into c-Si during thermal annealing,” in *IEEE 43rd Photovoltaic Specialists Conference (PVSC)* (June 2016), pp. 2451–2454.

- ²⁶⁷G. Yang, A. Ingenito, O. Isabella, and M. Zeman, “IBC c-Si solar cells based on ion-implanted poly-silicon passivating contacts,” *Solar Energy Materials and Solar Cells* **158**, 84–90 (2016).
- ²⁶⁸K. Prabhakaran, F. Maeda, Y. Watanabe, and T. Ogino, “Distinctly different thermal decomposition pathways of ultrathin oxide layer on Ge and Si surfaces,” *Applied Physics Letters* **76**, 2244 (2000).
- ²⁶⁹N. Miyata, H. Watanabe, and M. Ichikawa, “Thermal Decomposition of an Ultrathin Si Oxide Layer around a Si(001)-(2x1) Window,” *Physical Review Letters* **84**, 1043–1046 (2000).
- ²⁷⁰S. A. Ajuria and R. Reif, “Early stage evolution kinetics of the polysilicon/singlecrystal silicon interfacial oxide upon annealing,” *Journal of Applied Physics* **69**, 662–667 (1991).
- ²⁷¹S. A. Ajuria, C. H. Gan, J. A. Noel, and L. R. Reif, “Quantitative correlations between the performance of polysilicon emitter transistors and the evolution of polysilicon/silicon interfacial oxides upon annealing,” *IEEE Transactions on Electron Devices* **39**, 1420–1427 (1992).
- ²⁷²A. Moldovan, F. Feldmann, K. Kaufmann, S. Richter, M. Werner, C. Hagendorf, M. Zimmer, J. Rentsch, and M. Hermle, “Tunnel oxide passivated carrier-selective contacts based on ultra-thin SiO₂ layers grown by photo-oxidation or wet-chemical oxidation in ozonized water,” in 2015 IEEE 42nd Photovoltaic Specialist Conference (PVSC) (June 2015), pp. 1–6.
- ²⁷³A. Ingenito, G. Nogay, Q. Jeangros, E. Rucavado, C. Allebé, S. Eswara, N. Valle, T. Wirtz, J. Horzel, T. Koida, et al., “A passivating contact for silicon solar cells formed during a single firing thermal annealing,” *Nature Energy* **3**, 800–808 (2018).
- ²⁷⁴E. H. Nicollian, J. R. Brews, and E. H. Nicollian, *MOS (metal oxide semiconductor) physics and technology* (Wiley New York et al., 1982).
- ²⁷⁵B. Nemeth, D. L. Young, M. R. Page, V. LaSalvia, S. Johnston, R. Reedy, and P. Stradins, “Polycrystalline silicon passivated tunneling contacts for high efficiency silicon solar cells,” *Journal of Materials Research* **31** (2016).
- ²⁷⁶W. Nemeth, H.-C. Yuan, V. LaSalvia, P. Stradins, and M. R. Page, “Hydrogenation of passivated contacts,” US Patent 9,911,873 (2018).
- ²⁷⁷M. Stodolny, J. Anker, C. Tool, M. Koppes, A. Mewe, P. Manshanden, M. Lenes, and I. Romijn, “Novel Schemes of p+ poly-Si Hydrogenation Implemented in Industrial 6” Bifacial Front-and-Rear Passivating Contacts Solar Cells,” in 35th European Photovoltaic Solar Energy Conference and Exhibition (2018), pp. 414–417.
- ²⁷⁸F. Feldmann, M. Simon, M. Bivour, C. Reichel, M. Hermle, and S. W. Glunz, “Efficient carrier-selective p- and n-contacts for Si solar cells,” *Solar Energy Materials and Solar Cells* **131**, 100–104 (2014).

- ²⁷⁹B. Nemeth, S. P. Harvey, J. V. Li, D. L. Young, A. Upadhyaya, V. LaSalvia, B. G. Lee, M. R. Page, and P. Stradins, “Effect of the SiO₂ interlayer properties with solid-source hydrogenation on passivated contact performance and surface passivation,” *Energy Procedia* **124**, 295–301 (2017).
- ²⁸⁰M. Schnabel, B. W. H. van de Loo, W. Nemeth, B. Macco, P. Stradins, W. M. M. Kessels, and D. L. Young, “Hydrogen passivation of poly-Si/SiO_x contacts for Si solar cells using Al₂O₃ studied with deuterium,” *Applied Physics Letters* **112**, 203901 (2018).
- ²⁸¹J. Schmidt, R. Peibst, and R. Brendel, “Surface passivation of crystalline silicon solar cells: present and future,” *Solar Energy Materials and Solar Cells* **187**, 39–54 (2018).
- ²⁸²Y. Larionova, M. Turcu, S. Reiter, R. Brendel, D. Tetzlaff, J. Krügener, T. Wietler, U. Höhne, J.-D. Kähler, and R. Peibst, “On the recombination behavior of p⁺-type polysilicon on oxide junctions deposited by different methods on textured and planar surfaces,” *physica status solidi (a)* **214**, 1700058 (2017).
- ²⁸³G. Kökbudak, R. Müller, F. Feldmann, A. Fell, R. Turan, and S. Glunz, “On the Determination of the Contact Resistivity for Passivating Contacts Using 3D Simulations,” in *Proc. of 33rd European Photovoltaic Solar Energy Conference and Exhibition* (2017), pp. 242–246.
- ²⁸⁴F. Feldmann, G. Nogay, P. Löper, D. L. Young, B. G. Lee, P. Stradins, M. Hermle, and S. W. Glunz, “Charge carrier transport mechanisms of passivating contacts studied by temperature-dependent J-V measurements,” *Solar Energy Materials and Solar Cells* **178**, 15–19 (2018).
- ²⁸⁵F. Feldmann, G. Nogay, J.-I. Polzin, B. Steinhauser, A. Richter, A. Fell, C. Schmiga, M. Hermle, and S. W. Glunz, “A Study on the Charge Carrier Transport of Passivating Contacts,” *IEEE Journal of Photovoltaics* **8**, 1503–1509 (2018).
- ²⁸⁶A. Fell, F. Feldmann, C. Messmer, M. Bivour, M. C. Schubert, and S. W. Glunz, “Adaption of Basic Metal-Insulator-Semiconductor (MIS) Theory for Passivating Contacts Within Numerical Solar Cell Modeling,” *IEEE Journal of Photovoltaics* **8**, 1546–1552 (2018).
- ²⁸⁷N. Folchert, R. Peibst, and R. Brendel, “Modeling recombination and contact resistance of poly-Si junctions,” *Progress in Photovoltaics: Research and Applications* **28**, 1289–1307 (2020).
- ²⁸⁸M. Rienäcker, A. Merkle, M. Schnabel, E. Warren, H. Schulte-Huxel, S. Kajari-Schröder, R. Niepelt, J. Schmidt, R. Brendel, P. Stradins, A. Tamboli, and R. Peibst, “Maximum power extraction enabled by monolithic tandems using interdigitated back contact bottom cells with three terminals,” in *33rd European Photovoltaic Solar Energy Conference and Exhibition* (2017).
- ²⁸⁹M. Rienäcker, E. L. Warren, M. Schnabel, H. Schulte-Huxel, R. Niepelt, R. Brendel, P. Stradins, A. C. Tamboli, and R. Peibst, “Back-contacted bottom cells with three terminals: maximizing power extraction from current-mismatched tandem cells,” *Progress in Photovoltaics: Research and Applications* **27**, 410–423 (2019).

- ²⁹⁰M. Rienäcker, E. L. Warren, T. F. Wietler, P. Stradins, A. C. Tamboli, and R. Peibst, “Three-Terminal Bipolar Junction Bottom Cell as Simple as PERC: Towards Lean Tandem Cell Processing,” in IEEE 46th Photovoltaic Specialists Conference (PVSC) (2019), pp. 2169–2175.
- ²⁹¹P. Stradins, M. Rienäcker, R. Peibst, A. Tamboli, and E. Warren, “A simple physical model for three-terminal tandem cell operation,” in IEEE 46th Photovoltaic Specialists Conference (PVSC) (IEEE, 2019), pp. 2176–2178.
- ²⁹²M. Schnabel, M. Rienäcker, T. R. Klein, E. L. Warren, H. Schulte-Huxel, M. F. A. M. van Hest, R. Peibst, P. Stradins, and A. C. Tamboli, “Three-Terminal GaInP/Si Tandem Cells Interconnected with a Conductive Adhesive,” in Material research society spring meeting & exhibit (Apr. 6, 2018).
- ²⁹³M. Schnabel, H. Schulte-Huxel, M. Rienäcker, E. L. Warren, P. F. Ndione, W. Nemeth, T. R. Klein, M. F. A. M. van Hest, J. Geisz, R. Peibst, P. Stradins, and A. C. Tamboli, “Three-Terminal III-V/Si Tandem Solar Cells Enabled by a Transparent Conductive Adhesive,” *Sustainable Energy & Fuels* (2019).
- ²⁹⁴E. L. Warren, W. E. McMahon, M. Rienäcker, K. VanSant, R. C. Whitehead, R. Peibst, and A. C. Tamboli, “A taxonomy for three terminal tandem solar cells,” *ACS Energy Letters* **5** (2020).
- ²⁹⁵S. Sakai and M. Umeno, “Theoretical analysis of new wavelength-division solar cells,” *Journal of Applied Physics* **51**, 5018–5024 (1980).
- ²⁹⁶N. Ito, T. Uesugi, S. Sakai, M. Umeno, and S. Hattori, “InGaAsP/InP Wavelength Division Solar Cells,” *Japanese Journal of Applied Physics* **20**, 121 (1981).
- ²⁹⁷C. Flores, “Fabrication process and performances of a new type of GaAs-GaAlAs cascade solar cell,” *Proc. 16th IEEE PVSC, San Diego*, 569 (1982).
- ²⁹⁸P. G. Borden, “Three-terminal solar cell circuit,” US4513168A (USA) (1984).
- ²⁹⁹J. M. Gee, “Novel two- and three-junction monolithic multijunction solar cells*,” *Technical Digest of the 2nd Int. Photovoltaic Science and Engineering Conf., Beijing, China, 1986, PVSEC*, p. 584 (1986).
- ³⁰⁰L. Mayet, M. Gavand, B. Montégu, and A. Laugier, “High efficiency AlGaAs-GaAs tandem solar cells with three terminals,” in *Proc. of IEEE 20th photovoltaic specialists conference (pvsc)* (1988), p. 597.
- ³⁰¹M. W. Wanlass, T. A. Gessert, G. Horner, K. A. Emery, and T. J. Coutts, “InP/Ga_{0.47}In_{0.53}As monolithic, two-junction, three-terminal tandem solar cells,” *Proc. 11th Space Photovoltaics Research and Technology Conference, Cleveland*, 16–1 (1990).
- ³⁰²M. Wanlass, “Monolithic tandem solar cell,” US5019177A (1989).
- ³⁰³T. Soga, M. Yang, T. Jimbo, and M. Umeno, “High-Efficiency Monolithic Three-Terminal GaAs/Si Tandem Solar Cells Fabricated by Metalorganic Chemical Vapor Deposition,” *Japanese Journal of Applied Physics* **35**, 1401–1404 (1996).

- ³⁰⁴M. Emziane and R. J. Nicholas, “Double-junction three-terminal photovoltaic devices: A modeling approach,” *Journal of Applied Physics* **102**, 074508 (2007).
- ³⁰⁵M. A. Steiner, M. W. Wanlass, J. J. Carapella, A. Duda, J. S. Ward, T. E. Moriarty, and K. A. Emery, “A monolithic three-terminal GaInAsP/GaInAs tandem solar cell,” *Progress in Photovoltaics: Research and Applications* **17**, 587–593 (2009).
- ³⁰⁶S. Sista, Z. Hong, M.-H. Park, Z. Xu, and Y. Yang, “High-efficiency polymer tandem solar cells with three-terminal structure,” *eng TS - PubMed, Advanced materials (Deerfield Beach, Fla.)* **22**, E77–80 (2010).
- ³⁰⁷L. Wang, “Three terminal SI-SI:GE monolithic tandem solar cells,” PhD thesis (University of Delaware, 2011).
- ³⁰⁸L. Wang, B. Conrad, A. Soeriyadi, X. Zhao, D. Li, M. Diaz, A. Lochtefeld, A. Gerger, I. Perez-Wurfl, and A. Barnett, “Current matched three-terminal dual junction GaAsP/SiGe tandem solar cell on Si,” *Solar Energy Materials and Solar Cells* **146**, 80–86 (2016).
- ³⁰⁹A. Soeriyadi, L. Wang, B. Conrad, M. Diaz, X. Zhao, D. Li, A. Lochtefeld, A. Gerger, A. Barnett, and I. Perez-Wurfl, “A Direct Method of Analysing the Current Matching Condition in a Multi-Junction Solar Cell,” in *Proceedings of 31st European Photovoltaic Solar Energy Conference and Exhibition* (2015), pp. 1456–1460.
- ³¹⁰A. H. Soeriyadi, L. Wang, B. Conrad, D. Li, A. Lochtefeld, A. Gerger, A. Barnett, and I. Perez-Wurfl, “Extraction of Essential Solar Cell Parameters of Subcells in a Tandem Structure With a Novel Three-Terminal Measurement Technique,” *IEEE Journal of Photovoltaics* **8**, 327–332 (2018).
- ³¹¹A. Martí and A. Luque, “Three-terminal heterojunction bipolar transistor solar cell for high-efficiency photovoltaic conversion,” *Nature Communications* **6**, 6902 (2015).
- ³¹²A. Marti, E. Antolin, P. Garcia-Linares, E. Lopez, J. Villa, and I. Ramiro, “Operation of the three terminal heterojunction bipolar transistor solar cell,” *physica status solidi c* **14**, 1700191 (2017).
- ³¹³P. G. Linares, E. Antolin, and A. Marti, “Novel heterojunction bipolar transistor architectures for the practical implementation of high-efficiency three-terminal solar cells,” *Solar Energy Materials and Solar Cells* **194**, 54–61 (2019).
- ³¹⁴M. H. Zehender, I. Garcia, S. A. Svatek, M. A. Steiner, P. Garcia-Linares, E. Warren, A. Tamboli, A. Marti, and E. Antolin, “Demonstrating the GaInP/GaAs three-terminal heterojunction bipolar transistor solar cell,” in *2019 IEEE 46th Photovoltaic Specialists Conference (PVSC) (IEEE, 2019)*, pp. 0035–0040.
- ³¹⁵E. Antolin, M. H. Zehender, P. Garcia-Linares, S. A. Svatek, and A. Marti, “Considerations for the design of a heterojunction bipolar transistor solar cell,” *IEEE Journal of Photovoltaics* **10**, 2–7 (2019).
- ³¹⁶T. Nagashima, K. Okumura, K. Murata, and Y. Kimura, “Three-terminal tandem solar cells with a back-contact type bottom cell,” in *Proc. of the 28th IEEE Photovoltaic Specialists Conference (IEEE, 2000)*, pp. 1193–1196.

- ³¹⁷E. L. Warren, M. G. Deceglie, P. Stradins, and A. C. Tamboli, “Modeling three-terminal III-V I Si tandem solar cells,” in *IEEE 44th Photovoltaic Specialist Conference (PVSC)* (IEEE, 2017), pp. 2488–2491.
- ³¹⁸E. L. Warren, M. G. Deceglie, M. Rienäcker, R. Peibst, A. C. Tamboli, and P. Stradins, “Maximizing tandem solar cell power extraction using a three-terminal design,” *Sustainable Energy Fuels* **2**, 1141–1147 (2018).
- ³¹⁹M. Schnabel, M. Rienäcker, A. Merkle, T. R. Klein, N. Jain, S. Essig, H. Schulte-Huxel, E. Warren, M. F. van Hest, J. Geisz, et al., “Iii-v/si tandem cells utilizing interdigitated back contact si cells and varying terminal configurations,” in *Proc. of IEEE 44th Photovoltaic Specialists Conference (PVSC)*, Vol. 2 (IEEE, 2017), pp. 1–5.
- ³²⁰G. W. Adhyaksa, E. Johlin, and E. C. Garnett, “Nanoscale back contact perovskite solar cell design for improved tandem efficiency,” *Nano Letters* **17**, 5206–5212 (2017).
- ³²¹T. Nagashima, T. Nishikawa, and Shizuoka-Ken, “Tandem Solar Cell,” **5009719** (2000).
- ³²²Z. Djebbour, W. El-Huni, A. Migan Dubois, and J.-P. Kleider, “Bandgap engineered smart three-terminal solar cell: new perspectives towards very high efficiencies in the silicon world,” *Progress in Photovoltaics: Research and Applications* **27**, 306–315 (2019).
- ³²³R. Santbergen, H. Uzu, K. Yamamoto, and M. Zeman, “Optimization of three-terminal perovskite/silicon tandem solar cells,” *IEEE Journal of Photovoltaics* **9**, 446–451 (2019).
- ³²⁴K. VanSant, E. Warren, M. Rienäcker, H. Schulte-Huxel, R. Peibst, J. Geisz, P. Stradins, and A. Tamboli, “Performance Comparison of III-V//Si Tandem Solar Cells in the Three-Terminal Configuration,” in *MRS Fall Meeting & Exhibit* (2019).
- ³²⁵K. T. VanSant, “Performance comparison of III-V-on-Si tandem solar cells in the 2-terminal, 3-terminal and 4-terminal configurations,” PhD thesis (Colorado School of Mines).
- ³²⁶T. Tayagaki, K. Makita, T. Tachibana, H. Mizuno, R. Oshima, H. Takato, and T. Sugaya, “Three-terminal tandem solar cells with a back-contact-type bottom cell bonded using conductive metal nanoparticle arrays,” *IEEE Journal of Photovoltaics* **10**, 358–362 (2019).
- ³²⁷T. Tayagaki, K. Makita, T. Tachibana, H. Mizuno, R. Oshima, H. Takato, and T. Sugaya, “Impact of loading topology and current mismatch on current–voltage curves of three-terminal tandem solar cells with interdigitated back contacts,” *Solar Energy Materials and Solar Cells* **221**, 110901 (2021).
- ³²⁸P. Tockhorn, P. Wagner, L. Kegelmann, J.-C. Stang, M. Mews, S. Albrecht, and L. Korte, “Three-terminal perovskite/silicon tandem solar cells with top and interdigitated rear contacts,” *ACS Applied Energy Materials* **3**, 1381–1392 (2020).
- ³²⁹P. Wagner, P. Tockhom, L. Kegelmann, S. Albrecht, and L. Korte, “Three-Terminal Perovskite/Silicon Tandem Solar Cells with Top and Interdigitated Back-Contacts,” in *47th IEEE Photovoltaic Specialists Conference (PVSC)* (IEEE, 2020), pp. 0457–0459.
- ³³⁰P. Wagner, “Interdigitated back-contact silicon heterojunction solar cells: development of patterning techniques and applications in tandem devices,” PhD thesis (Technische Universität Berlin, 2021).

- ³³¹J. Buencuerpo, J. F. Geisz, M. S. Young, T. R. Klein, W. E. McMahon, E. L. Warren, and A. C. Tamboli, “Stringing monolithic three terminal III-V tandems,” in Proc. of 47th IEEE Photovoltaic Specialists Conference (PVSC) (IEEE, 2020), pp. 0538–0539.
- ³³²W. McMahon, H. Schulte-Huxel, J. Buencuerpo, M. Young, T. Klein, J. Geisz, A. Tamboli, and E. Warren, “Voltage-Matched Strings using 3-Terminal Tandems: Fundamentals and End Losses,” in Proc. of 47th IEEE Photovoltaic Specialists Conference (PVSC) (IEEE, 2020), pp. 0266–0266.
- ³³³W. E. McMahon, H. Schulte-Huxel, J. Buencuerpo, J. F. Geisz, M. S. Young, T. R. Klein, A. C. Tamboli, and E. L. Warren, “Homogenous voltage-matched strings using three-terminal tandem solar cells: fundamentals and end losses,” *IEEE Journal of Photovoltaics* **11**, 1078–1086 (2021).
- ³³⁴R. Witteck, S. Blankemeyer, M. Siebert, M. Köntges, and H. Schulte-Huxel, “Partial shading of one solar cell in a photovoltaic module with 3-terminal cell interconnection,” *Solar Energy Materials and Solar Cells* **219**, 110811 (2021).
- ³³⁵F. Gota, M. Langenhorst, R. Schmager, J. Lehr, and U. W. Paetzold, “Energy yield advantages of three-terminal perovskite-silicon tandem photovoltaics,” *Joule* **4**, 2387–2403 (2020).
- ³³⁶J. F. Geisz, W. E. McMahon, J. Buencuerpo, M. S. Young, M. Rienäcker, A. C. Tamboli, and E. L. Warren, “Characterization of multiterminal tandemphotovoltaic devices and their subcellcoupling,” *Cell Reports Physical Science* **2** (2021).
- ³³⁷A. De Vos, “Endoreversible thermodynamics and chemical reactions,” *The Journal of Physical Chemistry* **95**, 4534–4540 (1991).
- ³³⁸P. Würfel, “The chemical potential of radiation,” *Journal of Physics C: Solid State Physics* **15**, 3967–3985 (1982).
- ³³⁹H. S. Fogler, *Chemical Reaction Engineering Elements*, 3rd Edition (Prentice-Hall Inc, New Jersey, USA, 2004), p. 976.
- ³⁴⁰P. Baruch, “A two-level system as a model for a photovoltaic solar cell,” *Journal of Applied Physics* **57**, 1347–1355 (1985).
- ³⁴¹A. De Vos, “The endoreversible theory of solar energy conversion: a tutorial,” *Solar Energy Materials and Solar Cells* **31**, 75–93 (1993).
- ³⁴²L. Chen, F. Sun, C. Wu, and J. Yu, “Performance characteristic of isothermal chemical engines,” *Energy Conversion and Management* **38**, 1841–1846 (1997).
- ³⁴³L. Chen, D. Xia, and F. Sun, “Optimal performance of an endoreversible chemical engine with diffusive mass transfer law,” *Proceedings of the Institution of Mechanical Engineers, Part C: Journal of Mechanical Engineering Science* **222**, 1535–1539 (2008).
- ³⁴⁴D. Xia, L. Chen, and F. Sun, “Optimal performance of a generalized irreversible chemical engine with diffusive mass transfer law,” *Mathematical and Computer Modelling* **51**, 127–136 (2010).

- ³⁴⁵H. Hooyberghs, B. Cleuren, A. Salazar, J. O. Indekeu, and C. Van den Broeck, “Efficiency at maximum power of a chemical engine,” *The Journal of Chemical Physics* **139**, 134111 (2013).
- ³⁴⁶S. Glunz, J. Nekarda, H. Mäckel, and A. Cuevas, “Analyzing back contacts of silicon solar cells by Suns- V_{OC} -measurements at high illumination densities,” in *Proc. of 22nd European Photovoltaic Solar Energy Conference and Exhibition, Vol. 3* (2007), p. 7.
- ³⁴⁷M. Bivour, M. Reusch, S. Schroer, F. Feldmann, J. Temmler, H. Steinkemper, and M. Hermle, “Doped layer optimization for silicon heterojunctions by injection-level-dependent open-circuit voltage measurements,” *IEEE Journal of Photovoltaics* **4**, 566–574 (2014).
- ³⁴⁸M. Bivour, “Silicon heterojunction solar cells: analysis and basic understanding,” PhD thesis (Albert-Ludwigs Universität Freiburg im Breisgau, 2017).
- ³⁴⁹R. Brendel, C. Kruse, A. Merkle, H. Schulte-Huxel, F. Haase, R. Peibst, “Screening Carrier Selective Contact Combinations for Novel Crystalline Si Cell Structures,” in *Proc. of 35th European Photovoltaic Solar Energy Conference and Exhibition* (2019), pp. 39–46.
- ³⁵⁰A. Richter, M. Hermle, and S. W. Glunz, “Reassessment of the Limiting Efficiency for Crystalline Silicon Solar Cells,” *IEEE Journal of Photovoltaics* **3**, 1184–1191 (2013).
- ³⁵¹A. Schenk, “Finite-temperature full random-phase approximation model of band gap narrowing for silicon device simulation,” *Journal of Applied Physics* **84**, 3684–3695 (1998).
- ³⁵²C. Reichel, F. Granek, J. Benick, O. Schultz-Wittmann, and S. W. Glunz, “Comparison of emitter saturation current densities determined by injection-dependent lifetime spectroscopy in high and low injection regimes,” *Progress in Photovoltaics: Research and Applications* **20**, 21–30 (2012).
- ³⁵³D. Tetzlaff, J. Krügener, Y. Larionova, S. Reiter, M. Turcu, F. Haase, R. Brendel, R. Peibst, U. Höhne, J.-D. Kähler, and T. Wietler, “A simple method for pinhole detection in carrier selective POLO-junctions for high efficiency silicon solar cells,” *Solar Energy Materials and Solar Cells* **173**, 106–110 (2017).
- ³⁵⁴BIPM, IEC, IFCC, ISO, IUPAC, IUPAP, and OIML, *JCGM 100:2008, Guide to the expression of uncertainty in measurement* (International Organization for Standardization, 2010).
- ³⁵⁵BIPM, IEC, IFCC, ISO, IUPAC, IUPAP, and OIML, *JCGM 101: 2008: Evaluation of measurement data Supplement 1 to the Guide to the expression of uncertainty in measurement Propagation of distributions using a Monte Carlo method* (International Organization for Standardization, 2008).
- ³⁵⁶M. Cox, P. Harris, and B. R.-L. Siebert, “Evaluation of Measurement Uncertainty Based on the Propagation of Distributions Using Monte Carlo Simulation,” *Measurement Techniques* **46**, 824–833 (2003).
- ³⁵⁷H.-J. Haw-Jye Ueng, D. Janes, and K. Webb, “Error analysis leading to design criteria for transmission line model characterization of ohmic contacts,” *IEEE Transactions on Electron Devices* **48**, 758–766 (2001).

- ³⁵⁸J. M. Ford, “Al/Poly-Si specific contact resistivity,” *IEEE Electron Device Letters* **4**, 255–257 (1983).
- ³⁵⁹D. Tetzlaff, J. Krügener, Y. Larionova, S. Reiter, M. Turcu, N. Folchert, R. Peibst, U. Höhne, J.-D. Kähler, and T. Wietler, “Finding pinholes in carrier selective polycrystalline Si / crystalline Si contacts: like a needle in a haystack,” in *European microscopy congress 2016: proceedings* (Wiley-VCH Verlag GmbH & Co. KGaA, Weinheim, Germany, Dec. 2016), pp. 370–371.
- ³⁶⁰D. Tetzlaff, M. Dzinnik, J. Krügener, Y. Larionova, S. Reiter, M. Turcu, R. Peibst, U. Höhne, J.-D. Kähler, and T. F. Wietler, “Introducing pinhole magnification by selective etching: application to poly-si on ultra-thin silicon oxide films,” *Energy Procedia* **124**, 7th International Conference on Silicon Photovoltaics, SiliconPV 2017, 3-5 April 2017, Freiburg, Germany, 435–440 (2017).
- ³⁶¹K. R. McIntosh and P. P. Altermatt, “A freeware 1D emitter model for silicon solar cells,” in *Proc. of 35th IEEE Photovoltaic Specialists Conference* (June 2010), pp. 002188–002193.
- ³⁶²K. McIntosh, P. P. Altermatt, T. Ratcliff, K. Fong, L. Black, S. Baker-Finch, and M. Abbott, “An examination of three common assumptions used to simulate recombination in heavily doped silicon,” in *Proc. of 28th European Photovoltaic Solar Energy Conference and Exhibition* (2013).
- ³⁶³R. Peibst, U. Römer, Y. Larionova, M. Rienäcker, A. Merkle, N. Folchert, S. Reiter, M. Turcu, B. Min, J. Krügener, D. Tetzlaff, E. Bugiel, T. Wietler, and R. Brendel, “Working principle of carrier selective poly-Si/c-Si junctions: Is tunnelling the whole story?” *Solar Energy Materials and Solar Cells* **158**, 60–67 (2016).
- ³⁶⁴M. Verbeek, “Schräg bedampfte Silizium-Solarzellen mit V-förmiger Oberflächenstruktur,” PhD thesis (Leibniz Universität Hannover, 1998).
- ³⁶⁵A. Metz, “Neuartige höchsteffiziente Silicium-Solarzellen mit schräg im Hochvakuum aufgedampften Al-SiO_x-n-Si-Tunnelkontakten,” PhD thesis (Leibniz Universität Hannover, 2000).
- ³⁶⁶R. A. Sinton and R. M. Swanson, “Simplified backside-contact solar cells,” *IEEE Transactions on Electron Devices* **37**, 348–352 (1990).
- ³⁶⁷P. Engelhart, N. Harder, T. Neubert, H. Plagwitz, B. Fischer, R. Meyer, and R. Brendel, “Laser processing of 22% efficient back-contacted silicon solar cells,” in *Proc. of 21st European Photovoltaic Solar Energy Conference and Exhibition* (2006), pp. 773–776.
- ³⁶⁸P. Engelhart, “Lasermaterialbearbeitung als Schlüsseltechnologie zum Herstellen rückseitenkontaktierter Siliciumsolarzellen,” PhD thesis (Leibniz Universität Hannover, 2007), p. 162.
- ³⁶⁹D. L. Young, W. Nemeth, V. LaSalvia, R. Reedy, S. Essig, N. Bateman, and P. Stradins, “Interdigitated back passivated contact (ibpc) solar cells formed by ion implantation,” *IEEE Journal of Photovoltaics* **6**, 41–47 (2016).

- ³⁷⁰C. Reichel, R. Müller, F. Feldmann, A. Richter, M. Hermle, and S. W. Glunz, “Influence of the transition region between p- and n-type polycrystalline silicon passivating contacts on the performance of interdigitated back contact silicon solar cells,” *Journal of Applied Physics* **122**, 184502 (2017).
- ³⁷¹G. Hurkx, H. de Graaff, W. Kloosterman, and M. Knuvers, “A new analytical diode model including tunneling and avalanche breakdown,” *IEEE Transactions on Electron Devices* **39**, 2090–2098 (1992).
- ³⁷²G. Hurkx, D. Klaassen, and M. Knuvers, “A new recombination model for device simulation including tunneling,” *IEEE Transactions on Electron Devices* **39**, 331–338 (1992).
- ³⁷³M. Shur, “Recombination current in forward-biased p-n junctions,” *IEEE Transactions on Electron Devices* **35**, 1564–1565 (1988).
- ³⁷⁴K. Lee and A. Nussbaum, “The influences of traps on the generation-recombination current in silicon diodes,” *Solid-State Electronics* **23**, 655–660 (1980).
- ³⁷⁵M. Dutoit and F. Sollberger, “Lateral Polysilicon p-n Diodes,” *Journal of The Electrochemical Society* **125**, 1648 (1978).
- ³⁷⁶R. Peibst, M. Rienäcker, B. Min, C. Klamt, R. Niepelt, T. F. Wietler, T. Dullweber, E. Sauter, J. Hübner, M. Oestreich, and R. Brendel, “From PERC to Tandem: POLO- and p+/n+ Poly-Si Tunneling Junction as Interface Between Bottom and Top Cell,” *IEEE Journal of Photovoltaics* **9**, 49–54 (2019).
- ³⁷⁷C. Hollemann, F. Haase, M. Rienäcker, V. Barnscheidt, J. Krügener, N. Folchert, R. Brendel, S. Richter, S. GroSSer, E. Sauter, J. Hübner, M. Oestreich, and R. Peibst, “Separating the two polarities of the POLO contacts of an 26.1%-efficient IBC solar cell,” *Scientific Reports* **10** (2020).
- ³⁷⁸N. Convers Wyeth, “Sheet resistance component of series resistance in a solar cell as a function of grid geometry,” *Solid-State Electronics* **20**, 629–634 (1977).
- ³⁷⁹S. B. Rim, T. Kim, D. D. Smith, and P. J. Cousins, “Bypass diode for a solar cell,” US Patent US8134217B2 (2010).
- ³⁸⁰D. D. Smith, P. Cousins, S. Westerberg, R. D. Jesus-Tabajonda, G. Aniero, and Y. C. Shen, “Toward the practical limits of silicon solar cells,” *IEEE Journal of Photovoltaics* **4** (2014).
- ³⁸¹C. Hollemann, F. Haase, S. Schäfer, J. Krügener, R. Brendel, and R. Peibst, “26.1%-efficient POLO-IBC cells: Quantification of electrical and optical loss mechanisms,” *Progress in Photovoltaics: Research and Applications* **27**, 950–958 (2019).
- ³⁸²K. McIntosh, T. Kho, K. Fong, S. Baker-Finch, Y. Wan, N. Zin, E. Franklin, D. Wang, M. Abbott, N. Grant, et al., “Quantifying the optical losses in back-contact solar cells,” in *2014 IEEE 40th photovoltaic specialist conference (pvsc)* (IEEE, 2014), pp. 0115–0123.
- ³⁸³R. A. Sinton and R. M. Swanson, “Recombination in highly injected silicon,” *IEEE Transactions on Electron Devices* **34**, 1380–1389 (1987).

- ³⁸⁴M. J. Kerr, A. Cuevas, and R. A. Sinton, “Generalized analysis of quasi-steady-state and transient decay open circuit voltage measurements,” *Journal of applied physics* **91**, 399–404 (2002).
- ³⁸⁵A. Fell, “A free and fast three-dimensional/two-dimensional solar cell simulator featuring conductive boundary and quasi-neutrality approximations,” *IEEE Transactions on Electron Devices* **60**, 733–738 (2013).
- ³⁸⁶A. Fell, K. C. Fong, K. R. McIntosh, E. Franklin, and A. W. Blakers, “3-d simulation of interdigitated-back-contact silicon solar cells with quokka including perimeter losses,” *IEEE Journal of Photovoltaics* **4**, 1040–1045 (2014).
- ³⁸⁷R. Brendel, “Modeling solar cells with the dopant-diffused layers treated as conductive boundaries,” *Progress in Photovoltaics: Research and Applications* **20**, 31–43 (2012).
- ³⁸⁸R. Brendel, T. Dullweber, R. Peibst, C. Kranz, A. Merkle, and D. Walter, “Breakdown of the efficiency gap to 29% based on experimental input data and modeling,” *Progress in Photovoltaics: Research and Applications* **24**, 1475–1486 (2016).
- ³⁸⁹A. Merkle, R. Peibst, and R. Brendel, “High efficient fully ion-implanted co-annealed and laser-structured back junction back contacted solar cells,” in *Proc. of 29th European Photovoltaic Solar Energy Conference and Exhibition* (2014), pp. 954–958.
- ³⁹⁰K. Rühle, M. K. Juhl, M. D. Abbott, L. M. Reindl, and M. Kasemann, “Impact of edge recombination in small-area solar cells with emitter windows,” *IEEE Journal of Photovoltaics* **5**, 1067–1073 (2015).
- ³⁹¹S. Schäfer, F. Haase, C. Hollemann, J. Hensen, J. Krügener, R. Brendel, and R. Peibst, “26%-efficient and 2 cm narrow interdigitated back contact silicon solar cells with passivated slits on two edges,” *Solar Energy Materials and Solar Cells* **200**, 110021 (2019).
- ³⁹²P. Verlinden, R. Sinton, and R. Swanson, “High efficiency large area back contact concentrator solar cells with a multilevel interconnection,” *International journal of solar energy* **6**, 347–366 (1988).
- ³⁹³D. Pysch, A. Mette, and S. Glunz, “A review and comparison of different methods to determine the series resistance of solar cells,” *Solar Energy Materials and Solar Cells* **91**, 1698–1706 (2007).
- ³⁹⁴R. Brendel, S. Dreissigacker, N.-P. Harder, and P. P. Altermatt, “Theory of analyzing free energy losses in solar cells,” *Applied Physics Letters* **93**, 173503 (2008).
- ³⁹⁵R. Peibst, M. Rienäcker, Y. Larionova, N. Folchert, F. Haase, C. Hollemann, S. Wolter, J. Krügener, J. Bayer, M. Dzinnik, R. Haug, and R. Brendel, “Towards 28 %-efficient si single junction solar cells with better passivating polo junctions and photonic crystals,” *Solar Energy Materials and Solar Cells* **238**, 111560 (2022).
- ³⁹⁶K. Yoshikawa, W. Yoshida, T. Irie, H. Kawasaki, K. Konishi, H. Ishibashi, T. Asatani, D. Adachi, M. Kanematsu, H. Uzu, and K. Yamamoto, “Exceeding conversion efficiency of 26% by heterojunction interdigitated back contact solar cell with thin film Si technology,” *Solar Energy Materials and Solar Cells* **173**, 37–42 (2017).

- ³⁹⁷Z. Yu, M. Leilaoui, and Z. Holman, “Selecting tandem partners for silicon solar cells,” *Nature Energy* **1**, 16137 (2016).
- ³⁹⁸M. Rienäcker, M. Schnabel, E. Warren, A. Merkle, H. SchulteHuxel, T. Klein, M. van Hest, M. Steiner, and J. Geisz, “Mechanically stacked dual-junction and triple-junction III-V/Si-IBC cells with efficiencies of 31.5% and 35.4%,” in *Proc. of 33rd European Photovoltaic Solar Energy Conference and Exhibition* (2017), pp. 1–4.
- ³⁹⁹R. Whitehead, K. VanSant, M. Rienäcker, J. Geisz, and A. Tamboli, *Optimizing the top cell absorbing layer thickness in 4T GaAs on Si tandem solar cells*, 2019 MRS Fall Meeting & Exhibit, Boston, USA, 2019.
- ⁴⁰⁰R. C. Whitehead, K. T. VanSant, E. L. Warren, J. Buencuerpo, M. Rienäcker, R. Peibst, J. F. Geisz, and A. C. Tamboli, “Optimization of four terminal rear heterojunction GaAs on Si interdigitated back contact tandem solar cells,” *Applied Physics Letters* **118**, 183902 (2021).
- ⁴⁰¹L. Esaki, “New phenomenon in narrow germanium pn junctions,” *Phys. Rev.* **109**, 603–604 (1958).
- ⁴⁰²D. L. Miller, S. W. Zehr, and J. S. Harris, “GaAs-AlGaAs tunnel junctions for multigap cascade solar cells,” *Journal of Applied Physics* **53**, 744–748 (1982).
- ⁴⁰³B. Yu, F. Zhu, H. Wang, G. Li, and D. Yan, “All-organic tunnel junctions as connecting units in tandem organic solar cell,” *Journal of Applied Physics* **104**, 114503 (2008).
- ⁴⁰⁴M. De Bastiani, A. S. Subbiah, E. Aydin, F. H. Isikgor, T. G. Allen, and S. De Wolf, “Recombination junctions for efficient monolithic perovskite-based tandem solar cells: physical principles, properties, processing and prospects,” *Materials Horizons* **7**, 2791–2809 (2020).
- ⁴⁰⁵M. Kessler, D. Münster, T. Neubert, C. Mader, J. Schmidt, and R. Brendel, “High-efficiency back-junction silicon solar cell with an in-line evaporated aluminum front grid,” in *Proc. of 37th IEEE Photovoltaic Specialists Conference (PVSC) (IEEE, 2011)*, pp. 001085–001090.
- ⁴⁰⁶S. Essig, C. Allebé, T. Remo, J. F. Geisz, M. A. Steiner, K. Horowitz, L. Barraud, J. S. Ward, M. Schnabel, A. Descoeur, D. L. Young, M. Woodhouse, M. Despeisse, C. Ballif, and A. Tamboli, “Raising the one-sun conversion efficiency of III-V/Si solar cells to 32.8% for two junctions and 35.9% for three junctions,” *Nature Energy* **6**, 17144 (2017).
- ⁴⁰⁷J. Burdick and T. Glatfelter, “Spectral response and I-V measurements of tandem amorphous-silicon alloy solar cells,” *Solar Cells* **18**, 301–314 (1986).
- ⁴⁰⁸F. Lindholm, J. Fossum, and E. Burgess, “Application of the superposition principle to solar-cell analysis,” *IEEE Transactions on Electron Devices* **26**, 165–171 (1979).
- ⁴⁰⁹Shang-Yi Chiang, B. Carbajal, and G. Wakefield, “Improved performance thin solar cells,” *IEEE Transactions on Electron Devices* **25**, 1405–1409 (1978).
- ⁴¹⁰M. Ghannam, “A new n+ pn+ structure with back side floating junction for high efficiency silicon solar cells,” in *Proc. of 22nd IEEE Photovoltaic Specialists Conference (PVSC) ()*, pp. 284–289.

- ⁴¹¹S. R. Wenham, S. J. Robinson, X. Dai, J. Zhao, A. Wang, Y. H. Tang, A. Ebong, C. B. Honsberg, and M. A. Green, “Rear surface effects in high efficiency silicon solar cells,” in Proc. of 1st World Conference on Photovoltaic Energy Conversion (WCPEC) (1994), pp. 1278–1282.
- ⁴¹²A. Goetzberger, J. Knobloch, and B. Voss, “Crystalline silicon solar cells,” New York, 114–118 (1998).
- ⁴¹³G. Virshup, “Measurement techniques for multijunction solar cells,” in Proc. of IEEE photovoltaic specialists conference (1990), pp. 1249–1255.
- ⁴¹⁴Andreas Bauer, “ZnO:Al-Elektroden in semitransparenten organischen Solarzellen und Tandemsolarzellen,” PhD thesis (Karlsruhe Institute of Technology, 2012).
- ⁴¹⁵S. Rühle, “Tabulated values of the Shockley-Queisser limit for single junction solar cells,” Solar Energy **130**, 139–147 (2016).
- ⁴¹⁶S. Rühle, “The detailed balance limit of perovskite/silicon and perovskite/CdTe tandem solar cells,” physica status solidi (a) **214**, 1600955 (2017).
- ⁴¹⁷R. Sinton, Young Kwark, J. Gan, and R. Swanson, “27.5-percent silicon concentrator solar cells,” IEEE Electron Device Letters **7**, 567–569 (1986).
- ⁴¹⁸H. Schulte-Huxel, J.-H. Petermann, S. Blankemeyer, V. Steckenreiter, S. Kajari-Schroeder, and R. Brendel, “Simultaneous contacting and interconnection of passivated emitter and rear solar cells,” Energy Procedia **92**, 515–522 (2016).
- ⁴¹⁹P. Verlinden, R. Swanson, R. Sinton, D. Kane, and M. Cullough, “Multilevel metallisation for large area point-contact solar cells,” in Proc. of 37th European Photovoltaic Solar Energy Conference and Exhibition (1988), pp. 1466–1471.
- ⁴²⁰H. Gummel, “A charge control relation for bipolar transistors,” Bell System Technical Journal **49**, 115–120 (1970).
- ⁴²¹H. Gummel and H. Poon, “An integral charge control model of bipolar transistors,” Bell System Technical Journal **49**, 827–852 (1970).
- ⁴²²M. Reisch, “Physics and modeling of bipolar junction transistors,” in *High-frequency bipolar transistors* (Springer, 2003), pp. 175–358.
- ⁴²³J.-P. Colinge and C. A. Colinge, *Physics of semiconductor devices* (Springer Science & Business Media, 2005).
- ⁴²⁴J. Borrego, V. Temple, and M. Adler, “Extension of Gummel’s charge control relation,” Solid-State Electronics **20**, 441–442 (1977).
- ⁴²⁵J. De Vos, “A new determination of the emissivity of tungsten ribbon,” Physica **20**, 690–714 (1954).
- ⁴²⁶E. H. Jung, N. J. Jeon, E. Y. Park, C. S. Moon, T. J. Shin, T.-Y. Yang, J. H. Noh, and J. Seo, “Efficient, stable and scalable perovskite solar cells using poly (3-hexylthiophene),” Nature **567**, 511–515 (2019).

- ⁴²⁷M. A. Green, E. D. Dunlop, J. Hohl-Ebinger, M. Yoshita, N. Kopidakis, and A. W. Ho-Baillie, “Solar cell efficiency tables (version 55),” *Progress in Photovoltaics: Research and Applications* **28**, 3–15 (2020).
- ⁴²⁸C. Wong, C.-H. Hsu, and Y. Taur, “Mobile ion gettering in passivated p+ polysilicon gates,” in *Digest of Technical Papers. 1990 Symposium on VLSI Technology (1990)*, pp. 123–124.
- ⁴²⁹Z. C. Holman, A. Descoeurdes, S. De Wolf, and C. Ballif, “Record Infrared Internal Quantum Efficiency in Silicon Heterojunction Solar Cells With Dielectric/Metal Rear Reflectors,” *IEEE Journal of Photovoltaics* **3**, 1243–1249 (2013).
- ⁴³⁰Z. C. Holman, M. Filipi, B. Lipovek, S. De Wolf, F. Smole, M. Topi, and C. Ballif, “Parasitic absorption in the rear reflector of a silicon solar cell: Simulation and measurement of the sub-bandgap reflectance for common dielectric/metal reflectors,” *Solar Energy Materials and Solar Cells* **120**, 426–430 (2014).
- ⁴³¹K. Ramspeck, S. Reissenweber, J. Schmidt, K. Bothe, and R. Brendel, “Dynamic carrier lifetime imaging of silicon wafers using an infrared-camera-based approach,” *Applied Physics Letters* **93**, 102104 (2008).
- ⁴³²S. E. Sofia, H. Wang, A. Bruno, J. L. Cruz-Campa, T. Buonassisi, and I. M. Peters, “Roadmap for cost-effective, commercially-viable perovskite silicon tandems for the current and future PV market,” *Sustainable Energy & Fuels* **4**, 852–862 (2020).
- ⁴³³F. Haase, C. Hollemann, S. Schafer, J. Krügener, R. Brendel, and R. Peibst, “Transferring the record p-type si polo-ibc cell technology towards an industrial level,” in *Proc. of 46th IEEE Photovoltaic Specialists Conference (PVSC) (2019)*, pp. 2200–2206.
- ⁴³⁴C. Kranz, S. Wyczanowski, U. Baumann, S. Dorn, S. Queisser, J. Schweckendiek, D. Pysch, and T. Dullweber, “Industrial cleaning sequences for al₂o₃-passivated perc solar cells,” *Energy Procedia* **55**, Proceedings of the 4th International Conference on Crystalline Silicon Photovoltaics (SiliconPV 2014), 211–218 (2014).
- ⁴³⁵S. Mack, J. Schube, T. Fellmeth, F. Feldmann, M. Lenes, and J.-M. Luchies, “Metallisation of boron-doped polysilicon layers by screen printed silver pastes,” *physica status solidi (RRL)–Rapid Research Letters* **11**, 1700334 (2017).
- ⁴³⁶H. E. Ciftpinar, M. K. Stodolny, Y. Wu, G. J. Janssen, J. Löffler, J. Schmitz, M. Lenes, J.-M. Luchies, and L. Geerligs, “Study of screen printed metallization for polysilicon based passivating contacts,” *Energy Procedia* **124**, 7th International Conference on Silicon Photovoltaics, SiliconPV 2017, 3-5 April 2017, Freiburg, Germany, 851–861 (2017).
- ⁴³⁷A. Chaudhary, J. HoSS, J. Lossen, R. van Swaaij, and M. Zeman, “Screen printed ag contacts for n-type polysilicon passivated contacts,” *AIP Conference Proceedings* **2147**, 040002 (2019).
- ⁴³⁸P. Padhamnath, J. Wong, B. Nagarajan, J. K. Buatis, L. M. Ortega, N. Nandakumar, A. Khanna, V. Shanmugam, and S. Duttgupta, “Metal contact recombination in monopoly solar cells with screen-printed & fire-through contacts,” *Solar Energy Materials and Solar Cells* **192**, 109–116 (2019).

- ⁴³⁹M. Hayes, B. Martel, S. Dubois, A. Morisset, and O. Palais, “Study of non fire-through metallization processes of boron-doped polysilicon passivated contacts for high efficiency silicon solar cells,” *AIP Conference Proceedings* **2147**, 040006 (2019).
- ⁴⁴⁰R. Peibst, C. Kruse, S. Schäfer, V. Mertens, S. Bordihn, T. Dullweber, F. Haase, C. Hollemann, B. Lim, B. Min, R. Niepelt, H. Schulte-Huxel, and R. Brendel, “For none, one, or two polarities-How do POLO junctions fit best into industrial Si solar cells?” *Progress in Photovoltaics: Research and Applications* **28**, 505–516.
- ⁴⁴¹M. Winter, S. Bordihn, R. Peibst, R. Brendel, and J. Schmidt, “Degradation and regeneration of n+-doped poly-si surface passivation on p-type and n-type cz-si under illumination and dark annealing,” *IEEE Journal of Photovoltaics* **10**, 423–430 (2020).
- ⁴⁴²H. Li, K. Kim, B. Hallam, B. Hoex, S. Wenham, and M. Abbott, “POCl₃ diffusion for industrial Si solar cell emitter formation,” *Frontiers in Energy* **11**, 42–51 (2017).
- ⁴⁴³C. Luderer, C. Reichel, F. Feldmann, M. Bivour, and M. Hermle, “Passivating and low-resistive poly-si tunneling junction enabling high-efficiency monolithic perovskite/silicon tandem solar cells,” *Applied Physics Letters* **115**, 182105 (2019).
- ⁴⁴⁴A. Tomasi, B. Paviet-Salomon, Q. Jeangros, J. Haschke, G. Christmann, L. Barraud, A. Descoeurdes, J. P. Seif, S. Nicolay, M. Despeisse, et al., “Simple processing of back-contacted silicon heterojunction solar cells using selective-area crystalline growth,” *Nature Energy* **2**, 1–8 (2017).
- ⁴⁴⁵A. Uruena, J. John, G. Beaucarne, P. Choulat, P. Eyben, G. Agostinelli, E. Van Kerschaver, J. Poortmans, and R. Mertens, “Local Al-alloyed contacts for next generation Si solar cells,” in *Proc. of 24th European Photovoltaic Solar Energy Conference* (2009), pp. 1483–1486.
- ⁴⁴⁶F. Huster et al., “Investigation of the alloying process of screen printed aluminium pastes for the BSF formation on silicon solar cells,” in *Proc. of the 20th European Photovoltaic Solar Energy Conference (WIP Renewable Energies Barcelona, Spain, 2005)*, pp. 1466–1469.
- ⁴⁴⁷T. Dullweber, “High-efficiency industrial perc solar cells for monofacial and bifacial applications,” in *High-efficient low-cost photovoltaics* (Springer, 2020), pp. 65–94.
- ⁴⁴⁸G. Agostinelli, J. Szlufcick, P. Choulat, and G. Beaucarne, “Local contact structures for industrial PERC-type solar cells,” in *Proc. of the 20th European Photovoltaic Solar Energy Conference* (2005), pp. 942–945.
- ⁴⁴⁹A. Spribille, F. Clement, D. Erath, J. Specht, D. Biro, and R. Preu, “Dispensing of etching paste and inkjetting of diffusion barrier for mwt solar cell processing,” in *Proceedings of the 25th european photovoltaic solar energy conference and exhibition* (2010), p. 2654.
- ⁴⁵⁰D. Stüwe, D. Mager, D. Biro, and J. G. Korvink, “Inkjet technology for crystalline silicon photovoltaics,” *Advanced Materials* **27**, 599–626 (2015).
- ⁴⁵¹P. Engelhart, N.-P. Harder, R. Grischke, A. Merkle, R. Meyer, and R. Brendel, “Laser structuring for back junction silicon solar cells,” *Progress in Photovoltaics: Research and Applications* **15**, 237–243 (2007).

- ⁴⁵²A. Knorz, M. Peters, A. Grohe, C. Harmel, and R. Preu, "Selective laser ablation of SiN_x layers on textured surfaces for low temperature front side metallizations," *Progress in Photovoltaics: Research and Applications* **17**, 127–136 (2009).
- ⁴⁵³S. Hermann, T. Dezhdar, N.-P. Harder, R. Brendel, M. Seibt, and S. Stroj, "Impact of surface topography and laser pulse duration for laser ablation of solar cell front side passivating SiN_x layers," *Journal of Applied Physics* **108**, 114514 (2010).
- ⁴⁵⁴H. Seidel, "Anisotropic etching of crystalline silicon in alkaline solutions," *Journal of The Electrochemical Society* **137**, 3626 (1990).
- ⁴⁵⁵T. Dullweber, C. Kranz, R. Peibst, U. Baumann, H. Hannebauer, A. Fülle, S. Steckemetz, T. Weber, M. Kutzer, M. Müller, et al., "PERC+: industrial PERC solar cells with rear Al grid enabling bifaciality and reduced Al paste consumption," *Progress in Photovoltaics: Research and Applications* **24**, 1487–1498 (2016).
- ⁴⁵⁶J. Müller, K. Bothe, S. Gatz, and R. Brendel, "Modeling the formation of local highly aluminum-doped silicon regions by rapid thermal annealing of screen-printed aluminum," *physica status solidi (RRL)–Rapid Research Letters* **6**, 111–113 (2012).
- ⁴⁵⁷C. Kranz, U. Baumann, B. Wolpensinger, F. Lottspeich, M. Müller, P. Palinginis, R. Brendel, and T. Dullweber, "Void formation in screen-printed local aluminum contacts modeled by surface energy minimization," *Solar Energy Materials and Solar Cells* **158**, Proceedings of the 6th International Conference on Silicon Photovoltaics, 11–18 (2016).
- ⁴⁵⁸J. Beier and B. Voss, "Humps in dark i-v-curves-analysis and explanation," in *Conference record of the twenty third ieee photovoltaic specialists conference - 1993 (cat. no.93ch3283-9)* (1993), pp. 321–326.
- ⁴⁵⁹S. J. Robinson, A. G. Aberle, and M. A. Green, "Recombination saturation effects in silicon solar cells," *IEEE Transactions on Electron Devices* **41**, 1556–1569 (1994).
- ⁴⁶⁰S. J. Robinson, "Non-ideal" electrical characteristics of crystalline silicon solar cells," eng, PhD thesis (University of New South Wales. School of Electrical Engineering and Computer Science, 1995).
- ⁴⁶¹T. R. Klein, B. G. Lee, M. Schnabel, E. L. Warren, P. Stradins, A. C. Tamboli, and M. F. van Hest, "Transparent Conductive Adhesives for Tandem Solar Cells Using Polymer-Particle Composites," *ACS Applied Materials & Interfaces* **10**, 8086–8091 (2018).
- ⁴⁶²J. F. Geisz, M. A. Steiner, I. Garcia, S. R. Kurtz, and D. J. Friedman, "Enhanced external radiative efficiency for 20.8% efficient single-junction gainp solar cells," *Applied Physics Letters* **103**, 041118 (2013).
- ⁴⁶³J. L. Young, M. A. Steiner, H. Döscher, R. M. France, J. A. Turner, and T. G. Deutsch, "Direct solar-to-hydrogen conversion via inverted metamorphic multi-junction semiconductor architectures," *Nature Energy* **2**, 1–8 (2017).
- ⁴⁶⁴S. Essig, M. A. Steiner, C. Allebé, J. F. Geisz, B. Paviet-Salomon, S. Ward, A. Descoedres, V. LaSalvia, L. Barraud, N. Badel, et al., "Realization of gainp/si dual-junction solar cells with 29.8% 1-sun efficiency," *IEEE Journal of Photovoltaics* **6**, 1012–1019 (2016).

- ⁴⁶⁵F. H. M. Spit and H. Bakker, “Diffusion of donor elements (125Sb, 82P, 74(73)As) in polycrystalline silicon,” *physica status solidi (a)* **97**, 135–142 (1986).
- ⁴⁶⁶D. Rover, P. Basore, and G. Thorson, “Solar cell modeling on personal computers,” in *Proc. of 20th IEEE Photovoltaic Specialists Conference (PVSC)* (1988), pp. 389–396.
- ⁴⁶⁷D. A. Clugston and P. A. Basore, “PC1D version 5: 32-bit solar cell modeling on personal computers,” in *Proc. of 26th IEEE Photovoltaic Specialists Conference (IEEE, 1997)*, pp. 207–210.
- ⁴⁶⁸J. Y. Seto, “The electrical properties of polycrystalline silicon films,” *Journal of Applied Physics* **46**, 5247–5254 (1975).
- ⁴⁶⁹R. Brendel, “Sunrays: A versatile ray tracing program for the photovoltaic community,” in *Proc. of 12th European Photovoltaic Solar Energy Conference* (1994), pp. 1339–1342.
- ⁴⁷⁰S. Reiter, N. Koper, R. Reineke-Koch, Y. Larionova, M. Turcu, J. Krügener, D. Tetzlaff, T. Wietler, U. Höhne, J.-D. Kähler, et al., “Parasitic absorption in polycrystalline si-layers for carrier-selective front junctions,” *Energy Procedia* **92**, 199–204 (2016).
- ⁴⁷¹E. D. Palik, *Handbook of optical constants of solids*, Vol. 3 (Academic press, 1998).
- ⁴⁷²S. Duttagupta, F. Ma, B. Hoex, T. Mueller, and A. G. Aberle, “Optimised antireflection coatings using silicon nitride on textured silicon surfaces based on measurements and multidimensional modelling,” *Energy Procedia* **15**, 78–83 (2012).
- ⁴⁷³C. Schinke, K. Bothe, P. Christian Peest, J. Schmidt, and R. Brendel, “Uncertainty of the coefficient of band-to-band absorption of crystalline silicon at near-infrared wavelengths,” *Applied Physics Letters* **104**, 081915 (2014).
- ⁴⁷⁴C. Schinke, P. Christian Peest, J. Schmidt, R. Brendel, K. Bothe, M. R. Vogt, I. Kröger, S. Winter, A. Schirmacher, S. Lim, et al., “Uncertainty analysis for the coefficient of band-to-band absorption of crystalline silicon,” *AIP Advances* **5**, 067168 (2015).
- ⁴⁷⁵A. G. Aberle, *Crystalline silicon solar cells: advanced surface passivation and analysis* (Centre for Photovoltaic Engineering. University of New South Wales, 1999).
- ⁴⁷⁶A. Wagenpfahl, D. Rauh, M. Binder, C. Deibel, and V. Dyakonov, “S-shaped current-voltage characteristics of organic solar devices,” *Physical Review B* **82**, 115306 (2010).
- ⁴⁷⁷R. Saive, “S-shaped current-voltage characteristics in solar cells: a review,” *IEEE Journal of Photovoltaics* **9**, 1477–1484 (2019).
- ⁴⁷⁸B. Mazhari, “An improved solar cell circuit model for organic solar cells,” *Solar energy materials and solar cells* **90**, 1021–1033 (2006).
- ⁴⁷⁹B. Romero, G. del Pozo, B. Arredondo, D. Martin-Martin, M. P. R. Gordo, A. Pickering, A. Perez-Rodriguez, E. Barrena, and F. J. Garcia-Sanchez, “S-Shaped I-V Characteristics of Organic Solar Cells: Solving Mazhari’s Lumped-Parameter Equivalent Circuit Model,” *IEEE Transactions on Electron Devices* **64**, 4622–4627 (2017).
- ⁴⁸⁰F. J. Garcia-Sanchez and B. Romero, “Equivalent Circuit Models for Next Generation Photovoltaic Devices with S-shaped I-V Curves,” in *Proc. of 8th International Symposium on Next Generation Electronics (ISNE)* (Oct. 2019), pp. 1–4.

- ⁴⁸¹R. V. K. Chavali, S. De Wolf, and M. A. Alam, “Device physics underlying silicon heterojunction and passivating-contact solar cells: a topical review,” *Progress in Photovoltaics: Research and Applications* **26**, 241–260 (2018).
- ⁴⁸²R. V. K. Chavali, J. V. Li, C. Battaglia, S. De Wolf, J. L. Gray, and M. A. Alam, “A generalized theory explains the anomalous sunsvoc response of si heterojunction solar cells,” *IEEE Journal of Photovoltaics* **7**, 169–176 (2017).
- ⁴⁸³L. Nagel, “A computer program to simulate semiconductor circuits,” PhD thesis (University of California, 1975).
- ⁴⁸⁴A. Kaminski, J. Marchand, A. Fave, and A. Laugier, “New method of parameters extraction from dark I-V curve,” in *Proc. of 26th IEEE Photovoltaic Specialists Conference* (1997), pp. 203–206.
- ⁴⁸⁵Tera Analysis Ltd., *Quickfield student edition*, version 6.3.
- ⁴⁸⁶D. L. Meier and D. K. Schroder, “Contact resistance: its measurement and relative importance to power loss in a solar cell,” *IEEE transactions on electron devices* **31**, 647–653 (1984).
- ⁴⁸⁷G. Krieger, Y. Kwark, and R. Swanson, “An extension of the reciprocity theorem to include high-level injection conditions,” *IEEE Transactions on Electron Devices* **37**, 319–321 (1990).

A. Appendix

A.1. Supplementary material for the section on lateral poly-Si pn junctions

A.1.1. Diffusion profile

It is assumed that the lateral phosphorous interdiffusion can be appropriately estimated by diffusion from an infinite phosphorous source with a plateau concentration of $1 \cdot 10^{20}$ active phosphorus dopants/cm² into the homogeneously doped boron region with a plateau concentration of $3 \cdot 10^{19}$ active boron dopants/cm². The diffusivity of 3.2×10^{-10} cm²/s of phosphorus for the diffusion process at 1050 °C is estimated from Spit and Bakker [465, equation 3] with a prefactor of 60 cm²/s and an activation energy of 2.96 eV. The values for the parameters are at the boundary of the error margins in Spit and Bakker [465, equation 3] and are chosen such that a diffusivity of $2.4 \cdot 10^{-10}$ cm²/s for 1035 °C is replicated. This value was found by Hollemann *et al.* for the phosphorus diffusion in similar POLO junction fabrication processes [377]. Figure 7.2b shows the estimated dopant concentration of phosphorus and boron at the junction.

A.1.2. Calculation of J - V characteristic by mean of PC1D

In order to calculate the J - V characteristic and to find the recombination lifetime τ_r within the poly-Si pn -junction, a more sophisticated device simulation is performed compared to the simple single diode analysis from subsection 7.2.1. For this purpose, the PC1D v. 5.9 model [466, 467] from figure A.1 serves as the model of the interdiffused pn -junction with the estimated dopant profile from subsection A.1.1. Since the carrier mobility is strongly dependent on morphology of the poly-Si layer and the doping concentration [468], its value is uncertain for the presented poly-Si layers, especially within the graded junction. However, the mobility should be in the range between approximately 1 cm²/Vs and 50 cm²/Vs [468]. With the upper boundary for the mobility of 50 cm²/Vs and e.g. a lifetime of 200 ps, one obtains a diffusion length of about 160 nm, which is of the same order of magnitude as the depletion region width of 130 nm for the linearly grade junction from subsection 7.2.1. Therefore, at least for small forward biasing, almost all charge carriers recombine within the depletion region rather than in the field-free regions. Thus, the mobility has almost no effect on the J - V characteristic below about 400 mV, but the lifetime τ_r changes the characteristic significantly. Figure A.2a compares the measured and simulated J - V characteristic for lifetimes between 50 ps and 200 ps and a mobility of 15 cm²/Vs. The simulation with 150 ps matches the experimentally determined characteristic in the low to moderate voltage regime, which agrees

A.1. SUPPLEMENTARY MATERIAL FOR THE SECTION ON LATERAL POLY-SI PN JUNCTIONS

DEVICE

Device area: 1 cm²
No surface texturing
No surface charge
No Exterior Front Reflectance
No Exterior Rear Reflectance
No internal optical reflectance
 Emitter contact enabled
 Base contact enabled
No internal shunt elements

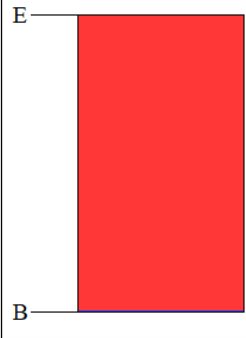
REGION 1

Thickness: 7 μm
 Material modified from program defaults
 Fixed electron mobility: 7 cm²/Vs
 Fixed hole mobility: 7 cm²/Vs
 Dielectric constant: 11.9
 Band gap: 1.124 eV
 Intrinsic conc. at 300 K: 1×10¹⁰ cm⁻³
 Refractive index: 3.58
 Absorption coeff. from internal model
 Free carrier absorption enabled
 P-type background doping: 3×10¹⁹ cm⁻³
 1st front diff.: N-type, 1×10²⁰ cm⁻³ peak
No 2nd front diffusion
No rear diffusion
 Bulk recombination: $\tau_n = \tau_p = 1.5 \times 10^{-4}$ μs
No Front-surface recombination
No Rear-surface recombination

EXCITATION

Excitation mode: Steady State
 Temperature: 25°C
Base circuit: Zero
Collector circuit: Zero
Light sources disabled

Device Schematic



First Front Diffusion

Enable n-type p-type OK Cancel

Profile: Uniform Exponential Gaussian Erfc

Peak Doping: 1.e20 cm-3

Depth Factor: 21.42 μm

Peak Position: -12 μm

Calculated:

Sheet Resistance at 300 K: 66.66 ohms/square

Junction Depth: 3.698 μm

For background doping density: 3.e19 cm-3

Figure A.1.: Screenshot of the PC1D v.5.9 model for the lateral poly-Si pn -junction showing the input parameter for the model calculations in figure A.2b. For the bulk recombination, a trap at a trap energy E_T of 20 meV is assumed.

with 40 ps from the simple single diode analysis. Moreover, by adjusting the mobility to a value of 7 cm²/Vs the PC1D simulation in figure A.2b resembles the J - V measurements over the entire voltage range. The excellent fit of the local ideality factors underlines the good agreement of the model with the experiment. At voltages below 200 mV, the good agreement of local idealities is only achieved, if a trap is assumed, which is 20 meV away from the center of the band gap rather than being in the center. Dutoit and Sollberger reported three trap centers with 5 meV, 10 meV and 25 meV with respect to the center of the band gap [375].

A.1.3. Reverse-bias characteristic of the poly-Si pn -junction

Figure A.3 shows the reverse-bias breakdown characteristic of the poly-Si pn -junction. The breakdown voltage is approximately 5.5 V.

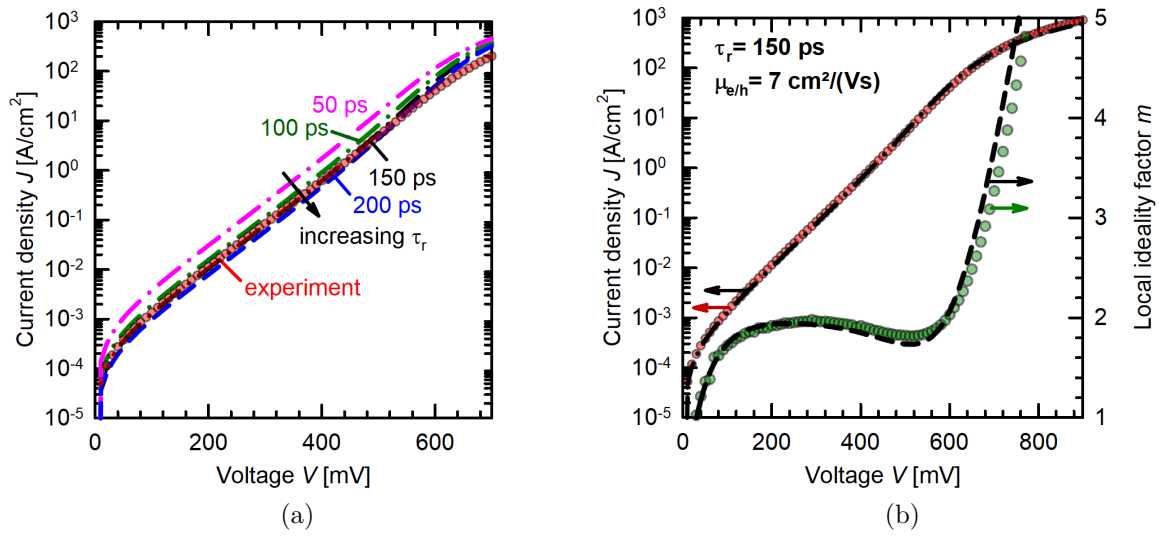


Figure A.2.: (a) Comparison of measured (red circles) and simulated (dash-dotted lines) J - V characteristic for carrier lifetimes between 50 ps and 200 ps. The assumed carrier mobility is 15 cm²/Vs. (b) Comparison of measured (red and green circles) and simulated (dash-dotted and dashed lines) J - V and m - V characteristic for a carrier lifetime of 150 ps and a carrier mobility of 7 cm²/Vs.

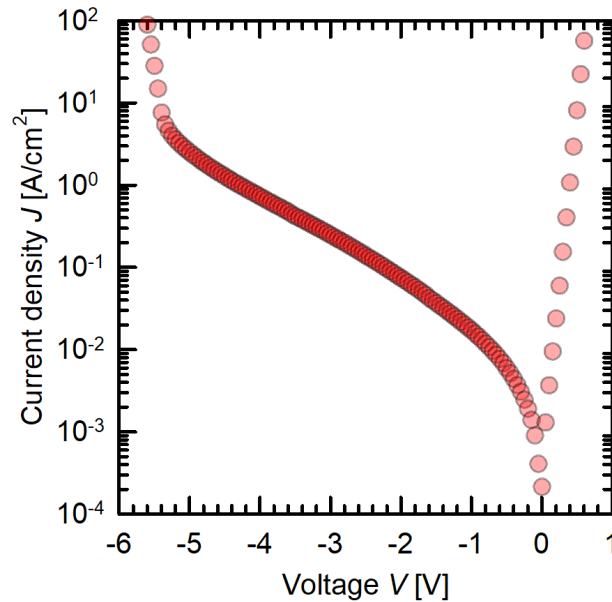


Figure A.3.: J - V characteristic of poly-Si *pn*-junction with a reverse breakdown at 5.5 V.

A.2. SUPPLEMENTARY MATERIAL FOR THE SECTION ON THE PERFORMANCE OF POLO-IBC CELL

Table A.1.: Input parameter for Sunrays simulations of the n^+ and p^+ POLO regions of the POLO-IBC cell from section 7.3

	Layer	Layer thickness [nm]	Data
Anti-reflection coating on upright pyramids	SiO ₂	120	Palik [471]
	SiN _y , n=1.9	55	Dutttagupta [472]
	SiN _y , n=2.4	12	Dutttagupta [472]
Absorber	c-Si	150 · 10 ³	Schinke [473, 474]
Planar rear side	p^+ poly-Si, $5 \cdot 10^{15} \text{ cm}^{-2}$ (n^+ poly-Si, $7.5 \cdot 10^{15} \text{ cm}^{-2}$)	150 (110)	Reiter [470]
	AlO _x	20	Palik [471]
	SiN _y , n=1.9	120	Dutttagupta [472]
	Al	1000	Palik [471]

A.2. Supplementary material for the section on the performance of POLO-IBC cell

A.2.1. Sunrays simulations

In order to study the optical properties of the POLO-IBC cell in section 7.3, a raytracing simulation is performed by means of the Sunrays software version 3.0.5 [469]. The POLO-IBC cell has at least three optically different regions: 60% of n^+ POLO contact region, 20% of p^+ POLO contact region and 20% of trench region. The input parameter for the simulation of the p^+ and n^+ POLO regions is summarized in table A.1. For the trench region the anti-reflection coating and the absorber layers are the same as for the POLO contact region in table A.1, but the rear side exhibits upright pyramids covered only by a 20 nm-thick AlO_x layer and a 75 nm-thick SiN_x layer with a refractive index $n = 1.9$.

Figure A.4a shows the obtained reflectance data from ray-tracing simulations for the three different regions and reflectance data measured on $2 \times 2 \text{ cm}^2$ reference samples representing the p^+ and n^+ POLO contact regions. The sample were fabricated on the cell wafer and therefore are optically almost identical to the cell regions. The simulated reflectance matches the measured one in the wavelength range between 350 nm and 1000 nm within 1%_{abs.}. Below and above this wavelength range, the maximum deviation between simulated and measured reflectances is 10%_{abs.}. However, the AM1.5G spectrum contains about only 11% of the total incident power density in this range. For wavelengths above 1000 nm, the used set of data for the poly-Si has a large impact on the parasitic absorption within the poly-Si and causes the deviation. For this reason, different sets of data from Reiter *et al.* [470] were tested and the best possible agreement was found with the data set used for figure A.4a.

In order to find the parasitic absorption of the front anti-reflection coating $A_{\text{para,sim}}$, the parasitic absorption of the ARC for the three regions were extracted from the same ray-tracing simulations as in figure A.4a. Figure A.4b shows the simulated parasitic absorption of the three regions and the area-weighted parasitic absorption $A_{\text{para,sim}}$, which is used in section

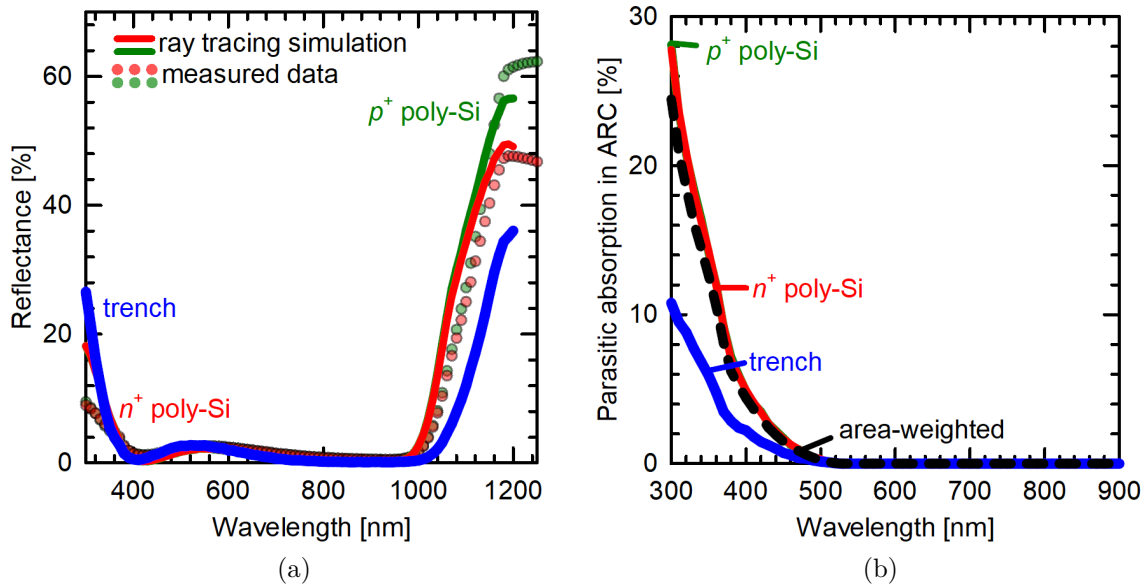


Figure A.4.: (a) Comparison of measured (circles) and simulated (solid lines) reflectance of the POLO-IBC cell regions with p^+ (green) and n^+ (red) poly-Si layers. Furthermore, the simulation of the trench region (blue solid line) is shown. (b) Sum of parasitic absorption and transmission of the simulated regions in (a) and the area-weighted sum, which represents the situation in the POLO-IBC cell.

7.3 to calculate the internal quantum efficiency.

Beside the parasitic absorption, the Sunrays simulations provide a breakdown of the loss channels for the POLO²-IBC cell, which can be found in table A.2. Furthermore, table A.2 contains a simulation with a perfect planar rear side and another with perfect textured rear side. To obtain a perfect rear side, the rear side is assumed to have a reflectivity of 1. The planar case represents the best possible scenario for the POLO²-IBC cell with a planar rear side and that of the textured case is the optimum with a textured rear side.

A.3. SUPPLEMENTARY MATERIAL FOR CHAPTER ON SELECTIVITY AND EXTRACTION EFFICIENCY

Table A.2.: Breakdown of optical loss channels in a POLO²-IBC cell by means of raytracing simulations of the three region and calculating area-weighted values. Note that front side reflection is part of the total reflection.

Structure of rear side	Current density [mA/cm ²]					
	area-weighted	n^+ poly-Si	p^+ poly-Si	trench	perfect, planar	perfect, textured
Incident from AM1.5G	46.3				46.3	
Total reflection	2.48	2.70	2.89	1.43	3.76	2.99
Front side reflection	0.42	0.42	0.42	0.42	0.42	0.42
Parasit. absorp. in ARC	0.24	0.24	0.25	0.25	0.24	0.24
Parasit. absorp. in poly-Si	0.96	1.30	0.89	0.00	0	0
Parasit. absorp. in Al	0.43	0.52	0.59	0.00	0	0
Transmission	0.63	0.00	0.00	3.13	0	0
Photogeneration	41.57	41.55	41.70	41.51	42.31	43.08

A.3. Supplementary material for chapter on selectivity and extraction efficiency

A.3.1. Electron transfer reaction

The following treatment is simplified presentation. For an accurate calculation, energy distribution of states, occupation and rate constants should be considered. The interested reader is referred to Gerischer [136] and Shockley [72] for example.

For the conduction band reaction, an occupied electron state e_C^- in the conduction band and an unoccupied electron state $V_{e_M^-}$ in the contact¹ yield an occupied electron state e_M^- in the contact and an unoccupied electron state $V_{e_C^-}$ in the conduction band.



The net transfer rate of electrons at the surface exchanged between the conduction band and the contact $\frac{dn_S}{dt} = r_C$ is the difference of the rates of electrons injected from the conduction band into the contact r_f^C with the forward rate constant k_f^C and vice verse rate r_r^C with the reverse rate constant k_r^C .

$$-\frac{dn_S}{dt} = r^C = r_f^C - r_r^C = k_f^C \cdot n_S \cdot [V_{e_M^-}] - k_r^C \cdot [e_M^-] \cdot [V_{e_C^-}] \quad (\text{A.1})$$

¹The contact is indicated as M in order to highlight, that this region has a single Fermi-level as it is the case for metals.

The quantities in square-brackets represent the concentration of each reaction species and $n_S = [e_C^-]$ is the electron concentration in the conduction band close to the contact surface. The number of unoccupied electron states in the conduction band is typically much larger than that of occupied states and therefore it can be assumed that the concentration $[V_{e_C^-}]$ stays approximately constant at its equilibrium value $[V_{e_C^-}]_0$. The single equilibrium Fermi-level in the contact region requires an instant equilibration of occupied and unoccupied electron states and therefore $[V_{e_M^-}]$ and $[e_M^-]$ are constant and equal to their equilibrium values $[V_{e_M^-}]_0$ and $[e_M^-]_0$.

Furthermore, at detailed balance equilibrium between conduction band and contact region, the net rate has to vanish, which implies that the following (law mass action) relation between forward and reverse reaction holds:

$$k_f^C \cdot n_{S0} \cdot [V_{e_M^-}]_0 = r_f^C = r_r^C = k_r^C \cdot [e_M^-]_0 \cdot [V_{e_C^-}]_0 \quad (\text{A.2})$$

With relation A.2 and the assumption of $k^C := k_f^C$, the net transfer rate is

$$-\frac{dn_S}{dt} = r^C = k^C \cdot [V_{e_M^-}]_0 \cdot (n_S - n_{S0}) = k^C \cdot [V_{e_M^-}]_0 \cdot n_{S0} \cdot \left(\frac{n_S}{n_{S0}} - 1 \right) \quad (\text{A.3})$$

The pseudo-first order reaction rate constant $\nu^C = k^C \cdot [V_{e_M^-}]_0$ is frequently referred to as the effective surface recombination velocity [105, 475]. Fonash [110] used the effective surface recombination velocity to define a perfect Ohmic carrier-selective contact and Wagenpfahl *et al.* model S-shaped current-voltage characteristics [476]. The current density of electrons flowing from the contact into the conduction band is defined as

$$j_n = -q \cdot \frac{dn_S}{dt} = j_{0n} \cdot \left(\frac{n_S}{n_{S0}} - 1 \right) \quad (\text{A.4})$$

The constant pre-factor, called equilibrium exchange current density, $j_{0n} = q \cdot k^C \cdot [V_{e_M^-}]_0 \cdot n_{S0}$ describes the exchange current density of electrons at detailed balance equilibrium.

For the valence band reaction, an occupied hole state h_V^+ in the valence band and an unoccupied hole state $V_{h_M^+}$ in the contact yield an occupied hole state h_M^+ in the contact and an unoccupied hole state $V_{h_V^+}$ in the valence band.



A similar derivation for the valence band reaction as for the conduction band reveals a net transfer rate of holes at the surface:

$$-\frac{dp_S}{dt} = r^V = k^V \cdot [V_{h_M^+}]_0 \cdot p_{S0} \cdot \left(\frac{p_S}{p_{S0}} - 1 \right) \quad (\text{A.5})$$

The corresponding hole current density flowing into the contact with equilibrium exchange current density $j_{0p} = q \cdot k^V \cdot [V_{h_M^+}]_0 \cdot p_{S0}$. reads:

$$j_p = -q \cdot \frac{dp_S}{dt} = q \cdot r^V = j_{0p} \cdot \left(\frac{p_S}{p_{S0}} - 1 \right) \quad (\text{A.6})$$

A.3.2. Selectivity calculated from the generalized charge control relation

In the literature of the bipolar junction transistors, a generalized form of Gummel’s charge control model [420, 421, 424] features a solution of the drift-diffusion model under general assumptions and provides a way to calculate a formula for selectivity of a general contact. In contrast to the “exponential law approach” of section 5.3, the majority carrier quasi-Fermi level is allowed to be non-flat and consequently the membrane is not necessarily field-free. Following Borrego *et al.*, the minority carrier (electron) current density $J_n(0)$ at the absorber/membrane interface at position $x = 0$ of a hole-selective contact reads [424, Equation 13]

$$J_n(0) = J_p(w) \frac{\mu_n \cdot Q_n(w)}{\mu_p \cdot Q_p(w)} - \frac{q^2 D_n}{Q_p(w)} \cdot [pn|_0 - pn|_w] \quad (\text{A.7})$$

$J_p(w)$ corresponds to the majority carrier (hole) current density at the membrane/electrode interface at position $x = w$. $Q_n(w) = \int_0^w qn dx$ and $Q_p(w) = \int_0^w qp dx$ are the minority (electron) and majority (hole) charges within the membrane. Dividing the charges $Q_n(w)$ and $Q_p(w)$ by the contact’s width w and the elementary charge q yields the average carrier densities $\bar{n} = \frac{Q_n(w)}{qw}$ and $\bar{p} = \frac{Q_p(w)}{qw}$. μ_n and μ_p are the respective carrier mobilities of electrons and holes and D_p is the hole diffusivity². The difference in the pn -products at the absorber/membrane boundary $pn|_0$ and at the membrane/electrode boundary $pn|_w$ drives the electron current densities.

By rearranging equation A.7, the ratio of hole to electron current density yields a formula for the selectivity, which contains a product of two factors.

$$S_p = \frac{J_p(w)}{J_n(0)} = \frac{\mu_p \cdot \bar{p}}{\mu_n \cdot \bar{n}} \cdot \left(1 + \frac{qD_n}{w\bar{p}} \cdot \frac{[pn|_0 - pn|_w]}{J_n(0)} \right) \quad (\text{A.8})$$

The first factor (blue) reflects the ratio $\frac{\bar{\sigma}_p}{\bar{\sigma}_n}$ of the average conductivities $\bar{\sigma}_p = q\mu_p\bar{p}$ for holes and $\bar{\sigma}_n = q\mu_n\bar{n}$ for electron. The ratio of conductivities depends on the state of operation of the solar cell via the carrier densities. The second factor (red) contains a ratio of the difference of the pn products versus the minority carrier current density $J_n(w)$, where of the ratio of the numerator and denominator goes to a value of -1 if the ratio of average conductivities $\frac{\bar{\sigma}_p}{\bar{\sigma}_n}$ goes to infinity. The second factor vanishes in this case, which ensures that equation 5.11 is fulfilled at OC.

The generalized charge control model provides an advantage over several different approaches because also uniform recombination in the membrane can be included easily. The original derivation of Borrego *et al.* includes this aspect, which modifies the red part of equation A.8 such that an additional term is added.

A.3.3. Equivalent circuit model for a contact selectivity-limited solar cell

Comment to the following investigations: The following investigation on the equivalent circuit models is motivated by fact that model A yielded unexpected results (at least for the

²Mobilities and diffusivities are assumed to be position-independent in reference [424], thus constants.

author of this thesis), when used to calculate the desired parameters at maximum power point and open-circuit conditions. The model A is used by several authors [124, 153] and is brought into question herein. However, it shouldn't be concluded that model A is wrong and model B is correct. To make a proper decision, it needs more investigations. In a private communication with A. L. Onno for example, Onno pointed out that the definition and calculation of iV_{OC} could be the reason for the surprising results. The author spend a lot of time to play around with and to think about both models and any alternative model. Finally, the author came to the conclusion that it is beyond the scope of this thesis and might be a topic of future research. Next, I thought about to removed the content completely from the thesis, but decided to keep it in the appendix for two reasons. First, the content motivates to think about the validity of the models and provides a starting point for further investigations. Second, I was surprised by the good agreement of model B with my expectations and Brendel's maximum efficiency calculation and don't want to hide this fact. Therefore, all investigation using the equivalent circuits moved into the appendix.

Anyway, the reader who prefers model A should not feel offended in any way, but rather invited to revisit the models. Therefore, I offer to collaborate on this particular subject in order to find an adequate answer to the questions raised, to which I have not found satisfactory answers on my own. An electrical equivalent circuit model represents a simplification to

the complex physical behavior of a solar cell and allows to calculate the current-voltage characteristic of the solar cell. The single diode model, which assumes ideal contacts, is the simplest representation and contains a Shockley recombination diode in parallel with a photo-generating current source. If non-ideal contacts are involved, like it is frequently the case for thin-film (organic, perovskite, CdTe, CIGS etc.) solar cells or Si solar cells featuring passivating contacts, then the J - V characteristic under illumination exhibits a characteristic S-shape deformation and the simple single diode model fails to describe the solar cell's J - V [477].

In the context of recent literature on the definition of selectivity, Onno *et al.* provided an intuitive equivalent circuit model based on a partial resistance framework [124] (see section 4.1.1) and Rau and Kirchartz [153] proposed a similar model with partial diodes instead of partial resistances based on the selectivity definition of Weber *et al.* [119] and Roe *et al.* [123]. Figure A.5a depicts the equivalent circuit model (A) with an ideal electron-selective contact and a non-ideal hole-selective contact added to the single diode model, as proposed by Rau and Kirchartz [153]. In this model, a bulk diode with a saturation current density $J_{0,B}$ is connected in parallel to the current source with a photo-generation current density J_{Ph} and the diodes with equilibrium exchange current density $J_{0,m}$ and $J_{0,M}$ represent the minority and majority carrier transfer processes at the hole contact, respectively. If the band diagram of the solar cell is overlaid with model A, as it is done by Onno *et al.* [124], then it suggest to be an intuitive description of a solar cell with selectivity-limited contacts³. However, the validity of model A is brought into question in the following and the alternative model B in figure A.6b is investigated as the simplest representation for a selectivity-limited solar cell,

³This was the motivation to use model A first.

A.3. SUPPLEMENTARY MATERIAL FOR CHAPTER ON SELECTIVITY AND EXTRACTION EFFICIENCY

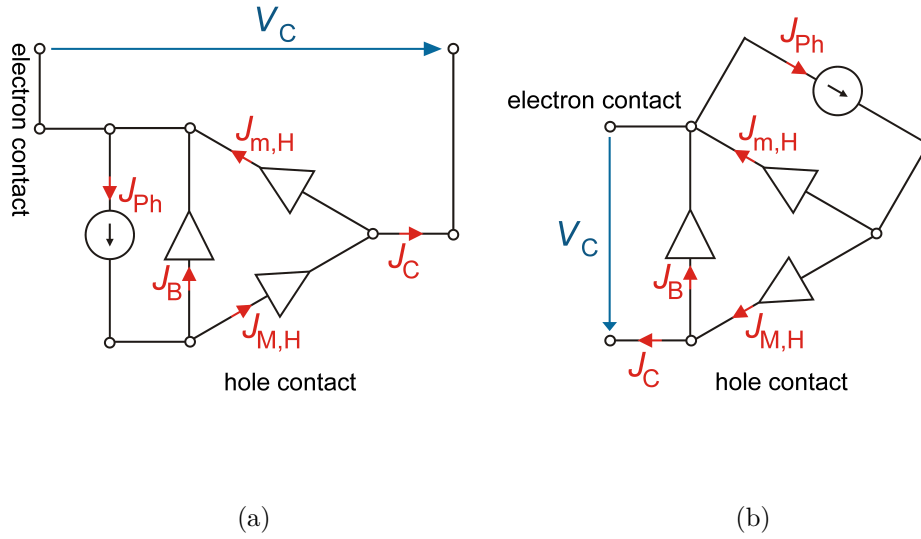


Figure A.5.: Equivalent circuit model of a solar cell with an ideal electron-selective contact and a non-ideal hole-selective contact as proposed (a) in reference [153] and (b) in this thesis and Mazhari [478]

which corresponds to Mazhari’s model⁴ for organic solar cells [478–480]. In contrast to model A, the bulk diode and the minority carrier diode are interchanged in model B, which is a significant change of the model and of the underlying physics with regard to the selectivity discussion. Moreover, if the hole- and electron-selective contacts become non-ideal, model A and model B deviate considerably. Since the purpose of the equivalent circuit model is to properly approximate the experimental behavior of a solar cell, the coincidence of the model prediction with the experiment judges about the validity of the model. However, also the interpretation of the physics of the model are essential. The Si solar cell with passivating a-Si/c-Si heterojunction contacts is a well documented examples of a selectivity-limited solar cell [126, 348, 481] and the behavior of three unique experiments can be predicted by a dc equivalent circuit model [481, 482]: the S-shape deformed light J - V characteristic, the dark J - V and the Suns- V_{OC} characteristic. Especially, the latter provides an appropriate benchmark for an equivalent circuit model of a contact selectivity-limited solar cell. The Suns- V_{OC} characteristic for a solar cell with a $J_{0,B} = 2.23 \cdot 10^{-15} \text{ A/cm}^2$ for the bulk recombination and a contact with an almost perfect passivation with $J_{0,m} = 2.23 \cdot 10^{-25} \text{ A/cm}^2$ is calculated with model A and model B for different equilibrium selectivity values $\log_{10}(S_0) = \log_{10}(\frac{J_{0,M}}{J_{0,m}})$ between 9 and 15 by using LTspice XVII⁵ [483]. At one sun condition a J_{ph} of 44 mA/cm^2 is assumed.

⁴In fact, Mazhari’s model does not correlate the two diodes with recombination at the contacts and in the bulk. Mazhari denotes one of the diodes to the dark diode and the other diode to the recombination diode.

⁵Suns-(i) V_{OC} simulations are performed at a global temperature of $40 \text{ }^\circ\text{C}$ and the saturation current densities of the diodes are defined at a local temperate of $25 \text{ }^\circ\text{C}$. Since the discussion of Suns-(i) V_{OC} data is of qualitative manner, the conclusions made about model A and B maintain their validity independent of the simulation temperature.

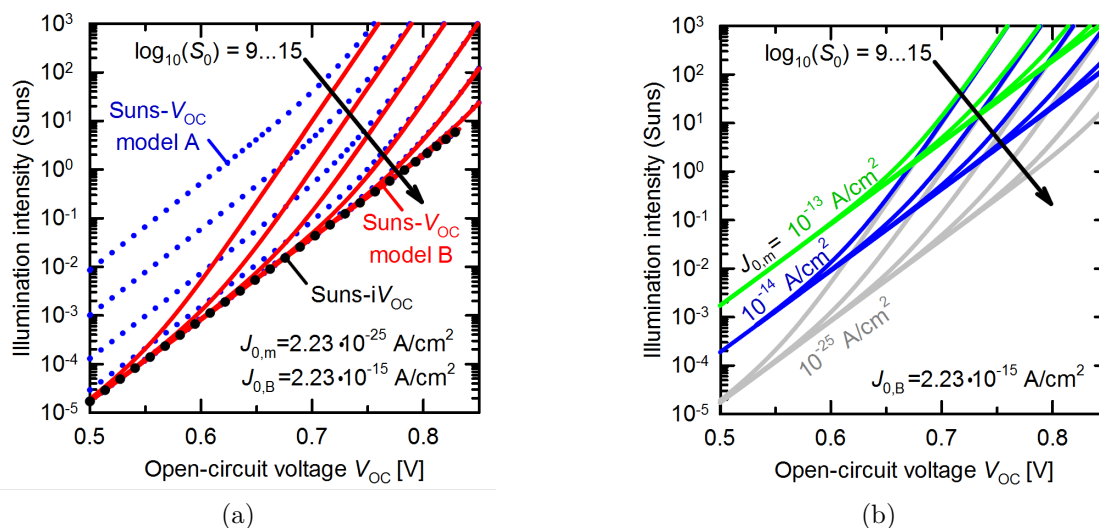


Figure A.6.: (a) Comparison of calculated Suns- V_{OC} characteristics of model A and B for $\log_{10}(S_0)$ between 9 and 15. (b) Influence of the minority carrier equilibrium exchange current density on the calculated Suns- V_{OC} characteristic of model B.

The Suns- iV_{OC} characteristic is calculated by replacing the majority carrier diode by a wire in the model, which implies that model A is equivalent to model B and that the S_0 value is infinite. Figure A.6a compares the calculated characteristics of model A and model B. As expected, the Suns- iV_{OC} characteristics (black dotted line) of both models coincide. The Suns- V_{OC} curve of model A (blue dotted line) at low illumination intensities shifts parallel away from the Suns- iV_{OC} curve towards higher illumination intensities with decreasing S_0 , which reflects a higher effective saturation current density and indicates that a degraded majority carrier transport at the contact enhances recombination in the cell⁶.

The predicted Suns- V_{OC} characteristics of model B (red solid line) on the other hand matches the Suns- iV_{OC} at low intensities for all S_0 values and deviates from it at higher intensities. The lower the selectivity is, the lower is the onset voltage, where iV_{OC} and V_{OC} start to deviate from each other and the voltage loss $\Delta V_{OC} = iV_{OC} - V_{OC}$ increases with increasing intensity.

From experiments in the literature, it is expected that the Suns- V_{OC} matches the Suns- iV_{OC} at low illumination intensities, as observed for model B, and that a voltage difference evolves at high illumination intensities due to an insufficient selectivity of the contact [122, 346–348]. In this regard, Model A as used herein and the with the used input parameters does not meet the expectations from the experimental behavior qualitatively. In contrast to that, the predictions of model B are qualitatively in good agreement with the expectations from experimental observation [348, Figure 6.1 and 6.2] and suggests that model B describes a

⁶It was found that this is due to the fact that $J_{0,m} = 2.23 \cdot 10^{-25} \text{ A/cm}^2$ and $J_{0,M} < J_{0,B}$ for $\log_{10}(S_0) = 9$ for example. The effect becomes smaller for larger $J_{0,m}$.

A.3. SUPPLEMENTARY MATERIAL FOR CHAPTER ON SELECTIVITY AND EXTRACTION EFFICIENCY

contact selectivity-limited solar cells in good approximation⁷. Figure A.6b provides further insights on the influence of the minority carrier exchange current density $J_{0,m}$ on the Suns- V_{OC} characteristic. An increasing $J_{0,m}$ represents an enhanced minority carrier recombination at the contact, which adds to the total effective saturation current density of the cell, and shifts the Suns- iV_{OC} characteristic upwards. At low illumination conditions, the Suns- V_{OC} follows the Suns- iV_{OC} again and the V_{OC} is dominated by the recombination, rather than the selectivity. This part of the characteristic identifies the recombination-dominated or iV_{OC} -limited regime for the given selectivity values. At high intensities, Suns- V_{OC} deviate from Suns- iV_{OC} and the selectivity-limited regimes shows up, where the Suns- V_{OC} curves with the same S_0 values converge independently from the recombination parameters chosen here.

A.3.4. Relationship between power conversion efficiency and selectivity

Finally, the good qualitative agreement with the expectations encourages to use model B for the calculation of the extraction efficiency and the power conversion efficiency from the S-shape deformed light J - V characteristics. For this purpose, a solar cell on a $2\Omega\text{cm}$ n -type doped $110\mu\text{m}$ -thick wafer with Lambertian light trapping with a photo-current density of 43.47 mA/cm^2 [28] is assumed, which is similar to that used by Brendel *et al.* [127]. In the case of perfect contacts, the J - V characteristic is governed by radiative recombination and Auger-recombination within the wafer bulk. The J - V characteristic of such a solar cell is determined following Schäfer and Brendel [28] and was kindly provided by S. Schäfer. In the framework of an equivalent circuit model, two parallel diodes with an ideality factor of unity for the radiative recombination and $2/3$ for Auger-recombination represent the intrinsic recombination within the bulk and the recombination pre-factors (saturation current densities) of the diodes are determined to $1.33 \cdot 10^{-15}\text{ A/cm}^2$ for radiative recombination and $3.27 \cdot 10^{-21}\text{ A/cm}^2$ for Auger-recombination by calibrating the diode model with the J - V characteristic provided by S. Schäfer.

In order to keep the model simple for the first part of the discussion, Auger-recombination is turned off to allow the solar cell's characteristic to follow an ideality of unity over the entire voltage range. Figure A.7a depicts the light J - V characteristic and highlights the MPP and OC operation points for a radiative recombination-limited and perfectly passivated solar cell, which was calculated by means of model B with $J_{0,B}$ of $1.33 \cdot 10^{-15}\text{ A/cm}^2$, $J_{0,m}$ of $5 \cdot 10^{-25}\text{ A/cm}^2$ and $\log_{10}(S_0)$ between 1 and 17. As long as $\log_{10}(S_0)$ is larger than 14, the J - V characteristics are almost identical to that of a solar cell with a perfectly selective contact and the solar cell is not limited by selectivity in this case. The resulting implied J - V characteristic reveals an $iV_{OC} = V_{OC}(S_0 \rightarrow \infty)$ of 799.6 mV , $iV_{MPP} = V_{MPP}(S_0 \rightarrow \infty)$ of 713.2 mV , $iJ_{MPP} = J_{MPP}(S_0 \rightarrow \infty)$ of 41.97 mA/cm^2 and a power conversion efficiency $i\eta = \eta(S_0 \rightarrow \infty)$ of 29.9% . For lower selectivity values, $V_{OC}(S_0)$, $V_{MPP}(S_0)$ and $\eta(S_0)$ decrease rapidly, while the decrease in $J_{MPP}(S_0)$ is moderate down to a $\log_{10}(S_0)$ value of about 5.

⁷It should be noted that model B is also inaccurate, if the solar cell is biased beyond OC conditions or the illumination is turned off. In this case, the only path for the current is through the bulk diode and the recombination at the contact becomes invisible. For model A, the bulk diode becomes invisible and the current has to flow through the minority carrier diode.

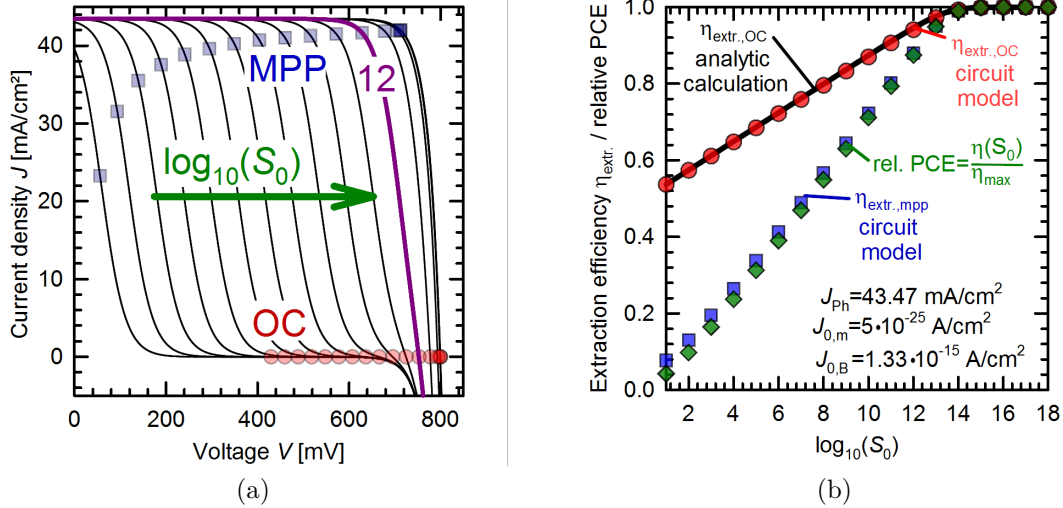


Figure A.7.: (a) Current-voltage characteristic calculated from model B for $\log_{10}(S_0)$ values between 1 and 17. Red circles and blue squares indicate the point of operation at MPP and OC. (b) Carrier extraction efficiency $\eta_{\text{extract.},\text{OC}}$ at OC and $\eta_{\text{extract.},\text{MPP}}$ at MPP, and the normalized power conversion efficiency is obtained from J - V data in figure A.7a.

Furthermore, the J - V curves become s-shape deformed for $\log_{10}(S_0)$ values below 12 (purple J - V curve in A.7a).

To find the relationship between the extraction efficiency at MPP and OC, the extraction efficiency at MPP and OC is calculated for each J - V characteristic with a particular selectivity by normalizing the voltage $V_{\text{MPP}}(S_0)$ at MPP and $V_{\text{OC}}(S_0)$ at OC by the implied voltage iV_{MPP} and iV_{OC} , respectively, of a solar cell with a perfectly selective contact. Figure A.7b quantifies the observed behavior of $V_{\text{OC}}(S_0)$ and $V_{\text{MPP}}(S_0)$ from figure A.7a in terms of the extraction efficiency at MPP and OC. For $\log_{10}(S_0)$ above 14, the extraction efficiency at MPP and OC approaches unity, shows a linear decrease with decreasing $\log_{10}(S_0)$ values below 12 and finally reaches $\eta_{\text{extract.},\text{MPP}} \approx 0$ and $\eta_{\text{extract.},\text{OC}} \approx 0.5$ for $S_0 = 1$. Since the extraction efficiency at MPP and OC as function of $\log_{10}(S_0)$ represents lines running from unity to zero and from unity and 0.5, respectively, the relation has to obey the following simple linear law:

$$\eta_{\text{extract.},\text{MPP}} \approx 2 \cdot \eta_{\text{extract.},\text{OC}} - 1 \quad (\text{A.9})$$

Indeed, figure A.8a confirms this relationship for a perfectly passivating contact ($J_{0,m} = 5 \cdot 10^{-25} \text{ A/cm}^2$). However, if $J_{0,m} > J_{0,B}$, then the contact dominates the total recombination current density and limits the internal voltage iV_{OC} below the bulk-limited $iV_{\text{OC,bulk}}$. The

A.3. SUPPLEMENTARY MATERIAL FOR CHAPTER ON SELECTIVITY AND EXTRACTION EFFICIENCY

ratio of the internal voltages defines the passivation efficiency of the contact

$$\eta_{\text{pass.}} = \frac{iV_{\text{OC}}}{iV_{\text{OC,bulk}}} = \frac{\ln\left(\frac{J_{\text{SC}}}{J_{0,\text{B}}+J_{0,\text{m}}} + 1\right)}{\ln\left(\frac{J_{\text{SC}}}{J_{0,\text{B}}} + 1\right)}. \quad (\text{A.10})$$

For the case of $\eta_{\text{pass.}} < 1$, the relationship between the extraction efficiency at OC and MPP becomes non-linear for high and low values, but shows a linear regime in-between. The lines (purple diamonds, blue triangles, green squares) in figure A.8a exhibit the same slope of approximately 2 as for the perfectly passivating contact, but shift towards the left upper corner. The linear law reads as

$$\eta_{\text{extract.,MPP}} \approx 2 \cdot \eta_{\text{extract.,OC}} - \frac{1}{\eta_{\text{pass.}}}. \quad (\text{A.11})$$

In addition to the equivalent circuit model calculation in figure A.7b, the extraction efficiency at OC is calculated by means of the (exact) analytic relationship between selectivity and extraction efficiency, as derived in section 5.4 from equation 5.15 and 5.8, and the iV_{OC} from the circuit model simulation⁸. The point-by-point deviation of the extraction efficiency between the analytic and equivalent circuit model prediction is below 0.5%_{rel.}. This excellent agreement on the one hand underlines the validity of model B and on the other hand promotes to use the analytic solution and its approximations (equation 5.30 and 5.31) to calculate the extraction efficiency.

The impact of the extraction efficiency and selectivity on the performance of the solar cell is investigated by comparing the extraction efficiency and the relative power conversion efficiency (PCE), which is determined by normalizing the PCE $\eta(S_0)$ by the implied PCE $i\eta$. The normalized PCE in A.7b follows the extraction efficiency at MPP over the entire selectivity range, because the voltage loss at MPP dictates the loss in PCE. This fact is also highlighted by equation A.12, where the normalized PCE calculates by multiplying the passivation efficiency⁹ with the extraction efficiency at MPP and with the normalized current density $\frac{J_{\text{MPP}}(S_0)}{iJ_{\text{MPP}}}$. Since the current density at MPP decreases much slower than the voltage with decreasing selectivity, the normalized current density exhibits values between 0.90 and unity down to $\log_{10}(S_0)$ values of 4. The normalized PCE is therefore approximately equal to the extraction efficiency $\eta_{\text{extract.,MPP}}$ multiplied with the selectivity-independent passivation efficiency, which is unity for a perfectly passivating contact.

$$\frac{\eta(S_0)}{i\eta} = \frac{V_{\text{MPP}}(S_0) \cdot J_{\text{MPP}}(S_0)}{iV_{\text{MPP,bulk}} \cdot iJ_{\text{MPP}}} = \eta_{\text{pass.}} \cdot \eta_{\text{extract.,MPP}} \cdot \frac{J_{\text{MPP}}(S_0)}{iJ_{\text{MPP}}} \approx \eta_{\text{pass.}} \cdot \eta_{\text{extract.,MPP}} \quad (\text{A.12})$$

Equation A.12 provides an important link between the extraction efficiency at MPP and the contact-limited PCE $\eta(S_0)$. The analytic relationships from section 5.4 together with equation

⁸Instead of the iV_{OC} from the simulation, one can also calculate iV_{OC} according to Shockley's diode theory. Then, the $iV_{\text{OC}} = \frac{k_B T}{q} \ln\left(\frac{J_{\text{SC}}}{J_{0,\text{B}}+J_{0,\text{m}}} + 1\right)$ and results in an almost identical value for the iV_{OC} of 799.5 mV.

⁹Note that it is assumed that the passivation efficiency at OC is equal to that at MPP. In fact, the values at MPP and OC deviate less than 4% for the investigate $J_{0,\text{m}}$ value up to $5 \cdot 10^{-11}$ A/cm² or a passivation efficiency of about 0.66

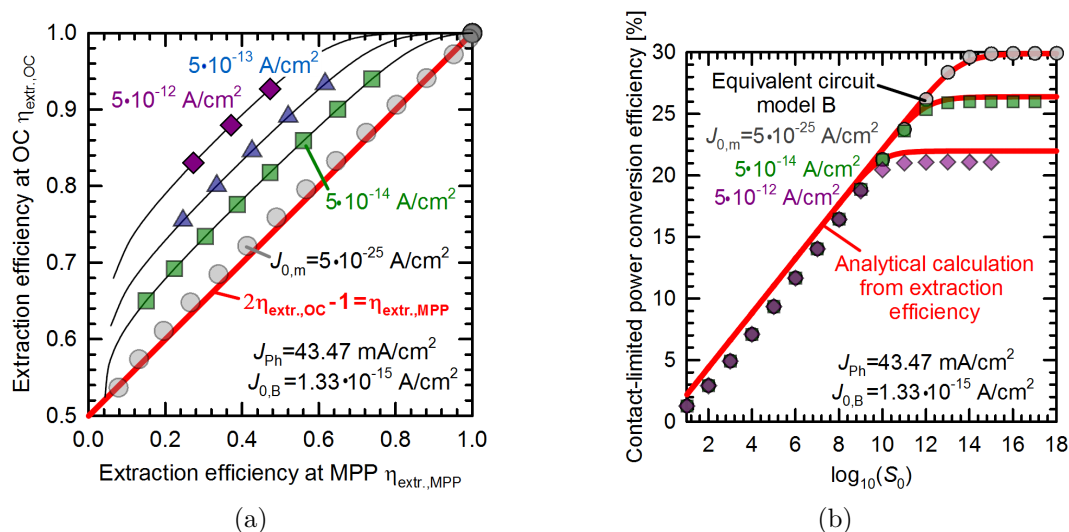


Figure A.8.: (a) Relationship between carrier extraction efficiency at OC and at MPP for minority carrier exchange current densities $J_{0,m}$ between $5 \cdot 10^{-25} \text{ A/cm}^2$ and $5 \cdot 10^{-12} \text{ A/cm}^2$. (b) Contact-limited PCE $\eta(S_0)$ for $J_{0,m}$ of $5 \cdot 10^{-25}$, $5 \cdot 10^{-14}$ and $5 \cdot 10^{-12} \text{ A/cm}^2$ calculated from model B and analytic equations.

A.9/A.11 allow to calculate the extraction efficiency at OC and MPP for any selectivity value and to study the contact-limited PCE $\eta(S_0)$.

Figure A.8b shows the power conversion efficiency as a function of the selectivity for passivation efficiencies ($J_{0,m}$ values) between about 0.7 ($J_{0,m} = 5 \cdot 10^{-12} \text{ A/cm}^2$) and unity ($J_{0,m} = 5 \cdot 10^{-25} \text{ A/cm}^2$). A solar cell with a passivation efficiency of unity (grey circles) approaches an extraction efficiency of unity for $\log_{10}(S_0)$ above 14. In this case, the solar cell is neither limited by the contact's passivation nor by carrier extraction and yields the bulk-limited efficiency $i\eta$ of 29.9%. This type of contact refers to a perfectly passivating and carrier-selective contact and yields the maximum PCE for a given absorber material. If $J_{0,m}$ increases above $J_{0,B}$ and the extraction efficiency remains close to unity ($\log_{10}(S_0) > 14$), then the passivation efficiency drops below unity and the PCE is limited to $i\eta \cdot \eta_{\text{pass}}$ by the contact's recombination (green squares and purple diamonds). In addition to the limitation from the passivation, a decreasing selectivity leads to a decrease of the carrier extraction efficiency below unity and reduces the PCE of the solar cell. The $\eta(S_0)$ curves for different passivation efficiencies in figure A.8b even converge to a single one for $\log_{10}(S_0) < 9$ for the chosen examples. The limitation from the extraction efficiency starts to outweigh the passivation efficiency and thus the selectivity confines the PCE independent of the passivation efficiency.

Beside the evaluation by means of the equivalent circuit model, it is also possible to calculate $\eta(S_0)$ analytically from equations A.12, A.10, A.9, 5.15, 5.8 and with $i\eta$ and $iV_{\text{OC,bulk}}$ from Shockley's diode theory [408, equation 20] and Green's approximation for the fill factor [91, equation 4]. By using the approximation in equation 5.31 for the linear selectivity-limited

A.3. SUPPLEMENTARY MATERIAL FOR CHAPTER ON SELECTIVITY AND EXTRACTION EFFICIENCY

regime, one obtains an explicit formula¹⁰ to calculate $\eta_{\text{linear}}(S_0)$ as follows.

$$\eta_{\text{linear}}(S_0) = \frac{i\eta}{iV_{\text{OC,bulk}}} \cdot \frac{k_B T}{q} \cdot \ln S_0 = \frac{i\eta}{iV_{\text{OC,bulk}}} \cdot \frac{k_B T}{q} \cdot \ln(10) \cdot \log_{10}(S_0) \quad (\text{A.13})$$

For the passivation-limited regime the efficiency saturates to

$$\eta_{\text{sat.}} = i\eta \cdot \eta_{\text{pass.}} \quad (\text{A.14})$$

The superposition of both approximations yields an explicit equation for $\eta(S_0)$ for the whole range of selectivities and passivation efficiencies as follows¹¹.

$$\eta(S_0) = \left(\left(\frac{1}{\eta_{\text{linear}}(S_0)} \right)^v + \left(\frac{1}{\eta_{\text{sat.}}} \right)^v \right)^{1/v} \quad (\text{A.15})$$

The exponent v controls how sudden the transition between both approximations occurs and a value of roughly 20 is found to give a reasonable agreement with model B for the transition region. The analytically calculated $\eta(S_0)$ from equation A.15 (red solid lines) reproduce the values of model B to a good degree of accuracy. The deviation of $\eta(S_0)$ values is below 4%_{rel.} for the passivation-limited part and below 10%_{rel.} for the selectivity-limited part. The deviation is identified to be due to the approximations made in equation A.12 regarding the currents and in A.9 regarding the slope and intercept values.

A.3.5. Maximum power conversion efficiency for a contact-limited solar cell

Finally, the question regarding the interrelation between the maximum possible efficiency and the selectivity is addressed. Figure A.8b and equation A.12/A.15 suggest, that one straight forward approach to obtain the maximum PCE for each selectivity value is to maximize the passivation efficiency to unity. For this case, it is concluded from equation A.12 that the maximum PCE is directly proportional to the extraction efficiency at MPP. For normalized PCEs $\frac{\eta(S_0)}{i\eta}$ below unity, also a combination of passivation efficiency below unity and extraction efficiency below unity can be found.

For a quantitative comparison with Brendel *et al.* [120, 127], the maximum PCE in figure A.9a is extracted from model B with a passivation efficiency of unity and with Auger-recombination turned on. Furthermore, the maximum PCE for a contact-limited solar cells for an absorber material with a band gap similar to methylammonium lead iodide (MAPI) perovskite is calculated. The analytic solutions for the Si and MAPI solar cells result from equation A.15 with $iV_{\text{OC,bulk}}$ and $i\eta$ from model B. Figure A.9a depicts the maximum PCE for contact-limited Si and MAPI solar cells. The assumed Si and MAPI solar cells approach the Auger-limited

¹⁰Passivation efficiency is assumed to be unity for this approximation. However, the formula also predicts $\eta(S_0)$, if passivation efficiency is not unity, since for the selectivity-limited regime $\eta(S_0)$ for the non-perfectly passivated contacts yields the same $\eta(S_0)$ as with a passivation efficiency of unity.

¹¹A similar approach was used in Brendel *et al.* [127]. Note that it is also possible to calculate $\eta(S_0)$ without this approximation, but without it no explicit formula is accessible.

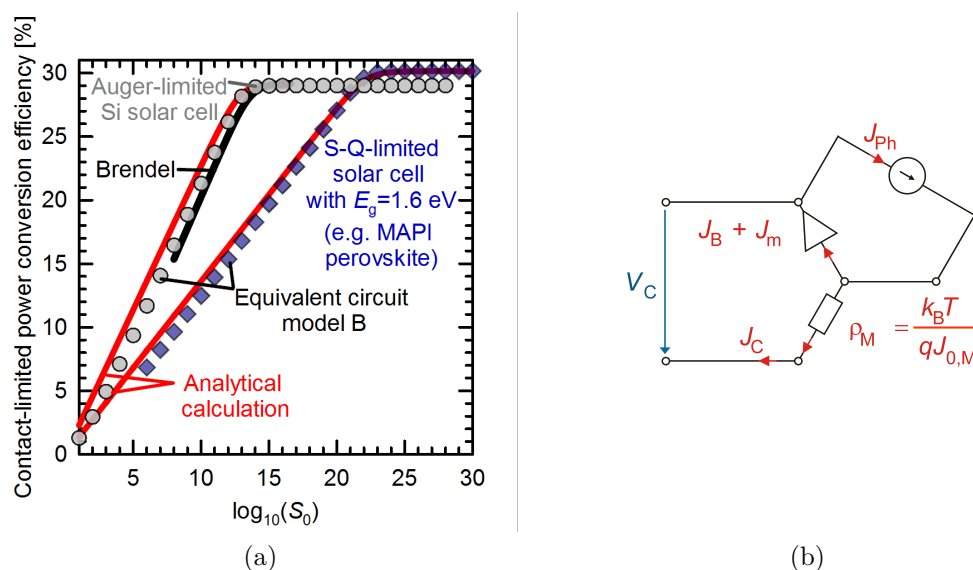


Figure A.9.: (a) The maximum PCE of a contact-limited solar cell with a Si absorber (grey circles) and an absorber with a band gap E_g of 1.6 eV (blue diamonds). Comparison of the maximum PCE of a Si solar cell from model B (grey circles), analytical calculations (red solid line) and Brendel *et al.* [127, equation 16] (black solid line). (b) Equivalent circuit model C as used by Brendel *et al.* to calculate the maximum PCE.

efficiency of 29% and the Shockley-Queisser-limiting efficiency¹² of 30.2%, respectively, for a perfectly selective and passivating contact. This is nearly the case for a $\log_{10}(S_0)$ value of 13-14 for Si and 22-23 for MAPI. As pointed out in section 5.4, the selectivity has to be larger for MAPI compared to Si to achieve a carrier extraction efficiency close to unity due to the higher implied open-circuit voltage of 1.31 V for MAPI compared to 0.755 V for Si. The equilibrium exchange current density for the minority carriers $J_{0,m}$ has to decrease to allow an increase of the internal voltage, but the equilibrium exchange current density for majority carriers $J_{0,M}$ has to stay the same to support the extraction of photo-generated carriers. This makes contacting of wide band gap absorbers more challenging and often leads to non-ohmic majority carrier transport and S-shape deformation of the J - V characteristic. The comparison of the maximum PCE for the Si solar cell according to Brendel's calculation, model B and the analytic solution reveals a good agreement. In contrast to model B, Brendel *et al.* utilize equivalent circuit model C in figure A.9b, where minority carrier transport is represented by a diode recombination pre-factor $J_{0,m} = J_{0,C} \cdot f_C$ and the majority carrier transport by a series resistance $\rho_M = \rho_C / f_C$. The areal fraction of the selective contact f_c scales the local contact properties $J_{0,C}$ and ρ_C and manipulates the global solar cell characteristic, but the selectivity remains constant for a given set of $J_{0,C}$ and ρ_C . Brendel *et al.* optimized the areal fraction and found a maximum efficiency for each selectivity value (figure A.9a). Down to a

¹²It is assumed that the recombination in the cell exhibits an ideality of unity, which is typically not the case for methylammonium lead iodide perovskites.

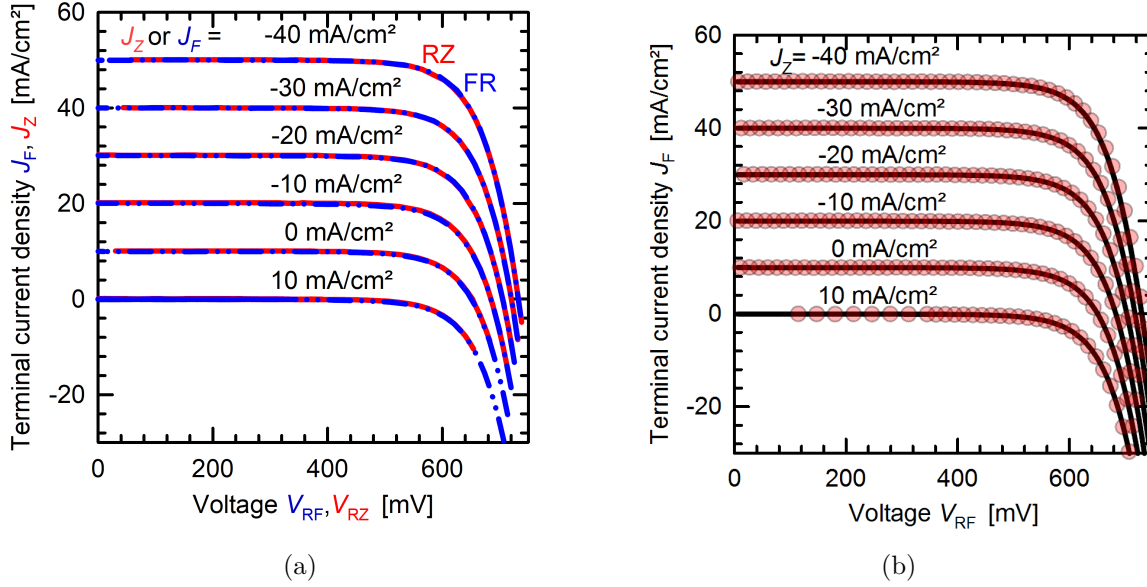


Figure A.10.: (a) Comparison of measured J_F - V_{RF} (blue dash-dotted line) characteristic for different J_Z and J_Z - V_{RZ} (red solid line) characteristic for different J_F . (b) Comparison of measured (red circles) and calculated (solid lines) J_F - V_{RF} characteristic for different J_Z .

$\log_{10}(S_0)$ value of about 14, $\rho_M < 200 \text{ m}\Omega\text{cm}^2$ and $J_{0,m}$ is below the saturation current density of the bulk. The contact hardly affects the efficiency and the efficiency is limited by the bulk. For $\log_{10}(S_0)$ values below 14, the optimized ρ_M increases with decreasing selectivity and saturates at about $670 \text{ m}\Omega\text{cm}^2$ below $\log_{10}(S_0)$ of 11-12. The recombination pre-factor $J_{0,m}$ decreases with decreasing selectivity down to $\log_{10}(S_0)$ of 11-12 and then decreases even stronger to compensate the saturation of ρ_M .

A.4. Supplementary for the section on unijunction bottom cells

A.4.1. Model parameters for 2T-operated 3T cell

In figure 8.5, it was shown that the J_F - V_{RF} (with $J_Z = 0 \text{ mA/cm}^2$) and J_Z - V_{RZ} (with $J_Z = 0 \text{ mA/cm}^2$) characteristics of the 2T-operated unijunction 3T IBC cell match each other almost perfectly. This was attributed to similar series resistances $R_S + R_i$ of the RZ and FR circuit due to similar R_Z and R_F values. According to the model in figure 8.11a with the assumption that $R_Z \approx R_F$, J_F - V_{RF} and J_Z - V_{RZ} characteristics should also match for other current density pairs J_Z and J_F . The J_F - V_{RF} and J_Z - V_{RZ} characteristics shown in figure A.10a exactly match each other and confirm this prediction. It is thus not important for a unijunction 3T-IBC bottom cell at which terminal the current density is fixed and at which

Table A.3.: J - V data and the corresponding 2T diode fit parameter for a 4 cm^2 2T-IBC reference cell measured with the LOANA system at standard test conditions and for a 2T-operated 1 cm^2 3T-IBC bottom cell measured at the Süss probe station at non-standard test conditions.

parameter	2T-IBC reference cell	3T cell light
J_{SC} [mA/cm^2]	30	10
V_{OC} [mV]	710	651
FF [%]	81.5	74.3
P [mW/cm^2]	17.36	4.84
J_{Ph} [mA/cm^2]	30	10
$J_{0,\text{D1}}$ [fA/cm^2]	26	20.8
$J_{0,\text{D2}}$ [nA/cm^2]	2.6	25
R_{SH} [$\text{k}\Omega\text{cm}^2$]	300	24
$R_{\text{S}} + R_{\text{i}}$ [$\text{m}\Omega\text{cm}^2$]	560	580

one it is swept. Therefore, the RZ and the FR circuit can be used equivalently to calibrate the inner part of the equivalent circuit model in figure 8.11 (between node 1 and 2).

The $J_{\text{F}}-V_{\text{RF}}$ characteristic with $J_{\text{Z}}=0\text{ mA}/\text{cm}^2$ calibrates the inner diode model by fitting the characteristic with a two-terminal two-diode model. The series resistance is assumed to be the sum of R_{S} and R_{F} , and can only be distinguished by using the 3T model. Table A.3 summarizes the J - V data and the extracted diode parameters for the 3T bottom cell under illumination and for a 4 cm^2 2T-IBC reference cell, which was measured under standard test conditions. The agreement of diode parameters of the reference cell and the 3T-IBC cell proves the extracted parameters to be physically meaningful and comparable to STC measurements. The reduced V_{OC} and FF of the 3T bottom cell compared with the reference cell result from the lower illumination level and a higher $J_{0,\text{D2}}$ value. The higher $J_{0,\text{D2}}$ -type recombination is caused by a higher local ideality factor most likely due to an incomplete removal of the parasitic poly-Si pn junction (see section 7.2).

By using the diode parameters and the 3T diode model, the $J_{\text{F}}-V_{\text{RF}}$ characteristic for $J_{\text{Z}}=0\text{ mA}/\text{cm}^2$ is calculated (figure A.10b). The calculation matches the experimental data well (normalized root mean square deviation is 0.6%), since the data was used to determine the fit parameters. The resistance R_{i} is equal to R_{F} in the lumped series resistance $R_{\text{S}} + R_{\text{i}}$. Since $J_{\text{Z}}=0\text{ mA}/\text{cm}^2$, R_{Z} has no effect on the characteristic and is neglected.

Model parameters for 3T-operated 3T cell

If J_{Z} is non-zero, the 3T model requires proper values for R_{F} and R_{Z} in order to match the measured characteristic. In the following R_{F} and R_{Z} are determined from the the observed voltage difference $V_{\text{ZF}} = V_{\text{RZ}} - V_{\text{RF}}$ and the parabolic-shaped $P_{3\text{T},\text{mpp},\text{total}}$.

The measured $J_{\text{F}}-V_{\text{RF}}$ characteristic (as shown in figure A.10b) for J_{Z} between $-40\text{ mA}/\text{cm}^2$ and $20\text{ mA}/\text{cm}^2$ is used to calculate the maximum power point from the total 3T power

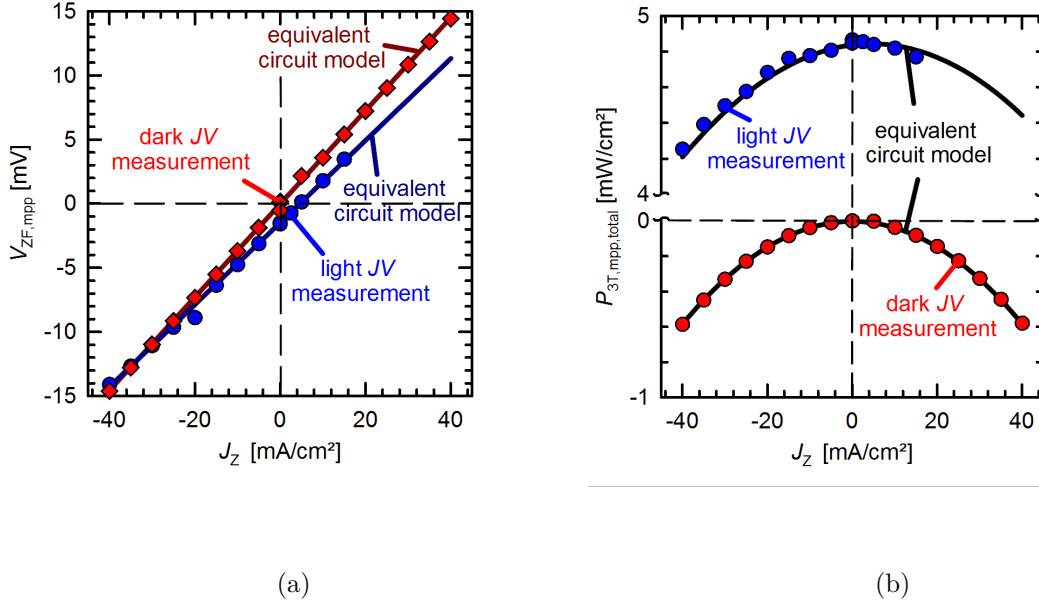


Figure A.11.: (a) Measured and simulated voltage difference between rear majority carrier contact Z and front majority carrier contact F at the maximum total power point. (b) The measured and simulated maximum total power density extracted from the unijunction 3T-IBC bottom cell as a function of J_Z for the illuminated (blue) and dark (red) 3T-IBC bottom cell.

density according to equation 1. The voltage between the rear and front base contact differs by $V_{ZF,mpc} = V_{RZ,mpc} - V_{RF,mpc}$ at maximum power point. The measured voltage difference $V_{ZF,mpc}$ and the corresponding power density $P_{3T,mpc,total}$ at the 3T maximum power point is shown in figure A.11.

The voltage difference $V_{ZF,mpc}$ depends linearly on the current density J_Z . In the framework of the 3T equivalent circuit model, V_{ZF} can be represented as the difference of the voltage drops across the resistances R_F and R_Z , which is caused by the current flow of the corresponding current densities J_F and J_Z through the resistor:

$$V_{ZF} = R_Z \cdot J_Z - R_F \cdot J_F = (R_Z + R_F) \cdot J_Z - R_F \cdot J_R \quad (\text{A.16})$$

When expressed in terms of J_Z and J_R only, $V_{ZF}(J_Z)$ is a linear function. The sum of the resistances R_Z and R_F determines the slope and the intercept with the vertical axis is the voltage drop across R_F , which is caused by the flow of J_R through the resistor.

At maximum power point operation, $J_{R,mpc}$ is approximately independent¹³ of J_Z in the investigated regime and equals the current density of the 2T-operated bottom cell of 9.2 mA/cm² for the light J - V data set. A linear regression analysis of $V_{ZF,mpc}(J_Z)$ from light J - V reveals a positive slope of 322.5 ± 4.6 m Ω cm² and an intercept point with the vertical axis

¹³In fact, the current density $J_{R,mpc}$ depends weakly on J_Z through the dependence of the cell voltage V_C on J_Z in equation 8.2 and 8.4.

of $V_{ZF,mpp}(J_Z = 0) = -1.52 \pm 0.09$ mV. The resistance values for R_F and R_Z amount to 165 ± 1 m Ω cm² and 157 ± 5.6 m Ω cm², respectively.

For the equipotential case of the two majority carrier contacts Z and F, the current densities $J_{Z,EP}$ and $J_{F,EP}$ are such that the voltage drops across R_Z and R_F compensate each other, which implies $V_{ZF,mpp}(J_{Z,EP}) = 0$ mV. Equation A.16 can be rearranged to yield equation A.17, which predicts a current density $J_{Z,EP}$ of 4.71 ± 0.35 mA/cm².

$$J_{Z,EP} = \frac{R_F}{R_F + R_Z} \cdot J_{R,mpp} \quad (\text{A.17})$$

Figure A.11a also shows data derived from dark J - V characteristics. Since no power is generated in dark, the maximum power point manifests as the point of minimum power loss and occurs at $J_{R,mpp} \approx 0$ mA/cm². All the data points for the dark case in figure A.11a are derived under this condition. The data reveals a slope of 363 ± 1.6 m Ω cm² and the straight line passes through the origin.

Since $J_{R,mpp} \approx 0$ mA/cm², equation A.16 and A.17 cannot be used to distinguish between R_Z and R_F in a dark measurement. However, using the dark J - V curves of the 2T-operated 3T IBC cell from figure A.10a at high voltages and the method described in reference [484], $R_S + R_F$ is determined to 422 ± 2.0 m Ω cm² and $R_S + R_Z$ to 415 ± 2.4 m Ω cm². With the condition $R_F + R_Z = 363 \pm 1.6$ m Ω cm², the system of linear equations is solved to obtain R_F of 185 ± 8.0 m Ω cm² and R_Z of 178 ± 8.3 m Ω cm².

The resistances R_Z and R_F do not only induce a voltage difference between contacts, but also dissipate electrical power into heat according to the Joule-Lenz law. The total 3T maximum power, which includes the power dissipation at the resistances, is calculated using equation 8.1, 8.3, 8.4 to be

$$P_{3T,mpp,total} = J_{R,mpp} \cdot V_{D,mpp} - R_S \cdot J_{R,mpp}^2 - R_Z \cdot J_{Z,mpp}^2 - R_F \cdot J_{F,mpp}^2 \quad (\text{A.18})$$

Rearranging equation A.18 and representing as function of $J_Z = J_{Z,mpp}$ and $J_{R,mpp}$ only, leaves us with a second order polynomial of J_Z .

$$P_{3T,mpp,total} = -(R_F + R_Z) \cdot J_Z^2 + 2R_Z \cdot J_{R,mpp} \cdot J_Z + J_{R,mpp} \cdot V_{D,mpp} - (R_S + R_F) \cdot J_{R,mpp}^2 \quad (\text{A.19})$$

Figure A.11b shows the resulting $P_{3T,mpp,total}$ for the light and dark measurement. The parabolic behavior of the measured data is consistent with equation A.19. The curvature of the parabola is specified by the coefficient of the quadratic term of J_Z , namely the sum of the resistances R_Z and R_F . Equation A.19 enables us to calculate R_Z and R_F in a second independent manner. Independent from the previous discussion of the voltage difference $V_{ZF,mpp}$, the resistances R_Z and R_F are determined by using a second order polynomial fit to the measured data of $P_{3T,mpp,total}$. The sum of R_Z and R_F amounts to 340 ± 16 m Ω cm² and 364 ± 0.8 m Ω cm² for the light and the dark measurement, respectively. This is in good agreement with the values obtained from the analysis of the voltage difference $V_{ZF,mpp}$ within the error margin of the fits. The good agreement underlines that the observed the voltage difference $V_{ZF,mpp}$ and the power loss originate from the resistors and validates the 3T model.

A.4. SUPPLEMENTARY FOR THE SECTION ON UNIJUNCTION BOTTOM CELLS

The J_Z value of the vertex point of the parabola, where power density is maximized, can be calculated from the vertex form equation of A.19 by using the coefficients of the quadratic and linear terms of J_Z in equation A.19.

$$J_{Z,3TP_{\max}} = -\frac{1}{2} \cdot \frac{2R_F \cdot J_{R,mp}}{-(R_F + R_Z)} = \frac{R_F}{R_F + R_Z} \cdot J_{R,mp} = J_{Z,EP} \quad (\text{A.20})$$

Equation A.20, which describes the operation point, where power is maximized, is identical to equation A.17, which determines the equipotential between the two majority carrier contacts Z and F. Consequently, the power output is maximized for the equipotential case. Since $V_{ZF,mp} = 0$ mV for the equipotential case, R_Z and R_F are in parallel and the majority carrier current divides across the two resistors according to the current divider rule. The current flows along the path of least resistance and minimizes the resistive power loss.

Warren *et al.* previously used TCAD simulations of a 3T bottom cell to show that the power is maximized for the equipotential case and that excess current flow between the two majority carrier contacts through the absorber can lead to power dissipation within the cell [318]. The 3T circuit model presented in this thesis refines this understanding to show that the current flow through resistors is responsible for the voltage drop and power loss.

An accurate determination of the current density $J_{Z,3TP_{\max}} = J_{Z,EP}$ from the light measurement data in figure A.11b is difficult, since the positive branch in figure A.11b provides limited data points with scattering around the vertex point. However, $J_{Z,3TP_{\max}}$ amounts to 1.8 ± 0.75 mA/cm², which is lower than 4.71 ± 0.35 mA/cm² as predicted from the analysis of $V_{ZF,mp}$. If the same analysis of $V_{ZF,mp}$ and $P_{3T,mp,total}$ is applied to the light J_Z - V_{RZ} measurement data in figure 8.6a, a good agreement between both analysis procedures is obtained: $R_Z + R_F = 335 \pm 1.7$ mΩcm² and $J_{F,EP} = 4.33 \pm 0.1$ mA/cm² from $V_{ZF,mp}$ and $R_Z + R_F = 359 \pm 30$ mΩcm² and $J_{F,EP} = 4.29 \pm 1.2$ mA/cm² from $P_{3T,mp,total}$. Since the equipotential operation point for RZ and FR operation is the same, the sum of the current densities $J_{F,EP} + J_{Z,EP}$ has to be equal to $J_{R,mp} = 9.2$ mA/cm², which is in good agreement to the determined sum of 9.04 ± 0.45 mA/cm² from the analysis of $V_{ZF,mp}$ of both data sets. All resistance values along with the equipotential current densities are summarized in table A.4. Finally, the determined values for the resistances R_Z and R_F and the diode parameters from table A.3 are used to calculate the J_F - V_{RF} characteristic, the voltage difference $V_{ZF,mp}$ and the power density $P_{3T,mp,total}$ for J_F between -40 mA/cm² and 40 mA/cm². Since the determined R_Z and R_F are nearly equal within the error margin for the light measurement, $R_Z = R_F = 160$ mΩcm² is chosen for the calculation under illumination. For the calculation of the dark scenario, $R_Z + R_F = 363$ mΩcm² and a finite $J_{Ph} = 10^{-9}$ mA/cm² is used. The calculated and experimentally determined J_F - V_{RF} characteristics in figure A.10b are in good agreement and thus the model can predict the power density $P_{3T,mp,total}$ (figure A.11b) and voltage difference between the front and rear majority carrier contacts $V_{ZF,mp}$ (figure A.11a) for the illuminated and dark bottom cell scenario.

A.4.2. Distributed series resistance in a unijunction 3T bottom cell

It is now interesting to discuss the origin and physical meaning of R_Z and R_F . Naturally, majority carrier transport resistances, which are distributed within the bottom cell, are

A.4. SUPPLEMENTARY FOR THE SECTION ON UNIJUNCTION BOTTOM CELLS

Table A.4.: Summary of the determined resistance values for R_Z and R_F for the dark and light measurements and the equipotential current density for the light measurement with $J_{R,mp\ddot{p}} = 9.2 \text{ mA/cm}^2$. Values are determined analyzing either $V_{ZF,mp\ddot{p}}$ or $P_{3T,mp\ddot{p},total}$. $J_{Z,EP}$ and the corresponding R_Z and R_F designated by an asterisk are uncertain values due to limited data points.

analyzed quantity		<i>FR</i>		<i>RZ</i>	
		$V_{ZF,mp\ddot{p}}$	$P_{3T,mp\ddot{p},total}$	$V_{ZF,mp\ddot{p}}$	$P_{3T,mp\ddot{p},total}$
dark	R_Z [$\text{m}\Omega\text{cm}^2$]	178 ± 8.3	178 ± 7.5	-	-
	R_F [$\text{m}\Omega\text{cm}^2$]	185 ± 8.0	186 ± 7.2	-	-
	$R_Z + R_Z$ [$\text{m}\Omega\text{cm}^2$]	363 ± 1.6	364 ± 0.8	-	-
light	R_Z [$\text{m}\Omega\text{cm}^2$]	157 ± 5.6	$273 \pm 42.5^*$	158 ± 3.1	167 ± 42.2
	R_F [$\text{m}\Omega\text{cm}^2$]	165 ± 1.0	$66 \pm 26.2^*$	177 ± 4.8	192 ± 72.2
	$R_Z + R_Z$ [$\text{m}\Omega\text{cm}^2$]	322.5 ± 4.6	340 ± 16.3	335 ± 1.7	359 ± 30.4
	$J_{Z,EP}$ [mA/cm^2]	4.71 ± 0.35	$(1.8 \pm 0.75)^*$	-	-
	$J_{F,EP}$ [mA/cm^2]	-	-	4.33 ± 0.1	4.29 ± 1.3

considered as the origin.

The lumped resistance value for the majority carrier transport is found by solving Poissons equation for the given geometries and sheet conductivities of the bottom cell by means of a finite element analysis implemented in the software QuickField [485]. Figure A.12 shows the cross-section of the sample and the corresponding simulated current density vector field for a bottom without photo-generation in the wafer and the n^+ poly-Si layer at the front side. The majority carriers (electrons in this case) are injected at the rear n^+ contact Z in to the n -type base. They flow from the metal grid at the rear side, through the metal/poly-Si and the poly-Si/c-Si wafer interface into the wafer. In the wafer, the electron current spreads horizontally (laterally) into the wafer and flows vertically towards the poly-Si layer at the front side. The lateral redistribution of electrons leads to a laterally roughly homogeneous current density vector field at the poly-Si/c-Si wafer interface at the front side. Electrons pass the poly-Si/c-Si wafer interface and flow mostly horizontal through the thin and highly conductive poly-Si layer towards the metal contact, where they have to cross the poly-Si/metal interface to be collected in the metal grid at the front side.

The majority carriers suffer a transport resistance on their way from the rear contact to the front contact at each interface (metal/poly-Si or poly-Si/c-Si), in the metal grids and lateral and vertical transport resistance in the wafer and poly-Si layer. The QuickField simulation in figure A.12 calculates the lateral and vertical transport, but excludes any contact resistances or metal grid resistances. The latter is estimated by using analytic approximations for the metal grid [486, equation 24], the contact resistances [486, equation 20] and the contact resistivity values from section 6.3. The sum of grid and contact resistances amounts to about $15 \text{ m}\Omega\text{cm}^2$. The QuickField simulation predicts a lumped resistance of $355 \text{ m}\Omega\text{cm}^2$ due to lateral and vertical majority carrier transport within the wafer and poly-Si layer on the front

A.4. SUPPLEMENTARY FOR THE SECTION ON UNIJUNCTION BOTTOM CELLS

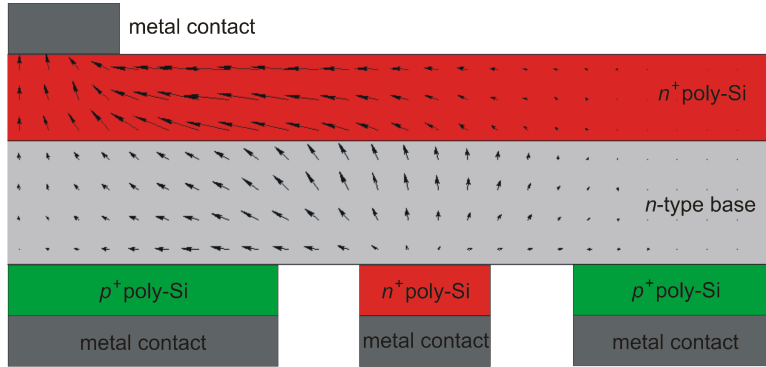


Figure A.12.: Schematic cross-section of the unijunction 3T bottom cell under investigation with the corresponding current-density vector field for majority carriers within the base and the poly-Si front contact. The poly-Si layer is artificially thickened, while the sheet resistance is kept constant, in the DC conduction calculation in QuickField [485] for visualization purposes.

side. The good agreement of the simulated series resistance (including grid and contact resistance) of $370 \text{ m}\Omega\text{cm}^2$ with the determined sum of R_Z and R_F values of about $360 \text{ m}\Omega\text{cm}^2$, suggests that R_Z and R_F originate from the distributed series resistance.

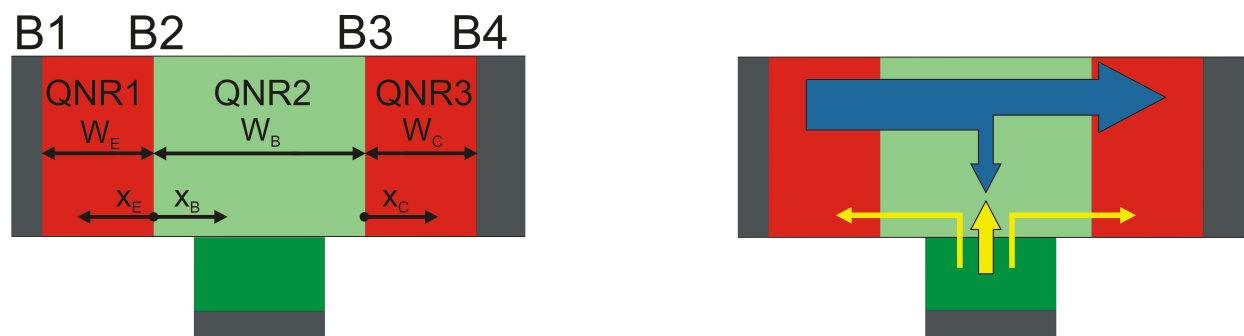
The form of the current vector field in the n^+ poly-Si layer at the front side is similar to that of an emitter in a both-side contacted cell and the lateral transport resistance is governed by the geometry of the front side grid. According to Wyeth [378, equation 21], the sheet resistance component of the resistance can be estimated to $191 \text{ m}\Omega\text{cm}^2$. The form of the vector field in the n -type base can be roughly represented by means of the superposition of a lateral and vertical current flow. The lateral resistance in the base is mainly due to the geometry of the rear side grid and amounts to $165 \text{ m}\Omega\text{cm}^2$. In conclusion, the lateral resistance within the poly-Si layer at the front side, which is determined by the front side geometry, has about the same value as R_F and the lateral resistance within the wafer, which reflects the rear side geometry, has approximately the same value as R_Z . Therefore, R_F correlates with the sum of all resistances at the front side and R_Z to those at the rear side. From this considerations, one can specify design rules for a unijunction 3T bottom cells in different operation modes. For the ideal case, $R_Z = R_F = 0$ and requires at least an infinitely large conductivity within the wafer. This is not achievable for a real device and the voltage difference $V_{ZF, \text{mpp}}$ between the two majority carrier contacts accompanied by the parabolic shape of $P_{3T, \text{mpp}, \text{total}}$ is an inherent property of unijunction 3T-IBC cells. However, for several scenarios e.g. small grid dimensions¹⁴ and large base conductivity¹⁵, the ideal case is approached.

¹⁴E.g. if the pitch approaches the wafer thickness.

¹⁵If grid dimensions are small, then the current flow becomes approximately single dimensional and the resistance can be approximately calculated by multiplying the wafer thickness with the specific wafer resistance. For a $150 \mu\text{m}$ -thick wafer with a specific resistance of $1 \Omega\text{cm}$, the resistance is $15 \text{ m}\Omega\text{cm}^2$ and induces a voltage difference below 1 mV for a maximum current densities of $40 \text{ mA}/\text{cm}^2$.

A.5. Supplementary for the section on bipolar junction bottom cells

A.5.1. Derivation of Ebers-Moll model with photo-generation



Legend

 p -type c-Si base	 Hole flow
 n^+ c-Si	 Electron flow
 p^+ c-Si	
 Metal	

Figure A.13.: Drift-diffusion model for BJT cell

Start from drift-diffusion model:

1. Poisson equation in depletion approximation:

$$\frac{d^2\phi}{dx^2} = -\frac{q}{\epsilon}(N_D^+ - N_A^-) \quad (\text{A.21})$$

2. Transport equations:

$$J_n = q\mu_n nE + qD_n \frac{dn}{dx} \quad (\text{A.22})$$

and

$$J_p = q\mu_p pE - qD_p \frac{dp}{dx} \quad (\text{A.23})$$

3. Continuity equations under steady state conditions:

$$\frac{dn}{dt} = 0 = \frac{1}{q} \frac{dJ_n}{dx} - (R - G) \quad (\text{A.24})$$

and

$$\frac{dp}{dt} = 0 = -\frac{1}{q} \frac{dJ_p}{dx} - (R - G) \quad (\text{A.25})$$

A.5. SUPPLEMENTARY FOR THE SECTION ON BIPOLAR JUNCTION BOTTOM CELLS

Figure A.13 shows a one-dimensional model of a npn BJT architecture, which divides in quasi-neutral regions (QNR1, QNR2, QNR3) and depletion regions (B1, B2, B3, B4). QNR1 represents the emitter, QNR2 the base-type absorber and QNR3 the collector. The cross-sectional area of QNR1 and QNR3 is equal, thus the area of B2 and B3 is equal and current densities can be used in the drift-diffusion model. Since design rules for interdigitated back contact solar cells dictate that the rear minority carrier contact covers nearly the full area and there is no reason why the front minority carrier contact should cover only a part of the front surface area, the assumption is approximately true for IBC cells.

The drift-diffusion model is solved in each quasi-neutral region, while well-established solutions for the depletion regions are used as boundary conditions for the QNR. For the QNR, which is field free, the following equations have to be solved:

$$\frac{d^2 \Delta n}{dx^2} = \frac{(R - G)}{D_n} = (R - G) \frac{\tau_n}{L_n^2} \quad (\text{A.26})$$

and

$$\frac{d^2 \Delta p}{dx^2} = \frac{(R - G)}{D_p} = (R - G) \frac{\tau_p}{L_p^2} \quad (\text{A.27})$$

The following assumptions are made for the QNR1 and QNR3:

1. QNR1/QNR3: recombination rate is much larger than generation rate, thus generation is neglected ($G = 0$). This assumption is true for optically thin and highly doped emitter and collector layers. Furthermore low-level injection conditions are assumed and the recombination rate $R = \frac{\Delta p}{\tau_p}$
2. QNR2: for simplicity, recombination rate is assumed to be much smaller than generation rate, thus recombination is neglected. Furthermore, generation is assumed to be homogeneous ($G = \text{const}$). The case of non-homogeneous generation (e.g. exponentially decaying generation) is discussed in section A.5.2.

For the boundaries B, following assumption are applied:

1. B1/B4: surface recombination at this boundary is blinded out by assuming that the boundary is far away and all excess carriers recombine before reaching it, so that

$$\Delta p_E(x_E \rightarrow \infty) = 0 \quad (\text{A.28})$$

and

$$\Delta p_C(x_C \rightarrow \infty) = 0 \quad (\text{A.29})$$

2. B2/B3: the well-known solution for the a pn -junction under low-level injection and without recombination or generation [60] is applied here, so that

$$\Delta p_E(x_E = 0) = p_{E,0} \left[\exp \left(\frac{qV_{EB}}{k_b T} \right) - 1 \right] \quad (\text{A.30})$$

$$\Delta n_B(x_B = 0) = n_{B,0} \left[\exp\left(\frac{qV_{EB}}{k_b T}\right) - 1 \right] \quad (\text{A.31})$$

$$\Delta n_B(x_B = W_B) = n_{B,0} \left[\exp\left(\frac{qV_{CB}}{k_b T}\right) - 1 \right] \quad (\text{A.32})$$

$$\Delta p_C(x_C = 0) = p_{C,0} \left[\exp\left(\frac{qV_{CB}}{k_b T}\right) - 1 \right] \quad (\text{A.33})$$

Solving

$$\frac{d^2 \Delta p}{dx^2} = \frac{\Delta p}{L_p^2} \quad (\text{A.34})$$

for QNR1 and QNR3 with boundary conditions from equation A.28 and A.30 for QNR1 and from A.33 and A.29 for QNR3, give:

$$\Delta p_E(x_E) = p_{E,0} \left[\exp\left(\frac{qV_{EB}}{k_B T}\right) - 1 \right] \exp\left(-\frac{x_E}{L_{p,E}}\right) \quad (\text{A.35})$$

and

$$\Delta p_C(x_C) = p_{C,0} \left[\exp\left(\frac{qV_{CB}}{k_B T}\right) - 1 \right] \exp\left(-\frac{x_C}{L_{p,C}}\right) \quad (\text{A.36})$$

For QNR2 following equation has to be solved with the boundary conditions from equation A.31 and A.32:

$$\frac{d^2 \Delta n}{dx^2} = -\frac{G\tau_{n,B}}{L_{n,B}^2} \quad (\text{A.37})$$

The excess carrier density in QNR2 is:

$$\Delta n_B(x_B) = -\frac{G\tau_{n,B}}{2L_{n,B}^2}(x_B^2 - W_B x_B) + n_{B,0} \frac{x_B}{W_B} \left[\exp\left(\frac{qV_{CB}}{k_B T}\right) - 1 \right] + \left(1 - \frac{x_B}{W_B}\right) \left[\exp\left(\frac{qV_{EB}}{k_B T}\right) - 1 \right] \quad (\text{A.38})$$

The minority carrier current density J_n in the base, is obtained from the excess carrier distribution by applying transport equation.

$$J_n(x_B) = qD_{n,B} \frac{d\Delta n_B}{dx_B} = -qG \left(x_B - \frac{W_B}{2}\right) + \frac{qD_{n,B}n_{B,0}}{W_B} \left[\exp\left(\frac{qV_{CB}}{k_B T}\right) - \exp\left(\frac{qV_{EB}}{k_B T}\right) \right] \quad (\text{A.39})$$

A.5. SUPPLEMENTARY FOR THE SECTION ON BIPOLAR JUNCTION BOTTOM CELLS

To calculate the minority carrier current density in the emitter or collector region, a change of variables needs to be performed to express the carrier densities in terms of x_B . The variables x_E and x_C are related to x_B as follows:

$$x_E = -x_B - W_{EB} \quad (\text{A.40})$$

$$x_C = x_B - W_B - W_{CB} \quad (\text{A.41})$$

From change of variable the following conclusion is made:

$$J_{p,E}(x_E) = -qD_{p,E} \frac{d\Delta p_C(x_E)}{dx_E} = qD_{p,E} \frac{d\Delta p_C(-x_B - W_{EB})}{dx_B} = -J_{p,E}(x_B) \quad (\text{A.42})$$

The current density in the emitter region is:

$$J_{p,E}(x_B) = -\frac{qD_{p,E}}{L_{p,E}} p_{E,0} \left[\exp\left(\frac{qV_{EB}}{k_B T}\right) - 1 \right] \exp\left(\frac{x_B + W_{EB}}{L_{p,E}}\right) \quad (\text{A.43})$$

The current density in the collector region is:

$$\begin{aligned} J_{p,C}(x_B) &= -\frac{q}{D_{p,C}} \frac{d\Delta p_C(x_C)}{dx_C} = -\frac{q}{D_{p,C}} \frac{d\Delta p_C(x_B - W_B - W_{CB})}{dx_B} \\ &= \frac{qD_{p,C}}{L_{p,C}} p_{C,0} \left[\exp\left(\frac{qV_{CB}}{k_B T}\right) - 1 \right] \exp\left(-\frac{x_B - W_B - W_{CB}}{L_{p,C}}\right) \end{aligned} \quad (\text{A.44})$$

The total current density is the sum of hole and electron currents at the corresponding edges of the depletion region. It is assumed that no generation or recombination takes place in the depletion region. Thus, for the emitter it reads:

$$\begin{aligned} J_{total,E} &= J_{p,E}(x_B = -W_{EB}) + J_n(x_B = 0) \\ &= -\frac{qD_{p,E}}{L_{p,E}} p_{E,0} \left[\exp\left(\frac{qV_{EB}}{k_B T}\right) - 1 \right] + qG \frac{W_B}{2} + \frac{qD_{n,B}}{W_B} n_{B,0} \left[\exp\left(\frac{qV_{CB}}{k_B T}\right) - \exp\left(\frac{qV_{EB}}{k_B T}\right) \right] \end{aligned} \quad (\text{A.45})$$

Using the definition $n_{B,0} = \frac{n_i^2}{N_B}$ and $n_{E,0} = \frac{n_i^2}{N_E}$ and rearranging yields:

$$\begin{aligned} J_{total,E} &= \frac{qGW_B}{2} + \frac{qD_{n,B}n_i^2}{W_B N_B} \left[\exp\left(\frac{qV_{CB}}{k_B T}\right) - 1 \right] - \left(\frac{qD_{n,B}}{W_B N_B} + \frac{qD_{p,E}}{L_{p,E} N_E} \right) \cdot n_i^2 \cdot \left[\exp\left(\frac{qV_{EB}}{k_B T}\right) - 1 \right] \\ &= \frac{J_{ph}}{2} + \alpha_R J_{CS} \cdot \left[\exp\left(\frac{qV_{CB}}{k_B T}\right) - 1 \right] - J_{ES} \cdot \left[\exp\left(\frac{qV_{EB}}{k_B T}\right) - 1 \right] \end{aligned} \quad (\text{A.46})$$

A.5. SUPPLEMENTARY FOR THE SECTION ON BIPOLAR JUNCTION BOTTOM CELLS

Using the definition $n_{C,0} = \frac{n_i^2}{N_C}$, the total collector current is:

$$\begin{aligned}
 J_{total,C} &= J_{p,C}(x_B = W_B + W_{CB}) + J_n(x_B = W_B) \\
 &= -\frac{qGW_B}{2} + \left(\frac{qD_{n,B}}{W_B N_B} + \frac{qD_{p,C}}{L_{p,C} N_C} \right) n_i^2 \left[\exp\left(\frac{qV_{CB}}{k_B T}\right) - 1 \right] - \left(\frac{qD_{n,B}}{W_B N_B} \right) n_i^2 \left[\exp\left(\frac{qV_{EB}}{k_B T}\right) - 1 \right] \\
 &= -\frac{J_{ph}}{2} + J_{CS} \left[\exp\left(\frac{qV_{CB}}{k_B T}\right) - 1 \right] - \alpha_F J_{ES} \left[\exp\left(\frac{qV_{EB}}{k_B T}\right) - 1 \right]
 \end{aligned} \tag{A.47}$$

Note that the introduced forward and reverse current gains α_F and α_R and the emitter and collector saturation current densities J_{ES} and J_{CS} are related via reciprocity relation $J_S := \alpha_R \cdot J_{CS} = \alpha_F \cdot J_{ES}$ and J_S is the base transport coefficient. By definition, the base current is:

$$\begin{aligned}
 J_B &= J_{total,E} - J_{total,C} \\
 &= (\alpha_R - 1)J_{CS} \left[\exp\left(\frac{qV_{CB}}{k_B T}\right) - 1 \right] + (\alpha_F - 1)J_{ES} \left[\exp\left(\frac{qV_{EB}}{k_B T}\right) - 1 \right] + J_{ph}
 \end{aligned} \tag{A.48}$$

The resulting set of equations for J_E , J_C and J_B completely describes a bipolar junction solar cell and is similar to the Ebers-Moll model, but with additional photo-current generators. The result that the photocurrent can simply be added to the model without illumination is not surprising, since the superposition principle (as demonstrated for pn -junction solar cells elsewhere [408]) applies because the differential equations A.34 and A.37 are linear. If the assumption concerning homogeneous generation is relaxed, the superposition principle is still valid, but the prefactor of J_{ph} , which describes how symmetric the photocurrent is distributed across emitter and collector junction and which is governed by the inhomogeneous part of the drift-diffusion model (generation profile and recombination rate), would be Γ and $1 - \Gamma$ instead of $\frac{1}{2}$. A detailed discussion is provided in A.5.2.

Similar to Ebers-Moll model, a forward current $J_F = J_{ES} \cdot [\exp(\frac{qV_{EB}}{k_B T}) - 1]$ and reverse current $J_R = J_{CS} \cdot [\exp(\frac{qV_{CB}}{k_B T}) - 1]$ can be defined and result in the following set of equations¹⁶.

$$\begin{array}{l}
 J_E = \alpha_R \cdot J_R - J_F + \Gamma \cdot J_{ph} \\
 J_C = J_R - \alpha_F \cdot J_F - (1 - \Gamma) \cdot J_{ph} \\
 J_B = (\alpha_R - 1) \cdot J_R + (\alpha_F - 1) \cdot J_F + J_{ph}
 \end{array} \tag{A.49}$$

It is known from literature that the general form of the established Ebers-Moll model, even if derived under simplified assumptions, is able to describe experimental data quite well.

¹⁶Note that the signs are such that without illumination, J_E is negative in forward active mode and J_C is negative in reverse active mode. This is due to the fact that the model equations are derived for a npn architecture. To obtain the model equations for the pnp architecture each equation needs to be multiplied by -1 on the right hand side of the equation.

A.5. SUPPLEMENTARY FOR THE SECTION ON BIPOLAR JUNCTION BOTTOM CELLS

However, the saturation current densities and current gains are describe by a more complex expression. Since those parameters are usually determined as fit parameters to the experiment, the Ebers-Moll model covers most of the physics of a bipolar junction transistor and thus does the same for a bipolar junction solar cell.

The model equations A.49 are often reformulated as a transport model. For the transport model the following definitions are used:

1. The current density resulting from electron injected from the emitter into the base is

$$J_{EC} := \alpha_F \cdot J_F \quad (\text{A.50})$$

2. The current density resulting from electron injected from the collector into the base is

$$J_{CE} := \alpha_R \cdot J_R \quad (\text{A.51})$$

3. The transfer current density, which represents the net current flow between emitter and collector, is defined by using the reciprocity relation and definition of J_S as:

$$J_{CT} = J_{EC} - J_{CE} = \alpha_F \cdot J_F - \alpha_R \cdot J_R = J_S \cdot \left[\exp\left(\frac{qV_{EB}}{k_B T}\right) - \exp\left(\frac{qV_{CB}}{k_B T}\right) \right] \quad (\text{A.52})$$

4. The common emitter forward current gain β_F and common collector reverse current gain β_R are related to the common base forward and reverse current gain α_F and α_R as follows:

$$\begin{aligned} \beta_F &= \frac{\alpha_F}{1 - \alpha_F} \\ \beta_R &= \frac{\alpha_R}{1 - \alpha_R} \end{aligned} \quad (\text{A.53})$$

Using the definitions, the Ebers-Moll model can be rewritten and yields the Ebers-Moll transport model.

$$\begin{aligned} J_{CT} &= J_{EC} - J_{CE} = J_S \cdot \left[\exp\left(\frac{qV_{EB}}{k_B T}\right) - \exp\left(\frac{qV_{CB}}{k_B T}\right) \right] \\ J_E &= -\left(\frac{J_{EC}}{\beta_F} + J_{CT} - \Gamma \cdot J_{ph}\right) \\ J_C &= \frac{J_{CE}}{\beta_R} - J_{CT} - (1 - \Gamma) \cdot J_{ph} \\ J_B &= -\left(\frac{J_{EC}}{\beta_F} + \frac{J_{CE}}{\beta_R}\right) + J_{ph} \end{aligned} \quad (\text{A.54})$$

In order to include secondary, but important, effects like high-level injection and depletion region recombination, the transport model is extended towards the Gummel-Poon model [421]. The Gummel-Poon model for bipolar junction transistors was derived using Gummel's charge control relation [420], which links the charge distribution in the base with the junction currents and voltages and has only minor restrictions for its validity. The steady-state

Gummel-Poon model is very similar to the transport model, but the prefactor $J_{S,Ebers-Moll}$ in the transfer current density is now a voltage dependent prefactor $\frac{J_S}{q_B(V_{EB},V_{CB})}$. The voltage dependent prefactor incorporates high-level injection effect into the model and cause the current gains to be current dependent, which can qualitatively be understood through the reciprocity relation¹⁷.

$$\begin{aligned}
 J_{CT} &= J_{EC} - J_{CE} = \frac{J_S}{q_B(V_{EB},V_{CB})} \cdot [\exp(\frac{qV_{EB}}{k_B T}) - \exp(\frac{qV_{CB}}{k_B T})] \\
 J_E &= -(\frac{J_{EC}}{\beta_F} + J_{CT} - \Gamma \cdot J_{ph} + J_{EB,SCR}) \\
 J_C &= \frac{J_{CE}}{\beta_R} - J_{CT} - (1 - \Gamma) \cdot J_{ph} + J_{CB,SCR} \\
 J_B &= -(\frac{J_{EC}}{\beta_F} + \frac{J_{CE}}{\beta_R} + J_{EB,SCR} + J_{CB,SCR}) + J_{ph}
 \end{aligned} \tag{A.55}$$

A.5.2. Calculation of Γ

In the previous sections A.5.1 and 8.4.2, an equivalent circuit model for a bipolar junction bottom cell was derived from the drift-diffusion model. The model contains two diodes and each of the diodes is paralleled by constant current sources, which represent photo-generation within the absorber. However, the current density $J_{Ph,Z}$ and $J_{Ph,F}$ in equation 8.6 of each current source depends on the assumptions made for the generation profile and recombination properties of the absorber. For the simplest case, where recombination in the quasi-neutral absorber region (QNR2) is turned off and a homogeneous generation profile is assumed, $J_{Ph,Z}$ becomes equal to $J_{Ph,F}$ (equation A.47). Thus, the total photo-generated current density J_{Ph} distributes equally across the two diodes.

Typically, the total photo-generated current density J_{Ph} is used in the context of solar cell and therefore it is advantageous to use J_{Ph} in combination with the normalized photo-generation current density at the sunny-side of the solar cell $\Gamma = \frac{J_{Ph,F}}{J_{Ph}}$ instead of $J_{Ph,F}$ and $J_{Ph,Z}$. Γ can take values between zero and unity. For the simplest case of homogeneous photo-generation, Γ has a value of 0.5.

However, homogeneous photo-generation is rarely achieved for typical operation conditions of solar cells. Therefore, it is interesting to study Γ for different photo-generation conditions. For this purpose, $J_{Ph,F}$ and J_{Ph} have to be calculated for different photo-generation profiles from the drift-diffusion model.

For the following calculations, the same assumptions are made for the drift-diffusion model as in section A.5.1, but the photo-generation in equation A.37 is now an arbitrary function of x .

$$\frac{d^2 \Delta n}{dx^2} = -\frac{g(x)}{D_{n,B}} \tag{A.56}$$

$g(x)$ is the generation profile. Furthermore, homogeneous boundary conditions ($\Delta n(x_B = 0) = 0$ and $\Delta n(x_B = W) = 0$) are applied instead of equations A.31 and A.32. This reflects

¹⁷The reciprocity relation is still valid in high-level injection under certain conditions [487]

A.5. SUPPLEMENTARY FOR THE SECTION ON BIPOLAR JUNCTION BOTTOM CELLS

short-circuit conditions for both diodes ($V_{DZ} = 0$ and $V_{DF} = 0$) and simplifies the algebra significantly. The homogeneous solution of equation A.56 with $g(x) = 0$ and homogeneous boundary conditions is $\Delta n_h = 0$. Since the differential equations of the drift-diffusion model are linear and obey superposition principle, the solution Δn with $g(x) \neq 0$ is the superposition of the homogenous and inhomogenous solutions $\Delta n = \Delta n_h + \Delta n_{inh}$. Since $\Delta n_h = 0$, the general solution $\Delta n = \Delta n_{inh}$ represents the inhomogeneous solution. Thus, the photo-generation current densities can be calculated under that conditions from transport equation as follows.

$$J_{Ph,F} = J_n(x=0) = qD_n \left. \frac{d\Delta n_{inh}}{dx} \right|_{x=0} \quad (A.57)$$

The total photo-generation current density is obtained by integrating the generation profile $g(x)$ over the total thickness W of the absorber.

$$J_{Ph} = q \int_0^W g(x) dx \quad (A.58)$$

For a homogeneous (constant) generation profile $g(x) = a$ with a constant generation rate a , $J_{Ph,F} = \frac{qaW}{2}$, $J_{Ph} = qaW$ and $\Gamma = \frac{1}{2}$.

Table A.5.: Calculated Γ for different generation profiles $g(x)$. a and b are constant coefficients.

generation profile $g(x)$	Γ
a	$1/2$
$a \frac{(W-x)}{W}$	$2/3$
$a \exp(-bx)$	$\frac{1}{1-\exp(-bW)} - \frac{1}{bW}$
arbitrary $g(x)$	$1 - \frac{1}{W} \cdot \frac{\int_0^W x \cdot g(x) dx}{\int_0^W g(x) dx}$

Table A.5 summarizes two additional special examples – linearly and exponentially decaying photo-generation profiles – and an explicit formula for the calculation of Γ for arbitrary generation profiles. The latter is obtained by finding an appropriate Green's function $\mathcal{G}(x, y)$, which solves equation A.56 for arbitrary generation profiles as follows.

$$\Delta n_{inh} = -\frac{1}{D_n} \int_0^W \mathcal{G}(x, y) \cdot g(y) dy \quad (A.59)$$

The Green's function for the operator in equation A.56 with homogeneous boundary conditions is found to be the following piece-wise function.

$$\mathcal{G}(x, y) = \begin{cases} \frac{y-W}{W} \cdot x & \text{if } 0 \leq x < y \\ \frac{x-W}{W} \cdot y & \text{if } y < x \leq W \end{cases} \quad (\text{A.60})$$

If $J_{\text{Ph,F}}$ is evaluated with equation A.57 by using equations A.59 and A.60, then $J_{\text{Ph,F}}$ reads as follows.

$$\begin{aligned} J_{\text{Ph,F}} &= qD_n \left. \frac{d\Delta n_{\text{inh}}}{dx} \right|_{x=0} = -q \int_0^W \left. \frac{d}{dx} \right|_{x=0} \mathcal{G}(x, y) \cdot g(y) dy \\ &= -q \int_0^W \left. \frac{d}{dx} \right|_{x=0} \left[\frac{y-W}{W} \cdot x \cdot g(y) \right] = q \int_0^W g(y) dy - q \int_0^W \frac{y}{W} \cdot g(y) dy \end{aligned} \quad (\text{A.61})$$

From equation A.61 and A.58, the following explicit formula for Γ can be given.

$$\Gamma = 1 - \frac{1}{W} \frac{\int_0^W x \cdot g(x) dx}{\int_0^W g(x) dx} = 1 - \frac{x_c}{W} \quad (\text{A.62})$$

Equation A.62 provides an interesting interpretation of the Γ factor. The second part of the equation is a well-known expression to calculate the “x-coordinate” of the centroid or center of mass x_c of a function. The center of mass for the generation profile is $(1 - \Gamma)W$ and $(1 - \Gamma)$ defines the thickness-normalized center of mass of the generation profile. This interpretation is consistent with table A.5, where the center of mass of a homogeneous generation profile ($g(x) = a$) is at the center and that of a triangular generation profile ($g(x) = ax$) at $1/3$ of the thickness away from the sunny side. Furthermore, equation A.62 enables one to calculate Γ from tabulated data numerically by integration.

Finally, figure A.14 illustrates the generation profiles of the the three special cases from table A.5 together with the x-coordinate of the centroid x_c of each generation profile. It is evident that x_c is $1/2$ for homogeneous generation and shifts towards $x_c = 0$ the more the photo-generation is localized at $x = 0$.

A.5.3. Calculation of the maximum power point for equipotential operation of a bipolar junction bottom cell

For equipotential operation of a bipolar junction bottom cell, it is assumed that $V_{DF} = V_{DZ} = V_{EP}$ and $J_{CT} = 0$. Replacing the voltages $V_{DF} = V_{DZ} = V_{EP}$ in equation 8.7 yields

$$\begin{aligned} P_{3T,\text{total,EP}} &= P_{\text{Ph,EP}} - P_{\text{D,EP}} \\ P_{\text{Ph,EP}} &= J_{\text{Ph}} \cdot V_{EP} \\ P_{\text{D,EP}} &= V_{EP} \cdot (J_{\text{DZ,EP}} + J_{\text{DF,EP}}) \\ P_{\text{CT}} &= 0 \end{aligned} \quad (\text{A.63})$$

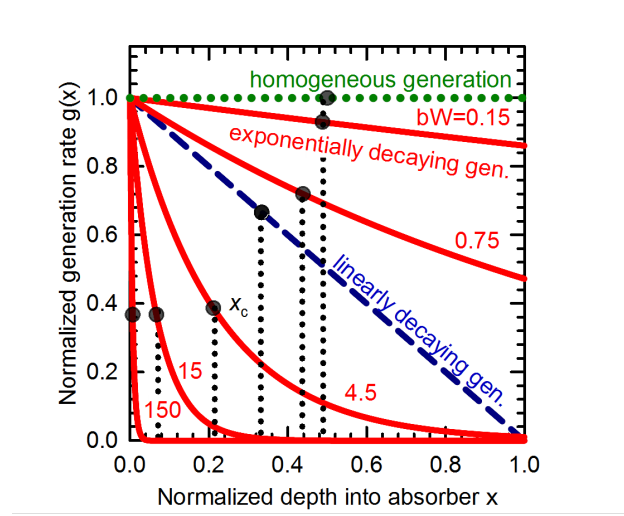


Figure A.14.: Normalized generation rate $g(x)$ as function of a normalized depth x for homogeneous (green dotted line), linearly decaying (blue dashed line) and exponentially decaying generation (red solid lines). For the exponentially decaying generation function $g(x) = \exp(-bx)$, bW is varied between 0.15 and 150. Black circles with black dotted lines indicate the x -coordinate of the centroid.

Inserting the current densities $J_{DZ,EP}$ and $J_{DF,EP}$, then $P_{3T,total,EP}$ becomes:

$$P_{3T,total,EP} = V_{EP} \cdot \left(J_{Ph} - (J_{0,DZ} + J_{0,DF}) \cdot \exp\left(\frac{qV_{EP}}{k_B T}\right) \right) \quad (A.64)$$

Note that the -1 in the diode current densities was safely neglected because it is assumed that V_{EP} is much larger than the thermal voltage $\frac{k_B T}{q}$. Next, $P_{3T,total,EP}$ is differentiated with respect to V_{EP} and the following equation is found after some algebra.

$$\frac{J_{Ph}}{J_{0,DZ} + J_{0,DF}} = \exp\left(\frac{qV_{EP,mpp}}{k_B T}\right) \cdot \left(1 + \frac{qV_{EP,mpp}}{k_B T} \right) \quad (A.65)$$

Applying the natural logarithm on both side, the equation becomes:

$$\ln \left[\frac{J_{Ph}}{J_{0,DZ} + J_{0,DF}} \right] = \ln \left[1 + \frac{qV_{EP,mpp}}{k_B T} \right] + \left(\frac{qV_{EP,mpp}}{k_B T} \right) \quad (A.66)$$

The right hand side is approximated by a 1st order Taylor series at $\frac{qV_{EP,mpp}}{k_B T} = 20$ to obtain

$$\ln \left[\frac{J_{Ph}}{J_{0,DZ} + J_{0,DF}} \right] \approx A_2 + A_1 \cdot \left(\frac{qV_{EP,mpp}}{k_B T} \right) \quad (A.67)$$

The coefficients are $A_1 = 0.955$ and $A_2 = 2$.

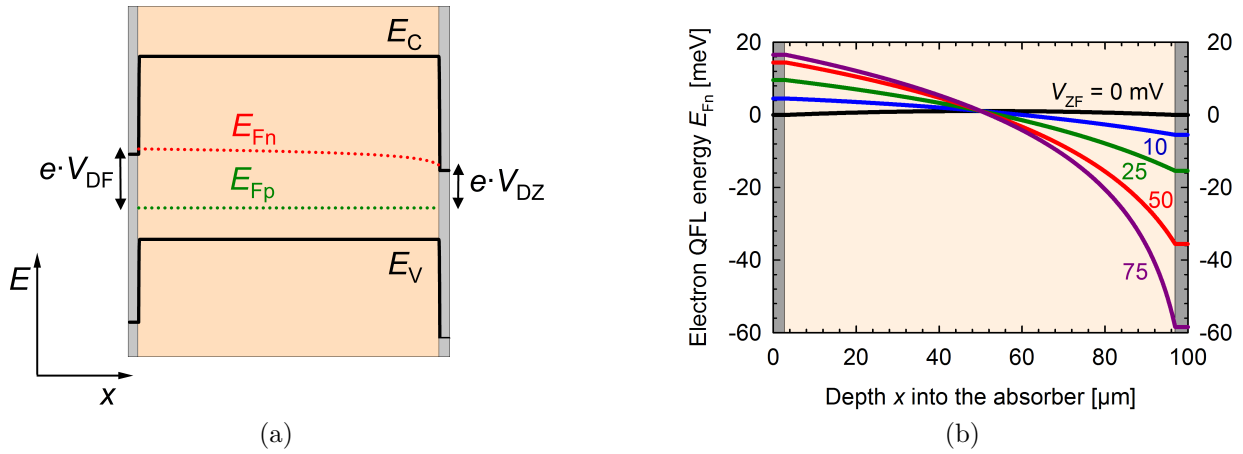


Figure A.15.: (a) The schematic band diagram of a *npn* structure as electron charge carriers find in an illuminated 3T bipolar junction bottom cell with $V_{DF} = 445$ mV and $V_{ZF} = 100$ mV, when they flow from the electron injecting front contact through a p-type absorber to the electron collecting rear contact. (b) Electron quasi-Fermi level of device in (a) under different V_{ZF} bias conditions.

A.5.4. PC1D simulation of bipolar junction bottom cell

Figure A.15a shows schematically the band diagram of an *npn* structure as found in a 3T bipolar junction bottom cell under illumination and at $V_{DF} = 445$ mV. All band diagrams were calculated using PC1D [466, 467] with similar input parameters as the cell in 8.2.2. If a voltage V_{ZF} is applied between F and Z terminal, then the electrons concentration in the absorber at the Z terminal decreased and that at the F terminal increases. This leads to a gradient in the electron quasi-Fermi level and an electron current flows from terminal F towards Z. The hole quasi-Fermi level remains flat. Figure A.15b shows how the electron quasi-Fermi level evolves upon biasing between contact Z and F. For $V_{ZF} = 0$, $V_{DF} = V_{DZ} = V_{EP}$ and the device is in equipotential operation. If V_{ZF} is increased, then the E_{Fn} is approximately linear at first up to a V_{ZF} of approximately $\frac{k_B T}{q}$ and then becomes non-linear. For the linear case $\frac{1}{2}(V_{DF} + V_{DZ}) \approx V_{EP}$.

A.5.5. Derivation equation 8.17 for the design guideline of bipolar junction bottom cells

In order to derive equation 8.17, equation 8.15 is used in the following form:

$$R_{\text{diff}} = \frac{W_B}{q \cdot \mu_{n,B} \cdot n_{B,0} \cdot \exp\left(\frac{qV_{EP,\text{mPP}}}{k_B T}\right)} \quad (\text{A.68})$$

The equilibrium minority carrier concentration $n_{B,0}$ is replaced by $n_{B,0} = \frac{n_i^2}{N_A}$. N_A can be further represented by the specific resistance ρ_B of the wafer, such that $N_A = \frac{1}{q\mu_{p,B}\rho_B}$ with the

A.5. SUPPLEMENTARY FOR THE SECTION ON BIPOLAR JUNCTION BOTTOM CELLS

(majority carrier) hole mobility $\mu_{p,B}$ in the wafer base. Inserting into equation A.68 yields

$$R_{\text{diff}} = \frac{1}{q^2 \cdot \mu_{n,B} \cdot \mu_{p,B} \cdot n_i^2} \cdot \frac{W_B}{\rho_B} \cdot \frac{1}{\exp \frac{qV_{\text{EP,mpp}}}{k_B T}} \quad (\text{A.69})$$

The ratio of the $\frac{\rho_B}{W_B}$ is the sheet resistance $R_{\text{Sheet,B}}$ of the wafer.

Next, $V_{\text{EP,mpp}}$ is replaced by equation 8.8, which is reproduced here for convenience:

$$V_{\text{DF,EP,mpp}} = V_{\text{DZ,EP,mpp}} = V_{\text{EP,mpp}} = \frac{k_B T}{q} [A_1 \cdot \ln \left(\frac{J_{\text{Ph}}}{J_{0,\text{DZ}} + J_{0,\text{DF}}} \right) - A_2] \quad (\text{A.70})$$

The diffusion resistance becomes

$$R_{\text{diff}} = \frac{1}{q^2 \cdot \mu_{n,B} \cdot \mu_{p,B} \cdot n_i^2} \cdot \frac{1}{R_{\text{Sheet,B}}} \cdot \frac{\exp(A_2)}{\left(\frac{J_{\text{Ph}}}{J_{0,\text{DZ}} + J_{0,\text{DF}}} \right)^{A_1}} \quad (\text{A.71})$$

By rearranging the quantities in the equation, one obtains:

$$R_{\text{diff}} = \frac{\exp(A_2)}{q^2 \cdot \mu_{n,B} \cdot \mu_{p,B} \cdot n_i^2} \cdot \frac{(J_{0,\text{DZ}} + J_{0,\text{DF}})^{A_1}}{R_{\text{Sheet,B}}} \cdot \frac{1}{(J_{\text{Ph}})^{A_1}} \quad (\text{A.72})$$

Since J_{Ph} corresponds to the photogeneration current density in the bottom cell, this quantity is referred to as $J_{\text{Ph,bottom}}$ in the following. Inserting the form of the diffusion resistance from equation A.72 into equation 8.16 yields equation 8.17 as follows.

$$P_{\text{CT,mpp}} \approx R_{\text{diff}} \cdot J_{\text{CT,mpp}}^2 = \frac{\exp(A_2)}{q^2 \cdot \mu_{n,B} \cdot \mu_{p,B} \cdot n_i^2} \cdot \frac{(J_{0,\text{DZ}} + J_{0,\text{DF}})^{A_1}}{R_{\text{Sheet,B}}} \cdot \frac{J_{\text{CT,mpp}}^2}{(J_{\text{Ph,bottom}})^{A_1}} \quad (\text{A.73})$$

A.5.6. Calculation of the current-mismatch loss factor χ

In order to obtain the current-mismatch loss factor χ , the following equation has to be calculated, where $\Gamma = 1$ is assumed for simplicity, $A_1 = 0.955$.

$$\chi = \frac{\left(\Gamma - \frac{(\Gamma \mp 1) \cdot J_{\text{ph,top}}}{J_{\text{max}}} \right)^2}{\left(1 - \frac{J_{\text{ph,top}}}{J_{\text{max}}} \right)^{A_1}} \quad (\text{A.74})$$

For the photogeneration current density $J_{\text{ph,top}}$ of the top cell as a function of the band gap the tabulated values for a Shockley-Queisser-limited single junction from reference [415] are used. For J_{max} the value of 44.23 mA/cm² for a band gap of 1.1 eV is used and the Si bottom cell is assumed to have this band gap of 1.1 eV for simplicity.

A.5.7. Calculation of the tandem efficiencies for a 3T tandem with a bipolar junction bottom cell

In section 8.4.2 the design guidelines for 3T tandem cell comprising bipolar junction bottom cell is discussed. For this purpose the efficiency of such a tandem cell is estimated for different design parameters. In the following the detailed calculation procedure is outlined for the estimation. It is intended to keep the calculation as simple as possible and to reduce the effort. Therefore, the following procedure provides a rough estimate rather than an accurate value, but it allows to discuss the general trends and provides the right order of magnitude for the efficiency. The tandem efficiency η is calculated as the sum of top cell efficiency η_{top} and the bottom cell efficiency η_{bottom} .

$$\eta = \eta_{\text{top}} + \eta_{\text{bottom}} \quad (\text{A.75})$$

Fortunately, Rühle [415] provides the tabulated values for Shockley-Queisser-limited single junction cell, which enables the author to perform a simple spreadsheet calculation to evaluate the tandem efficiency.

The top cell efficiency and the photogenerated current density $J_{\text{ph,top}}$ for a particular top cell band gap are taken from Rühle [415]. For a band gap of 1.8 eV, η_{top} and $J_{\text{ph,top}}$ amount to 26.86% and 19.65 mA/cm², respectively. The η_{top} and $J_{\text{ph,top}}$ for a band gap of 1.55 are spline interpolated and amount to 30.9% and 27.1 mA/cm², respectively. This is close to the values of 31% and 27.3 mA/cm² calculated in reference [416].

The efficiency of the bottom cell is estimated in two steps. First an efficiency without considering the transport losses due to minority and majority carrier transport is calculated and in a second step the losses are subtracted from the calculated efficiency. The bottom cell efficiency without transport losses is calculated as the product of the photogeneration current density $J_{\text{ph,bottom}}$, the open-circuit voltage $V_{\text{OC,bottom}}$ and the fill factor $\text{FF}_{\text{bottom}}$, divided by the incident power density of 1000 W/m².

$$\eta_{\text{bottom,no loss}} = \frac{J_{\text{ph,bottom}} \cdot V_{\text{OC,bottom}} \cdot \text{FF}_{\text{bottom}}}{P_{\text{in}}} \quad (\text{A.76})$$

In the following it is assumed that all photon with an energy larger than the assumed optical band gap of 1.1 eV for the bottom cell are either absorbed by the top or the bottom cell, such that $J_{\text{ph,bottom}} + J_{\text{ph,top}} = J_{\text{max}}$. Therefore, the photogenerated current density is calculated as $J_{\text{ph,bottom}} = J_{\text{max}} - J_{\text{ph,top}}$. This implies that the optical coupling between top and bottom cell is perfect. Furthermore, parasitic absorption or reflection are absent and luminescence coupling effects are neglected. A single-junction cell with a band gap of 1.1 eV generates a photo-generation current density of 44.23 mA/cm² [415] and is used for J_{max} . For the bottom cell with a top cell of 1.55 eV and 1.8 eV, $J_{\text{ph,bottom}}$ amounts to 17.1 mA/cm² and 24.6 mA/cm², respectively.

Next, the open-circuit voltage $V_{\text{OC,bottom}}$ is estimated from a single-diode model with an ideality of unity according to equation 2.29. The sum of the diode saturation current densities $J_{0,\text{DZ}} + J_{0,\text{DF}}$ and $J_{\text{ph,bottom}}$ are used as input parameter for equation 2.29. The reader might ask why equation 2.29 is useful for bipolar junction bottom cells. It can be shown from

A.5. SUPPLEMENTARY FOR THE SECTION ON BIPOLAR JUNCTION BOTTOM CELLS

equation 8.6 for $J_Z = J_F = 0$ that $V_{DZ,OC} \approx V_{DF,OC}$ if $J_S \gg J_{0,DZ}$ and $J_S \gg J_{0,DF}$. In this case equation 2.29 can be applied to calculate $V_{DZ,OC} \approx V_{DF,OC}$. The last quantity – the fillfactor – is obtained according to Green [91]. The validity of the latter for bipolar junction bottom cells is not clear. At least, if one of the junctions is floating e.g. the rear junction, then the bipolar junction bottom cells is a solar cell, to which Green’s formula applies and should serve as estimate for the FF here.

If $J_{ph,bottom} = J_{max}$ and $J_{0,DZ} + J_{0,DF}$ is $2.6 \cdot 10^{-16}$ A/cm² then a $V_{OC,bottom}$, a FF_{bottom} and $\eta_{bottom,no\,loss}$ of 842 mV, 86.6% and 32.27%, respectively, is calculated, which is in good agreement with the tabulated values [415]. For the same $J_{0,DZ} + J_{0,DF}$ and a top cell with a band gap of 1.8 eV, one obtains a $V_{OC,bottom}$, a FF_{bottom} and $\eta_{bottom,no\,loss}$ of 827 mV, 86.5% and 17.6%, respectively. Adding η_{top} of 26.86% to $\eta_{bottom,no\,loss}$ results in a tandem efficiency of 44.4%, which is in fair agreement with the calculated maximum efficiency of 45.3% for a tandem cell with a silicon bottom cell with a band gap of 1.12 eV and a top cell with a band gap of 1.8 eV in reference [416]. A tandem with a top cell with a band gap of 1.55 eV instead of 1.8 eV yields a calculated efficiency of 42.9% with the spreadsheet calculation compared to 43.7% from reference [416]. In summary, the agreement between the simple spreadsheet calculation and the detailed calculation in reference [416] is good enough for the discussion of design guidelines for bipolar junction bottom cells. For the design consideration from below, $\eta_{bottom,no\,loss}$ is calculated for each particular $J_{0,DZ} + J_{0,DF}$, which is assumed to be independent from $R_{Sheet,B}$ for simplicity.

The next step is to calculate the losses associated with the transport of minority and majority charge carriers. To calculate the minority carrier transport loss, equation 8.18 with the current densities from above, but with variable $J_{0,DZ} + J_{0,DF}$ and $R_{Sheet,B}$, is used. Note that equation 8.18 was derived for a single-dimensional transport from the front minority carrier contact to the rear minority carrier contact. This is approximately accurate from IBC cells with a large area fraction from the minority carrier contact.

To include majority carrier transport in the considerations, again a single dimensional transport is assumed. In contrast to the minority carrier transport, majority carrier transport occurs parallel to the wafer surface from the point of generation to the majority carrier selective contact. Moreover, it is assumed that the majority carrier contact is represented by a line without spatial extent in transport direction and a line spacing of 2 mm. The latter corresponds to a typical pitch for IBC cells, which can be fabricated with industrial equipment. The transport from the front side of the wafer to the rear side is neglected. This approximation applies to IBC cells with a pitch much larger than the wafer thickness and the lateral transport losses $P_{lateral}$ can be described as a function of $R_{Sheet,B}$, the pitch p and the photogeneration current density $J_{ph,bottom}$ according to Wyeth [378].

$$P_{lateral} = \frac{R_{Sheet,B}}{12} \cdot p^2 \cdot J_{ph,bottom}^2 \quad (A.77)$$

The total loss in power conversion efficiency $\Delta\eta_{transp}$ is calculated as follows.

$$\Delta\eta_{transp} = \frac{P_{CT,mpp} + P_{lateral}}{P_{in}} \quad (A.78)$$

Finally, $\Delta\eta_{\text{transp}}$ is subtracted from $\eta_{\text{bottom,no loss}}$ to obtain η_{bottom} and the respective tandem efficiency.

A.5.8. 3T operation of the simplified PERC-like 3T bipolar junction cell

The 3T operating modes are examined below using the bottom cell without TJ, but in the ideal case of a well-functioning TJ, no difference is expected for a bottom cell with TJ.

For this investigation, the 4 cm^2 cells are cleaved from the 156 mm-pseudo square wafers and an aluminum contact grid with a finger distance of 2 mm is deposited on the front side. The 2T current-voltage characteristic $J_{\text{F}}-V_{\text{RF}}$ and $J_{\text{Z}}-V_{\text{RZ}}$ of the FR and RZ circuits after cleaving and deposition of the front side grid in figure A.16a is recorded by using LOANA solar cell analysis system. The current-voltage characteristic of the FR circuit matches that of the RZ circuit, but the fill factor for the RZ circuit is slightly lower by 1.1%_{abs.} due to a larger series resistance of $3.88\ \Omega\text{cm}^2$ for the RZ circuit compared to $3.61\ \Omega\text{cm}^2$ for the FR circuit. If one assumes that the contribution of the majority carrier transport is comparable for both measurements, it can be concluded that the minority carriers at the rear side have a more resistive path from the cell into the contact. Under the assumption that the n^+ POLO junction as well as the metal grids contribute only a negligible part to the total resistance, either the metal/ n^+ POLO contact resistance or lateral transport through the n^+ POLO layer is responsible for the contribution to the total resistance of the FR and RZ circuits.

The contact resistance of the Al/ n^+ POLO contact at the front side was found to be below $1\ \text{m}\Omega\text{cm}^2$ in section 6 and can be neglected here. The lateral transport resistance for electrons at the front side is estimated according to Wyeth [378, equation 21] with a poly-Si sheet resistance of $50\ \Omega/\square$ to about $0.2\ \Omega\text{cm}^2$. The lateral transport resistance for electrons at the rear side can be neglected due to narrow-spaced Ag contacts. From this considerations, it can be concluded that the Ag/ n^+ POLO contact at the rear side contributes approximately $0.5\ \Omega\text{cm}^2$ to the total series resistance and the contact resistance is of the order of $30\ \text{m}\Omega\text{cm}^2$ for a contact area fraction of about 6%.

In the following, the full operation space of the 3T bottom cell is examined in the same way as described in subsection 8.2.3, but the illumination is applied to the bifacial rear side of the cell by a halogen lamp, such that a $J_{\text{Z,SC}}$ of $15.1\ \text{mA}/\text{cm}^2$ is reached. The $J_{\text{Z}}-V_{\text{RZ}}$ and $J_{\text{F}}-V_{\text{RF}}$ characteristic are recorded for fixed J_{F} values between $-10\ \text{mA}/\text{cm}^2$ and $22.5\ \text{mA}/\text{cm}^2$ and the maximum of the total 3T power is calculated for each J_{F} value. Figure A.16b summarizes the resulting total 3T power at the maximum power point of the 3T bottom cell and the corresponding powers extracted from the FR and RZ circuit for each J_{F} . Figure A.16b resembles figure 8.9b with four different modes of operation and the same qualitative discussion applies here as for figure A.16b.

The total 3T power curve $P_{3\text{T},\text{mpp},\text{total}}$ shows a maximum at an equipotential current density $J_{\text{F,EP,mpp}}$ of about $5.6\ \text{mA}/\text{cm}^2$, which is approximately located in the middle between the current-matched current density (grey dotted line) and $J_{\text{F,mpp}} = 0$. The equipotential current density $J_{\text{F,EP,mpp}}$ results from minimizing the power dissipation from current transfer through the base $P_{\text{CT,mpp}}$ and dissipation from resistances $P_{\text{res,mpp}}$. For simplicity, two simplified cases are considered, where either $P_{\text{CT,mpp}}$ or $P_{\text{res,mpp}}$ is neglected. Considering the dissipation due

A.5. SUPPLEMENTARY FOR THE SECTION ON BIPOLAR JUNCTION BOTTOM CELLS

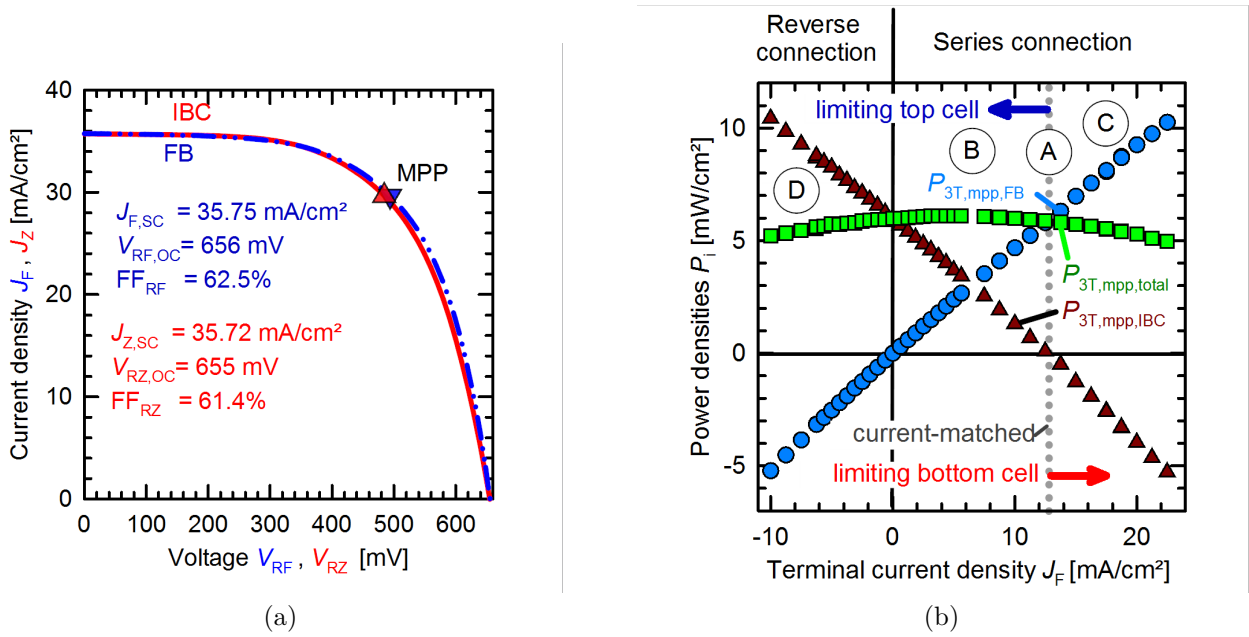


Figure A.16.: (a) Two-terminal J_Z - V_{RZ} and J_F - V_{RF} characteristic of the RZ and FR circuit of the screen printed 3T bipolar junction bottom cell with TJ as measured under one-sun illumination. (b) Power densities for J_F values between $-10 \text{ mA}/\text{cm}^2$ and $22.5 \text{ mA}/\text{cm}^2$: The total three-terminal (3T) power density $P_{3T, mpp, total}$ (green squares) and the corresponding fraction of $P_{3T, mpp, total}$ contributed by the FR circuit $P_{3T, mpp, FR}$ (blue circles) and the RZ circuit $P_{3T, mpp, RZ}$ (brown triangles). Operation modes A, B, C, D correspond to figure (a), (b), (c), (d) in figure 8.10

to the transfer current density $J_{CT,mpp}$ only, one would expect that the equipotential current density is governed by the Γ factor. Since the bottom cell is illuminated from the rear side, it is expected that $\Gamma \approx 0.2$ and the maximum of the 3T power curve should appear close to the equipotential current density $J_{F,EP,mpp} \approx 2.5 \text{ mA/cm}^2$.

In the context of the unijunction cell in section 8.4.1, where carrier transport in the base is efficient and thus dissipation due to current transfer is neglected, it was found that the equipotential current density is defined by the current divider rule (equation A.20) for finite “external” resistances. Because the series resistance for electrons on the front side is smaller ($R_F \approx 0.2 \Omega\text{cm}^2$) compared to that on the rear side ($R_Z \approx 0.5 \Omega\text{cm}^2$) of the bottom cell in figure A.16a, the current divider rule predicts an equipotential current density $J_{F,EP,mpp}$ of about 9.1 mA/cm^2 .

In summary, minimizing the dissipation due to current transfer through the base shifts $J_{F,EP,mpp}$ towards $J_{F,mpp} = 0$ and minimizing dissipation due to “external” resistances shifts $J_{F,EP,mpp}$ towards the current-matched case, where $J_{Z,mpp} = 0$. When the total power loss is minimized, both shifts compensate each other in this particular case and the $J_{F,EP,mpp}$ is approximately in the middle between $J_{F,mpp} = 0$ and $J_{F,mpp} = J_{F,2T,mpp}$ (current-matched case).

For $J_{F,mpp} \neq J_{F,EP,mpp}$, the power density decreases proportional to $(J_{F,mpp} - J_{F,EP,mpp})^2$. The factor of proportionality – the curvature of the parabola – is $3.78 \Omega\text{cm}^2$. As discussed in subsection 8.4.2, the curvature can be estimated from equation 8.15 under the assumption that the “external” resistances can be neglected. By using the measured wafer resistivity of $20 \Omega\text{cm}$ (equivalent to a doping density of $6.8 \cdot 10^{14} \text{ cm}^{-3}$), a wafer thickness of $150 \mu\text{m}$, an electron mobility of $755 \text{ cm}^2/(\text{Vs})$, a temperature of 28°C and an equipotential voltage of 474 mV in equation 8.15, a diffusion resistance of $9.8 \Omega\text{cm}^2$ is calculated. The calculated diffusion resistance of $9.8 \Omega\text{cm}^2$ overestimates the measured value of $3.78 \Omega\text{cm}^2$ by more than a factor of two. A probable reason for the difference is that the equipotential voltage of 474 mV , which is recorded at the external contacts, underestimates the internal voltage and thus the injection level within the wafer. If an equipotential voltage of 499 mV is assumed, the diffusion resistance reduces to a value of $3.77 \Omega\text{cm}^2$. Indeed, if a resistance-free two-diode model is fitted to the $J_{Z,SC}-V_{RZ,OC}$ characteristic of the 2T-LOANA measurement and a photo-generation current density of 15 mA/cm^2 is assumed, the model indicates that the internal voltage at a calculated maximum power point exceeds 500 mV and supports the speculation that the equipotential voltage is underestimated.

Finally, the diffusion resistance of $3.78 \Omega\text{cm}^2$ is relatively high due to a moderate performance (moderate equipotential voltage) of the very first batch of cells and can cause a high loss if the bottom cell is operated with large transfer current densities as it is expected for operation mode C and D. The opposite conclusion can be made for operation mode B, where the top cell is current-limiting and the transfer current densities are relatively small.

B. List of symbols

- $T_{\mathbf{H}}$ temperature of hot reservoir
- $T_{\mathbf{C}}$ temperature of cold reservoir
- ΔS entropy difference transfer from the hot to the cold reservoir
- \mathcal{W} work
- $\eta_{\mathbf{C}}$ Carnot efficiency
- P power output
- $t_{\mathbf{c}}$ time of to complete one thermodynamic cycle
- t time coordinate
- F, F_i thermodynamic force for transport i
- J, J_i flux density for transport i
- L, L_i linear transport coefficient for transport i
- $\frac{\partial s}{\partial t}$ entropy production rate
- T temperature
- $\frac{\partial q_{\text{irr}}}{\partial t}$ heat flux density due to irreversible transport
- η_{mpp} efficiency at maximum power output
- K heat conductance
- $T_{\mathbf{iH}}$ internal temperature at the hot side of reversible heat engine
- q elementary charge
- σ_n electron conductivity
- σ_p hole conductivity
- σ total conductivity
- μ_n electron mobility

D_n electron diffusivity

μ_p hole mobility

D_p hole diffusivity

n electron concentration

n_0 equilibrium electron concentration

n_n0 equilibrium electron concentration on the n -type side of the depletion region

$n_n(x_n)$ non-equilibrium electron concentration on the n -type side of the edge of the depletion region

$n_p(-x_p)$ non-equilibrium electron concentration on the p -type side of at the edge of the depletion region

n_p0 equilibrium electron concentration on the p -type side of the depletion region

Δn excess electron concentration

p hole concentration

p_0 equilibrium hole concentration

Δp excess hole concentration

n_i intrinsic carrier concentration

x spatial coordinate

x_n position of the edge of the depletion region in the n -type region

$-x_p$ position of the edge of the depletion region in the p -type region

$\rho(x)$ charge density

E_C conduction band energy

N_C effective density of state in the conduction band

E_V valence band energy

N_V effective density of state in the valence band

E_G band gap energy

E energy coordinate

$f(E)$ Fermi distribution function

$E_{\mathbf{F}}$ Fermi energy

$E_{\mathbf{FM}}^{\mathbf{A}}$ Fermi energy at the electrode A

$E_{\mathbf{FM}}^{\mathbf{B}}$ Fermi energy at the electrode B

$E_{\mathbf{Fn}}$ quasi-Fermi level energy of electrons

$E_{\mathbf{Fp}}$ quasi-Fermi level energy of holes

$\Delta\mu = E_{\mathbf{Fn}} - E_{\mathbf{Fp}}$ quasi-Fermi level splitting

$k_{\mathbf{B}}$ Boltzmann constant

$E_{\mathbf{vac}}$ vacuum energy level

$\Phi_{\mathbf{n}}$ work function potential of electrons

$\Phi_{\mathbf{p}}$ work function potential of holes

$\Phi_{\mathbf{Bi}}$ built-in potential

$\Phi_{\mathbf{Bi,EB}}$ built-in potential between emitter and base region

$\Phi_{\mathbf{Bi,BC}}$ built-in potential between collector and base region

$\phi(x)$ electrostatic potential

$\mathcal{E}(x)$ electric field

ϵ permittivity

$W_{\mathbf{B}}$ width of the base or absorber

V voltage

$J_{\mathbf{n}}$ electron current density

$J_{\mathbf{p}}$ hole current density

J total current density

$J_{\mathbf{Ph}}$ photo-generation current density

$R, R(x)$ total recombination rate

$R_{\mathbf{i,LLi}}$ recombination rate of recombination path i at low-level injection conditions

$R_{\mathbf{i,LLi,0}}$ recombination rate pre-factor of recombination path i at low-level injection conditions

$R_{\mathbf{i,HLi}}$ recombination rate of recombination path i at high-level injection conditions

$R_{i,\text{HLi},0}$ recombination rate pre-factor of recombination path i at high-level injection conditions

m, m_i ideality factor of diode or recombination path i

J_{0m} recombination pre-factor with ideality factor m

J_{01} recombination pre-factor of diode 1 with ideality factor m_1

J_{02} recombination pre-factor of diode 2 with ideality factor m_2

$G, G(x)$ total generation rate

R_S series resistance

R_{SH} shunt resistance

P_{in} incident power density

V_{mpp} voltage at maximum power point operation

V_{OC} voltage at open-circuit operation

J_{mpp} current density at maximum power point operation

J_{SC} current density at short-circuit operation

FF fill factor

pFF pseudo fill factor

η power conversion efficiency

η_{abs} absorption efficiency

$\eta_{\text{thermalization}}$ thermalization efficiency

$\eta_{\text{thermodynamic}}$ thermodynamic efficiency

$\eta_{\text{extract,OC}}$ carrier extraction efficiency at open-circuit conditions

$m(V)$ local ideality factor at voltage V

m_{OC} local ideality factor at open-circuit conditions

FF fill factor

V_{EB} voltage between emitter and base contact of a transistor

V_{BC} voltage between collector and base contact of a transistor

V_{EC} voltage between emitter and collector contact of a transistor

- $J_{\mathbf{E}}$ emitter current density of a transistor
- $J_{\mathbf{C}}$ collector current density of a transistor
- $J_{\mathbf{B}}$ base current density of a transistor
- $\beta_{\mathbf{F}}$ forward common-emitter current gain
- $\beta_{\mathbf{R}}$ reverse common-emitter current gain
- $\alpha_{\mathbf{F}}$ forward common-base current gain
- $\alpha_{\mathbf{R}}$ reverse common-base current gain
- $\alpha_{\mathbf{T}}$ base transport factor
- $\gamma_{\mathbf{E}}$ emitter injection efficiency
- $J_{\mathbf{F}}$ forward current density
- $J_{\mathbf{R}}$ reverse current density
- W sample thickness
- $\Delta\sigma$ excess conductivity
- Δn_0 initial excess carrier density
- $R_{\mathbf{eff}}$ effective recombination rate
- $\tau_{\mathbf{eff}}$ effective carrier lifetime
- $\tau_{\mathbf{Auger+rad}}$ intrinsic carrier lifetime due to Auger- and radiative recombination
- $\tau_{\mathbf{bulk}}$ carrier lifetime due to bulk SRH recombination
- $\tau_{\mathbf{surf}}$ carrier lifetime due to surface recombination
- $J_{\mathbf{rec}}$ recombination current density
- $J_{\mathbf{rec,surf}}$ surface recombination current density
- $J_{\mathbf{0s}}$ surface saturation current density
- $n_{\mathbf{s}}$ electron concentration at the surface of the semiconductor
- $p_{\mathbf{s}}$ hole concentration at the surface of the semiconductor
- $n_{\mathbf{i,s}}$ intrinsic carrier concentration at the surface of the semiconductor
- $\rho_{\mathbf{c}}$ contact resistivity

$R_{\mathbf{T}}$ total resistance in TLM measurements

$R_{\mathbf{c}}$ contact resistance in TLM measurements

$R_{\mathbf{bulk}}$ bulk transport resistance in TLM measurements

$R_{\mathbf{Sheet}}$ sheet resistance

d, d_1, d_2, \dots distance between TLM metal pads

$L_{\mathbf{T}}$ transfer length in TLM measurements

L contact width in TLM measurements

Z contact length in TLM measurements

$iV_{\mathbf{OC}}$ internal voltage at open-circuit conditions

$V_{\mathbf{OC}}$ external voltage at open-circuit conditions

$J_{\mathbf{m}}$ minority carrier current density at a contact

$J_{\mathbf{M}}$ majority carrier current density at a contact

$J_{\mathbf{c}}$ recombination pre-factor at a contact

$V_{\mathbf{T}}$ thermal voltage

$\rho_{\mathbf{m}}$ minority carrier resistance at a contact

$\rho_{\mathbf{M}}$ majority carrier resistance at a contact

$\rho_{\mathbf{n}}$ electron resistance at a contact

$\rho_{\mathbf{p}}$ hole resistance at a contact

$j_{\mathbf{n}}$ electron carrier current density at a contact

$j_{0\mathbf{n}}$ equilibrium electron exchange current density at a contact

$j_{\mathbf{p}}$ hole carrier current density at a contact

$j_{0\mathbf{p}}$ equilibrium hole exchange current density at a contact

$j_{\mathbf{total}}$ net current density at a contact

$S_{\mathbf{Brendel}}$ selectivity metric according to Brendel and Peibst

$\eta_{\mathbf{ASU}}$ selectivity metric according to Koswatta and Onno *et al.*

$S_{\mathbf{n,Weber}}$ selectivity metric for electrons according to Tan *et al.*, Weber *et al.* and Roe *et al.*

- S_{kin} selectivity as defined in this thesis
- S selectivity without recombination-generation processes in the membrane
- S_0 selectivity coefficient of a selective contact
- $\Sigma(F_M, F_m)$ operation state dependent part of selectivity of a selective contact
- S^* selectivity with recombination-generation processes in the membrane
- r_{D} rate of desired process at a contact
- r_{U} rate of undesired process at a contact
- J_{M} current density of the desired process at a contact
- J_{m} current density of the undesired processes at a contact
- J_{rg} current density of the recombination-generation processes at a contact
- w_{M} thickness of the selective membrane
- $E_{\text{FE,n}}$ chemical potential of electrons in the chemical engine of the electron contact
- $E_{\text{FE,p}}$ chemical potential of holes in the chemical engine of the electron contact
- $E_{\text{FH,n}}$ chemical potential of electrons in the chemical engine of the hole contact
- $E_{\text{FH,p}}$ chemical potential of hole in the chemical engine of the hole contact
- E_{FE} electrode potential at the electron contact
- E_{FH} electrode potential at the hole contact
- $J_{\text{E,n}}$ partial electron current density at the electron contact
- $J_{\text{E,p}}$ partial hole current density at the electron contact
- $J_{\text{H,n}}$ partial electron current density at the hole contact
- $J_{\text{H,p}}$ partial hole current density at the hole contact
- $J_{\text{tot,E}}$ net current density at the electron contact
- $J_{\text{tot,H}}$ net current density at the hole contact
- P_{E} electrical energy flux density at the electron contact
- P_{H} electrical energy flux density at the hole contact
- P_{out} total power density of solar energy converter

V_{ext} external voltage

η_{extract} carrier extraction efficiency

$\eta_{\text{extract,mpp}}$ carrier extraction efficiency at maximum power point operation

ρ_{0p} resistivity for majority carriers through the selective membrane

$\rho_{\text{electrode}}$ resistivity for majority carriers through the electrode

$\Delta V_{\text{electrode}}$ voltage drop due to a current flow through the electrode

V_{term} terminal voltage at the electrode

$\Delta V_{\text{OC,max}}$ maximum possible voltage loss at a contact

$i\eta$ implied efficiency for a solar cell with perfectly selective contacts

iJ_{MPP} implied current density at MPP for a solar cell with perfectly selective contacts

iV_{MPP} implied voltage at MPP for a solar cell with perfectly selective contacts

$\eta(S_0)$ efficiency for a solar cell with a contact selectivity coefficient S_0

$J_{\text{MPP}}(S_0)$ current density at MPP for a solar cell with a contact selectivity coefficient S_0

$V_{\text{MPP}}(S_0)$ implied voltage at MPP for a solar cell with a contact selectivity coefficient S_0

$J_{\text{C,poly}}$ recombination pre-factor for a POLO junction

$\rho_{\text{C,poly}}$ contact resistivity for a POLO junction

S_{10} logarithmic selectivity coefficient according to Brendel and Peibst

N_{D} donor concentration

N_{A} acceptor concentration

x_j spatial distance from the junction

a impurity gradient of a graded junction

W_0 space-charge width at zero-bias conditions

τ_r carrier lifetime within the depletion region

J_{Pi} current density of diode i of the parasitic junction

$J_{\text{P,0i}}$ saturation current density of diode i of the parasitic junction

$R_{\text{S,para}}$ series resistance within the parasitic junction

ξ_{PD}	areal fraction of parasitic junction with respect to the cell area
A_{PD}	area of the parasitic junction
L_{PD}	meander length of the parasitic junction
d_{PD}	height of the parasitic junction
A_{cell}	cell area
$A_{\text{para,sim}}$	simulated parasitic absorption in the anti-reflection coating
m_{rec}	ideality factor of non-ideal recombination diode
$J_{0,\text{rec}}$	saturation current density of non-ideal recombination diode
$J_{0,i}$	recombination pre-factor of the surface i
$J_{0\text{S,total}}$	recombination pre-factor of all surfaces
$\rho_{\text{c,Al/poly-Si}}$	contact resistivity of the Al/poly-Si contact
$\rho_{\text{c,poly-Si/c-Si}}$	junction resistivity of the poly-Si/c-Si junction
$A_{\text{Al/poly-Si}}$	area of the Al/poly-Si contact
$A_{\text{poly-Si/c-Si}}$	area of the poly-Si/c-Si junction
J_{F}	current density of contact terminal F
J_{R}	current density of contact terminal R
J_{Z}	current density of contact terminal Z
V_{FZ}	voltage between contact terminal F and Z
V_{RF}	voltage between contact terminal R and F
V_{RZ}	voltage between contact terminal R and Z
$P_{3\text{T,total}}$	total power density of 3T bottom cell
$P_{3\text{T,FR}}$	power density of the FR circuit of the 3T bottom cell
$P_{3\text{T,RZ}}$	power density of the RZ circuit of the 3T bottom cell
$P_{2\text{T,FR}}$	power density of the FR circuit of the 3T bottom cell operated with RZ circuit opened
$P_{2\text{T,RZ}}$	power density of the RZ circuit of the 3T bottom cell operated with FR circuit opened
$\Delta P_{3\text{T,mpp,total}}$	power density loss in a 3T bottom cell operated at MPP due to transport of charge carriers

$R_{\mathbf{F}}$ resistance corresponding to terminal F

$R_{\mathbf{Z}}$ resistance corresponding to terminal Z

$J_{\mathbf{F},3\mathbf{TPmax}}$ current density at terminal F, for which the 3T power output is maximized

$J_{\mathbf{F},\mathbf{EP}}$ equipotential current density at terminal F, for which $V_{\mathbf{ZF}} = 0$

$J_{\mathbf{CT}}$ transfer current density

$J_{\mathbf{S}}$ base transport coefficient

$V_{\mathbf{DF}}$ voltage of diode at terminal F

$V_{\mathbf{DZ}}$ voltage of diode at terminal Z

$J_{\mathbf{Ph,Z}}$ photo-generation current density at terminal Z

$J_{\mathbf{Ph,F}}$ photo-generation current density at terminal F

$J_{\mathbf{DZ}}$ diode current density at terminal Z

$J_{\mathbf{DF}}$ diode current density at terminal F

$J_{\mathbf{0,DZ}}$ saturation current density of diode at terminal Z

$J_{\mathbf{0,DF}}$ saturation current density of diode at terminal F

Γ normalized photo-current density with respect to the sunny side of the solar cell

$P_{\mathbf{Ph}}$ photo-generated power density

$P_{\mathbf{D}}$ power density dissipated as diode recombination

$P_{\mathbf{CT}}$ power density dissipated due to transfer of carrier between terminal F and Z

$V_{\mathbf{DF,EP,mpp}}$ equipotential voltage at diode DF at MPP

$V_{\mathbf{DZ,EP,mpp}}$ equipotential voltage at diode DZ at MPP

$V_{\mathbf{EP,mpp}}$ equipotential voltage at MPP

A_1, A_2 coefficients for Taylor approximation to calculate equipotential voltage at MPP

$R_{\mathbf{diff}}$ diffusion resistance of a bipolar junction bottom cell

$J_{\mathbf{ph,bottom}}$ photo-generated current density in a bipolar junction bottom cell

$J_{\mathbf{ph,top}}$ photo-generated current density in a top cell

$J_{\mathbf{max}}$ maximum photo-generated current density in the bottom cell with transparent top cell

$R_{\text{Sheet,B}}$ sheet resistance of the wafer base of the bipolar junction bottom cell

ξ current-mismatch factor

J_{T} current density at the front contact of the top cell T

V_{TR} voltage between the front contact of the top cell T and the root contact of the bottom cell

C. List of publication

C.1. Peer-reviewed journal articles

1. M. Rienäcker, B. Borkenhagen, G. Lilienkamp, W. Daum, “Tailoring Si(100) substrate surfaces for GaP growth by Ga deposition: A low-energy electron microscopy study”, *Journal of Applied Physics*, 118(5), 055701 (2015)
2. R. Peibst, U. Römer, Y. Larionova, M. Rienäcker, A. Merkle, N. Folchert, S. Reiter, M. Turcu, B. Min, J. Krügener, D. Tetzlaff, E. Bugiel, T. Wietler, R. Brendel, “Working principle of carrier selective poly-Si/c-Si junctions: Is tunnelling the whole story?”, *Solar Energy Materials & Solar Cells*, 158, 60 (2016)
3. J. Werner, A. Walter, E. Rucavado, S.-J. Moon, D. Sacchetto, M. Rienäcker, R. Peibst, R. Brendel, X. Niquille, S. De Wolf, P. Löper, M. Morales-Masis, S. Nicolay, B. Niesen and C. Ballif, “Zinc tin oxide as high-temperature stable recombination layer for mesoscopic perovskite/silicon monolithic tandem solar cells”, *Applied Physics Letters*, 109(109):233902 (2016)
4. M. Rienäcker, M. Bossmeyer, A. Merkle, U. Römer, F. Haase, J. Krügener, R. Brendel, R. Peibst, “Junction Resistivity of Carrier-Selective Polysilicon on Oxide junctions and Its Impact on Solar Cell Performance”, *IEEE Journal of Photovoltaics*, 7,11 (2017)
5. J. Krügener, F. Haase, M. Rienäcker, R. Brendel, R. Peibst, H.-J. Osten, “Improvement of the SRH Bulk Lifetime upon Formation of n-Type POLO Junctions for 25% Efficient Si Solar Cells”, *Solar Energy Materials & Solar Cells*, 173, 85 (2017)
6. T. F. Wietler, D. Tetzlaff, J. Krügener, M. Rienäcker, F. Haase, Y. Larionova, R. Brendel, R. Peibst, “Pinhole Density and Contact Resistivity of Carrier Selective Junctions with Polycrystalline Silicon on Oxide”, *Applied Physics Letters*, 110:253902 (2017)
7. E. L. Warren, M. G. Deceglie, M. Rienacker, R. Peibst, A. C. Tamboli, and P. Stradins, “Maximizing tandem solar cell power extraction using a three-terminal design”, *Sustainable Energy Fuels*, 2 (6), 1141-1147 (2018)
8. F. Haase, C. Klamt, S. Schäfer, A. Merkle, M. Rienäcker, J. Krügener, R. Brendel, and R. Peibst, “Laser contact openings for local poly-Si-metal contacts enabling 26.1 %-efficient POLO-IBC solar cells”, *Solar Energy Materials & Solar Cells*, 186, 184-193 (2018)

9. N. Folchert, M. Rienäcker, A. A. Yeo, B. Min, R. Peibst, R. Brendel, “Temperature-Dependent Contact Resistance of Carrier Selective Poly-Si on Oxide Junctions”, *Solar Energy Materials & Solar Cells*, 185, 425-430 (2018)
10. M. Schnabel, M. Rienäcker, E. L. Warren, J. F. Geisz, R. Peibst, P. Stradins, A. C. Tamboli, “Equivalent Performance in Three-Terminal and Four-Terminal Tandem Solar Cells”, *IEEE Journal of Photovoltaics*, 8 (6), 1584-1589 (2018)
11. M. Rienäcker, E. L. Warren, M. Schnabel, H. Schulte-Huxel, R. Niepelt, R. Brendel, P. Stradins, A. C. Tamboli, R. Peibst, “Backcontacted bottom cells with three terminals: Maximizing power extraction from currentmismatched tandem cells”, *Prog. Photovolt. Res. Appl.*, 27, 410 423 (2019)
12. K. T. VanSant, J. Simon, J. F. Geisz, E. L. Warren, K. L. Schulte, A. J. Ptak, M. S. Young, M. Rienäcker, H. Schulte-Huxel, R. Peibst, and A. C. Tamboli , “Toward Low-Cost 4-Terminal GaAs//Si Tandem Solar Cells”, *ACS Applied Energy Materials*, 2 (4), 23752380 (2019)
13. R. Peibst, M. Rienäcker, B. Min, C. Klamt, R. Niepelt, T. F. Wietler, T. Dullweber, E. Sauter, J. Hübner, M. Oestreich, and R. Brendel, “From PERC to Tandem: POLO- and p+/n+ Poly-Si Tunneling Junction as Interface Between Bottom and Top Cell”, *IEEE Journal of Photovoltaics*, 9 (1), 49-54 (2019)
14. M. Schnabel, H. Schulte-Huxel, M. Rienäcker, E. L. Warren, P. F. Ndione, B. Nemeth, T. R. Klein, M. F. A. M. van Hest, J. F. Geisz, R. Peibst, P. Stradins, and A. C. Tamboli , “Three-terminal IIIV/Si tandem solar cells enabled by a transparent conductive adhesive”, *Sustainable Energy Fuels*, 4 (2), 549-558 (2020)
15. C. Hollemann, F. Haase, M. Rienäcker, V. Barnscheidt, J. Krügener, N. Folchert, R. Brendel, S. Richter, S. GroSSer, E. Sauter, J. Hübner, M. Oestreich, R. Peibst, “Separating the two polarities of the POLO contacts of an 26.1%-efficient IBC solar cell”, *Scientific Reports*, 10, 658 (2020)
16. E. L. Warren, W. E. McMahon, M. Rienäcker, K. T. VanSant, R. C. Whitehead, R. Peibst, and A. C. Tamboli, “A Taxonomy for Three-Terminal Tandem Solar Cells”, *ACS Energy Letters*, 5 (4), 1233-1242 (2020)
17. S. Gharibzadeh, I. M. Hossain, P. Fassel, Abdollahi. B. Nejand, T. Abzieher, M. Schultes, E. Ahlswede, P. Jackson, M. Powalla, S. Schäfer, M. Rienäcker, T. Wietler, R. Peibst, U. Lemmer, B. S. Richards, and U. W. Paetzold, “2D/3D Heterostructure for Semitransparent Perovskite Solar Cells with Engineered Bandgap Enables Efficiencies Exceeding 25% in Four-Terminal Tandems with Silicon and CIGS”, *Advanced Functional Materials*, 1909919 (2020)
18. I. M. Hossain, Y. J. Donie, R. Schmager, M. S. Abdelkhalik, M. Rienäcker, T. F. Wietler, R. Peibst, A. Karabanov, J. A. Schwenzer, S. Moghadamzadeh,

- U. Lemmer, B. S. Richards, G. Gomard, and U. W. Paetzold, “ Nanostructured front electrodes for perovskite/c-Si tandem photovoltaics”, *Opt. Express*, 28 (6), 8878-8897 (2020)
19. K. T. VanSant, E. L. Warren, J. F. Geisz, T. R. Klein, S. W. Johnston, H. Schulte-Huxel, M. Rienäcker, R. Peibst, and A. C. Tamboli, “ Design Flexibility of 3-Terminal Tandems: A Performance Comparison Between GaInP//Si and GaAs//Si”, *ACS Energy Letters*, under review (2020)
20. R. Whitehead, K. T. VanSant, E. L. Warren, J. Buencuerpo, M. Rienäcker, R. Peibst, J. F. Geisz, A. C. Tamboli, “ Optimization of four terminal rear heterojunction GaAs on Si interdigitated back contact tandem solar cells”, *Applied Physics Letters* 118 (18), 183902 (2021)

C.2. Conference proceedings

1. R. Peibst, U. Römer, Y. Larionova, H. Schulte-Huxel, T. Ohrdes, M. Häberle, B. Lim, J. Krügener, D. Stichtenoth, T. Wütherich, C. Schöllhorn, J. Graff and R. Brendel, “Building blocks for back-junction back-contacted cells and modules with ion-implanted poly-Si junctions”, , in *Proc. of 40th IEEE Photovoltaic Specialists Conference (PVSC), Denver, CO, USA*, pp. 08520856 (2014)
2. M. Rienäcker, A. Merkle, U. Römer, H. Kohlenberg, J. Krügener, R. Brendel, R. Peibst, “Recombination behavior of photolithography-free back junction back contact solar cells with carrier-selective polysilicon on oxide junctions for both polarities”, *Energy Procedia*, 92: 412-418 (2016)
3. R. Brendel, M. Rienäcker, R. Peibst, “A quantitative measure for the carrier selectivity of contacts to solar cells”, *In Proc. of 32nd European Photovoltaic Solar Energy Conference and Exhibition*, pp. 447-451 (2016)
4. M. Schnabel, M. Rienäcker, A. Merkle, T. R. Klein, N. Jain, S. Essig, H. Schulte-Huxel, E. Warren, M. F.A.M. van Hest, J. Geisz, J. Schmidt², R. Brendel, R. Peibst, P. Stradins, A. Tamboli, “III-V/Si Tandem Cells Utilizing Interdigitated Back Contact Si Cells and Varying Terminal Configurations”, *In Proc. of 44th IEEE Photovoltaic Specialists Conference (PVSC), Washington DC, USA*, pp. 3371-3375 (2017)
5. M. Rienäcker, M. Schnabel, E. Warren, A. Merkle, H. Schulte-Huxel, T.R. Klein, M.F.A.M. van Hest, M.A. Steiner, J. Geisz, S. Kajari-Schröder, R. Niepelt, J. Schmidt, R. Brendel , P. Stradins, A. Tamboli and R. Peibst, “Mechanically stacked dual-junction and triple-junction III-V/Si-IBC cells with efficiencies of 31.5% and 35.4%”, *In Proc. of 33rd European Photovoltaic Solar Energy Conference and Exhibition, Amsterdam, Netherlands*, pp. 1-4 (2017)

6. **H. Schulte-Huxel, T. J. Silverman, D. J. Friedman, M. G. Deceglie, M. Rienäcker, M. Schnabel, E. L. Warren, R. Niepelt, M. R. Vogt, P. Stardins, R. Peibst and A. C. Tamboli** , “Yield analysis and comparison of GaInP/Si and GaInP/GaAs tandem solar cells”, *AIP Conference Proceedings*, 1999, 120002 (2018)
7. **R. Peibst, M. Rienäcker, B. Min, C. Klamt, R. Niepelt, T. Wietler, T. Dullweber, E. Sauter, J. Hübner, M. Oestreich, R. Brendel**, “p+/n+ polysilicon-on-oxide tunneling junctions as an interface of p-type PERC cells for tandem applications”, *In Proc. of 7th World Conference on Photovoltaic Energy Conversion (WCPEC-7)*, Waikoloa, Hawaii, USA, pp. 2635-2637 (2018)
8. **K. VanSant, M. Schnabel, J. Simon, J. Geisz, A. Ptak, M. Young, D. Guiling, W. Olavarria, M. Rienäcker, H. Schulte-Huxel, R. Niepelt, S. Kajari-Schroeder, R. Brendel, R. Peibst, A. Tamboli**, “HVPE-Grown GaAs//Si Tandem Device Performance”, *In Proc. of 7th World Conference on Photovoltaic Energy Conversion (WCPEC-7)*, Waikoloa, Hawaii, USA, pp. 2776-2778 (2018)
9. **E. L. Warren, M. Rienäcker, M. G. Deceglie, M. Schabel, Robby Peibst, A. C. Tamboli, P. Stradins**, “Operating principles of three-terminal solar cells”, *In Proc. of 7th World Conference on Photovoltaic Energy Conversion (WCPEC-7)*, Waikoloa, Hawaii, USA, pp. 2648-2650 (2018)
10. **E. L. Warren, M. Rienäcker, M. G. Deceglie, M. Schabel, Robby Peibst, A. C. Tamboli, P. Stradins**, “Operating principles of three-terminal solar cells”, *In Proc. of 7th World Conference on Photovoltaic Energy Conversion (WCPEC-7)*, Waikoloa, Hawaii, USA, pp. 2648-2650 (2018)
11. **M. Rienäcker, E. L. Warren, T. F. Wietler, A. C. Tamboli, R. Peibst**, “Three-Terminal Bipolar Junction Bottom Cell as Simple as PERC: Towards Lean Tandem Cell Processing”, *In Proc. of 46th IEEE Photovoltaic Specialists Conference (PVSC)*, Chicago, IL, USA, pp. 2169-2175 (2019)
12. **P. Stradins, M. Rienaecker, R. Peibst, A. Tamboli and E. Warren**, “A simple physical model for three-terminal tandem cell operation”, *In Proc. of 46th IEEE Photovoltaic Specialists Conference (PVSC)*, Chicago, IL, USA, pp. 2176-2178 (2019)
13. **E. L. Warren, W. E. McMahon, M. Rienaecker, K. T. VanSant, R. C. Whitehead, R. Peibst, and A. C. Tamboli**, “Fundamentals of three-terminal tandem solar cells: a comprehensive taxonomy”, *In Proc. of 47th IEEE Photovoltaic Specialists Conference (PVSC)*, Virtual Meeting, (2020)
14. **S. Gharibzadeh, I. M. Hossain, P. Fassel, A. Mertens, S. Schafer, M. Rienacker, T. Wietler, R. Peibst, U. Lemmer, B. S. Richards, and U. W. Paetzold**, “2D Surface Passivation in Semi-transparent Perovskite Top Solar Cells with Engineered Bandgap for Tandem Photovoltaics”, *In Proc. of 47th IEEE Photovoltaic Specialists Conference (PVSC)*, Virtual Meeting, (2020)

15. **I. M. Hossain, S. Gharibzadeh, P. Fassel, A. Mertens, S. Schäfer, M. Rienäcker, T. Wietler, R. Peibst, U. Lemmer, B. S. Richards, and U. W. Paetzold**, “2D Surface Passivation for Semi-Transparent Perovskite Solar Cells with Engineered Bandgap for 4T Tandem Photovoltaics”, *In Proc. of 37th European Photovoltaic Solar Energy Conference and Exhibition, Online Event, (2020)*
16. **I. M. Hossain, K. Goth, Y. J. Donie, R. Schmager, S. Gharibzadeh, M. Rienäcker, T. F. Wietler, R. Peibst, S. Moghadamzadeh, J. A. Schwenzer, U. Lemmer, B. S. Richards, G. Gomard, U. W. Paetzold**, “Periodic and disordered nanophotonic front electrodes for perovskite-based tandem photovoltaics”, *In Proc. of Organic, Hybrid, and Perovskite Photovoltaics XXI*, Vol. 11474, p. 114740M (2020)

C.3. Given conference talks

1. **M. Rienäcker, A. Merkle, U. Römer, H. Kohlenberg, J. Krügener, R. Brendel, R. Peibst**, “Recombination behavior of photolithography-free back junction back contact solar cells with carrier-selective polysilicon on oxide junctions for both polarities”, 6th International Conference on Silicon Photovoltaics (6th SiliconPV), Chambéry, France, 07.-09.03.2016
2. **M. Rienäcker, M. Bossmeyer, A. Merkle, U. Römer, F. Haase, J. Krügener, R. Brendel, R. Peibst**, “Junction Resistivity of Carrier-Selective Polysilicon on Oxide junctions and Its Impact on Solar Cell Performance”, 43rd Photovoltaic Specialists Conference (43rd IEEE PVSC), Portland, OR, USA, 05.-10.06.2016
3. **M. Rienäcker, M. Schnabel, E. Warren, A. Merkle, H. Schulte-Huxel, T.R. Klein, M.F.A.M. van Hest, M.A. Steiner, J. Geisz, S. Kajari-Schröder, R. Niepelt, J. Schmidt, R. Brendel, P. Stradins, A. Tamboli and R. Peibst**, “Maximum power extraction enabled by monolithic tandems using interdigitated back contact bottom cells with three terminals”, Opening plenary talk at 33rd European Photovoltaic Solar Energy Conference and Exhibition, Amsterdam, Netherlands, 25.09.2017
4. **M. Rienäcker, E. L. Warren, T. F. Wietler, A. C. Tamboli, R. Peibst**, “Three-Terminal Bipolar Junction Bottom Cell as Simple as PERC: Towards Lean Tandem Cell Processing”, 46th IEEE Photovoltaic Specialists Conference (PVSC), Chicago, IL, USA, 16.-21.06.2019
5. **M. Rienäcker, V. Titova, J. Schmidt, R. Peibst**, “Measuring selectivity and extraction efficiency – The three-terminal Suns-VOC method applied to an n-type c-Si/SiO_y/TiO_x/Al junction”, 11th International Conference on Silicon Photovoltaics (11th SiliconPV) 20.04.2021

D. Acknowledgment (Danksagung)

Zu guter Letzt möchte ich mich bei allen bedanken, die zum Gelingen meiner Dissertation beigetragen haben, insbesondere bei...

Last but not least, I would like to thank everyone who helped make my doctoral studies a success, especially...

- ... meinem Doktorvater Prof. Dr. Robby Peibst für die gute Betreuung, die vielen Ideen und die gewährten Freiheiten.
- ... Prof. Dr. Uwe Rau für die Bereitschaft das Koreferat zu übernehmen und Prof. Dr. Hans-Jörg Osten für das Übernehmen des Prüfungsvorsitzes.
- ... Heike Kohlenberg für die hervorragende Zusammenarbeit, das exzellente Umsetzen meiner Ideen im Reinraum und die schöne Zeit neben der Arbeit.
- ... Agnes Merkle für die lehrreiche und angenehme Zusammenarbeit zu Rückkontaktso-larzellen im HERCULES-Projekt und die schönen Dienstreisen.
- ... Guido Glowatzki, Raymond Zieseniss, Bernd Koch und Dr. Jan Krügener für die gute Zusammenarbeit und die große Hilfe beim Prozessieren am MBE/LNQE.
- ... Marcel Boßmeyer für die gute Zusammenarbeit während seiner Abschlussarbeit.
- ... *my collaborators at NREL Dr. Adele Tamboli, Dr. Emily Warren, Dr. Kaitlyn VanSant, Dr. Manuel Schnabel, Dr. Paul Stradins, Dr. Bill McMahon, Dr. John Geisz and Dr. David Young for the fruitful collaboration on three-terminal tandems, enjoyable monthly team meetings and for their hospitality during the visit in Golden.*
- ... *Prof. Dr. Arthur Onno from Arizona State University and Prof. Dr. Rolf Brendel from ISFH for fruitful discussions on the definition of selectivity.*
- ... meinen Korrekturlesern Agnes M., Arthur O., Boris V.-W., Emily W., Jan K., Paul S., Robert W., Sascha W. Sören S. und Udo R..
- ... meinen Bürokollegen Alexandra, Arne, Boris, Dimitri, Jörg, Lasse und Valeriya für die gute Arbeitsathmosphäre.
- ... vielen weiteren Kollegen am ISFH für die Einweisungen, die Hilfe beim Prozessieren und Messen und für ein gutes Arbeitsklima.
- ... meiner Familie, meiner Frau Birte und meinen Kindern Finn und Clara für die Unter-stützung und Liebe.

Michael Rienäcker

Diplom-Ingenieur

PERSONAL DATA

date of birth 12/23/1984
place of birth Fergana (Uzbekistan)
citizenship German

EDUCATION

05/2015 **PhD studies**, *Institute for Materials and Devices, Leibniz Universität Hannover.*
–09/2020 title of PhD thesis: „Three-terminal tandem solar cells enabled by back-contacted bottom cells featuring passivating, carrier-selective polysilicon based junctions“
10/2007 **Power System Engineering (focus on solar cells)**, *Clausthal University of Technology, Clausthal-Zellerfeld.*
–09/2014 diploma thesis with focus on III-V on Si epitaxy for tandem solar cells : „Untersuchung der Stufendynamik auf der Silizium(100)-Oberfläche mit Gallium-Vorbelegung“ (investigations on step dynamics of Si(100) during Ga deposition)

RESEARCH EXPERIENCE

Since **Project manager**, *Research team of Prof. Dr. Robby Peibst: Emerging solar cell technologies*, Institute for Solar Energy Research Hameln/ Emmerthal GmbH, Emmerthal.
10/2020
05/2015 **PhD student**, *Research team of Prof. Dr. Robby Peibst: Emerging solar cell technologies*, Institute for Solar Energy Research Hameln/ Emmerthal GmbH, Emmerthal.
–09/2020
10/2013 **Intern**, *Research team of Prof. Dr. Robby Peibst: Emerging solar cell technologies*,
–01/2014 Institute for Solar Energy Research Hameln/ Emmerthal GmbH, Emmerthal.

AWARDS

10.2015 **Award for outstanding thesis**, *Founded by „Verein von Freunden der TU Clausthal“, Clausthal-Zellerfeld.*
09.2017 **Conference opening plenary talk and student award**, *33rd European Photovoltaic Solar Energy Conference and Exhibition, 2017, Amsterdam, Netherlands.*